The University Of Sheffield.

Stator Winding Fault Detection Techniques for Permanent Magnet Machine Drives

By

Rongguang Hu

A thesis submitted in partial fulfilment of the requirements for the degree of Doctor of Philosophy

Department of Electronic and Electrical Engineering

Faculty of Engineering

The University of Sheffield

December 2018

Abstract

The increasing application of permanent magnet (PM) machines in emerging safety critical sectors such as electric vehicles and “more electric” aircrafts due to their high torque density and high efficiency has raised the demand for high availability (or reliability). Health monitoring for the machines is becoming an important tool for improving drive availability by facilitating intelligent maintenance and avoiding catastrophic failure.

This thesis is concerned with the diagnostics of the turn-to-turn fault, also known as turn fault, in PM machine stator windings by enhancing the detectability, robustness against transient states, and reducing the sensitivity towards other faults especially high resistance connection (HRC) fault.

Firstly, it proposes a turn fault detection method based on current residual and angular integration. The fault feature is enhanced in the current residual while the impacts of transient states are minimized by the angular integration. Secondly, the fault features at the switching sideband harmonics are also studied and a fault indicator based on the PWM ripple currents is proposed and tested on different permanent magnet machines. Thirdly, to distinguish the HRC fault from the turn fault, both the impedance around switching sideband frequencies and high frequency voltage injection are investigated, which explore the different behaviours of resistive and inductive asymmetry at high frequency. The robustness against transient states is achieved by the signal processing in the designed circuit board. Finally, to improve the fault detectability at high frequency, an artificial neutral point is established to provide zero sequence voltage measurements at both fundamental and high frequencies, and the results allow for a better classification of HRC and turn faults with less impact from operating conditions. The investigation and implementation of turn fault detection techniques for a commercial permanent magnet alternator with a unique structure is also performed.

Acknowledgements

First and foremost, I would like to express my most sincere gratitude to my supervisor Professor Jiabin Wang, for the continuous support on my Ph.D. career, for his patience, motivation and enthusiasm. His invaluable guidance and immense knowledge has helped and enlightened me throughout the research and thesis writing. I also would like to thank my second supervisor Dr. Andrew R Mills for his guidance into the new field of pattern recognition and machine learning, which will help me to broaden my horizons in the future work.

I would like to thank Rolls-Royce plc for the funding and support of my Ph.D. research, and for the opportunity of communication and networking in the industry. And also my sincere thanks to Dr. Keir Wilkie and Dr. David A Hewitt for the pleasant collaboration and inspiring discussion on the projects.

I am also very grateful to my genuine friends and cheering working colleagues Dr. Xiao Chen, Dr. Chaohui Liu, Dr. Liang Chen, Dr. Tianfu Sun, Dr. Bo Wang, Dr. Bhaskar Sen, Dr. Sreeju S Nair, Yanwen Shi, Shangjian Dai, Zhengmeng Liu, and Jian Zhen. They are always there to offer help and support.

I am also indebted to my beloved Miss Wenjun Zhang, for the warmth and happiness that accompany me through the UK life. Last but not the least, my eternal gratitude goes to my parents for their unlimited support, encouragement and love, without which, I can never pursue my dreams.

Table of Contents

Abstract III

Acknowledgements V

Table of Contents VII

CHAPTER 1 Introduction 1

1.1 Electrical machines 1

1.2 Health monitoring 3

1.3 Fault types 6

1.3.1 Electrical faults 8

1.3.2 Mechanical faults 10

1.3.3 Magnetic faults 12

1.4 Challenges 14

1.5 Overview of research 16

1.6 List of Publications 18

CHAPTER 2 Current Residual Based Stator Turn Fault Detection 20

2.1 Introduction 20

2.2 Modelling of Interior Permanent Magnet Machine 24

2.2.1 Healthy machine model 25

2.2.2 Machine model under turn fault condition 28

2.3 Residual acquired from machine model 34

2.3.1 Dq voltage residual 34

2.3.2 Dq current residual 36

2.4 Fault Detection 38

2.4.1 Fault indicator and detection steps 38

2.4.2 Sensitivity to other fault types 40

2.5 Experiments 41

2.5.1 Machine setup 41

2.5.2 Validation of the machine mathematical model 45

2.5.3 Influence of controller bandwidth 47
2.5.4 Fault detection at steady state 48
2.5.5 Fault detection at transient state 52
2.6 Conclusions 55
CHAPTER 3 PWM Ripple Currents Based Turn Fault Detection 56
3.1 Introduction 56
3.2 Analytical Study of HF PWM ripple currents 57
3.2.1 Turn fault detection technique based on PWM ripple currents 57
3.2.2 Analysis of HF PWM ripple currents 59
3.3 Turn fault indicator analysis 63
3.3.1 Prediction of HF PWM ripple currents 63
3.3.2 Fault indicator 66
3.4 Simulation results 68
3.5 Experiment Results 72
3.6 Extension to 3 phase SPM machines 78
3.6.1 Machine Model in Turn Fault Conditions 79
3.6.2 Turn fault indicator 82
3.6.3 Simulation Results 87
3.7 Extension to 3 phase IPM machines 90
3.8 Conclusions and discussions 99
CHAPTER 4 Detection and Classification of Turn Fault and High Resistance Connection Fault based on High Frequency Signals 101
4.1 Introduction 101
4.2 The effect of HRC fault on the turn fault detection method 104
4.2.1 The effect of HRC fault on the current residual based method 104
4.2.2 The effect of HRC on the PWM ripple current based method 106
4.3 Fault feature analysis 108
4.3.1 Turn fault conditions 108
4.3.2 High resistance connection fault 110

4.4 Fault detection and classification 111
4.5 Simulation results 114
4.6 High resistance connection fault features in IPM 119
4.7 Experiments in IPM Drive 122
4.7.1 High resistance connection fault setup 123
4.7.2 Current and voltage measurement and RMS detection 124
4.7.3 Experimental results 125
4.8 High frequency voltage injection based detection and classification 130
4.8.1 Injected high frequency signal 130
4.8.2 Theoretical analysis 133
4.8.3 Digital signal processing 136
4.8.4 Experimental results 137
4.9 Conclusions and discussions 145
CHAPTER 5 Detection and Classification of Turn Fault and High Resistance Connection Fault based on Zero Sequence voltage 147
5.1 Introduction 147
5.2 Fault feature analysis 148
5.2.1 Zero sequence voltage measurement 148
5.2.2 Healthy conditions 149
5.2.3 Turn fault conditions 151
5.2.4 High resistance connection fault conditions 152
5.3 Fault detection and classification 153
5.4 Simulation study 156
5.5 Experimental results 158
5.5.1 Fault detection and classification 158
5.5.2 Evaluation of the fault indicators 163
5.5.3 Turn fault detection at no load conditions 166
5.5.4 Turn fault detection at transient states 168
5.6 Conclusions and discussions 171

CHAPTER 6 Experimental Testing of Fault Detection on a Permanent Magnet Alternator.....173

6.1 Introduction.....173

6.2 Hardware components.....173

6.2.1 Prototype Trent 7000 PMA.....173

6.2.2 Power conditioning.....175

6.2.3 Signal processing platform.....177

6.3 Experimental setup.....181

6.4 Experimental tests.....184

6.4.1 Normal operations.....184

6.4.2 Inter-turn short circuit fault.....185

6.4.3 Fault detection based on fundamental component or RMS value of zero sequence voltage.....189

6.4.4 Fault detection based on the ratio between the fundamental and 3rd harmonics of the zero sequence voltage.....193

6.4.5 Fault detection based on switching sideband harmonics in zero sequence voltage.....196

6.4.6 Fault detection based on 2nd harmonic of phase current vector.....199

6.5 Conclusion.....202

CHAPTER 7 Conclusions and Future Work.....203

7.1 Conclusions.....203

7.1.1 Turn fault detection based on current residual.....203

7.1.2 Angular integration of dc component.....203

7.1.3 Turn fault detection based on PWM ripple currents.....204

7.1.4 Turn fault detection and discrimination from HRC fault based on switching harmonic high frequency impedance.....204

7.1.5 Turn fault detection and discrimination from HRC fault based on high frequency voltage injection.....205

7.1.6 Turn fault and HRC fault detection base on zero sequence voltage 206

7.1.7 Comparisons of all the proposed turn fault techniques.....206

7.2 Future work 207

7.2.1 Turn fault when fault resistance is not zero 207

7.2.2 The prognostics for turn fault..... 207

7.2.3 The classification from other fault types..... 208

A Appendix…….. 209

A1 The DSP codes for the current residual detection 209

A2 The DSP codes for the high frequency voltage injection 212

A3 The signal measurement and conditioning circuit design 217

A4 The data acquisition and digital signal processing of Xilinx Zynq-7000 SoC ZC702 Evaluation Kit..... 220

List of Figures……224

List of Tables…….. 234

Bibliography…… 235

CHAPTER 1 Introduction

1.1 Electrical machines

Electrical machines have been researched and developed over a century, from conventional DC/AC motors to more advanced ones with higher efficiency and better performance. With the development of power electronics, electrical machines can be controlled for various applications, and more advanced control algorithms and techniques can be implemented to enhance the machine performance. Since they are environmentally friendly with no pollutant gas emission, there is a trend for them to replace conventional combustion engines and hydraulic actuation systems. At present, they are being applied widely into many industries, including manufacturing, transportation, services, renewable energy and household appliances with a great potential.

One of the most attractive and promising application of electrical machines is electric vehicle[1][2]. Vehicles driven by internal combustion engine have been existed for more than a hundred years. But with the increasing concerns on energy consumption and air pollution, electric vehicles driven by electrical machines are regarded as the best solution for reduction of CO2 and pollutant emission. The basic requirements of an electric machine in this field are:

1) High torque density and power density
2) Wide speed range
3) High efficiency over wide ranges
4) Wide constant power operating capability
5) High torque capability for start-up and hill climbing
6) High intermittent overload capability for overtaking

Another emerging application is more electric aircraft[3][4]. Generally, most of the drives in aircrafts are hydraulics for actuation functions, pneumatics for pressurization and de-icing. Electrical power is only used for avionics and utility functions. In the 1980s, the US initiated several programs to develop electrical actuation technologies for aircraft applications and then a concept called more electric aircraft (MEA) was proposed in 1990s. High-performance machines for aerospace applications are typically integrated into starter-generator embedded within an engine, in electro-mechanical

actuators for primary flight surfaces control, in the electric fuel pump, and in landing gear nose wheel steering system. From a system point of view, the required capability for an aircraft application should be based on the following factors: reliability, power density, efficiency, weight, control features and complexity, thermal robustness, and size[5][6].

Currently, the electrical machines that can be adopted in those applications are limited to induction machines (IM), switched reluctance machines(SRM), and permanent magnet synchronous machines (PMSM)[3][7]. Among these machine types, induction machine drive is the most mature technology[8]. In an IM, the magnetic field generated by the stator currents interacts with the induced rotor currents to create torque. They are considered as the potential machines for the electric propulsion of electric vehicles and hybrid electric vehicles (HEV)s, owing to their reliability, low cost, low maintenance, and ability to operate in hostile environments. It has been pointed in [8] that one of the major disadvantages is the inherent rotor copper losses, resulting in low efficiency, lower power density, which is more serious for high speed and large power motor. The switched reluctance machine has the simple and robust rotor structure, and the low cost. They are capable of fault-tolerant operation and can be controlled with good torque–speed characteristics. The torque is produced by the change of magnetic reluctance, which is dependent on the rotor position. Thus, the disadvantage is the significant torque ripples, as well as the vibration and acoustic noise due to the radial force pulsation, which are quite critical for certain applications. Permanent magnet synchronous machines utilize permanent magnet (PM) to provide an independent excitation source. They can be classified in to surface-magnet mounted and interior-magnet mounted, depending on the arrangement of the PMs. For PM machines with special structures which are referred as permanent magnet assisted synchronous reluctance machine (PMA SynRM) machine, both the permanent magnet torque and reluctance torque are combined to produce the total driving torque. As a result, the higher torque density and higher efficiency can be achieved for a wider speed range. A comprehensive comparison of the performance of these three machine types are given in Table 1-1, according to [3][9].

Table 1-1 Comparisons of different machine types

Performance indicator	IM	SRM	PMSM
Power density	Moderate	Moderate	High
Robustness	Moderate	High	Moderate

Efficiency	Moderate	High	High
Cost	Low	Low	High
Wide speed range	Moderate	High	High
Torque ripple	Low	High	Low
Acoustic noise	Low	Moderate	Low

With increasing requirements for high power/torque density and high efficiency, permanent magnet machines are becoming more and more attractive. Generally, they are classified as being either sinusoidal or trapezoidal back EMF machines, also known as BLAC and BLDC. Moreover, in order to meet the requirements for a specific application, topologies and control algorithms should be designed with advanced techniques which have been subject to numerous researches. In many emerging applications, high reliability of the PMSM is of great importance. Since the magnet-induced back EMF cannot be turned off in an event of inverter or winding insulation failure, the fault may cause serious damage to the machine, resulting in very high repair or replacement cost, unless the fault is detected and the fault tolerant control measure is adopted swiftly. Therefore, health monitoring is essential, which may help reveal the hidden state of machine health, detect an incipient fault or predict the remaining useful life, thus avoiding a real failure.

1.2 Health monitoring

Since a fault or failure of key components in a machine drive system is of great concern in safety-critical applications, condition based health monitoring is studied extensively with the purpose to maximize equipment availability, and to minimize the risk of the severe consequences and the maintenance cost[10].

This requires the monitoring of the health of the critical components and developing proper diagnostic or prognostic strategies to detect and identify incipient faults and predict the remaining useful life (RUL)[11][12][13]. Both of them are the two main categories under the healthy monitoring scope, but have different characteristics and response time scale.

Diagnostics is aimed to investigate the occurrence, cause, type or location of the abnormal condition, while prognostics is concerned with predicting the future trend of the condition based on the analysis of the available information. Therefore, the properties of promptness and accuracy are essential for diagnostics, whereas the ability

to rational forecast and estimate the remaining useful life is more important for the prognostics.

The long degradation process of an impending fault in a machine system is shown in Fig. 1-1, which indicates the time when an early incipient fault develops, and depicts how the component reaches a failure state and eventually to complete catastrophic failure under continuing usage.

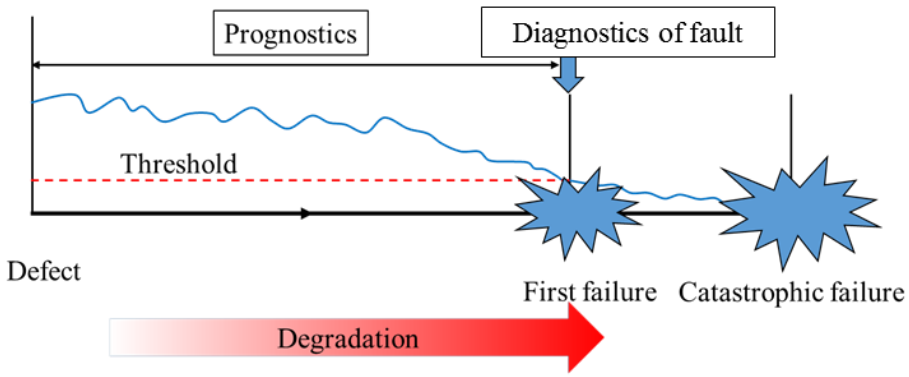

Fig. 1-1 Failure progress in time line

It is evident that the diagnostics of fault can only be effective on the moment or after the first failure has occurred. Thus, the damage to the machine and the risk of catastrophic failure are closely connected with the swiftness of the fault detection and mitigation measures. In order to take action before the fault occurrence, prognostics should be conducted all the time during the degradation process. The prediction of the failure time and its probability can be more and more accurate with the increasing operating time. Thus, the actual failure can be avoided with timely maintenance.

Because of their different objectives, the framework of a diagnostic program and that of a prognostic program should also be different. A diagnostic program consists of data acquisition, signal processing with feature extraction, and decision making, as shown in Fig. 1-2. The final decision fault type and location is made by comparing the extracted feature with the knowledge base, which can be derived from the historical data, physical models, or expert experience. For prognostics, several other steps are required, such as degradation models, performance assessment, and prediction [11]. The relation between the monitored data and the health condition need to be established. Then the degradation patterns need to be identified so that a proper mathematical model can be utilised to fit the pattern. Finally, the prediction algorithms are used to forecast the degradation of the machine performance, by using statistics, time series analysis, pattern recognition, or artificial intelligence techniques.

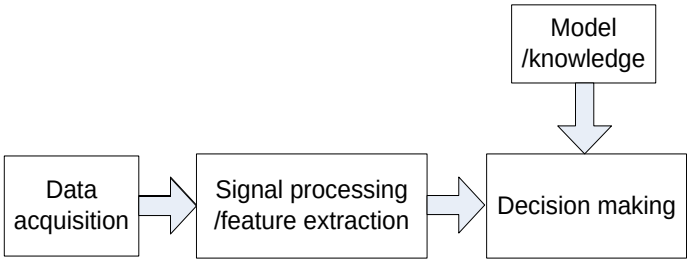

Fig. 1-2 Diagnostic program

Data acquisition is the process of collecting and storing useful data for the monitored system. It can be acoustic data, vibration data, pressure, temperature, moisture, etc. For the electrical machine system, current, voltage, speed and torque are also the commonly sampled data. Key properties for the data acquisition are the sampling frequency, bandwidth, and the data storage space. Their demands are dependent on the data variation frequency and the data processing algorithms. However, they can also be limited by the capability of the hardware. The acquired data are usually divided into three types: value type, waveform type, and multidimensional type[14]. The value type data such as temperature and pressure can provide the information for the current status directly. Thus, data processing algorithms are usually designed for the other two data types. For the waveform type data, the commonly used tools are the time-domain analysis, frequency-domain analysis, and time-frequency analysis. Time-domain analysis deals with mean, peak-to-peak values, standard deviation, or root mean square values. The most widely used conventional frequency-domain analysis is the spectrum analysis with fast Fourier transform(FFT)[15], which is capable to identify and isolate specific frequency components. However, the drawback is the inability to handle the non-stationary waveform signals which occur during transient operation. Thus, time-frequency domain analysis is developed[16]. Short time Fourier transformation, wavelet transformation, Wigner–Ville distribution, Choi–Williams and others provide broad perspectives to examine the signal, and enhance the feature extraction capability. For the multi-dimensional data type, complexity lies in the correlation structure among the data in different dimensions, especially when the dimensions are large. The principle component analysis(PCA)[17], independent component analysis(ICA) are the useful tools to reduce the data dimension and extract the core information. For the decision making step, there are three main strategies that can be implemented: data-driven approaches, model based approaches and the hybrid of the two approaches. The aim is to build the relationship between the information or features obtained and the typical machine faults. Data-driven approaches contains statistical approaches such as support vector machine (SVM), Hidden Markov Model

(HMM), and artificial intelligence approaches such as Artificial neural networks (ANN), Evolutionary algorithms (EA), Fuzzy logic systems. They can cope with various and complex systems but may require vast data and training time. The model-based approaches utilise physical or mathematical model of the monitored machine. With the explicit model available, residuals between the actual and normal values can be generated. Then the residuals are evaluated for the fault detection, isolation and identification. A correct and accurate model can make such approaches more effective. The hybrid approaches integrate both the data-driven and the model-based approaches and exploits the advantages of both to enhance the effectiveness and reliability of the diagnostics.

As has been stated, for the prognostics, the prognostic models are the key steps in order to predict the future condition. Data-driven techniques mentioned above are also commonly used for those models. Together with other techniques such as particle filtering[18], extended Kalman filtering[19], Gaussian process regression[20], fuzzy logic, neuro-fuzzy(NF)system, they are extensively reviewed and compared in [13]. They can all accommodate non-stationary and non-linear systems, but differ in the requirement of historic data and computation time.

For this thesis, only the fault diagnostics algorithms and techniques are explored exclusively for permanent magnet machines, while the fault prognostics is not covered.

1.3 Fault types

In an electrical machine, faults may occur on the stator, rotor and the mechanical components such as shaft and bearings. Surveys have been made to investigate the distribution of different types of fault and their probabilities in terms of the fault location. Results in [21] and [22] are illustrated in Fig. 1-3 and Fig. 1-4, respectively, for different application areas. As can be seen, the bearing faults always account for the largest portion of the fault types, whereas the stator winding faults are the second largest. If the causes of different faults are concerned in permanent magnet machines, then they can be classified into electrical fault, mechanical fault and magnetic fault, as shown in Fig. 1-5, according to[23].

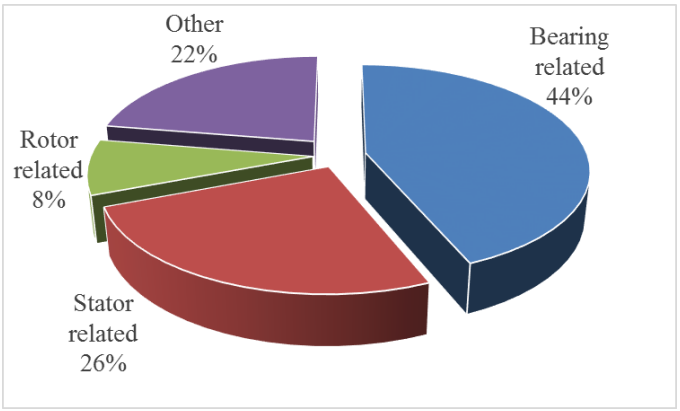

Fig. 1-3 Distribution of faults in [21]

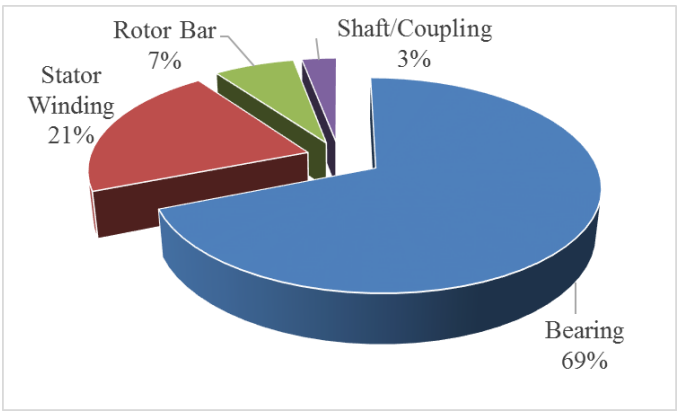

Fig. 1-4 Distribution of faults in [22]

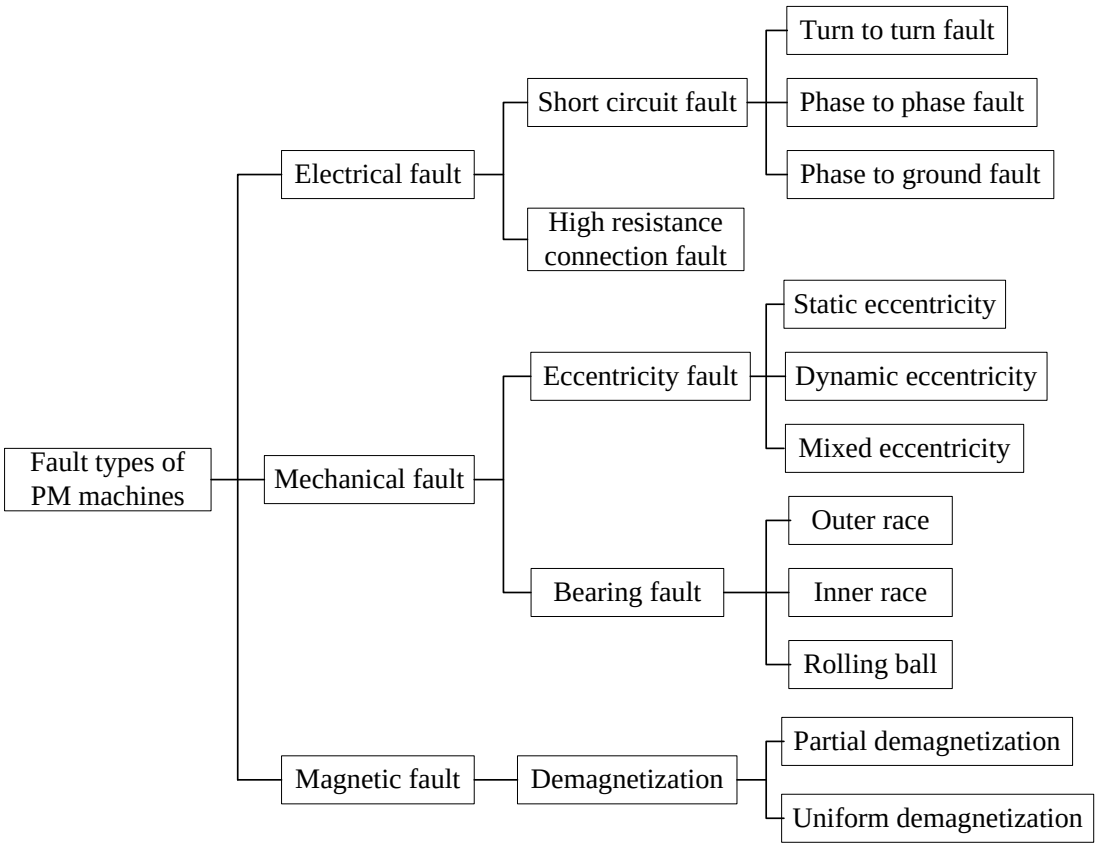

Fig. 1-5 Fault types in permanent magnet machines

1.3.1 Electrical faults

Electrical faults include the short-circuited fault and the high resistance connection fault. The short circuit can emerge between different turns within one phase windings, or between the windings of different phases, or between the windings and ground, constituting the turn-to-turn, phase-to-phase and phase-to-ground faults.

1.3.1.1 Turn-to-turn fault

It has been reported that short-circuit faults can start from an incipient turn-to-turn fault (or referred to as turn fault) [24] which occur due to insulation failures but develop into more serious phase-to-phase or phase-to-ground faults very quickly if no preventive mitigation or maintenance is performed. Insulation failures are attributed to many causes, such as excessive temperature, voltage stresses, vibration, and aging[25].

When there is a severe turn fault, a large circulation current will be generated in the shorted paths. Such large current may demagnetize the magnet irreversibly, degrading the operating performance. More seriously, it also gives rise to the temperature which accelerates the insulation deterioration process. As a result, the damage to the machine can be quick, thus, prompt diagnostic algorithms are essential and have been widely researched. The equivalent circuit in Fig. 1-6(a) is widely used to describe the turn-to-turn fault, assuming fault occurs in phase A. The winding is divided into healthy and faulted parts, with a resistance R_f representing the level of the insulation failure. The short-circuit current is inversely proportional to R_f and the percentage of the faulted turns over the total turns μ. It reaches the highest value when R_f is zero with only one turn fault.

In order to better demonstrate the relationships between the currents and voltages, mathematical models are developed. Models exhibit a trade-off between complexity and accuracy. From the simplest parameters based linear model as described in [26] to the more complex look-up table based nonlinear model in [27], they are the first step in the development of turn fault detection schemes. From these models, it can be inferred that the effect of turn fault on the basic voltage equations is the change of the inductance, which can be used as the feature to detect turn fault. According to [28], the diagnostic methods for the turn fault can be classified into 6 groups according to the used fault indicators: phase currents based, parameter estimation based, voltage based, search coil based, mechanical outputs based and mixed variables based methods. Among them, the

machine current signature analysis is most researched. The frequency components in phase currents shown in (1-1) considering saturation and stator slots have been analysed in [29], where p is the number of the pole pairs, and K_{sa} is a nonnegative integer, f_e is the supply fundamental frequency. It has been reported that the magnitudes of these frequency components will change in turn fault conditions, which can be used as applicable criterion for turn fault recognition. Subsequently, time-frequency analysis is applied due to its adaptability to transient states and fast response. However, for different topologies, the featured frequency components need to be studied separately. The 2nd harmonic in the dq axis currents and negative sequence components are also examined for the turn fault detection in [30][31]. They can be applicable for more generic machines as long as they are initially balanced.

$$f_{current} = \left(1 \pm \frac{2K_{sa}+1}{p}\right) f_e \tag{1-1}$$

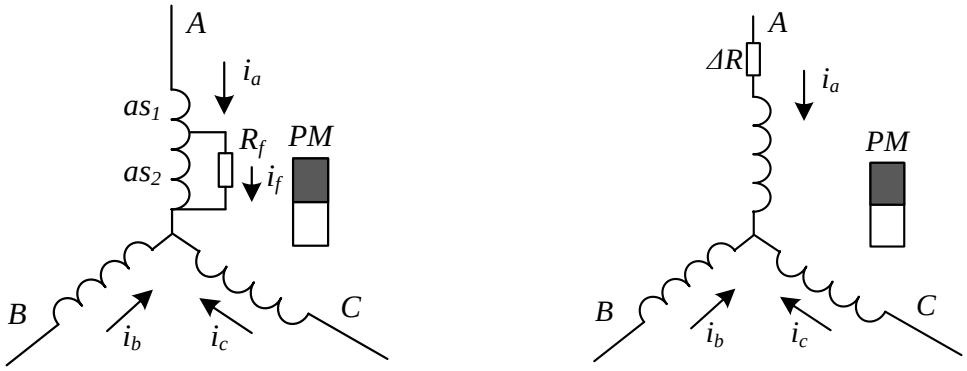

Fig. 1-6 Equivalent circuits of (a) turn-to-turn fault and (b)HRC fault

1.3.1.2 High resistance connection (HRC) fault

High resistance connection fault is the fault when unexpected excessive resistance is introduced into the winding cable connection circuit while the inductance is not influenced. It may be caused by thermal cycling and vibration, or damage of the contact surfaces due to pitting, corrosion, or contamination[32]. It can introduce unbalance to stator voltages and currents, decrease average torque, and increase torque pulsation, losses and heating. While HRC faults only degrade the machine performance and cause damage to the connector or contactor rather than a serious damage to the machine, the detection is not as time critical as the detection of turn fault[33]. The equivalent circuit for an HRC fault is shown in Fig. 1-6(b), where the fault is modelled by adding an additional resistor ΔR to the phase winding. In the basic voltage equations, it only results in changes in the resistance, and does not affect other parameters. However, it

generates similar symptoms to turn faults, such as the 2nd harmonic in dq currents/voltages and negative sequence components[34]. Thus ambiguity will be produced if these features are used for fault detection and classification. Since it is essential to classify the two fault types for the sake of appropriate remedy actions, further research is needed.

1.3.2 Mechanical faults

Eccentricity faults and bearing faults constitute the mechanical faults in the rotary machines.

1.3.2.1 Eccentricity

Eccentricity can be caused by the imperfections during the manufacturing stage, bearing wear, bent machine shaft, stresses applied to the shaft and mechanical resonance at critical speed. According to [35], the inherent level of static, dynamic, or mixed eccentricity is typically within 10% of the airgap.

The air gap between the stator and the rotor is non-uniform with eccentricity while should be distributed uniformly in a healthy machine. The asymmetric flux distribution and unbalanced magnetic pull (UMP) between the stator and the rotor will be generated. This UMP increases with eccentricity and cause vibration, noise, and excessive wear of the bearings, which, in turn may further increase the eccentricity. Thus, it is also essential to detect eccentricity and implement mitigation measures at the early stage to protect the machine from further damage.

There are three types of eccentricity, which are static eccentricity (SE), dynamic eccentricity (DE), and mixed eccentricity (ME). In SE, the rotor and rotation axis centre deviates from that of the stator, but is still motionless, as shown in Fig. 1-7(a). It will cause the airgap in certain section of the stator constantly smaller than the normal gap while the airgap in opposite section constantly bigger. As a result, the constant asymmetry in three phase inductance will be produced. In DE, the rotor geometric axis centre is also rotating around a certain centre, causing the airgap varies periodically, as shown in Fig. 1-7 (b). The impact on the three phase inductances is the introduction of additional harmonics, but symmetry still remains in average sense. In ME, both SE and DE exist, which makes the condition even worse, but are more likely to occur in a real system.

MCSA has been the most popular approach for eccentricity detection[36][15][37]. Under rotor eccentricity, the frequency components in current will exhibit apparent features[37][38][39], and equation (1-2) is suggested as the reliable indicator for detecting such eccentricity.

$$f_{ecc} = \left[1 \pm \left(\frac{2k-1}{p}\right)\right] f_e \tag{1-2}$$

where f_{ecc} and f_e are the feature and fundamental frequency components, p is the number of pole-pairs and k is a positive integer.

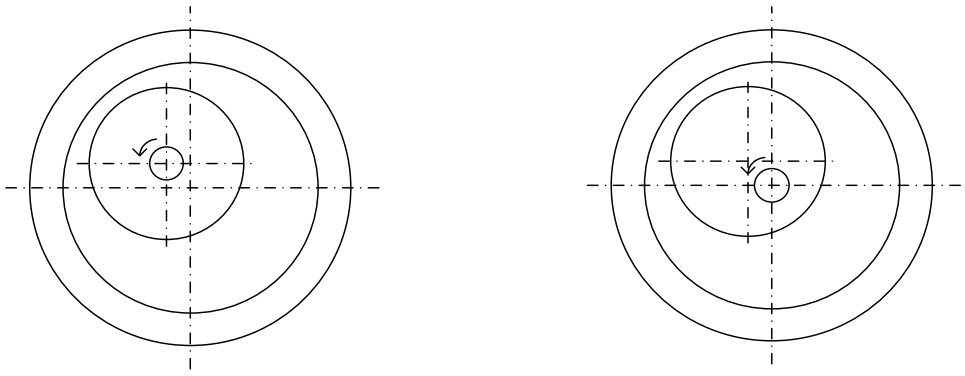

(a) Static eccentricity (b) Dynamic eccentricity

Fig. 1-7 Static and dynamic eccentricity

1.3.2.2 Bearing fault

Since rolling ball bearings are used to support the rotor in most electrical machines, they incur the largest proportion of the fault types. Rolling bearings consist of an inner and outer race, which are separated by rolling elements such as balls or cylindrical rollers. Flaking or pitting of bearings might occur when fatigue causes small pieces to break loose from the bearing. Other causes can be vibration, bearing current, thermal stresses which may further deteriorate the bearing lubrication[40].

Both intrusive and nonintrusive condition monitoring of bearing failures are explored in [40]. Different types of sensors can be utilized, such as vibration sensors, thermal sensors. In addition, chemical analysis, acoustic emission monitoring and sound pressure measurement are also used to detect bearing faults. However, they require specialized devices and equipment.

As has been pointed out in [41], if a damage is present in the bearing, shock pulses with characteristic frequencies f_c occur, when a ball passes through the damaged point. These characteristic frequencies depend on the affected part of the bearing and are

calculated by means of the geometry of the rolling elements and the mechanical rotational frequency. A radial motion of the rotor will occur in condition of bearing damage, thus, it is similar to the symptoms of dynamic eccentricity faults where specific frequency components in phase currents are produced, which are widely utilized for the monitoring of bearing condition[42], shown in (1-3). Also, the inductances start to contain additional harmonics but remain symmetric.

$$f_{current} = \left| f_e \pm k f_c \right| \tag{1-3}$$

1.3.3 Magnetic faults

As permanent magnets are the essential component for a permanent magnet machine, demagnetization is the common issue of the magnetic faults.

1.3.3.1 Demagnetization

Demagnetization fault occurs when the flux density inside permanent magnets in a PM machine is below the knee point. This phenomenon is usually caused by physical damage, high temperature stress, oxidation and corrosion, inverse magnetic fields and aging [43]. There are two types of demagnetization, uniform demagnetization on all magnets, and partial demagnetization on a few magnets or in certain regions[44]. The uniform demagnetization occurs when all the PMs in the machine are demagnetized with the same level and pattern, thus the back EMF is reduced symmetrically. It usually occurs when the rotor temperature rises uniformly or excessive currents are applied. In contrast, partial demagnetization may occur due to local heating or local excessive current caused by a turn-to-turn, phase-to-phase or a phase-to-ground fault. In this case, the additional harmonics can be introduced into the back EMF because of the non-uniform impact. But in terms of the three phase back EMF waveforms in one fundamental cycle, the impact is still symmetrical because the fault affects all three phases.

Due to the reduction of back EMF, larger stator current is needed in order to provide a required torque, which causes higher copper losses and degrade the efficiency. More heat will be generated and the demagnetization process can be accelerated. Partial demagnetization will cause variations of air gap flux density, stator currents and voltages and output torque. As a consequence, it will generate unbalanced magnetic pull, leading to acoustic noise and vibrations in the machine [43].

Different fault detection and diagnostic methods have been studied to detect motor faults, the most common of which are MCSA, vibration analysis and magnetic flux. Specific harmonics in the phase current will be generated due to the asymmetry caused by the partial demagnetization, as shown in (1-4) [45]. However, according to [46], the same frequency components can also be caused by dynamic eccentricity, which makes these faults difficult to distinguish. In the case of uniform demagnetization, no additional harmonics will be generated, thus, other techniques to monitor the magnet strength and back-EMFs are proposed[15][36].

$$f_{demag} = \left(1 \pm \frac{k}{p}\right) f_e \tag{1-4}$$

where f_{demag} is the demagnetization frequency components.

Among these possible fault types for a permanent magnet machine, turn-to-turn fault is the most severe but with a benign symptom, which requires the prompt detection and mitigation. Thus, this thesis focuses on the diagnostics of the turn-to-turn fault.

The basic voltage equations of the PM machine consist of resistive voltage drop, armature induced voltages, and permanent magnet electromotive force, given in (1-5). The parameters are balanced in healthy conditions but can be affected in fault conditions. Whether the effect on parameters in three phases is asymmetric or not determines some fault features. The fault detection method and the discrimination from other faults should consider which parameters are affected. The affected parameters in all possible fault types and their symmetries are summarised in Table 1-2, based on the previous discussions. Since turn fault detection is studied in this thesis mainly by asymmetric effects, the impact of other fault types on the proposed fault indicators will also be discussed.

$$\begin{cases} u_{an} = Ri_a + \dfrac{d(L_a i_a)}{dt} + \dfrac{d(M_{ab} i_b)}{dt} + \dfrac{d(M_{ac} i_c)}{dt} + e_a \\ u_{bn} = Ri_b + \dfrac{d(L_b i_b)}{dt} + \dfrac{d(M_{ab} i_a)}{dt} + \dfrac{d(M_{bc} i_c)}{dt} + e_b \\ u_{cn} = Ri_c + \dfrac{d(L_c i_c)}{dt} + \dfrac{d(M_{ac} i_a)}{dt} + \dfrac{d(M_{bc} i_b)}{dt} + e_c \end{cases} \tag{1-5}$$

Table 1-2 The effects of different faults on the parameters in voltage equations

Fault types	Most affected parameters	Symmetric or asymmetric
Turn-to-turn fault	Inductance, resistance	Asymmetric

HRC fault	Resistance	Asymmetric
Static eccentricity	Inductance	Asymmetric
Dynamic eccentricity	Inductance	Symmetric
Mix eccentricity	Inductance	Asymmetric
Bearing fault	Inductance	Symmetric
Uniform demagnetization	Back EMF	Symmetric
Partial demagnetization	Back EMF	Symmetric

1.4 Challenges

For the diagnostics of the faults in a permanent magnet machine, methods are reviewed and compared extensively in [23][47][48]. The machine current signal analysis (MCSA) is the most commonly used technique to detect most faults and is widely applied, although the identification and classification of fault is difficult. The common problem is that under transient states, fundamental frequency is varying, causing the conventional FFT unable to calculate frequency components any more. Advanced techniques such as short time Fourier transform (STFT) and wavelet transform (WT) have shown great potential[43][49]. However, STFT requires high processing power [50] and is not very flexible since the window function needs be pre-selected and fixed. Thus, the application to the speed and load variations are limited. The WT can provide good resolution in time for high-frequency components and a good resolution in frequency for low-frequency components. Thus, it features the capability of tracking frequency components under nonstationary states. The disadvantage is that the selection of the basic wavelet function could compromise the performance in identifying transient elements hidden within a dynamic signal [51]. If the same wavelet family is used over the entire data, the detectability can be degraded when fault current signatures are weak[52]. Other time-frequency analysis algorithms developed to provide better performances, such as Wigner-Ville distribution (WVD)[52], Pseudo-WVD, Zao-Atlas-Marks (ZAM) distribution[53], Hilbert-Huang transformation(HHT)[54]. However, the computational complexity is involved and they are more time consuming than FFT or WT.

In most cases, the fault features are only significant on one or only a few frequency components such as the 2^{nd} harmonics of the dq axis currents and voltages [30][55], fundamental component in the zero sequence voltages[56] or the induced voltage in the search coil [57]. Thus, those complex signal processing techniques are not necessary, while order tracking algorithms should be preferred, such as Kalman filtering[57], trigonometry and filtering based frequency tracking[56], Vold–Kalman filtering order

tracking (VKF-OT) [58], and computed order tracking (COT) [59]. However, when filtering is involved, the selection of bandwidth a key issue. A narrow bandwidth can separate close components but the response time is longer. The computed order tracking requires a resampling process before the conventional FFT processing, thus the computational burdens are increased.

For turn-to-turn short-circuited fault, the largest faulted current can be generated with only a single turn fault. However, due to the small proportion with regard to the total turns connected in series in one phase winding, the impact on the phase current or voltage is the smallest, as has been stated in [28]. This dilemma requires dedicated research on the increased detection sensitivity to the turn fault with small number of short-circuited turns.

Apart from the fault detection techniques based on the fundamental components and the lower frequency harmonics, high frequency components are also researched in [60][61]. Two types of high frequency components are proposed for then turn fault detection, i.e. the additional injected high frequency voltages and the inherent PWM switching high frequency harmonics. The high frequency negative sequence current, high frequency negative sequence impedance, and the high frequency zero-sequence voltage are proposed as the fault indicators in the former one. It is less sensitive to operating conditions of the machine, i.e., the flux linkage, load torque/current and fundamental frequency, as well as to the influence of control loops, but the effect of the additional voltage injection is inevitable. The latter one requires no additional signal injection, but takes the advantage of the inverter and the PWM voltages in the PM machine drive system, and analyses the natural high frequency signal in the phase currents. It is less intrusive, but dependent on the operating conditions. However, the performance of both types of high frequency based turn fault detection in the transient states have not been addressed.

While the conventional MCSA based turn fault detection method examines the phase current signals and extract the featured harmonics, it is no longer applicable for the no load conditions where the currents are zero. However, the back EMF in the shorted turns can still be active and generate a high fault current at a high speed. The risk of damaging the machine still remains. Thus, the detectability at no load conditions should be examined.

For most of the fault detection methods proposed in the existing publications, only the specific type of fault is considered while the effects of other faults are not mentioned. However, other faults may produce similar features in the frequency components and parameters asymmetry. For example, the zero sequence voltage is used for both inter turn fault and the high resistance connection fault detection in [56][62] respectively, but has not considered the other fault. The existing detection and classification techniques for the turn fault and HRC fault conditions use the amplitudes and angles of the zero sequence voltage, negative sequence current, fundamental current and impedance. However, the dependence on the parameters and their susceptibility to operating conditions and temperature make it less reliable. Also, the effect of transient states has not been considered yet.

1.5 Overview of research

The main purpose of this thesis is to address the challenges identified in section 1.4 in order to contribute reliable and robust turn fault diagnostic techniques for permanent magnet machines. The thesis contains 7 chapters and the content of each chapter is briefly outlined below.

Chapter 1 introduces the electric drive application trend in electrical vehicle and more electric aircraft, and compares different candidate machine types. For the requirement of high reliability, the concept of healthy monitoring and its two main objectives, i.e. fault diagnostics and prognostics are explained. The possible fault types of the permanent magnet machine are presented and the turn fault is selected as the research topic. The challenges of the fault diagnostics research are also highlighted.

Chapter 2 proposes a turn fault detection method based on the negative sequence component of the current residual, being the difference between the phase current measurement and estimation from a machine model. The fault features can be enhanced in the current residual if the model error is small, making detection more straightforward. Angular integration based negative sequence component extraction is implemented to minimize the impact of the transient states. Since the negative sequence component is examined rather than the featured harmonics in phase currents, the technique can be applied more widely to all balanced multi-phase machines. The analysis and test results also suggest that the effect from the controller can be minimised with the introduction of the current residual, which used to be one of the concerns of

utilizing current/voltage frequency components. However, since the negative sequence components are essentially caused by the asymmetry, other fault types might also generate similar features.

Chapter 3 investigates the switching sideband harmonics of phase currents and their application for the turn fault detection. The pulse-width modulated (PWM) drive is a natural source of high frequency voltage, and the fault features caused by change in inductance in a fault condition are contained in the corresponding PWM ripple currents. Their RMS value of the ripple currents in each phase are compared, and the resultant relative deviation is considered as the fault feature. The effect of transient states can be eliminated. Although the resistive and magnetic asymmetries can be removed in the high frequency region since the PWM ripple current is predominantly determined by inductance, they still affect the high frequency voltages through their influence on modulation index which comes from the control output. Thus the discrimination from other possible faults needs further study.

Chapter 4 first investigates the classification techniques for the turn fault and high resistance connection (HRC) fault based on the inherent high frequency components in both voltages and currents. The high frequency impedance can be defined and calculated, whose dependency on the current controller is eliminated because the influence on high frequency voltage equations has been accounted, which is different from the characteristic of the PWM ripple currents. With or without the deviations of the high frequency impedance is used to distinguish the turn fault and HRC fault, and is well-suited for surface-mounted PM machine whose phase inductances are almost constant. However, the HRC fault may also incur small deviations in the calculated high frequency impedance in the interior PM machine, where the phase inductance contains 2^{nd} harmonic, which complicates the classification. A high frequency voltage injection based technique is also investigated, in which the injected signals and the fault features can be independent from the operating conditions. The inductance asymmetry as a result of a turn fault can be exclusively detected. Thus, the HRC fault, demagnetization fault, dynamic eccentricity and bearing fault can be ruled out while the turn fault can be diagnosed.

Chapter 5 investigates the turn fault and HRC fault detection and classification based on zero sequence voltage. The measured zero sequence voltage only contains the fault signatures, through which the detectability are enhanced. Both the inherent high

frequency and fundamental frequency components are utilized for the fault detection. In the same way, the resistive and magnetic asymmetry can be ignored at high frequency, thus, turn fault can be diagnosed more exclusively. The robustness of turn fault detection during transient states and the detectability at no load conditions are also verified. Once fault negative for a turn fault is determined, the HRC fault detection can be achieved based on the fundamental frequency component analysis.

Chapter 6 explores possible turn fault detection techniques for a Rolls-Royce Trent 7000 engine permanent magnet alternator. Due to its unique structure, characteristics and control mode, which are very different from conventional PM machines, the previous proposed turn fault detection methods cannot be directly applied. Based on the measured signals, several fault indicators are examined and compared in both healthy and faulted conditions. And the optimal fault detection method for this machine is obtained and demonstrated.

Chapter 7 presents the conclusions and suggestions for future work.

1.6 List of Publications

Some parts of the research work reported in this thesis have been published in peer reviewed journals and international conferences, while other parts are under preparations. They are listed as follows.

Published papers:

1. R. Hu, J. Wang, A. Mills, E. Chong, Z. Sun, “PWM Ripple Currents Based Turn Fault Detection for Multiphase Permanent Magnet Machines”, IEEE Transactions on Industry Applications, vol. 53, no. 3, pp. 2740-2751, 2017.

2. R. Hu, J. Wang, A. Mills, E. Chong, Z. Sun, “PWM Ripple Currents Based Turn Fault Detection for 3-phase Permanent Magnet Machines”, IEEE International Electric Machines and Drives Conference (IEMDC 2017).

3. R. Hu, J. Wang, A. Mills, E. Chong, Z. Sun, “Turn Fault Detection for Surface-Mounted Permanent Magnet Synchronous Machine Based On Current Residual”, IEEE International Electric Machines and Drives Conference (IEMDC 2017).

4. R. Hu, J. Wang, A. Mills, E. Chong, Z. Sun, “Detection and Classification of Turn Fault and High Resistance Connection Fault in Inverter-fed Permanent Magnet Machines Based on High Frequency Signals”, IET International Conference on Power Electronics, Machines and Drives (PEMD 2018).

Papers under review and preparation:

1. R. Hu, J. Wang, A. Mills, E. Chong, Z. Sun, “Current Residual Based Stator Inter-Turn Fault Detection in Permanent Magnet Machines”, IEEE Transactions on Industrial Electronics, under review.

2. R. Hu, J. Wang, A. Mills, E. Chong, Z. Sun, “Detection and Classification of Turn Fault and High Resistance Connection Fault in Permanent Magnet Machines based on Zero Sequence voltage”, to be submitted IEEE Transactions on Power Electronics

3. R. Hu, J. Wang, A. Mills, E. Chong, Z. Sun, “Inter-turn fault detection in Permanent Magnet Machines based on High Frequency Voltages Injection”, to be submitted IEEE Transactions on Power Electronics

CHAPTER 2 Current Residual Based Stator Turn Fault Detection

2.1 Introduction

As explained in Chapter 1, turn-to-turn short circuit fault (also known as turn fault, or inter-turn fault) is among the most common machine failures, accounting for 21-37% of the faults in electrical machines [25][28]. Moreover, they are also one of the most severe faults [40], especially in the permanent magnet (PM) machines. The main cause of the turn faults is winding insulation deterioration as described in [63], which results from combined mechanical, electrical and thermal stresses in the stator winding. The stresses may lead to an insulation break-down between the coil conductors, which may short some of the turns. When a severe turn fault occurs, excessively high current will circulate in the shorted turns driven by induced voltages including the back electromagnetic force (EMF) and increase the winding temperature to a level where severe damage or even breakdown of the whole insulation occurs[64]. In some PM machines, the large short-circuit current can produce localized magnetic field intensity higher than the coercivity of the magnets, thereby demagnetizing the magnets irreversibly [25]. Also, a large percentage of the insulation failures starts from a turn-to-turn insulation problem and subsequently develops into more severe insulation faults, such as coil-to-coil, phase-to-phase, and phase-to-ground short circuits, all of which lead to catastrophic damage to the machine[63]. Therefore a swift detection of turn-to-turn short fault during machine operation is essential to avoid the subsequent damages, and reduce the repair cost and service outage time.

In recent years, turn fault detection has been extensively studied, numerous and various techniques and methods have been proposed. Among them, one of the most popular techniques is based on the machine current signal analysis (MCSA)[65][66]. Since the symmetrical distribution of magnetic flux in healthy normal operating condition is broken by the turn fault, several unique harmonics emerge. For different machine types, even different winding configurations, the featured harmonics are also different, which need individual analysis[67].

The significance of the frequency components in the machine current, however, is dependent on the control strategy. For permanent magnet machines that are commonly used in areas of electric vehicles and servo systems, a closed-loop current control

scheme is usually applied to regulate the current waveforms in a nearly perfect manner. In [68], the authors compared the behaviours of an induction machine under voltage mode and closed-loop current control mode, and have suggested that under the influence of the closed-loop control, the original fault indicators are no longer effective. It was proven in [69] that for a controller with higher bandwidth, the fault information can exists in both current and voltage signals. Therefore, in addition to the frequency components in the machine current, the frequency components from the machine phase voltages can also be used for the fault detection.

Among the featured frequency components in the electrical signals, the 2^{nd} harmonic in dq currents [30] and voltages is favoured by many authors[70][71][55]. The main cause of the 2^{nd} harmonic in the fault condition is that turn fault breaks the symmetry of the three phase balanced system. Thus without the consideration of other fault types, the emergence of the 2^{nd} harmonic in dq currents and voltages indicates the occurrence of the turn fault. Other methods based on the 2^{nd} harmonic of power[72][73], and the park's vector[74][75][76] can be seen as the extensions but with the same principle. Similarly, the negative sequence components are also the results of the broken symmetry when turn fault occurs, which has been pointed out in [40] that this is equivalent to the detection technique based on the 2^{nd} harmonic. Therefore, the detection based on the negative sequence currents, voltages are also widely researched[31][77]. To exploit both the negative sequence voltage and current, the identification of negative impedance is proposed in [78][79] in which the current regulating effect of the motor controller is accounted.

Apart from the traditional phase currents and voltages, other signals are also studied for the turn fault detection, which might need additional hardware other than the current transducers. The detection method based on the induced voltage on a search coil embedded in the rotor or stator is proposed in [80][81], which is also a promising indicator, even sensitive to a one-turn fault. In [82] it is demonstrated that the electromagnetic signature of a search coil is capable of detecting many types of fault, including static and dynamic eccentricity, turn-to-turn short circuit, phase-to-ground short circuit, and partial or uniform demagnetization. However, it is an invasive technique and it is not suitable for machines that have already been deployed, since only new motors under manufacturing or the damaged motors withdrawn from service can be inserted with the search coils. The harmonics of zero sequence voltage are also applied

for the turn fault detection in [58][67]. The sensitivity and accuracy can be improved compared with the method based on the phase currents, especially at lower speed. However, the neutral point of the stator windings as well as an extra voltage sensor is required. Other signals such as the spectrum of the magnetic flux measured by external flux sensor[83], and electromagnetic torque[84][85] are also proposed with their own unique merits and restrictions.

Once the featured signal is determined for turn fault detection, the frequency components extraction techniques need to be applied. The simplest way to perform frequency analysis is the fast Fourier transform (FFT)[67]. In [30], it has also been used to monitor the 2^{nd} harmonic of the q-axis current. When performing FFT, the frequencies of the signal concerned should be assumed constant for accurate detection, which means that the machine should operate in steady-state. Since this is not always the case, FFT is not a reliable for the extraction of these features. To obtain the fault signature under non-stationary conditions, it is necessary to perform analysis in time and frequency domains simultaneously. Short-time Fourier transform (STFT), which is the extension of FFT can be employed [86]. However, a trade-off must be made between time and frequency resolution. A short-duration window provides good time resolution at the expense of poor frequency resolution, whereas a long-duration window provides good frequency resolution at the expense of reduced-time resolution. Once the window is fixed, it is only applicable for a limited range of speed and load variations, limiting the detection over a wide range of operating conditions.

To overcome the problem, an alternative tool for fault feature extraction are used in [50], which is the continuous wavelet transform (CWT). The advantage over STFT is that the wavelet function is scalable, which enhances the wavelet transformation's adaptability to a wide range of frequency resolutions. Discrete wavelet transform (DWT) algorithms have also been developed and applied[87][88][89][90]. In [86], both STFT and DWT are analysed and tested experimentally, while the results show that DWT is obviously better than STFT. It is suggested in [91] that oscillations, shift sensitive, aliasing are the three main shortcomings of the DWT and can be overcome by the dual-tree complex wavelet transform (DTCWT). Other improvement of DWT such as stationary wavelet transform (SWT)[92] and wavelet packet transform (WPT)[93] are also applied in the frequency analysis for the fault detection. There are other time-frequency analysis algorithms developed to provide even better performances, such as

Wigner-Ville distribution (WVD)[52], Pseudo-WVD, Choi-Williams distribution [94], Zao-Atlas-Marks (ZAM) distribution [53], Hilbert-Huang transformation(HHT)[54]. Some of them are compared in [95][96][97], and conclusions are made, which are very helpful for the selection of an appropriate method. However, it should be pointed out that they greatly increase the computation complexity and time consumption of the data processing.

The frequency analysis techniques above are all purely based on the time series of voltage and current data. However, for the machine drive systems with a position sensor, the rotor position angle is always available, which can help extract the components of interest. The computed order tracking (COT) technique is proposed in [98] in which many restrictions of the FFT based methods are overcome. The original signal sampled at a constant time interval is resampled at a constant angular interval. The resampled data are equivalent to the constant frequency data in time domain while the order and amplitude information is reserved. Consequently, the normal FFT can be applied to the resampled data to obtain the spectrum of order where fault feature lies. Thus it can be used to detect the fault in nonstationary operating condition. Since in most cases, only a few frequency components are sensitive to turn faults, there is no need to obtain the whole spectrum of the signal. In this case, the Vold-Kalman filter order tracking (VKF-OT) is usually applied[58][49][99], where the fault-related harmonics are tracked while the rest of components are removed. It can extract both the amplitude and phase of the analysed orders from the original data in the time domain, and presents improved order resolution compared to other order tracking techniques[100]. These two conventional order tracking techniques in rotating machine diagnostics are compared in [101], and concerns of high computational burdens are also raised due to involved matrix inversion if a larger sized signal is analysed.

With these signal feature extraction algorithms, almost any variation in frequency components can be monitored and turn fault can be detected. In general, however, the more advanced are the techniques, the more demanding for computing power and data storage they may be[25][43][48]. The demand for storage space and processing time may be excessive to be implemented in a machine drive system with an ordinary microcontroller.

The machine signal analysis based techniques described above do not require the accurate physical model of the machine. However, if the machine's mathematical model

is available, then another turn fault detection technique based on the residual between the measured and model-estimated signals has also been developed. In these methods, the machine model can be established from lumped parameters[102][103], finite element simulated data, or even trained neutral network[77], depicting the normal behaviour of the machine. The most straightforward way to detect the fault by using the machine model is to detect the residual value, which is the difference between the model estimation and real measurement. The residual value is then regarded as the indicator. With the same voltage input into the machine and the model, the residual between the measured and estimated current can be extracted for fault detection in [102][103][104]. Likewise, with the same current input, the voltage residuals are used[70][77] in the case of closed-loop current control. In order to enhance the detection reliability, the residuals in both voltages and currents are used for the detection in [105].

In this chapter, a new current residual based turn fault detection method with angular integration order tracking algorithm is proposed. It combines the aforementioned two turn fault detection methods (frequency components based and residual based methods) to improve the detectability of a single turn fault and the robustness in transient states. The machine model in healthy conditions is established by finite element analysis and is utilized to estimate the machine currents in healthy conditions for given d- and q- axis voltage command. Through the comparison with the current measurements, the current residuals are produced, where the fault signatures are enhanced, since other unwanted components are eliminated. After transforming into the backward rotating frame, angular integration is applied to extract the dc values of the negative sequence components. The impact of the transient states can be, therefore, minimized. As a result, a single turn fault with a benign fault signature can be detected more reliably in both transient and steady state operations. The algorithm has been tested on a triple redundant 3x3-phase permanent magnet assisted synchronous reluctance machine (PMA SynRM).

2.2 Modelling of Interior Permanent Magnet Machine

As described in the introduction, the key feature of the current residual based turn fault detection is the use of the machine model in healthy conditions to emulate the machine behavior and to compare it with the measurement. If the machine is healthy, then the predicted output from the model and the measurement from the machine should be consistent. Thus, the analysis of the machine model is essential to produce the

residual, and to introduce the fault detection indicator. To simplify the analysis, the machine model described in this section neglects time and space harmonics, and magnetic saturation. This provides a physical insight of the signature associated with a turn fault for the development of fault detection techniques. However, the assumption is not required for implementation of the developed fault detection technique.

2.2.1 Healthy machine model

2.2.1.1 Healthy machine model in abc frame

For a typical, commonly used three phase permanent magnet machine, the equivalent circuit of the machine driving system can be illustrated in Fig. 2-1. The constant DC voltage is converted into pulse width modulation (PWM) switching voltages with symmetrical sinusoidal fundamental components through a three phase full-bridge inverter to power the three phase windings. The windings of each phase can be represented by the series connected resistance and self-inductance. When all the windings are excited with currents, the effect on the voltage of each winding may be represented in the form of mutual-inductance. The neutral point *n* of the windings is usually floating and not accessible.

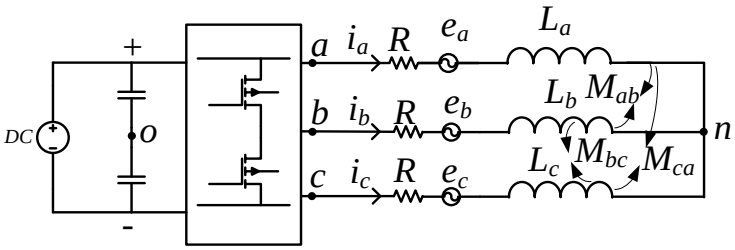

Fig. 2-1 Equivalent circuit of a three phase machine driving system

Generally, the three phase windings are distributed symmetrically in space, and the phase resistances are usually equal. For a surface-mounted permanent magnet machine, the equivalent air gap seen by the armature reaction field is large and approximately uniform for all the positions since the permeability of the magnets is close to that of air. As the result, both the self- and mutual- inductances given in (2-1) are identical and independent of the rotor position.

$$\begin{cases} L_a = L_b = L_c = L \\ M_{ab} = M_{bc} = M_{ca} = M \end{cases} \tag{2-1}$$

For interior permanent magnet machines, the physical machine airgap is usually uniform. However, since the permanent magnets are inserted inside of the rotor, the

permeance seen by the armature reaction field varies with the rotor position, leading to rotor position dependent self- and mutual-inductances. The effect can be approximated by 2nd harmonics. By way of example, the variations of the self- and mutual-inductances of phase A of the 36 slots 3 pole pairs PMA SynRM with rotor position at 1A in one electrical cycle obtained from the finite element analysis are shown in Fig. 2-2. By ignoring the high order harmonics, the self- and mutual- inductances can be expressed as (2-2).

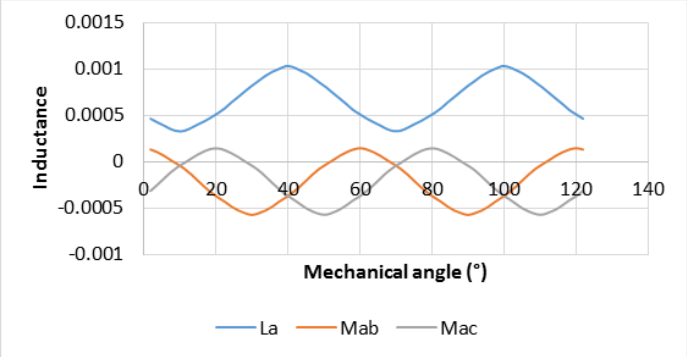

Fig. 2-2 Self- and mutual- inductances of phase A

$$\begin{cases} L_a = L_{ls} + L_{am} \approx L_{ls} + L_\Sigma - L_\Delta \cos(2\omega_e t) \\ L_b = L_{ls} + L_{bm} \approx L_{ls} + L_\Sigma - L_\Delta \cos(2\omega_e t - \frac{4\pi}{3}) \\ L_c = L_{ls} + L_{cm} \approx L_{ls} + L_\Sigma - L_\Delta \cos(2\omega_e t - \frac{2\pi}{3}) \\ M_{ab} = M_{ba} \approx -\frac{1}{2} L_\Sigma - L_\Delta \cos(2\omega_e t - \frac{2\pi}{3}) \\ M_{bc} = M_{cb} \approx -\frac{1}{2} L_\Sigma - L_\Delta \cos(2\omega_e t) \\ M_{ca} = M_{ac} \approx -\frac{1}{2} L_\Sigma - L_\Delta \cos(2\omega_e t - \frac{4\pi}{3}) \end{cases} \quad (2\text{-}2)$$

where ω_e is electrical angular speed. L_{ls} denotes the winding leakage inductance, L_Σ the component of the inductances that is independent of the rotor position, and L_Δ the magnitude of the rotor position-dependent inductance resulting from the rotor saliency.

When voltages are applied to the phase windings, the generated currents will produce magnetic flux linkage. Together with the permanent magnet flux linkage $\boldsymbol{\lambda}_{PM}$ shown in (2-3), the total flux linkage $\boldsymbol{\lambda}_s$ of a phase winding varies with time due to the time-varying current and rotor position. The time derivatives of the flux linkages together with the voltage drop on the resistance are equal to the phase voltages. The voltage equations for each phase winding can be expressed as (2-4).

$$\boldsymbol{\lambda}_s = \mathbf{L}_s \mathbf{i}_s + \boldsymbol{\lambda}_{PM} \tag{2-3}$$

$$\mathbf{U}_s = \mathbf{R}_s \mathbf{i}_s + d\boldsymbol{\lambda}_s / dt \tag{2-4}$$

Where $\mathbf{U}_s = \begin{bmatrix} u_{an} & u_{bn} & u_{cn} \end{bmatrix}^T$ $\mathbf{i}_s = \begin{bmatrix} i_a & i_b & i_c \end{bmatrix}^T$

$$\mathbf{L}_s = \begin{bmatrix} L_{aa} & M_{ab} & M_{ac} \\ M_{ba} & L_{bb} & M_{bc} \\ M_{ca} & M_{cb} & L_{cc} \end{bmatrix}$$

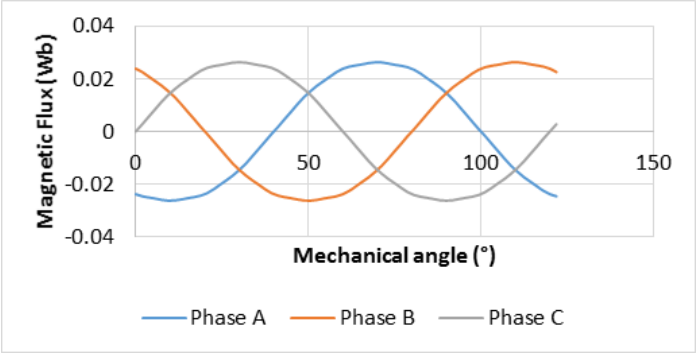

Fig. 2-3 Permanent magnet flux linkages

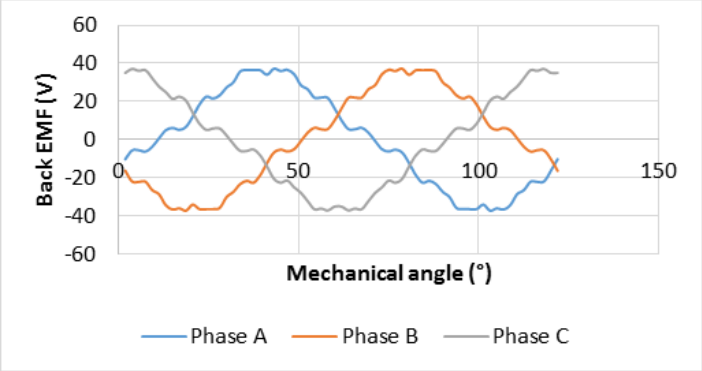

Fig. 2-4 Back EMF at 4000 rpm

The permanent magnet flux linkage curves of the PMA SynRM obtained from the finite element analysis are shown in Fig. 2-3, and they can be expressed as (2-5) if higher order harmonics are neglected. The back EMFs at the speed of 4000 rpm are shown in Fig. 2-4. The high order voltage ripples are caused by slotting effect.

$$\boldsymbol{\lambda}_{PM} = \begin{bmatrix} \lambda_a \\ \lambda_b \\ \lambda_c \end{bmatrix} \approx \lambda_{pm} \begin{bmatrix} \sin\theta_e \\ \sin(\theta_e - 2\pi/3) \\ \sin(\theta_e - 4\pi/3) \end{bmatrix} \tag{2-5}$$

where θ_e is the electrical angle, and it is the function of electrical angular speed ω_e and time t. λ_{pm} is the magnitude of the fundamental component of the permanent magnet flux linkage.

2.2.1.2 Healthy machine model in rotating dq frame

In order to simplify the modelling and to make it easier for machine control, Park transformation is usually adopted. The variables in the three phase abc frame are converted to the rotating dq frame with the transformation matrix **P** denoted by (2-6)and (2-7), where *X* can represent voltage *u*, current *i*, or flux linkage λ.

$$\mathbf{P}=\frac{2}{3}\begin{bmatrix}\cos\theta_e & \cos(\theta_e-2\pi/3) & \cos(\theta_e-4\pi/3)\\ -\sin\theta_e & -\sin(\theta_e-2\pi/3) & -\sin(\theta_e-4\pi/3)\end{bmatrix} \tag{2-6}$$

$$\begin{bmatrix}X_d\\ X_q\end{bmatrix}=\mathbf{P}\begin{bmatrix}X_a\\ X_b\\ X_c\end{bmatrix} \tag{2-7}$$

When the Park transformation is applied to the flux linkage and phase voltage equations (2-3)(2-4), they can be rewritten as (2-8)(2-9).

$$\boldsymbol{\lambda}_{dq}=\mathbf{P}\boldsymbol{\lambda}_{dq}=\mathbf{L_{dq}}\mathbf{i}_{dq}+\begin{bmatrix}\lambda_{pm} & 0\end{bmatrix}^T \tag{2-8}$$

$$\mathbf{U}_{dq}=\mathbf{R}_s\mathbf{i}_{dq}+d\boldsymbol{\lambda}_{dq}/dt \tag{2-9}$$

where $\mathbf{L_{dq}}=\mathbf{P}\mathbf{L}_s\mathbf{P}^{-1}=\begin{bmatrix}L_d & 0\\ 0 & L_q\end{bmatrix}$, $\mathbf{U_{dq}}=\begin{bmatrix}u_d\\ u_q\end{bmatrix}$, $\mathbf{i_{dq}}=\begin{bmatrix}i_d\\ i_q\end{bmatrix}$, $\boldsymbol{\lambda}_{\mathbf{dq}}=\begin{bmatrix}\lambda_d\\ \lambda_q\end{bmatrix}$.

By substituting (2-8) into (2-9), the mathematical machine model in the rotating dq reference frame can be expressed in (2-10)when high order harmonics are neglected.

$$\begin{cases}u_d=R_si_d+L_d\dfrac{di_d}{dt}-\omega_eL_qi_q\\ u_q=R_si_q+L_q\dfrac{di_q}{dt}+\omega_e(L_di_d+\lambda_{pm})\end{cases} \tag{2-10}$$

where u_d and u_q are the d- and q- axis voltages, i_d and i_q are the d- and q- axis currents, L_d and L_q are the d- and q- axis inductances.

2.2.2 Machine model under turn fault condition

2.2.2.1 Machine model in abc frame

The turn fault occurs when the different turns of the same coil begin to contact each other due to the degradation of the insulation between them. If the insulation degradation is severe, the contact resistance can be very low, which forms a short-

circuit path. If the contact resistance is zero in the extreme case, that part of the coil conductors is fully short circuited.

Without loss of generality, the turn fault is assumed to be in phase A, whose winding is divided into healthy and faulted parts, as shown Fig. 2-5. The contact resistance is denoted as R_f. The ratio of the number of the short-circuited turns over the total number of the turns in one phase is defined as μ, which represents the fault range between 0 and 1. The self-inductances in the healthy and faulted parts, and the mutual inductance between them are also defined. Since the back EMF can be considered proportional to the number of turns, the EMFs in healthy and faulted parts can be calculated accordingly.

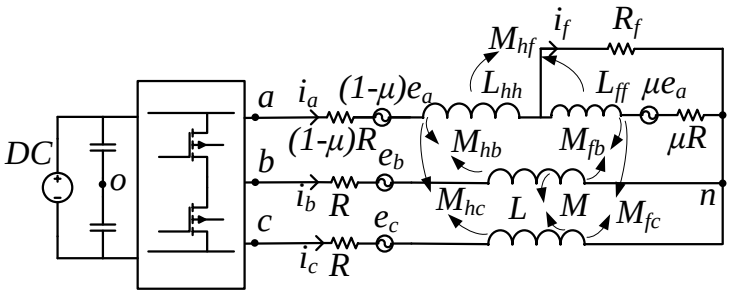

Fig. 2-5 Equivalent circuit and parameters in turn fault condition

Based on the equivalent circuit, the model for fault conditions can be expressed in (2-11) and (2-12), where u_{ah} and u_{af} denote the voltages in the healthy and faulted parts of phase A winding respectively, and i_f denotes the fault current caused by the short circuit.

$$\boldsymbol{\lambda}_s^{tf} = \mathbf{L}_s^{tf}\mathbf{i}_s^{tf} + \boldsymbol{\lambda}_{PM}^{tf} \tag{2-11}$$

$$\mathbf{U}_s^{tf} = \mathbf{R}_s^{tf}\mathbf{i}_s^{tf} + \frac{d\boldsymbol{\lambda}_s^{tf}}{dt} \tag{2-12}$$

where $\mathbf{U}_s^{tf} = \begin{bmatrix} u_{ah} & u_{af} & u_{bn} & u_{cn} \end{bmatrix}^T$, $\mathbf{i}_s^{tf} = \begin{bmatrix} i_a & i_a - i_f & i_b & i_c \end{bmatrix}^T$

$$\boldsymbol{\lambda}_{PM}^{tf} = \begin{bmatrix} 1-\mu & & & \\ & \mu & & \\ & & 1 & \\ & & & 1 \end{bmatrix} \begin{bmatrix} \lambda_a \\ \lambda_a \\ \lambda_b \\ \lambda_c \end{bmatrix}, \mathbf{R}_s^{tf} = R\begin{bmatrix} 1-\mu & \mu & 1 & 1 \end{bmatrix}, \mathbf{L}_s^{tf} = \begin{bmatrix} L_{hh} & M_{hf} & M_{hb} & M_{hc} \\ M_{hf} & L_{ff} & M_{fb} & M_{fc} \\ M_{hb} & M_{fb} & L & M \\ M_{hc} & M_{fc} & M & L \end{bmatrix}$$

L_{hh} is the self-inductance of the healthy part of the faulted phase A. L_{ff} is the self-inductance of the shorted part of the faulted phase A. M_{hf} is the mutual-inductance between the healthy and shorted parts of the phase A. L_{hb} is the mutual-inductance between phase B and the healthy part of phase A. L_{hc} is the mutual-inductance between

phase C and the healthy part of phase A. L_{fb} is the mutual-inductance between phase B and the shorted part of phase A. L_{fc} is the mutual-inductance between phase C and the shorted part of phase A.

Since the self-inductance is proportional to the square of the number of turns, and the mutual-inductance is to the product of the number of turns of the two associated coils, the self- and mutual- inductances in turn fault conditions can be approximately obtained from (2-13), for a single coil per phase machine. For machines with more than one coil per phase, it is not strictly valid according to [106]. Nevertheless, for the sake of simplicity, the analysis of the fault behavior under such relation can still be useful for developing fault detection algorithm.

$$\begin{cases} L_{hh} = (1-\mu)^2 L_a \\ M_{hf} = \mu(1-\mu)L_a \\ M_{hb} = (1-\mu)M_{ab} \\ M_{hc} = (1-\mu)M_{ac} \\ L_{ff} = \mu^2 L_a \\ M_{fb} = \mu M_{ab} \\ M_{fc} = \mu M_{ac} \end{cases} \tag{2-13}$$

Rearrange the phase voltage equations by applying $u_{an} = u_{ah} + u_{af}$, the three phase voltage equations in turn fault conditions can be derived as (2-14).

$$\mathbf{U}_s = \mathbf{R}_s \mathbf{i}_s + \frac{d\boldsymbol{\lambda}_s^{TF}}{dt} - \mu R \begin{bmatrix} i_f & 0 & 0 \end{bmatrix} \tag{2-14}$$

$$\boldsymbol{\lambda}_s^{TF} = \mathbf{L}_s \mathbf{i}_s + \boldsymbol{\lambda}_{PM} - \mu \begin{bmatrix} L_a & M_{ab} & M_{ac} \end{bmatrix}^T i_f \tag{2-15}$$

where $\mathbf{U}_s = \begin{bmatrix} u_{an} & u_{bn} & u_{cn} \end{bmatrix}^T, \mathbf{i}_s = \begin{bmatrix} i_a & i_b & i_c \end{bmatrix}$

The voltage equation of the faulted part can be expressed as (2-16). For the same number of shorted turns, the lower R_f is, the larger i_f could reach, and the worse the scenario could be. Thus to evaluate the most severe condition and for sake of simplicity, R_f is assumed to zero in further analysis.

$$u_f = R_f i_f = \mu R(i_a - i_f) + \frac{d\lambda_f}{dt} \tag{2-16}$$

$$\lambda_f = \mu \begin{bmatrix} L_a & M_{ab} & M_{ac} \end{bmatrix} \mathbf{i}_s - \mu^2 L_a i_f + \mu \lambda_a \tag{2-17}$$

It can be concluded from the expressions above that i_f can be expressed by the combination of i_a, i_b, i_c, and the time derivative of λ_a. With high-order harmonics neglected, the fault current i_f can be expressed in (2-18), where I_{f1} denotes the amplitude, and is dependent on machine speed. θ_1 is the associated phase angles.

$$i_f \approx I_{f1}\sin(\theta_e + \theta_1) \tag{2-18}$$

2.2.2.2 Machine model in rotating dq frame

When the three phase quantities are transformed into the rotating dq frame, the dq voltages and flux linkages can be expressed in (2-19) and (2-20).

$$\mathbf{U}_{dq} = \mathbf{R}_s\mathbf{i}_{dq} + d\boldsymbol{\lambda}_{dq}^{TF}/dt - \tfrac{2}{3}\mu R_s i_f \begin{bmatrix}\cos\theta_e & -\sin\theta_e\end{bmatrix} + \begin{bmatrix}0 & -\omega_e \\ \omega_e & 0\end{bmatrix}\boldsymbol{\lambda}_{dq}^{TF} \tag{2-19}$$

$$\begin{cases} \boldsymbol{\lambda}_{dq}^{TF} = \mathbf{P}\boldsymbol{\lambda}_{dq}^{TF} = \mathbf{L}_{\mathbf{dq}}\mathbf{i}_{dq} + \begin{bmatrix}\lambda_{PM} & 0\end{bmatrix}^T + \boldsymbol{\Delta\lambda}_{dqf} \\ \boldsymbol{\Delta\lambda}_{dqf} = -\dfrac{2}{3}\mu i_f \begin{bmatrix}L_d\cos\theta_e & -L_q\sin\theta_e\end{bmatrix}^T \end{cases} \tag{2-20}$$

Compared with the dq flux linkages in the healthy condition in (2-8), an additional term $\boldsymbol{\Delta\lambda}_{dqf}$ related to the fault current is produced in fault condition. Together with the additional term on the resistive part, the change in the dq voltages Δu_{df} and Δu_{qf} can be derived in (2-21), indicating the fault signatures, under the same dq currents. The interactions of the fault current given in (2-18) with the $\sin\theta_e$ and $\cos\theta_e$ terms in Δu_{df} and Δu_{qf} produce a dc component, and 2nd harmonics in the dq voltages, as given in (2-22). The first term is associated with the change of the positive-sequence voltage, whereas the second term is associated with the change of negative-sequence voltage due to the fault. The subscript "dc" denotes dc component, and "2nd" denotes 2nd harmonic.

If the same voltages shown in (2-21) are applied to a machine model equations of (2-23) in healthy conditions, then the dq currents can be expressed in (2-24), where i_d' and i_q' denote the predicted dq currents with the machine model under healthy conditions. Thus, the change in the dq currents due to the fault under the same applied dq voltages can also be used as fault signatures.

$$\begin{cases} u_d = R_s i_d + L_d \dfrac{di_d}{dt} - \omega_e L_q i_q + \Delta u_{df} \\ u_q = R_s i_q + L_q \dfrac{di_q}{dt} + \omega_e (L_d i_d + \lambda_{pm}) + \Delta u_{qf} \\ \Delta u_{df} = +\dfrac{2}{3}\mu\omega_e L_d i_f \sin\theta_e - \dfrac{2}{3}\mu\omega_e L_d \cos\theta_e \dfrac{di_f}{dt} \\ \qquad -\dfrac{2}{3}\mu\omega_e L_q i_f \sin\theta_e - \dfrac{2}{3}\mu R i_f \cos\theta_e \\ \Delta u_{qf} = +\dfrac{2}{3}\mu\omega_e L_q i_f \cos\theta_e + \dfrac{2}{3}\mu\omega_e L_q \sin\theta_e \dfrac{di_f}{dt} \\ \qquad -\dfrac{2}{3}\mu\omega_e L_d i_f \sin\theta_e + \dfrac{2}{3}\mu R i_f \cos\theta_e \end{cases} \tag{2-21}$$

$$\begin{cases} \Delta u_{df} \approx \Delta u_{df\_dc} + \Delta u_{df\_2nd} \\ \Delta u_{qf} \approx \Delta u_{qf\_dc} + \Delta u_{qf\_2nd} \end{cases} \tag{2-22}$$

$$\begin{cases} u_d = R_s i_d' + L_d \dfrac{di_d'}{dt} - \omega_e L_q i_q' \\ u_q = R_s i_q' + L_q \dfrac{di_q'}{dt} + \omega_e (L_d i_d' + \lambda_{pm}) \end{cases} \tag{2-23}$$

$$\begin{cases} i_d' = i_d - \dfrac{2}{3}\mu i_f \cos\theta_e \\ i_q' = i_q + \dfrac{2}{3}\mu i_f \sin\theta_e \end{cases} \tag{2-24}$$

2.2.2.3 Disturbance generated by fault in control block

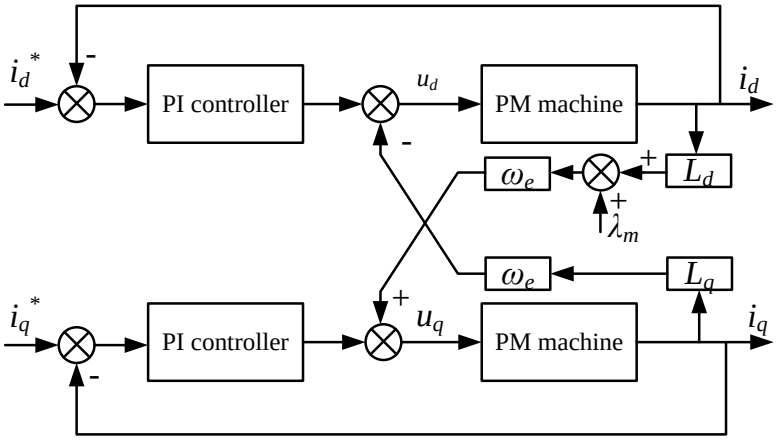

Fig. 2-6 Permanent magnet machine current control diagram

The control block of the machine driving system is illustrated in Fig. 2-6, where conventional proportional and integral (PI) controllers are used to track the current reference, which comes from the torque or flux demand from the speed control block.

Thus the dq axis voltages for the machine can be expressed as (2-25), by neglecting the nonlinearities in the inverter. With the comparison of (2-25) and (2-21), and the consideration that the current reference is dc constant, which can be tracked with zero steady state error by the appropriate design of the PI gains, the equivalent control system block diagram in response to the 2nd harmonic disturbances Δu_{df} , Δu_{qf} can be illustrated in Fig. 2-7.

$$\begin{aligned} u_d &= K_{pd}\Delta i_d + K_{id}\int \Delta i_d dt - \omega_e L_q i_q \\ u_q &= K_{pq}\Delta i_q + K_{iq}\int \Delta i_q dt + \omega_e (L_d i_d + \lambda_m) \end{aligned} \tag{2-25}$$

The PI gains can be determined by pole-zero cancellation. Thus, $K_{pd}= \omega_c L_d$, $K_{id}= \omega_c R$, $K_{pq}= \omega_c L_q$, $K_{iq}= \omega_c R$, where ω_c is the current controller bandwidth which is set to 400 Hz.

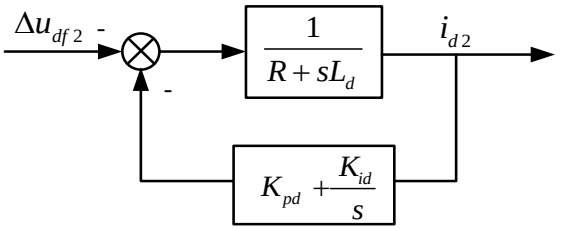

(a)

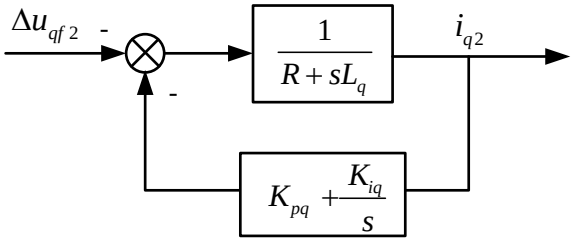

(b)

Fig. 2-7 Equivalent transfer function block diagrams to the 2nd harmonic disturbances due to a turn fault in (a) d-axis and (b) q-axis.

$$\begin{cases} \dfrac{i_{d2}}{\Delta u_{df2}} = \dfrac{1}{L_d}\dfrac{s}{(s+\omega_c)(s+\tau_d)} \\ \dfrac{i_{q2}}{\Delta u_{qf2}} = \dfrac{1}{L_q}\dfrac{s}{(s+\omega_c)(s+\tau_q)} \\ \tau_d = \dfrac{R}{L_d} \\ \tau_q = \dfrac{R}{L_q} \end{cases} \tag{2-26}$$

From the simplified transfer function block diagram, the transfer functions between the outputs of 2nd harmonic i_d and i_q, and the disturbance inputs can be obtained in (2-26). With typical machine parameters selected as L_d=0.38mH, L_q=1.02mH, R=0.025Ω, the amplitude-frequency responses are shown in Fig. 2-8.

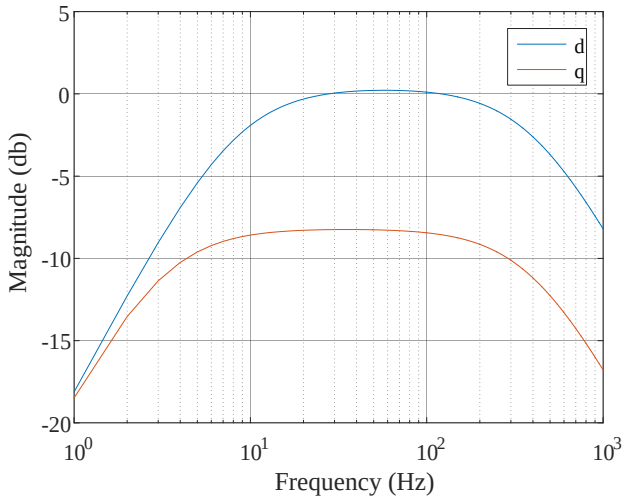

Fig. 2-8 The amplitude frequency curve of the control diagram with 2nd harmonic disturbances

For most machines and their operating conditions, the fundamental electrical frequency and control bandwidth are usually under 1 kHz, thus, the 2nd harmonic in the dq voltages are unlikely to be filtered out in the output. Therefore, the dq currents will inevitably contains 2nd harmonic. And from the voltage equations, the 2nd harmonic will also exist in the dq axis voltages. Therefore, the 2nd harmonic in both the dq currents and voltages can be used to detect turn faults with order tracking techniques. However, they are also affected by the controller bandwidth. Also, the presence of large dc components in the dq currents and voltages could introduce noises into the order tracking process, making the feature extraction less stable.

2.3 Residual acquired from machine model

2.3.1 Dq voltage residual

It can be concluded that the dq voltage equations of the machine under turn fault conditions is different from that in healthy conditions. Thus, if the machine model in healthy operations can be obtained, the voltages in healthy condition can be estimated with the measured currents. By comparing the actual voltages with the estimation, the voltage residual can indicate whether fault has occurred. The diagram of estimating the voltage residual is shown in Fig. 2-9.

For an interior permanent magnet machine, the dq inductances and flux linkages are not only dependent on rotor position, but also affected by dq currents largely. This nonlinearity can be better represented by the flux linkages as functions of the dq currents and rotor position angle. This relationship, or flux linkage map, can be obtained from finite element analysis. Fig. 2-10 shows the dq flux linkage map of the PMA SynRM at 0° rotor position. Flux linkages at any intermediate point can be obtained by linear interpolation. With the flux map available, the mathematical model for estimation can be rewritten in (2-27), where the inputs to the model, i_d, i_q, and mechanical angle θ_m are available from the measurement. Since the mathematical relationships between the input voltages u_d, u_q and the measured current i_d, i_q have been expressed in (2-21), it is clear that voltage residual calculated in (2-28) equals to the voltage change caused by the fault. Thus, the fault feature signals are captured.

$$\begin{cases} u_{d\_e} = R_s i_d + \dfrac{d\lambda_d}{dt} - \omega_e \lambda_q \\ u_{q\_e} = R_s i_q + \dfrac{d\lambda_q}{dt} + \omega_e \lambda_d \\ \lambda_d = f(i_d, i_q, \theta_m) \\ \lambda_q = g(i_d, i_q, \theta_m) \end{cases} \tag{2-27}$$

$$\begin{cases} u_{d\_re} = u_{d\_e} - u_d = -\Delta u_{df} \\ u_{q\_re} = u_{q\_e} - u_q = -\Delta u_{qf} \end{cases} \tag{2-28}$$

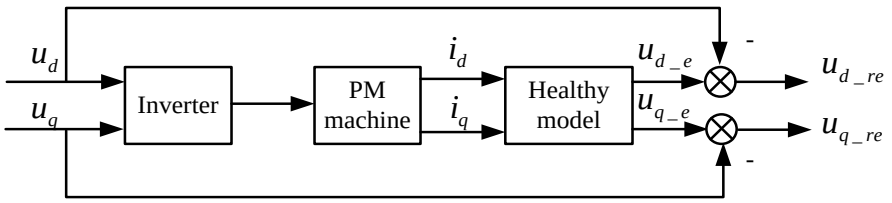

Fig. 2-9 Voltage residual generation structure

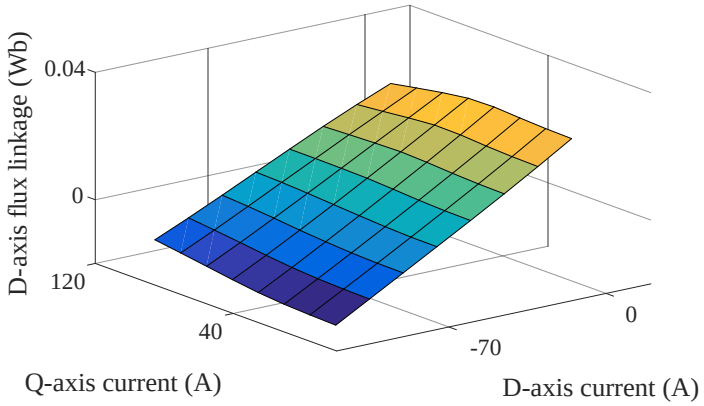

(a)

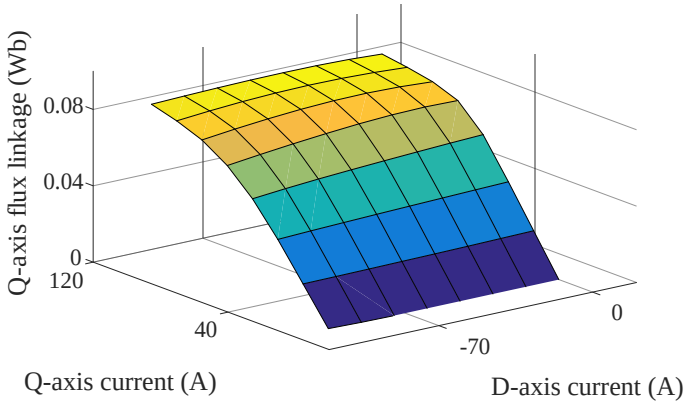

(b)

Fig. 2-10 Flux linkage maps versus d- and q-axis currents at rotor position = 0°. (a) d-axis flux linkage. (b) q-axis flux linkage.

2.3.2 Dq current residual

As be seen from the equations (2-27) that in order to estimate the voltages, the derivatives of dq flux linkages need to be calculated. However, because of the switching noises in the current due to the PWM operation of the inverter, and the nonlinear relationship between the current and flux linkages, such computation is prone to noise.

In contrast, the flux linkages can be obtained from integration of the voltages, which can reduce the noise. Therefore, the mathematical model to estimate the currents with the voltage inputs in (2-29) is employed. Firstly, the dq flux linkages are calculated by the integration of the net voltages shown in the 1st and 2nd equations in (2-29). Then, the inverse flux linkage functions are used to obtain the dq currents with the estimated dq flux linkage and the measured rotor position. The inverse are calculated in advance and the data are stored for the fault detection in real time. By way of example, Fig. 2-11 shows the inverse dq current maps versus dq flux linkages at 0° rotor position. Together with the measured dq currents, the current residual can be obtained as shown in Fig. 2-12, which should be close to zero in healthy condition if the model is sufficiently accurate. From the analysis in (2-23)(2-24), the current residual in the fault condition representing the difference between the healthy and faulted machine behaviours can be expressed as (2-30), where the original fault signatures in the currents are extracted. It can be deduced that the current residuals are only related to the fault current and the percentage of the shorted turns, and is independent of the current controller bandwidth.

Whereas phase currents are usually measured in a drive system, voltage transducers are not necessary for drive control. In order to avoid the use of extra voltage transducers, the voltages for the input to the model are replaced by the dq voltage commands from

the output of the current controller. The voltage drop and non-linear characteristics of the inverter result in the voltages applied to the machine and to the model being different. Also, with the consideration that small errors might also exist in the mathematical model, the current residual may deviate from zero even in healthy conditions. Therefore, by simply comparing the dq current residual to zero is not a good solution for fault detection.

$$\begin{cases} \lambda_d = \int (u_d - R_s i_{d\_e} + \omega_e \lambda_q) dt \\ \lambda_q = \int (u_q - R_s i_{q\_e} - \omega_e \lambda_d) dt \\ i_{d\_e} = f^{-1}(\lambda_d, \lambda_q, \theta_m) \\ i_{q\_e} = g^{-1}(\lambda_d, \lambda_q, \theta_m) \end{cases} \tag{2-29}$$

$$\begin{cases} i_{d\_re}^p = i_d - i_{d\_e} = +\frac{2}{3}\mu i_f \cos\theta_e \approx i_{d\_re\_dc}^p + i_{d\_re\_2nd}^p \\ i_{q\_re}^p = i_q - i_{q\_e} = -\frac{2}{3}\mu i_f \sin\theta_e \approx i_{q\_re\_dc}^p + i_{q\_re\_2nd}^p \end{cases} \tag{2-30}$$

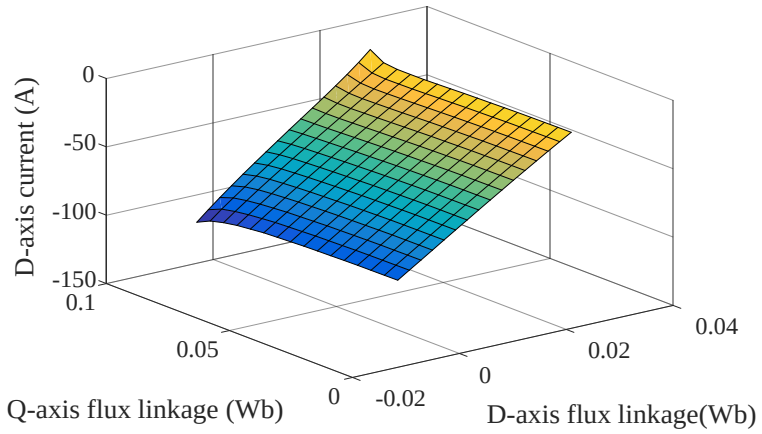

(a)

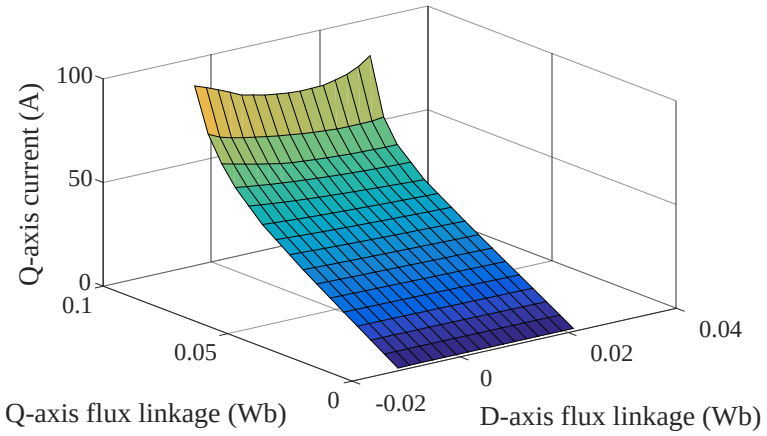

(b)

Fig. 2-11 Current maps versus d- and q-axis flux linkages at rotor position =0°. (a) d-axis current. (b) q-axis current.

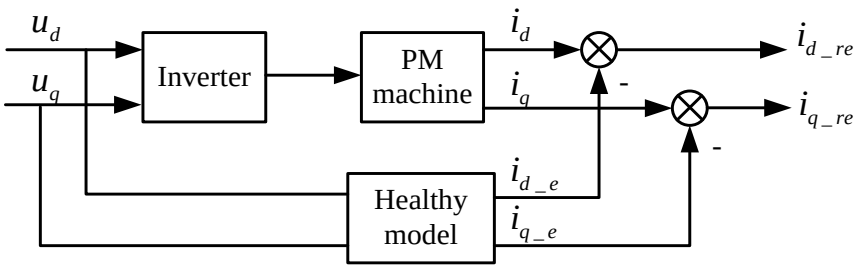

Fig. 2-12 Current residual generation structure

If the machine is balanced in three phases in healthy conditions, those errors in the voltages and machine models only add to the dc component in the dq current residual while no 2nd harmonic will be introduced. Therefore, the 2nd harmonic in the current residual can be used as a good fault indicator according to (2-30). Since the dc component in the dq current residuals are greatly eliminated by the estimation, the 2nd harmonic is more pronounced in the current residuals under the fault condition, thereby improving signal-to-noise ratio of the fault detection process. Thus, the turn fault detection should be based on the 2nd harmonic positive sequence dq current residual as the fault indicator, as expressed in (2-31).

$$FI^{p} = \begin{bmatrix} i^{p}_{d\_re\_2nd} \\ i^{p}_{q\_re\_2nd} \end{bmatrix} \tag{2-31}$$

2.4 Fault Detection

2.4.1 Fault indicator and detection steps

Various frequency components extraction techniques can be applied for the detection of the 2nd harmonic in the positive sequence dq current residual. Alternatively, the current residuals in the positive rotating dq frame can be transformed into the backward (negative) rotating dq frame, then the fault indicator of the 2nd harmonic is converted into the dc value of the negative sequence components, as shown in (2-32). To maximize detection sensitivity, the magnitude of the dc values of the negative sequence dq current residuals, given in (2-33), is defined as the fault indicator. Thus, the turn fault detection is mainly be based on the extraction of the dc components, where the superscript *n* denotes negative sequence components.

$$\begin{bmatrix} i_{d\_re}^{n} \\ i_{q\_re}^{n} \end{bmatrix} = \begin{bmatrix} \cos 2\theta_e & -\sin 2\theta_e \\ \sin 2\theta_e & \cos 2\theta_e \end{bmatrix} \begin{bmatrix} i_{d\_re}^{p} \\ i_{q\_re}^{p} \end{bmatrix} = \begin{bmatrix} i_{d\_re\_dc}^{n} + i_{d\_re\_2nd}^{n} \\ i_{q\_re\_dc}^{n} + i_{q\_re\_2nd}^{n} \end{bmatrix} \tag{2-32}$$

$$FI^{n} = \sqrt{{i_{d\_re\_dc}^{n}}^{2} + {i_{q\_re\_dc}^{n}}^{2}} \tag{2-33}$$

In a real machine drive system, the back EMF and non-ideal inverter as well as magnetic saturation and rotor saliency will introduce higher order harmonics even in healthy conditions. In the negative rotating dq frame, these harmonics can coexist with the 2nd harmonic due to the model inaccuracy. Only the dc component of the residual current in the negative rotating frame is the indicator of a turn fault, thus all other harmonics need to be eliminated. Low pass filters or notch filters can be used to filter out the harmonics, but the filter parameters need to vary with operating frequency. When the speed or frequency is varying, the filter response and, hence the quality of detection deteriorates.

Since the rotor position angle is always available for the PM machine drive systems, the dc component can be estimated more accurately within one electrical cycle, regardless of speed or frequency change. Through the integration of the negative sequence current residual within 2π electric radians shown in (2-34), all the harmonics can be eliminated, and the dc component can be obtained exclusively. Thus, the integration results and the then the fault indicator in (2-33) should be zero in healthy conditions, but non-zero in turn fault conditions. A threshold can be determined empirically based on the experimental observations in healthy conditions. And if the fault indicator is higher than the threshold, a turn fault is detected.

$$\begin{bmatrix} i_{d\_re\_dc}^{n} \\ i_{q\_re\_dc}^{n} \end{bmatrix} = \frac{1}{2\pi} \int_{\theta_e - 2\pi}^{\theta_e} \begin{bmatrix} i_{d\_re}^{n}(\theta_e) \\ i_{q\_re}^{n}(\theta_e) \end{bmatrix} d(\theta_e) \tag{2-34}$$

It should be noted that the angular integration based dc component extraction and the fault detection based on the comparison with the threshold work well in both steady and speed transient states. However, if there is a current (or load torque) transient, causing the varying magnitude of the negative sequence current residual, then the integration results may fluctuate. Thus the fault indicator might also be higher than the predefined threshold for a period even in healthy condition, and a false alarm might be triggered. However, the fluctuation will quickly decay to zero in healthy conditions In

order to avoid false alarm, a load transient evaluation process is included in the fault detection process.

Once the fault indicator exceeds the threshold, then an angle counter is activated and records the angle increment. Otherwise, the counter is reset to zero. If the angle recorded in the counter is always small than the predefined transient evaluation period, then it should due to the fluctuation caused by a load transient. Conversely, if the angle is greater than such period, then it should be caused by the turn fault. The determination of this evaluation period is a tradeoff between the risk of false alarm and the detection response time, and can be determined as 2π according to the test results. Based on the above description of the fault signature extraction with the consideration of load transients, the whole signal processing and turn fault detection flow chart is shown in the upper and lower parts of Fig. 2-13, respectively.

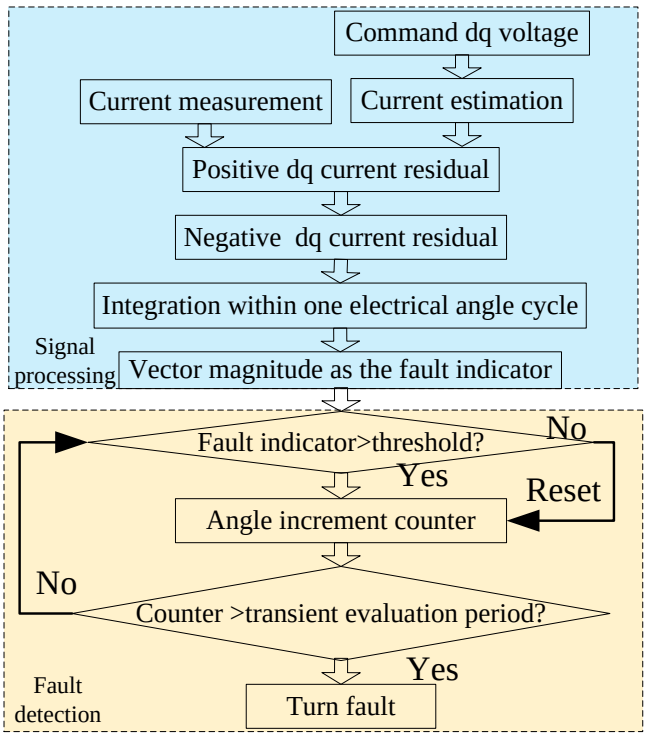

Fig. 2-13 Fault detection flow chart

2.4.2 Sensitivity to other fault types

As has been explained in Chapter 1, the effects of other fault types on the proposed fault indicator also need be discussed. Since voltage equations at the fundamental frequency are utilised, any constant asymmetry in the inductance, resistance and back EMF will generate the similar symptoms. Thus, the HRC faults and the static eccentricity faults which produce resistive and inductive asymmetry can cause the

ambiguity to the detection results. Hence, to effectively detect turn fault, these fault types need to be diagnosed in advance or their probability is guaranteed to be very low. Other faults such as dynamic eccentricity, bearing fault and demagnetization, however, do not impact the effectiveness of this turn fault detection method.

2.5 Experiments

2.5.1 Machine setup

A fault tolerant machine drive based on permanent magnet assisted synchronous reluctance machine (PMA SynRM) reported in [107] is used for the validation of the proposed fault detection method. The machine has 36 slots and 3 pole pairs, with three independent 3-phase windings, which are segregated into triple redundant 3-phase winding configuration, as shown in Fig. 2-14.

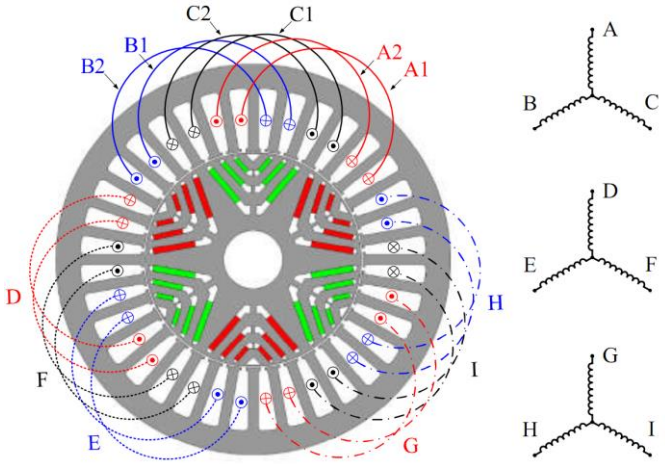

Fig. 2-14 Triple redundant PMA SynRM with segregated windings

Since there is no overlap between two different 3-phase winding sets, the risk of inter 3-phase set short circuit fault is largely reduced. Also, the degradation or failure on the windings of one set and the heat generated by the fault are not likely to transmit to the windings of the other sets. Each 3-phase winding set ABC, DEF, GHI forms a balanced 3-phase system in space and time, and is controlled independently by three separate inverters. Such physical, thermal and electrical isolation guarantees the fault tolerant capability when a fault occurs in one 3-phase winding set and a mitigation action is taken [107], while the other two 3-phase winding sets are still operational to provide the torque. Although it is named 9-phase machine in some parts of this thesis, it is controlled in the same way as a 3-phase machine in healthy operation, thus all the analysis and methods aimed at 3-phase machine can also be applied to this machine without modifications.

The machine specification is shown in Table 2-1.The test rig set up is shown in Fig. 2-15. The 9-phase machine is oil cooled and the heat is taken away by the flowing oil circulation in the cooling jacket. The machine shaft is connected to the dynamometer via an inline torque transducer. The machine speed is determined by the dynamometer under speed control. The torque of the machine is determined by the machine currents which can be controlled by the driving system shown in Fig. 2-16, consisting of three standard 3-phase inverters controlled by three DSP cores independently. Each DSP core samples the phase currents from the LEM current transducers and the typical current control with PI regulator and SVPWM scheme is implemented. The sampling and PWM frequency is set to 10 kHz. The dq current references are determined from the maximum torque per ampere (MTPA) table obtained from the initial test which establishes the relationship between the torque and dq currents. A single turn short-circuit fault in coil B2 of the 3-phase winding set ABC is emulated by closing the relay shown in Fig. 2-17. Additional resistance of around 1.4 mΩ is introduced as the R_f in the shorted loop by this setup. The action of relay is controlled by one DSP core and the closing time period is limited to 0.3s to avoid too much heat due to the high fault current. The resistance in the short-circuited path is minimized by using thick cables. Due to the current limit of the relay, all the fault detection tests are conducted below 1000 rpm for the sake of safety. Since the fault signature decreases with speed, the tests at low speed are more appropriate to demonstrate sensitivity and robustness of the detection technique.

The fault detection algorithm is converted into C code, and is inserted to the main function of the current control part alongside with the relay control in the DSP. The flux linkage current table in (2-27) is firstly extracted from finite element analysis software Flux 12.0 by varying i_d, i_q in the ranges of -105~0A, 0~105A at the step of 15A, and varying θ_m from 0 to 120° (0~360° in electrical angular degree) at the step of 2.5°. The numbers of i_d, i_q and θ_m samples in the FE calculation are 8, 8 and 49 respectively. During the calculation of the inverse table in MATLAB, both the defined d and q flux linkage vectors contain 16 sample points, making both inverse tables of i_d and i_q contain the total 16×16×49 elements. These inverse tables together with the three dimensional table-data-look-up function are stored in a header file and are called during the execution of the control program.

The DSPs communicate with a personal computer (PC) via controller area network (CAN) bus. A LabVIEW interface is built to monitor the machine currents and transmit

control instructions in real time, as shown in Fig. 2-18 and Fig. 2-19. The measured data that are generated in real time during the operation can be transmitted back to the PC and is saved in the Excel file. The waveforms shown in the following part come from the transmitted data and they can show the behaviour of the machine in healthy and faulted conditions, and the performance of the proposed fault detection method.

Table 2-1 Machine Specifications

Specification	Symbol	Value
Base speed	n_b	4000rpm
Maximum speed	n_m	19200rpm
Rated power	P_r	35kW
Rated current	I_{rated}	120A
Nominal DC link voltage	V_{dc}	270V
Turn number of each coil	N	8
Faulted turn number	N_f	1
PM flux linkage	λ_{pm}	0.025Wb
Resistance	R_s	0.025Ω
d-axis inductance	L_d	0.38mH
q-axis inductance	L_q	1.02mH

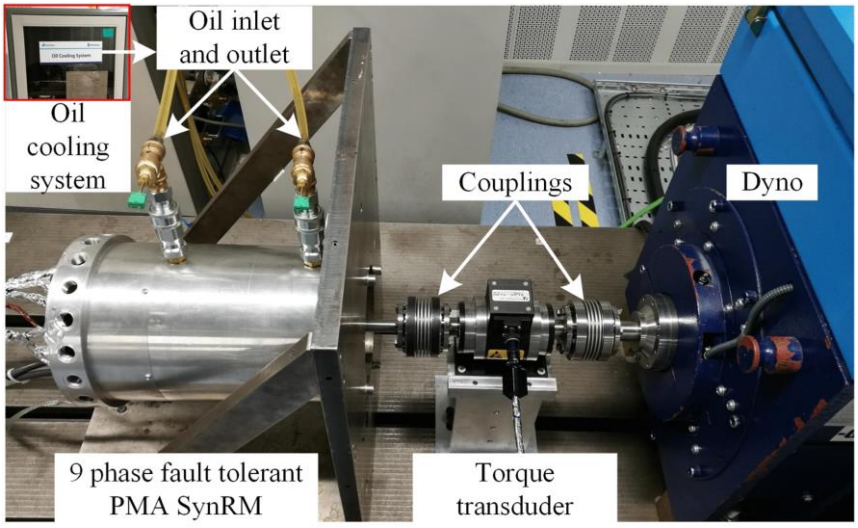

Fig. 2-15 The nine phase PMA SynRM test rig

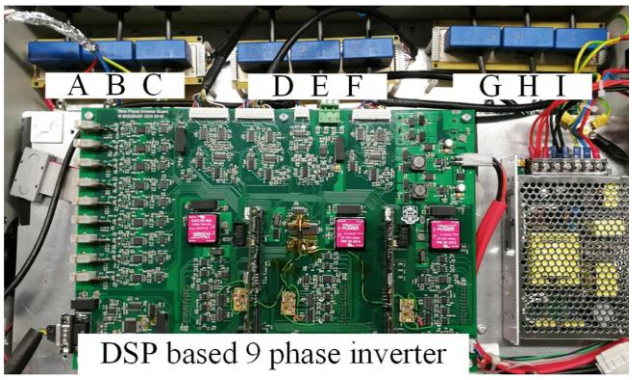

Fig. 2-16 DSP based nine phase inverter

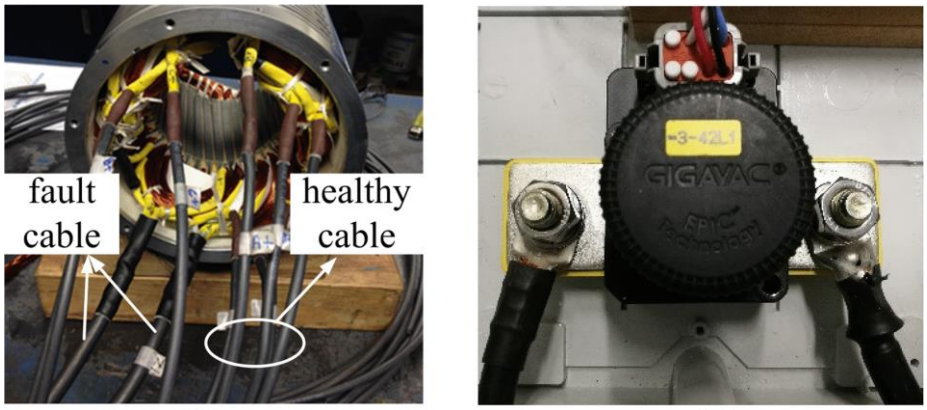

Fig. 2-17 Turn fault test setup (a) cable leads (b) turn fault relay.

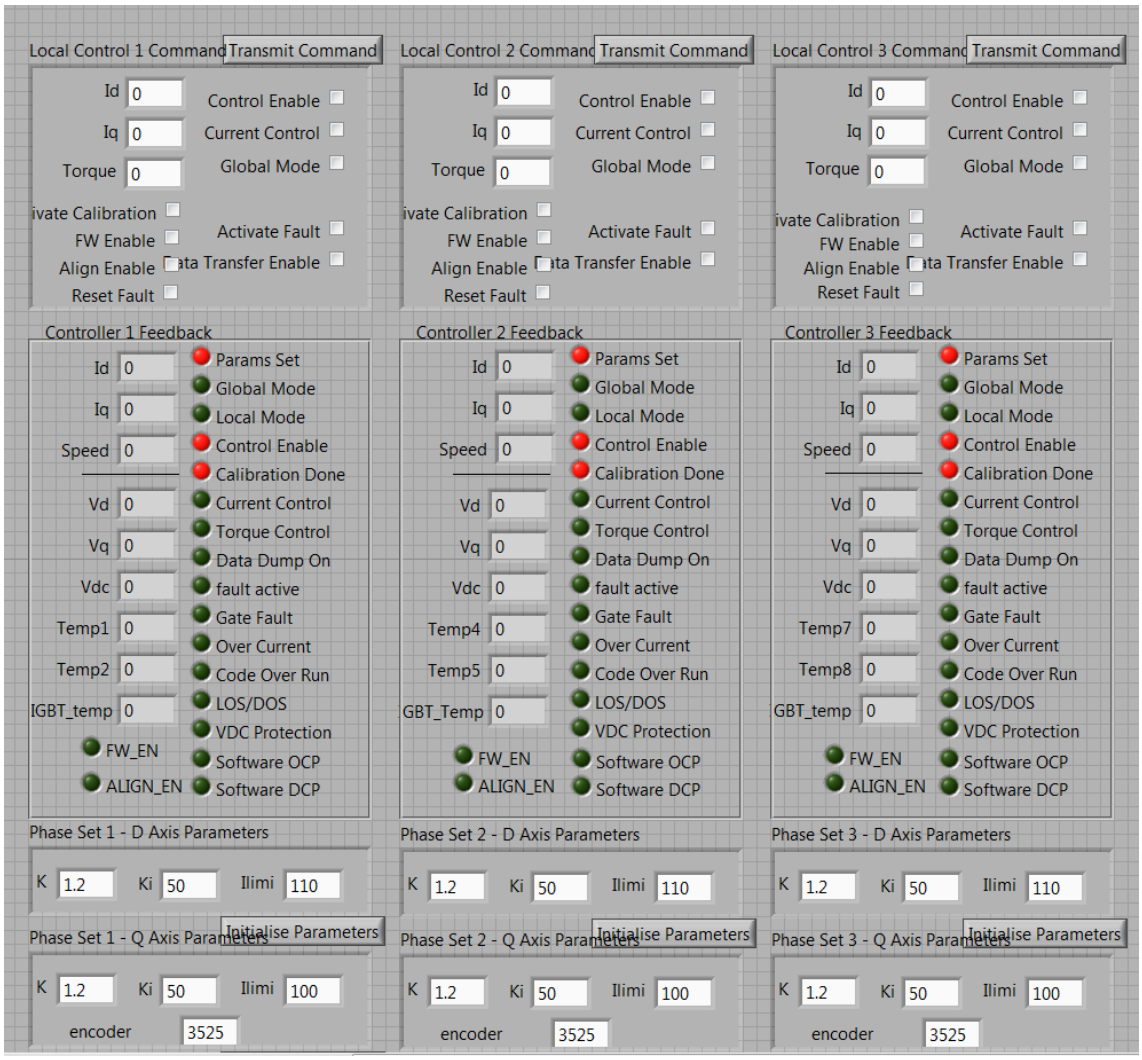

Fig. 2-18 The LABVIEW interface for machine monitoring based on CAN bus communication

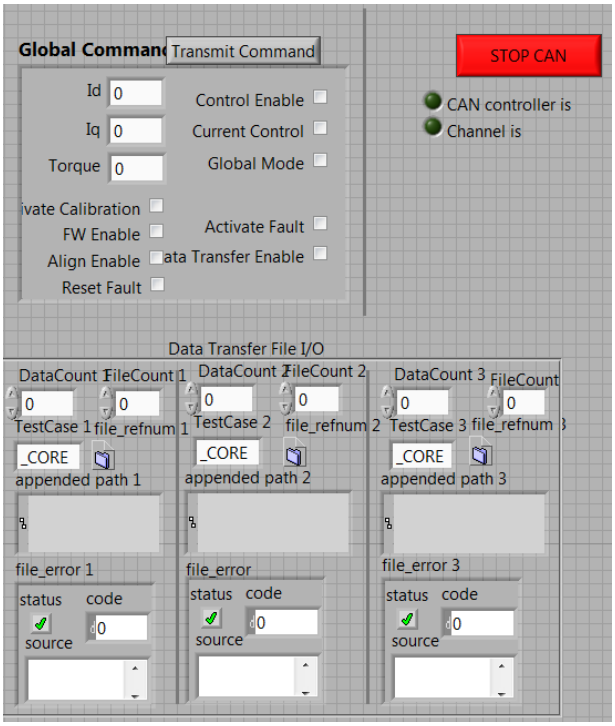

Fig. 2-19 The LABVIEW interface for machine controlling and data transferring

2.5.2 Validation of the machine mathematical model

In order to improve sensitivity and robustness of the fault detection, the common features in the current residual which are not caused by the fault should be minimised. Hence, the error due to the mathematical model which is not related to the fault needs to be small. Thus, the accuracy of the machine model is examined first.

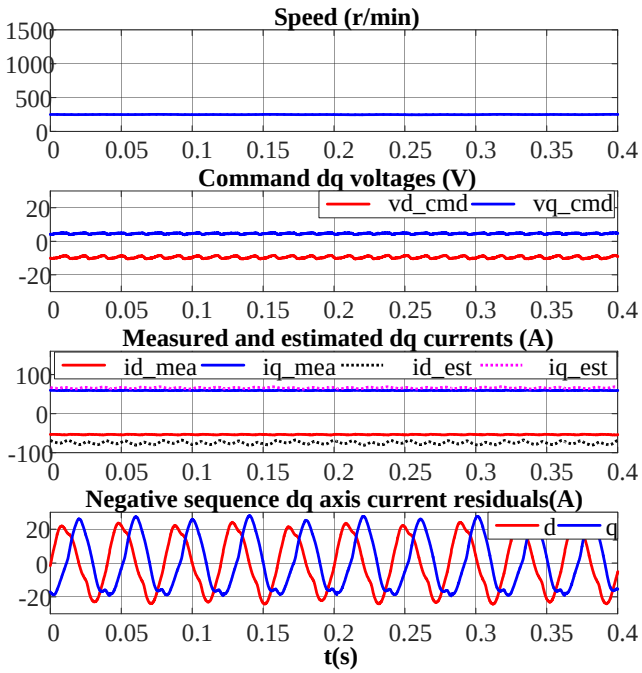

(a)

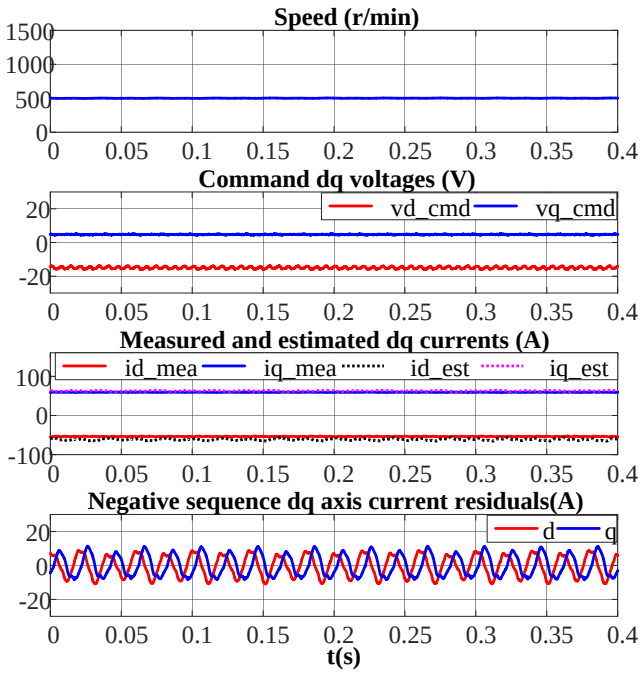

(b)

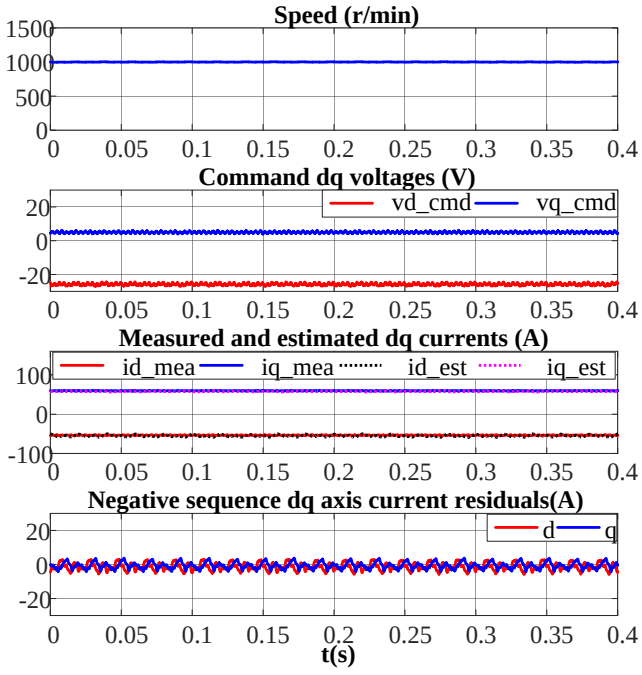

(c)

Fig. 2-20 The performance of current estimation by machine model at 80A (i_d = -53.5A, i_q = 59.5A) at different speeds of (a)250 rpm (b) 500 rpm (c)1000 rpm

Fig. 2-20 shows the dq current estimation results and negative sequence dq current residuals at different speeds in healthy condition with the phase current amplitude of 80A. The given i_d reference is -53.5A and the i_q reference is 59.5A. The subscript "cmd" denotes the dq command voltages, "mea" and "est" denote the measured and estimated currents. They are used in all the test results presented thereafter in this chapter. As can be seen, the ripples in the measured dq currents are small, especially at

lower speed of 250 rpm. The higher ripples shown in the command dq voltages are mainly due to the higher order harmonics from the back EMF and slotting effect. The error in the current estimation can be seen more significant at lower speed but is much reduced at higher speed of 1000 rpm. Therefore, the accuracy of the current estimation is higher at higher speed. This error is mainly caused by the difference between the command dq voltages and the actual driving dq voltages due to the inverter voltage drop. Such voltage drop is not related to the speed while the total dq voltages increases with speed because of back EMF and synchronous reactance, hence the proportion of the inverter voltage drop decreases as the speed increases. As a result, the machine mathematical model is more accurate at higher speed.

2.5.3 Influence of controller bandwidth

Conventional signals such as the measured dq currents and the command dq voltages, can also be used to extract the 2^{nd} harmonic for the fault detection. One of the problems is that the magnitude of the 2^{nd} harmonic is affected by the current controller bandwidth. In contrast, according to (2-30) in section 2.3.2, the current residuals are only related to the fault current and the percentage of the shorted turns, and are independent of the controller bandwidth. Thus, in order to validate this quality, experimental tests with different bandwidths are conducted. The machine is operating at 1000rpm with 50A phase current. The tested bandwidths are 400 Hz and 800 Hz. The positive sequence measured dq currents, command dq voltages, and the dq current residuals are compared in Fig. 2-21(a), (b) and (c) respectively, when a single turn fault is injected at 0.11s. It is clear that with the increase of bandwidth, the 2^{nd} harmonics in the measured dq currents decease in the fault conditions, while the 2^{nd} harmonics in the command dq voltages increase. However, in terms of the dq axis residual currents, very little change can be observed. Therefore, the effect of the current controller bandwidth on the current residual based fault indicator is minimised, while the fault signatures are enhanced.

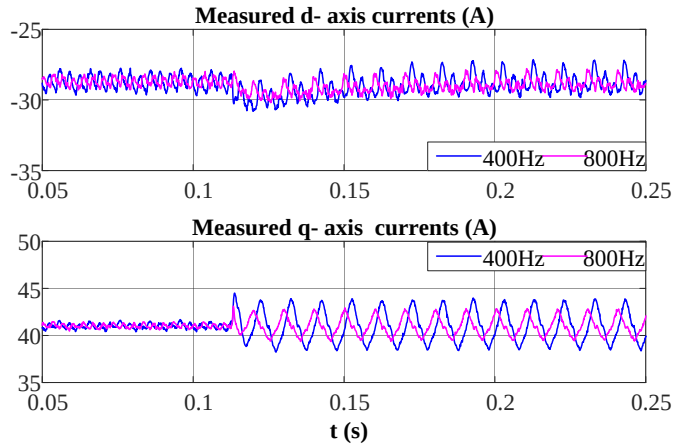

(a)

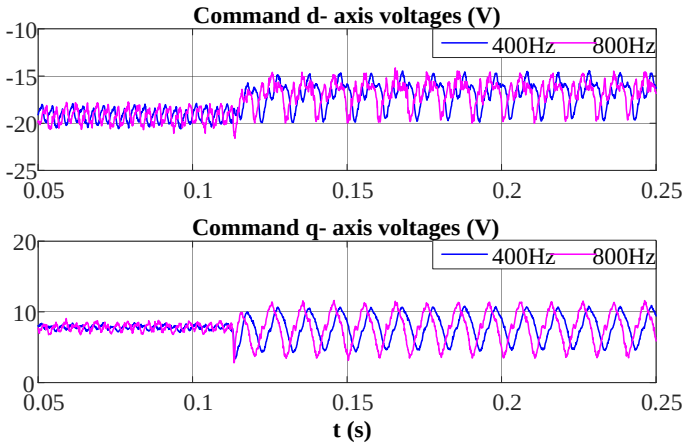

(b)

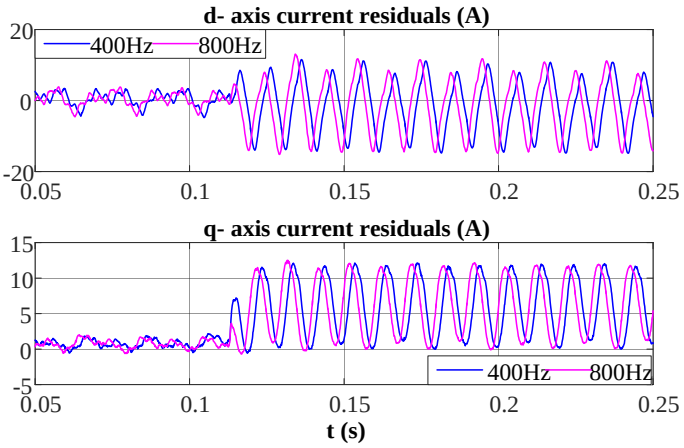

(c)

Fig. 2-21 Comparisons of the positive sequence (a) measured dq currents (b) command dq voltages (c) dq residual currents at 1000rpm 50A with different current controller bandwidths

2.5.4 Fault detection at steady state

To validate the fault detection method, a single turn fault, which has the most benign fault signature, is activated at 0.12s. The measurement and detection results are shown in Fig. 2-22 and Fig. 2-23. The machine is operating at 500 rpm with 50A phase current (i_d=-28.7A, i_q=41A). When a single turn fault occurs, the fault current flowing in the

short-circuited path can reach the peak value of 250A. The 2nd harmonics increase significantly in the command dq voltages, the measured and estimated dq currents, as illustrated in Fig. 2-24. The 2nd harmonics as the fault signatures are preserved during the calculation of current residuals and are transformed into dc components in the negative rotating dq frame. The dc components of both negative sequence d and q current residuals are extracted by angular integration, and their vector magnitude is compared with the threshold. When it exceeds the threshold, the angle counter is activated. When the counter reaches 2π, which indicates that the vector magnitude of the dc components is persistently greater than the threshold, the fault is detected effectively. The time duration for this process is about 0.04s for 500rpm.

To demonstrate the benefit of implementing the machine model to obtain the current residual, the fault signatures extracted from the measured dq currents and command dq voltages without the use of the machine model, and the current residuals with the model are compared at 1000rpm with 50A phase current using the same angular integration technique and the vector magnitude calculation when the same fault as described previously is injected at 0.12s. It can be observed from Fig. 2-25(a) that the magnitude of the dc component vector extracted from the negative sequence measured dq currents exhibit excessive fluctuation which would lead to incorrect detection response. Also, the deviation of the dc vector magnitude in the fault condition is small. It is, therefore, difficult to set an appropriate threshold to differentiate the healthy and faulted conditions. Although the fault signatures are increased slightly in the negative sequence command dq voltages shown in Fig. 2-25(b), the fault detection sensitivity is still compromised due to the fluctuations and indistinctive change in the turn fault conditions. With the application of the machine model to generate the current residuals, the extracted negative sequence dc components and the vector magnitude shown in Fig. 2-25(c) are much less volatile and more pronounced due to the suppression of the unwanted components, thus, the sensitivity and robustness of fault detection using the current residual can be largely enhanced.

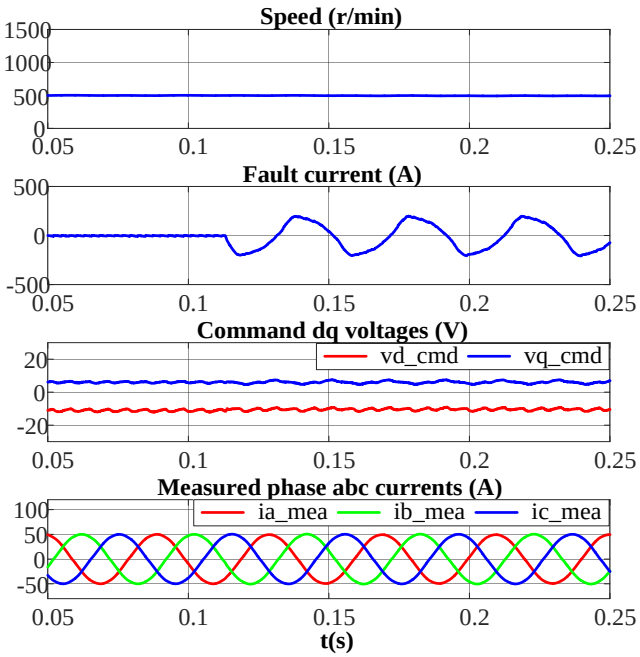

Fig. 2-22 Operating condition of 500 rpm, 50A (i_d = -28.7A, i_q = 41A)

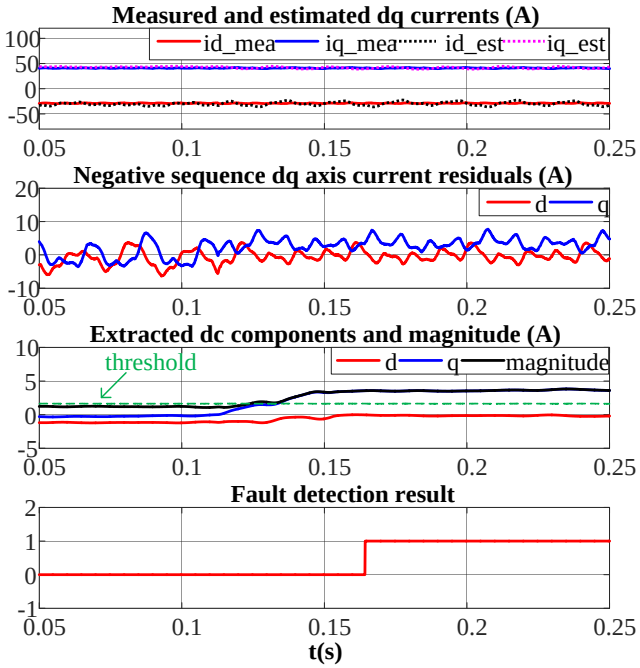

Fig. 2-23 Fault detection process and result

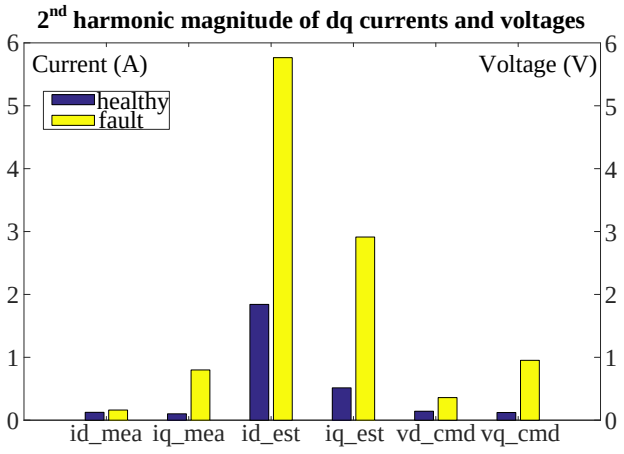

Fig. 2-24 The variations of the 2nd harmonic magnitude in dq currents and voltages

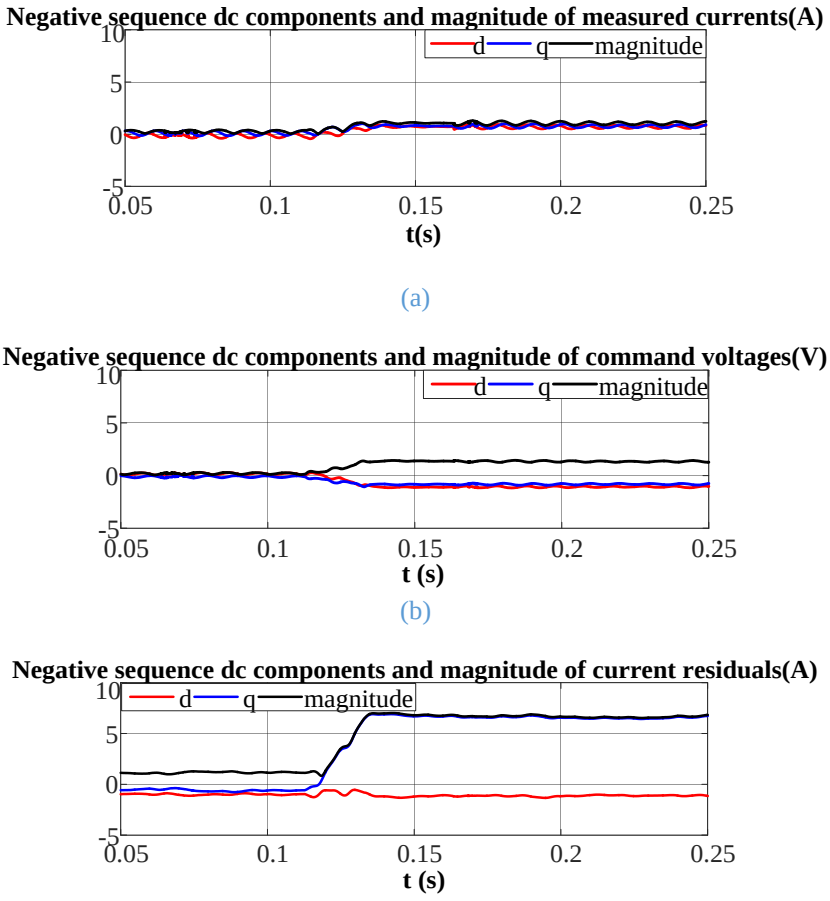

Fig. 2-25 Fault features extraction in dq current residuals at 1000rpm, 50A

For different operating conditions, the magnitude of the negative sequence dq current residuals vector magnitude are shown in Fig. 2-26, where 'H' denotes healthy conditions and 'TF' denotes turn fault conditions. As can be seen, in healthy conditions, the fault indicator is not zero, but is slightly dependent on the load current. This is mainly caused by the inherent impedance unbalance among the three phases. In turn fault conditions, deviations of the fault indicator from the healthy conditions are observed, and increase proportionally with the speed and current. Thus, the detection at very low speeds and currents are less sensitive. Based on the test results, a threshold as the function of current should be defined. With the consideration of measurement noise and error, a margin of 0.5 is set for the determination of the threshold in this case. It can be deduced that the turn fault in any operating conditions with the speed no lower than 250rpm and the current no lower than 10A can be detectable. When examining the no load (0 A) conditions, it is clear that the turn fault at 750 rpm and 1000rpm speeds can still be detected. This is different from the MCSA based fault detection method, which is no longer applicable under no load conditions due to the loss of current signals.

However, the fault signatures are still preserved in the command dq voltages, which are transferred to the current residuals, making the fault detection still effective, even if the phase currents are zero. When the speed is as lower as 500rpm and 250rpm with 0A current, the fault indicator is too small, and the fault cannot be detected. Nevertheless, the fault current is also very low at such low speeds, and the risk of causing damage to the machine can be neglected. Thus, the overall detection zone can be obtained, as shown in (2-35), where I is the phase current magnitude, and ω_r is the rotating speed.

$$\begin{aligned}&\left\{(\omega_r, I)\middle|250rpm \le \omega_r \le 750rpm, I \ge 10A\right\}\\&\cup\left\{(\omega_r, I)\middle|\omega_r \ge 750rpm, I \ge 0A\right\}\end{aligned} \tag{2-35}$$

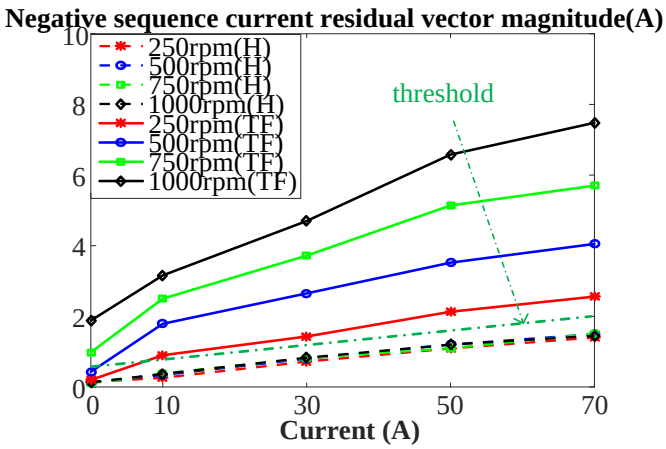

Fig. 2-26. Variations of negative sequence dq current residuals vector magnitude with speed and current in healthy and turn fault conditions

2.5.5 Fault detection at transient state

The turn fault detection during transient states and the effectiveness of angular integration based dc component extraction are also tested. Firstly, the test is performed with acceleration set to 1000 rpm/s via the dynamometer when the machine is initially operating at 700 rpm and 50A load current, and the resultant speed and detection response in the healthy condition are shown in Fig. 2-27. With the angular integration based order tracking, the processing interval is always kept to one electrical cycle regardless of the speed change. Thus, the extracted negative sequence dc components and their vector magnitude are not affected. In this way, false alarms can be avoided. When the fault occurs during the acceleration shown in Fig. 2-28, it can be detected as swiftly as in steady state operations.

Secondly, the effect of the current step change in healthy condition on the proposed detection method is tested and illustrated in Fig. 2-29. The speed is controlled by the dynamometer at 250 rpm initially and a step change in load current from 20A to 80A is

applied at 0.2s. Due to the limited response time of the dynamometer, the sudden change in the torque cause small deviations and fluctuations of the speed. The current step change leads to the magnitude variation of the dq current residuals, and hence the magnitude variation of the 2nd harmonics in the negative sequence dq current residuals. As can be seen, when the angular integration is performed, the extraction of dc component is affected by this variation, and the fluctuation in the calculated vector magnitude of the dc components is seen. Although, the magnitude of the dc component vector can cross the threshold for a while when the angle counter starts accumulating from zero, it will decrease to below the threshold due to fluctuation, causing the angle counter to reset. Eventually, the angle counter never exceeds the determined transient evaluation period of 2π. Thus, according to the fault detection steps in Fig. 2-13, this load transient condition will not cause a false alarm. When the fault occurs at 0.21s during the load transient as shown in Fig. 2-30, the fault detection is effective, since the magnitude of the dc component vector has been over the threshold for the predefined evaluation period.

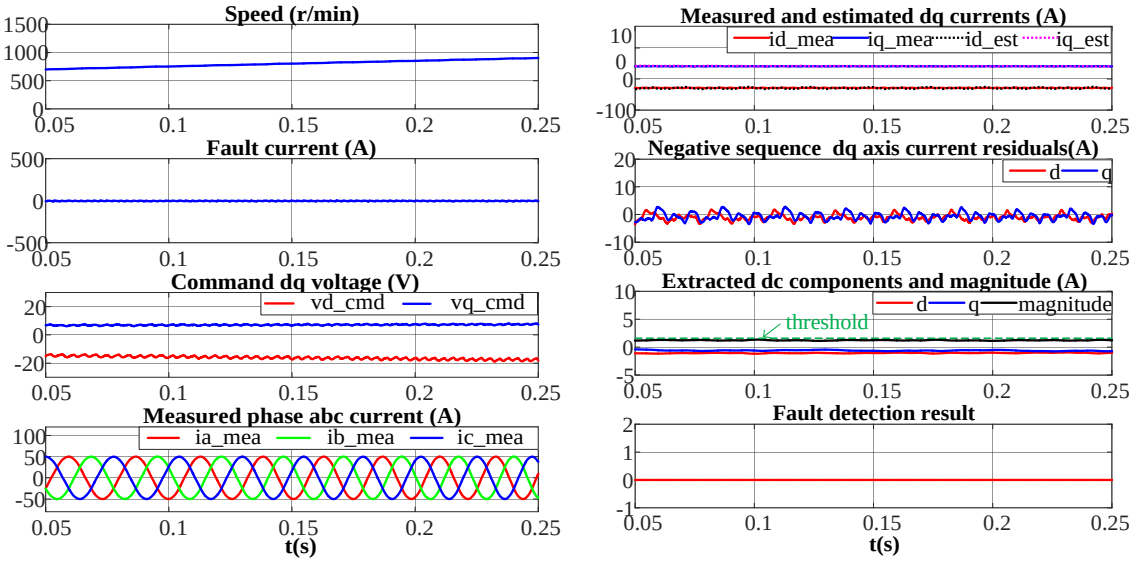

(a) (b)

Fig. 2-27 Healthy condition with increasing speed (a) operating condition, (b) fault detection process and result

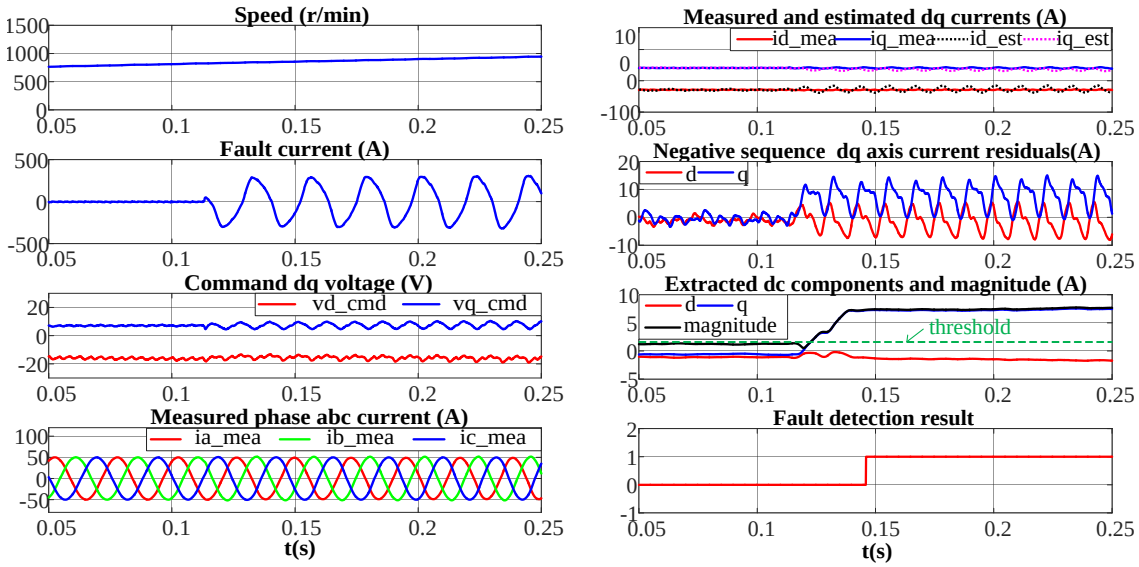

(a) (b)

Fig. 2-28 Turn fault condition with increasing speed (a) operating condition, (b) fault detection process and result

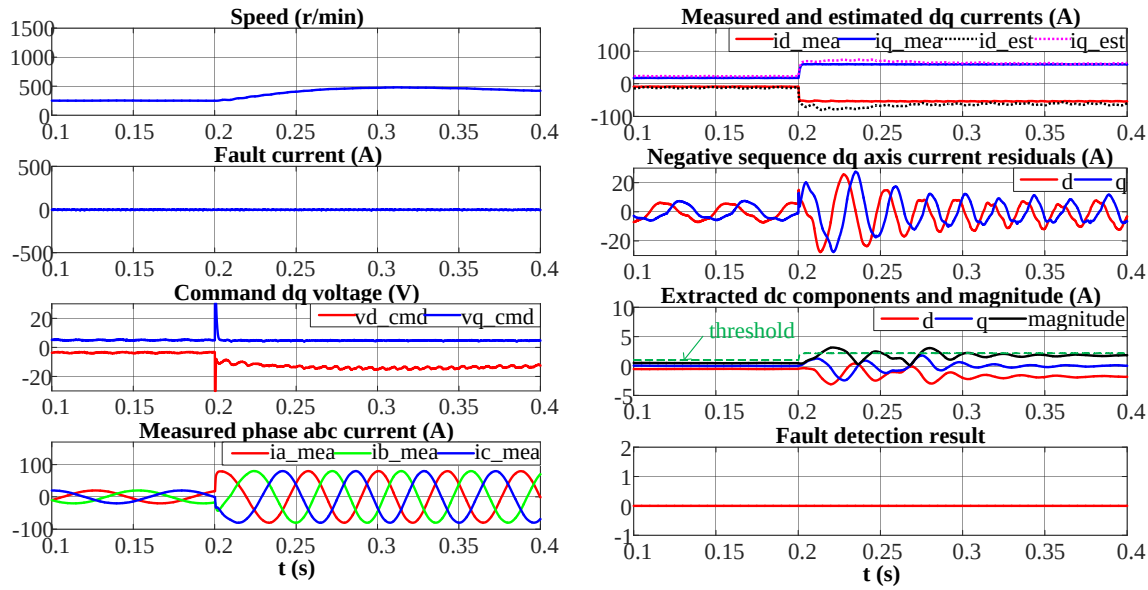

(a) (b)

Fig. 2-29 Healthy condition with current step change (a) operating condition, (b) fault detection process and result

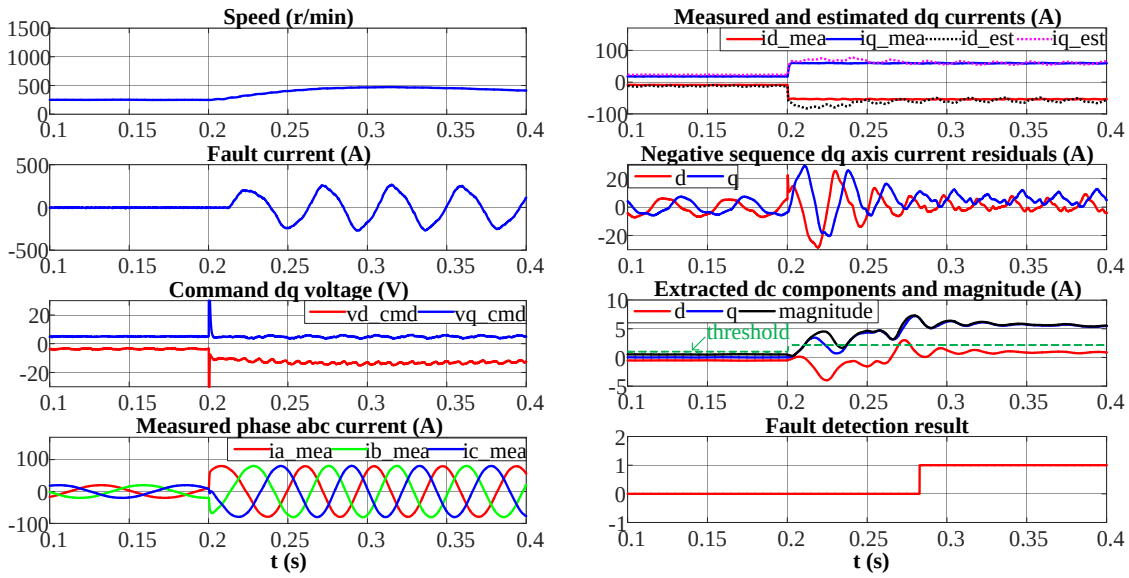

Fig. 2-30 Turn fault condition with current step change (a) operating condition, (b) fault detection process and result

2.6 Conclusions

In this chapter, a turn fault detection technique based on negative sequence dq current residuals by employing the machine model has been proposed. It has been demonstrated that the fault signatures can be enhanced when most of the unwanted components are eliminated in the current residuals. The influence of the control bandwidth on the fault signature has also been reduced greatly. The fault indicator is defined as the magnitude of the negative sequence dc components of the dq current residuals, which are extracted by the angular integration, through which, the impact of transient states is minimized. Extensive experimental results validate the analysis and proposed turn fault detection technique, demonstrating its effectiveness and robustness.

CHAPTER 3 PWM Ripple Currents Based Turn Fault Detection

3.1 Introduction

Apart from the machine electrical signature analysis and the machine model-based turn fault detection methods introduced in Chapter 2, high frequency signal based detection methods have also been studied by many researchers. Different from the former methods which are all based on the fundamental or the lower frequency components that are directly affected by the control strategy and the operating condition, the latter ones utilise the high frequency signal superimposed on the fundamental voltages, and analyse the corresponding high frequency current signals. Measurement of the high frequency negative sequence current or impedance is used to detect turn fault at an incipient stage in [60][108]. It has demonstrated that the sensitivity to operating conditions of the machine, i.e., the flux linkage, load torque/current and fundamental frequency, as well as to the influence of control loops, is reduced. The selection of the high frequency components is further analysed in [109], and the zero-sequence carrier-signal voltage is also proposed as the fault indicator. Additionally, in [110][111], the method of space modulation profiling (SMP) was used to detect any changes in the saliency, which can indicate the occurrence of fault in the stator winding. It is pointed out in [112], however, that the application of the above techniques can be limited in interior permanent magnet (IPM) machines due to the rotor saliencies. Thus, the pulsating-type voltage injection method is proposed in which the high frequency square wave voltage is superimposed on d-axis voltage. However, signal injection method introduces additional noise in the current and increases acoustic emissions of the motor-drive system [113][114]. Also, due to the frequency limitation of the injection, the application at high speed is problematic.

An improved method has been proposed in [61] by using the inherent PWM switching harmonics. It takes the advantage of the fact that most PM machines are fed through a pulse-width modulated (PWM) drive, which intrinsically contains rich high frequency components due to the switching. Thus, no extra signal injection is needed. The root mean square (RMS) value of the high frequency ripple current is measured as the fault indicator, and the faulted phase can also be identified. Since the ripple current exists in healthy condition and is dependent on modulation index, or operating condition,

extensive tests are inevitable for the establishment of the lookup map, and yet the map obtained in steady state tests may not be effective to monitor the machine conditions during a transient state. To circumvent these problems, this chapter proposes an improved technique for the five-phase fault tolerant surface mounted permanent magnet (SPM) machine drive.

In this chapter, the inherent high frequency PWM ripple currents are also utilized. The features of these high frequency components in turn fault conditions are analysed. A band-pass filter (BPF) is designed to extract the selected sideband components, and their RMS values are measured and compared among each other. It is shown that the RMS ripple current ratios between two adjacent phases provide a very good means of detecting turn fault with a high signal-to-noise ratio. The detection method can identify the faulted phase, tolerate inherent imbalance of the machine, and is hardly affected by transient states. The method is assessed by simulations and experiments on a five-phase permanent magnet machine drive. The implementation of this method on the three phase SPM and IPM is also investigated via simulations and experiments.

3.2 Analytical Study of HF PWM ripple currents

3.2.1 Turn fault detection technique based on PWM ripple currents

In the previous research [61], a turn fault detection technique based on PWM ripple current measurement was proposed and applied to a 10-slot, 12-pole, 5-phase surface mounted permanent magnet (SPM) machine with one coil per phase. The geometry of the machine is shown in Fig. 3-1. It is an alternate tooth wound SPM machine which exhibits inherent fault tolerance due to both physical and magnetic separation of the phase windings with virtually no mutual magnetic coupling between the phases.

The schematic of a single winding of the machine under the turn fault conditions with N_f faulted turns out of a total N number turns is shown in Fig. 3-2. Based on the schematic, the high frequency admittance of the winding under fault conditions is derived in (3-1), where R_{hh}, R_{ff}, L_{hh} and L_{ff} are the resistance and self-inductance of the healthy and fault turns, respectively and M_{hf} is the mutual inductance between the healthy and faulted winding parts. R_f is the resistance in the shorted path and is assumed

zero in the analysis for sake of simplicity. With the machine parameters from Table 3-1 and Table 3-2, the variation of the admittance against frequency can be obtained. It is clear that at high frequency, the difference between the admittances in turn fault and healthy conditions is more significant, making it promising for turn fault detection with high frequency signals.

$$Y(j\omega)=\frac{I(j\omega)}{V(j\omega)}=\frac{1}{R_{hh}+j\omega L_{hh}-\dfrac{\omega^2 M_{hf}^{\ 2}}{R_{ff}+j\omega L_{ff}}} \tag{3-1}$$

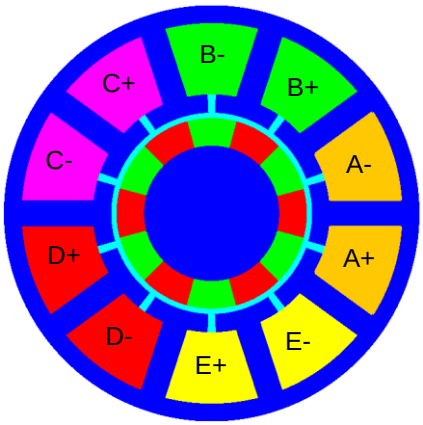

Fig. 3-1 Geometry of 10-slot, 12-pole SPM machine [61]

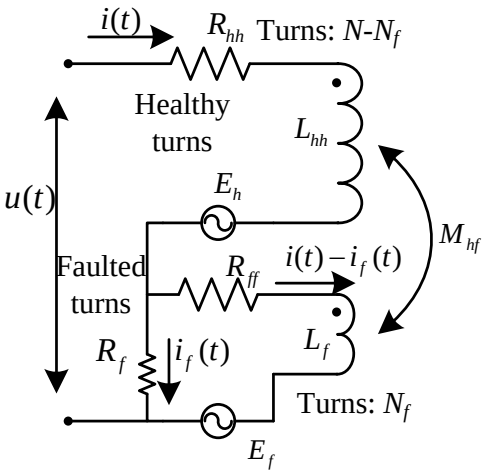

Fig. 3-2 Schematic of winding under turn fault [61]

The previous detection technique is based on measurement of RMS PWM ripple currents which increase in fault conditions. However, they are also dependent on PWM modulation index, and hence operating conditions, which implies that operation-dependent thresholds have to be established by extensive tests. While such a process to determine the thresholds may be possible in a laboratory condition, it is impractical in real applications. Further the thresholds obtained in steady-state tests may not be

effective for monitoring machine conditions in transient. Thus, it is desirable to develop a new fault indicator that is relatively constant in most operating conditions, and is also unaffected by transient states.

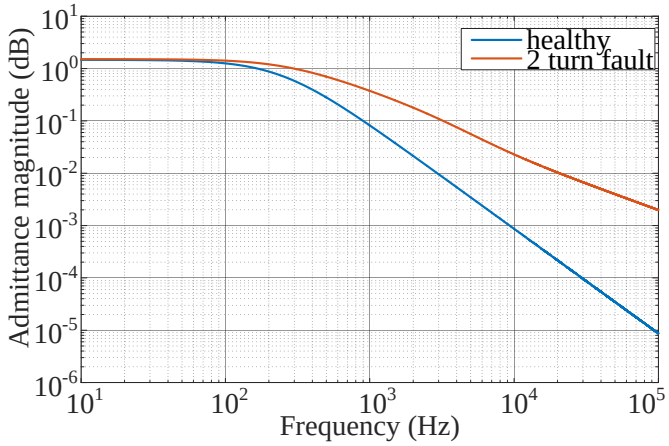

Fig. 3-3 Comparison of admittance magnitude in healthy and 2 turn fault condition

In order to determine such a fault indicator, the variation of high frequency (HF) currents due to turn fault is analysed based on a simplified fault model. Although errors may exist in the simplified model, the results give insightful understanding of how HF currents change in fault conditions, and provide guidance to define and evaluate a new fault indicator.

3.2.2 Analysis of HF PWM ripple currents

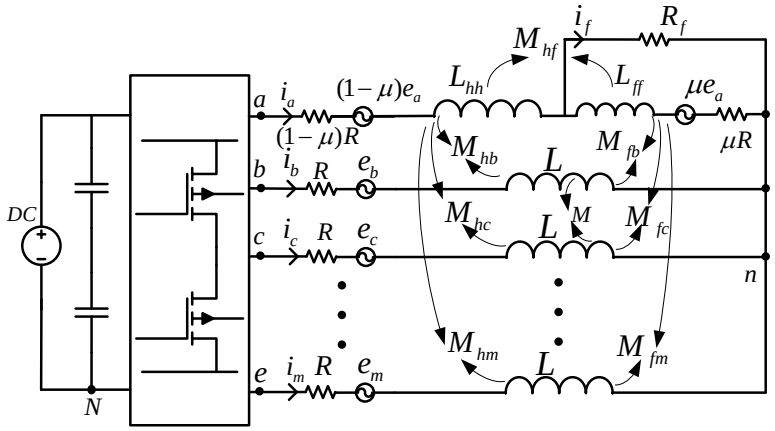

Fig. 3-4 Equivalent circuit under turn fault condition in phase A

For generality, a multi-phase machine with m number of phases is assumed. The star connection of the phase windings with their equivalent circuits and the power converter under a turn fault condition in phase A are shown in Fig. 3-4, where i_a, i_b,…,i_m are the phase currents, i_f is the current in the shorted branch. e_a, e_b … e_m are phase back-EMFs, L and M are self- and mutual-inductances of the healthy phases respectively. μ is the percentage of number of shorted turns N_f over the total number of turns N per phase.

M_{fb}, …, M_{fm} are the mutual inductances between the faulted turns and other healthy phases, while M_{hb}, …, M_{hm} are the mutual inductances between the healthy turns and other healthy phases.

Based on the equivalent circuit shown in Fig. 3-4, the governing equations that describe the relationships between the voltages and currents when a turn fault occurs in phase A are given in (3-2).

$$\begin{cases} u_{ah} = (1-\mu)Ri_a + L_{hh}\dfrac{di_a}{dt} + M_{hf}\dfrac{d(i_a - i_f)}{dt} + M_{hb}\dfrac{di_b}{dt} + \ldots + M_{hm}\dfrac{di_m}{dt} + (1-\mu)e_a \\ u_{af} = \mu R(i_a - i_f) + M_{hf}\dfrac{di_a}{dt} + L_{ff}\dfrac{d(i_a - i_f)}{dt} + M_{fb}\dfrac{di_b}{dt} + \ldots + M_{fm}\dfrac{di_m}{dt} + \mu e_a \\ u_a = u_{ah} + u_{af} + u_{nN} \\ u_b = Ri_b + L\dfrac{di_b}{dt} + M_{hb}\dfrac{di_a}{dt} + M_{fb}\dfrac{d(i_a - i_f)}{dt} + \ldots + M\dfrac{di_m}{dt} + e_b + u_{nN} \\ \vdots \\ u_m = Ri_m + L\dfrac{di_m}{dt} + M_{hm}\dfrac{di_a}{dt} + M_{fm}\dfrac{d(i_a - i_f)}{dt} + \ldots + M\dfrac{di_{m-1}}{dt} + e_m + u_{nN} \end{cases} \tag{3-2}$$

where u_{ah}, u_{af} are the voltages in the healthy and faulted parts of phase A winding, u_a, u_b … u_m are the inverter output voltages referred to the ground (N), u_{nN} is the voltage between the neutral point (n) and the ground. The unknown u_{nN} is obtained in (3-3) by summing the m voltage equations in (3-2) and rearranging. By eliminating it the current can be directly related to the inverter output voltage.

$$u_{nN} = \frac{\sum u_{a\ldots m}}{m} + \frac{1}{m}(M_{hf} + L_{ff})\frac{di_f}{dt} + \frac{1}{m}\mu R i_f + \frac{1}{m}(M_{fb} + \ldots + M_{fm})\frac{di_f}{dt} \tag{3-3}$$

For high frequency currents due to PWM operation, the contribution of the back EMFs can be ignored because they are of low frequency. Hence, the equations in (3-2) can be rearranged by removing the back EMF and eliminating u_{nN} with (3-3) in the form of high frequency components in PWM voltages u_A, u_B …, u_M , shown in (3-4), where i_A, i_B …, i_M are high frequency currents in each phase, and i_{Fa} is the high frequency current in the short circuit branch. For the sake of simplicity, the relationship between the self- and mutual-inductances and μ may be approximated in (3-5), where j denotes the rest of healthy phases, b, c, …, m. This is true in the machines which have low leakage flux, or the machine with one coil per phase[106]. The basic parameters of the prototype machine in healthy and fault conditions are extracted from finite element analysis (FEA) software FLUX2D, and are shown in Table 3-1 and Table 3-2 respectively. Since this

machine is an SPM machine, the saturation due to the current is insignificant. Even though the short current is much larger than the rated, the effect of small number of faulted turns (2 turns in the study) on saturation is also very small. Therefore, the saturations in both healthy and fault conditions are neglected, and all the inductances are assumed to be constant.

$$\begin{cases} u_A = (u_a - \dfrac{\sum u_{a\ldots m}}{m})_{HF} = Ri_A + (L-M)\dfrac{di_A}{dt} - \dfrac{m-1}{m}(M_{hf} + L_{ff})\dfrac{di_{Fa}}{dt} \\ \qquad\qquad - \dfrac{m-1}{m}\mu R i_{Fa} + \dfrac{1}{m}(M_{fb} + \ldots + M_{fm})\dfrac{di_{Fa}}{dt} \\ u_B = (u_b - \dfrac{\sum u_{a\ldots m}}{3})_{HF} = Ri_B + (L-M)\dfrac{di_B}{dt} + \dfrac{1}{m}(M_{hf} + L_{ff})\dfrac{di_{Fa}}{dt} \\ \qquad\qquad - M_{fb}\dfrac{di_{Fa}}{dt} + \dfrac{1}{m}\mu R i_{Fa} + \dfrac{1}{m}(M_{fb} + \ldots + M_{fm})\dfrac{di_{Fa}}{dt} \\ \vdots \\ u_M = (u_m - \dfrac{\sum u_{a\ldots m}}{3})_{HF} = Ri_M + (L-M)\dfrac{di_M}{dt} + \dfrac{1}{m}(M_{hf} + L_{ff})\dfrac{di_{Fa}}{dt} \\ \qquad\qquad - M_{fm}\dfrac{di_{Fa}}{dt} + \dfrac{1}{m}\mu R i_{Fa} + \dfrac{1}{m}(M_{fb} + \ldots + M_{fm})\dfrac{di_{Fa}}{dt} \\ 0 = \mu R(i_A - i_{Fa}) + M_{hf}\dfrac{di_A}{dt} + L_{ff}\dfrac{d(i_A - i_{Fa})}{dt} + M_{fb}\dfrac{di_B}{dt} + \ldots + M_{fm}\dfrac{di_M}{dt} \end{cases} \tag{3-4}$$

$$\begin{aligned} L_{hh} &= (1-\mu)^2 L \\ L_{ff} &= \mu^2 L \\ M_{hf} &= \mu(1-\mu)L \\ M_{hj} &= (1-\mu)M, \quad (j = b,c,\ldots,m) \\ M_{fj} &= \mu M, \quad (j = b,c,\ldots,m) \end{aligned} \tag{3-5}$$

With (3-5), equations (3-4) can be simplified to (3-6), where *s* denotes the Laplace operator. The first *m* equations show the relations among the high frequency voltages, the high frequency phase currents and the fault current. It is clear that the differences in the currents are mainly caused by the additional terms of fault current. In healthy conditions, the fault current is zero, hence all high frequency currents should be symmetric with the same amplitude. The last equation in (3-6) relates the HF fault current to the HF phase A current, which can be substituted into the rest equations to establish the relation between the HF currents and HF phase voltages. After defining a coefficient k_f in (3-7), the final expressions for HF voltage phasors in all phases can be written in (3-8), in the form of corresponding HF currents and phase A voltage.

Table 3-1 Machine data

Specification	Value	Specification	Value
No. of phases	5	Phase resistance	0.68
No. of poles	12	Phase inductance	2.8mH
No. of slots	10	Rated current	6.0 A
No. of turns per phase	62	Maximum speed	3000r/min
Back-EMF(peak)	37V	Rated torque	1.86 Nm
DC voltage	60V	Switching frequency	10k Hz

Table 3-2 Machine parameters under fault conditions

Parameter	Fault conditions	
N_f	2 turn fault	20 turn fault
R_h	0.66	0.46
R_f	0.02	0.22
L_{hh}	2.6mH	1.3mH
L_{ff}	2.8μH	0.28mH
M_{hf}	83μH	0.6mH

$$\begin{cases} u_A = [(L-M)s+R]i_A - \dfrac{m-1}{m}\mu[(L-M)s+R]i_{Fa} \\ u_B = [(L-M)s+R]i_B + \dfrac{1}{m}\mu[(L-M)s+R]i_{Fa} \\ \vdots \\ u_M = [(L-M)s+R]i_M + \dfrac{1}{m}\mu[(L-M)s+R]i_{Fa} \\ i_{Fa} = \dfrac{[(L-M)s+R]}{\mu Ls+R} i_A \end{cases} \tag{3-6}$$

$$k_f = \frac{\mu[(L-M)s+R]}{[L+(m-1)M]\mu s+[m-\mu(m-1)]R} \tag{3-7}$$

$$\begin{cases} u_A = [(L-M)s+R]i_A - (m-1)k_f u_A \\ u_B = [(L-M)s+R]i_B + k_f u_A \\ \vdots \\ u_M = [(L-M)s+R]i_M + k_f u_A \end{cases} \tag{3-8}$$

Since the first term on the right in (3-8) are associated with the impedance in healthy conditions, the calculation and comparison of HF currents in each phase can be performed by applications of HF voltages. As the HF voltages are approximately symmetric with small number of shorted turns, it is very easy to use such a procedure to calculate the ratio of the resultant HF currents in two adjacent phases. Fig. 3-5 shows the schematic phasors diagram and their relative magnitudes for the five-phase machine for a given HF voltage component.

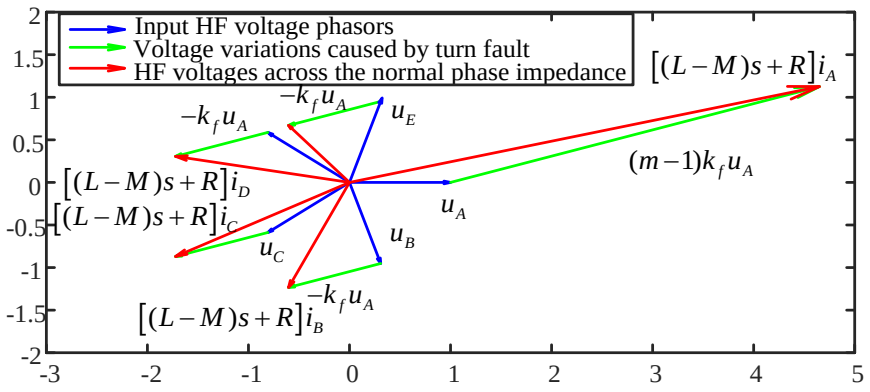

Fig. 3-5 Phasor plot in fault conditions

The HF voltage across the normal phase impedances should be equal to the input HF voltages in healthy conditions, but deviate from them to different extents in turn fault conditions. Since the fault occurs in phase A, the amplitude change in HF current of phase A is the largest. Although the influence of turn fault on the other phase voltage, represented by the green arrows in Fig. 3-5, is the same, the resultant changes of HF currents in each phase, which are proportional to the red arrows, are different.

The amplitude of HF current is dependent on HF voltages, which is determined by modulation index. Thus, a non-constant threshold whose value is related to operating conditions is needed, if turn fault detection is based on the amplitude variation of the HF currents. Since the change of the HF currents is dependent on operating conditions, the margin between the threshold and actual value to avoid false alarm is also non-constant, which compromises the sensitivity and robustness of the fault detection.

However, once a fault scenario is assumed, the phasor plot in Fig. 3-5 can be determined. If the HF voltages change with operating conditions, the amplitude of phasors will also change proportionally. The proportional change will not affect the relative amplitudes of the HF currents in all phases. Therefore, the comparison of HF currents in adjacent phases in the form of ratio is investigated.

3.3 Turn fault indicator analysis

3.3.1 Prediction of HF PWM ripple currents

PWM operation of an inverter produces a specific set of high frequency voltages whose frequency and magnitude can be analysed.

Assuming sine-PWM is employed, the frequency components of the inverter output voltage can be expressed in(3-9)[115], and its spectrum is shown in Fig. 3-6(a).

$$
\begin{aligned}
v(t) &= \frac{V_D M_m}{2}\cos(\omega_r + \theta_r) \\
&+ \frac{2V_D}{\pi}\sum_{x=1}^{\infty}\frac{1}{x}J_0(x\frac{\pi}{2}M_m)\sin x\frac{\pi}{2}\cos\left[x(\omega_c t+\theta_c)\right] \\
&+ \frac{2V_D}{\pi}\sum_{x=1}^{\infty}\sum_{y=-\infty}^{\infty}\frac{1}{x}J_y(x\frac{\pi}{2}M_m)\sin\left[(x+y)\frac{\pi}{2}\right]\cos\left[x(\omega_c t+\theta_c)\pm y(\omega_r t+\theta_r)\right]
\end{aligned}
\tag{3-9}
$$

where V_D is the dc voltage, M_m is modulation, ω_c is switching frequency, ω_r is the fundamental frequency, θ_r is the phase angle of the fundamental modulation signal, θ_c is the initial phase angle of the carrier wave. J_y is the Bessel function of the y^{th} order. x and y are nonnegative integers, and when x is odd, then y is even, and vice versa.

It can be seen from (3-9) that the frequency and magnitude of the voltage components can be expressed in (3-10) and in (3-11).

$$f = xf_c \pm yf_r \tag{3-10}$$

$$Ma_{xy} = \frac{2V_D}{\pi}\frac{1}{x}J_y(x\frac{\pi}{2}M_m) \tag{3-11}$$

where $f_c = 2\pi\omega_c$ and $f_r = 2\pi\omega_r$. The side band frequency components will only exist at xf_c , $xf_c \pm 2f_r$, $xf_c \pm 4f_r$,for x=1, 3, 5, …; and $xf_c \pm f_r$, $xf_c \pm 3f_r$, for x=2, 4, 6,…

The switching frequency of the inverter is set to 10 kHz for the machine under study, and the frequency components with the modulation of 0.3 shown in Fig. 3-6(a) accord with those in (3-10). After elimination of the zero sequence voltages based on (3-4), the spectrum of u_A is shown in Fig. 3-6 (b). The side band frequency components with x greater than 2 are ignored, since their amplitudes are much smaller.

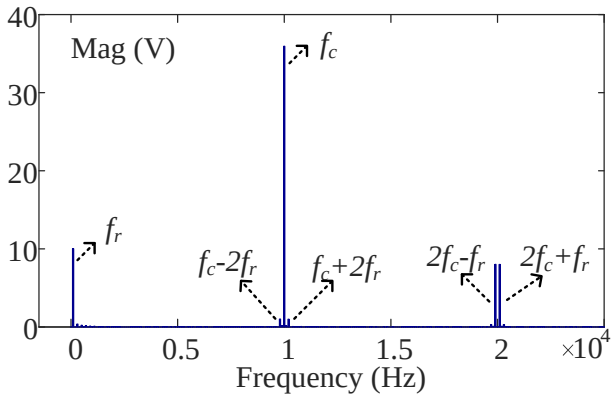

(a)

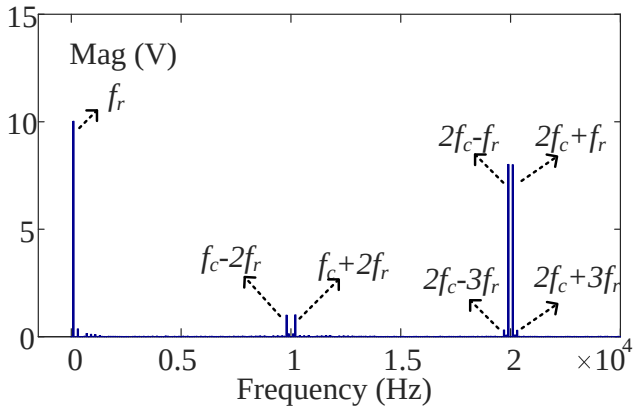

(b)

Fig. 3-6 (a) Spectrum of SPWM voltage. (b) Spectrum of SPWM voltage after elimination of zero sequence voltages

The magnitudes for the sideband around 10 kHz, Ma_{12}, and for the sidebands around 20 kHz, Ma_{21} and Ma_{23}, can be evaluated by (3-11) and their variations with modulation index are illustrated in Fig. 3-7. It is seen that over a wide range of modulation, the magnitude of the sideband at $2f_c \pm f_r$ is the largest. Although the magnitude at $2f_c \pm 3f_r$ is relatively small, its frequency is very close to$2f_c \pm f_r$. As a result, the combined magnitude of the two sideband HF components around 20 kHz is much larger than that around 10 kHz in most cases. These two components are chosen for further evaluation. To extract them from measured currents, a 4th order bandpass filter can be designed with the centre frequency of 20 kHz, and the band width of 2kHz.

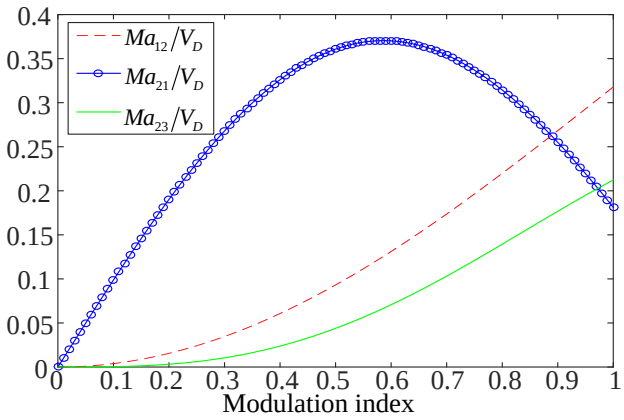

Fig. 3-7 Variations in sideband frequency magnitudes with modulation index

After filtering by the bandpass filter, the HF currents contain 4 frequency components, $2f_c \pm f_r$, $2f_c \pm 3f_r$. The voltage components that generate the corresponding currents are given in (3-12). The HF currents at each frequency can be calculated by (3-7) and (3-8) as described in section 3.2, with the admittance associated with each frequency component defined in (3-13). The expression for HF currents in phase A after

filtering can be written as (3-14) and its root-mean-square (RMS) value is further assessed.

$$\begin{aligned} u_A &= u_{A3-} + u_{A-} + u_{A+} + u_{A3+} \\ &= \frac{2V_D}{\pi} \cdot \begin{Bmatrix} J_3(\pi M_m)\cos\left[(2\omega_c - 3\omega_r)t + \theta_{u3-})\right] \\ - J_1(\pi M_m)\cos\left[(2\omega_c - \omega_r)t + \theta_{u1-})\right] \\ - J_1(\pi M_m)\cos\left[(2\omega_c + \omega_r)t + \theta_{u1+})\right] \\ + J_3(\pi M_m)\cos\left[(2\omega_c + 3\omega_r)t + \theta_{u3+})\right] \end{Bmatrix} \end{aligned} \tag{3-12}$$

$$K_{a3-} = \frac{|i_{A3-}|}{|u_{A3-}|}, K_{a-} = \frac{|i_{A-}|}{|u_{A-}|}, K_{a+} = \frac{|i_{A+}|}{|u_{A+}|}, K_{a3+} = \frac{|i_{A3+}|}{|u_{A3+}|} \tag{3-13}$$

$$i_A = \frac{2V_D}{\pi} \cdot \begin{Bmatrix} K_{a3-} \cdot J_3(\pi M_m)\cos\left[(2\omega_c - 3\omega_r)t + \theta_{i3-})\right] \\ - K_{a1-} \cdot J_1(\pi M_m)\cos\left[(2\omega_c - \omega_r)t + \theta_{i1-})\right] \\ - K_{a1+} \cdot J_1(\pi M_m)\cos\left[(2\omega_c + \omega_r)t + \theta_{i1+})\right] \\ + K_{a3+} \cdot J_3(\pi M_m)\cos\left[(2\omega_c + 3\omega_r)t + \theta_{i3+})\right] \end{Bmatrix} \tag{3-14}$$

3.3.2 Fault indicator

The RMS value of a signal given in (3-15) can be obtained by an analogue RMS converter which consists of a square function, a low-pass filter (LPF) and a root-square function, as shown in Fig. 3-8. Ideally, all the frequency components except the dc component should be filtered out through the low-pass filter, thus the output should be a dc signal.

$$RMS(V_{in}) = V_{out} = \sqrt{Average(V_{in}^{\ 2})} \tag{3-15}$$

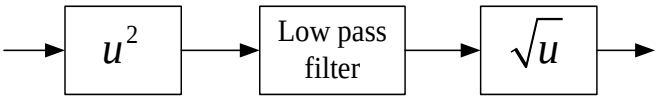

Fig. 3-8 Signal processing block diagram of RMS converter

When the input to the RMS converter i_A is expressed in (3-14), the ideal output can be written as (3-16). Although RMS current i_{A_rms} changes when turn fault occurs, there is no simple way to define a threshold since $i_{A\_rms\_h}$ and $i_{A\_rms\_f}$ in healthy and fault conditions are dependent on modulation index, as shown in Fig. 3-9. Thus, the threshold must be determined as a function of modulation index, rather than a constant, which, will increase the complexity. At low modulation index, the margin between the RMS currents in fault and healthy conditions become small, which would reduce detectability.

$$i_{A\_rms} = \frac{2V_D}{\pi}\sqrt{\begin{aligned}&[K_{3a-}\cdot J_3(\pi M_m)]^2 + [K_{1a-}\cdot J_1(\pi M_m)]^2 \\ &+[K_{1a+}\cdot J_1(\pi M_m)]^2 + [K_{3a+}\cdot J_3(\pi M_m)]^2\end{aligned}} \tag{3-16}$$

$$i_{B\_rms} = \frac{2V_D}{\pi}\sqrt{\begin{aligned}&[K_{3b-}\cdot J_3(\pi M_m)]^2 + [K_{1b-}\cdot J_1(\pi M_m)]^2 \\ &+[K_{1b+}\cdot J_1(\pi M_m)]^2 + [K_{3b+}\cdot J_3(\pi M_m)]^2\end{aligned}} \tag{3-17}$$

$$k_{AB} = \frac{i_{A\_rms}}{i_{B\_rms}} = \sqrt{\begin{aligned}&\frac{[K_{3a-}\cdot J_3(\pi M_m)]^2 + [K_{1a-}\cdot J_1(\pi M_m)]^2}{+[K_{1a+}\cdot J_1(\pi M_m)]^2 + [K_{3a+}\cdot J_3(\pi M_m)]^2} \\ &\frac{[K_{3b-}\cdot J_3(\pi M_m)]^2 + [K_{1b-}\cdot J_1(\pi M_m)]^2}{+[K_{1b+}\cdot J_1(\pi M_m)]^2 + [K_{3b+}\cdot J_3(\pi M_m)]^2}\end{aligned}} \tag{3-18}$$

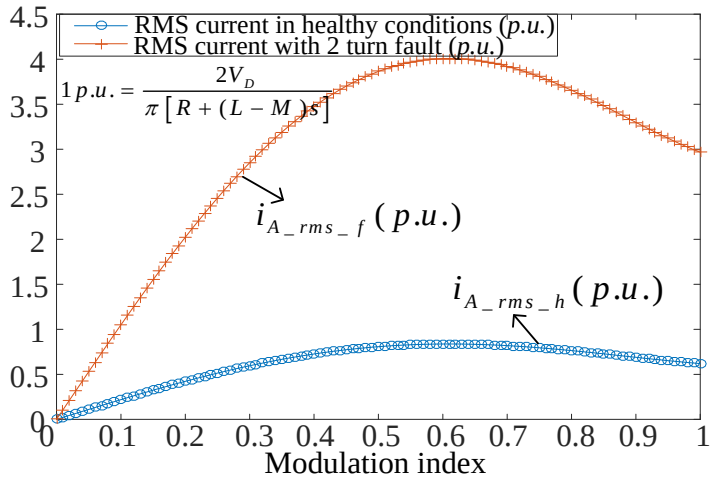

Fig. 3-9 Normalized RMS current variations in phase A under healthy and 2-turn fault conditions with modulation index,

Therefore, the comparison of the RMS ripple currents between phases is studied for the purpose of better fault detections. The ideal output of the RMS current for phase B can be similarly derived and is given in (3-17), and their ratio of the RMS currents in phases A and B under healthy and fault conditions is shown in (3-18). It can be shown that $K_{3a-}=K_{3b-}$, $K_{1a-}=K_{1b-}$, $K_{1a+}=K_{1a+}$, $K_{3a+}=K_{3b+}$, under healthy conditions and, hence, the ratio should be 1, regardless of modulation index. Under fault conditions, the ratio is unequal to 1, albeit it is still dependent on modulation index. The ratio variations with modulation index under healthy and 2-turn fault conditions are compared in Fig. 3-10 for the prototype machine whose parameters are given in Table 3-2. It can be seen that for the whole range of modulation index from 0 to 1, the ratio in fault conditions deviates significantly from 1 and the slight variation at higher modulation index will not affect fault detection. The large deviation from the healthy value of 1 under the fault condition indicates a high signal-to-noise ratio and a constant threshold will be sufficient to ensure sensitive and robust fault detection. Further, during a transient state

when speed or load torque changes in healthy conditions, the modulation will change, but the ratio k_{AB_h} should remain 1 according to Fig. 3-10. Thus, the fault detection with the RMS current ratio as indicator will be effective in both transient and steady-state.

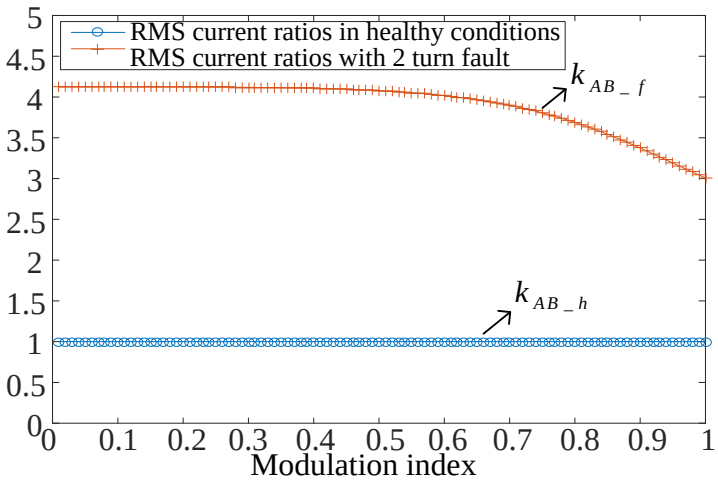

Fig. 3-10 Variations of RMS current ratios with modulation index under healthy and 2-turn fault conditions.

Note that the ratios for other phases can also be calculated in a similar way, but among them k_{AB} is the largest and is used as the indicator because the turn fault is assumed to occur in phase A in this case. In real applications, the faulted phase can be arbitrary, thus the ratios for each two adjacent phases need to be calculated in real time. In healthy conditions, all the ratios should be 1. In fault conditions, the ratios differ from each other. If any ratio is larger than the predefined threshold, then a fault can be detected. Also, the largest ratio can identify the phase where the turn fault occurs.

The above analysis is based on ideal conditions with simplified models for the convenience of feature extraction. The conclusion obtained is mainly qualitative, while the exact ratio under fault may not be predicted accurately. However, it can at least prove in theory that the ratios of the selected RMS ripple currents is superior to the amplitude as the turn fault indicator. The applicability of these analytic results is explored in simulation and experimental studies in the next sections.

3.4 Simulation results

The proposed turn-fault detection technique is assessed by MATLAB/SIMULINK simulations on the 5-phase fault tolerant PM machine shown in Fig. 3-1 with parameters listed in Table 3-1 and Table 3-2. The 5 phases are star connected and fed by a 5-phase inverter as shown in Fig. 3-4. The inverter operates under sine-PWM at 10 kHz switching frequency. To accord with the analysis, a 2-turn fault is injected in phase A at

0.03s. Fig. 3-11 shows the phase currents in A, B, C, D and E, and their HF currents after bandpass filtering and amplifying in both healthy and 2-turn fault conditions, when the drive responds to a speed demand at 1000 r/min with i_q=6A. It is evident that the HF currents of all the phases and their RMS values are equal when the machine is healthy. When turn fault occurs in phase A, the HF and RMS currents differ among all the phases with those of phase A being the largest.

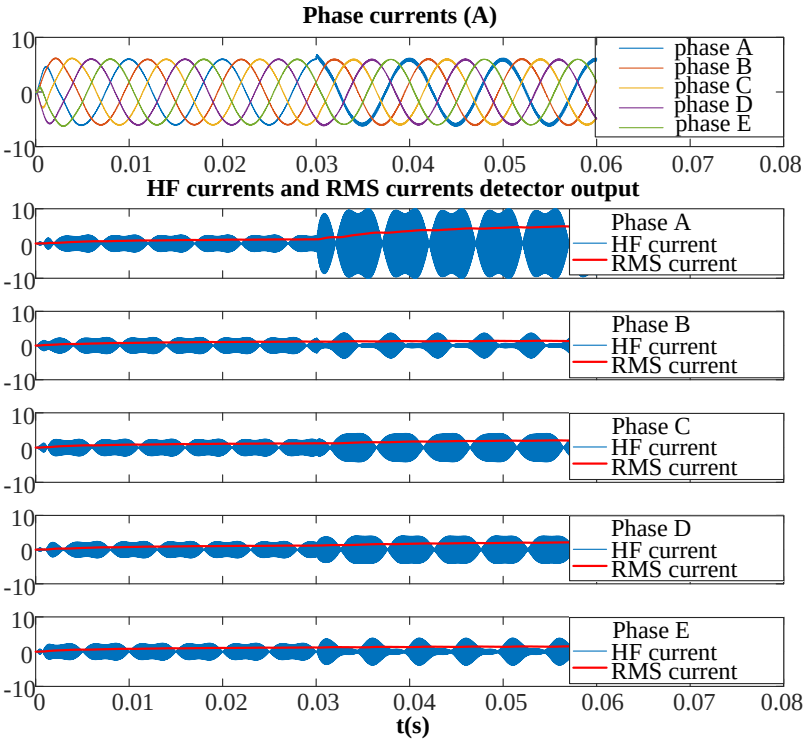

Fig. 3-11 HF and RMS currents in both healthy and 2-turn fault conditions

To test the robustness of fault detection in transients, the variations of speed and torque, shown in Fig. 3-12, are introduced in the simulation and a 2-turn fault is injected at 0.3s in phase A. The detecting results are shown in Fig. 3-13. In the simulation, the RMS currents are obtained by the signal processing function of the RMS converter shown in Fig. 3-8.

As can be observed, the RMS currents contain undesired ripples. This is because the ideal low pass filter in RMS detector is not possible and the sidebands associated with the fundamental frequency are present in the converter outputs. Thus, the output of the RMS converter will contain the frequency components at twice of the fundamental frequency which causes the output fluctuations. Consequently, the ratios also contain ripples, which makes the detection less robust if they are to be compared with a constant threshold. Thus, to eliminate these ripples, a simple digital low-pass filter with its

corner frequency equal to the fundamental frequency can be applied to enhance the robustness of detection.

It is seen from Fig. 3-14 that in the healthy condition, the RMS currents in each phase are equal and the ratios are 1, and they are immune to speed variation, except for the initial transient. The step change in torque does affect the ratios slightly, but the influence is insignificant and can be ignored. The ratio deviation from 1 during the initial transient is due to the fact that there is no sufficient data for RMS calculation. After one revolution, correct RMS values in each phase are obtained, and the ratios are no longer affected by subsequent changes in speed. In the fault condition, the ratios deviate from 1 with the largest above 3. Such a large deviation gives a high signal-to-noise ratio with a constant threshold without the need for extensive experimental tests and calibrations.

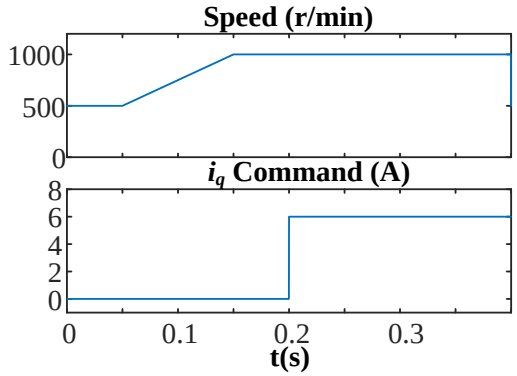

Fig. 3-12 Operating conditions

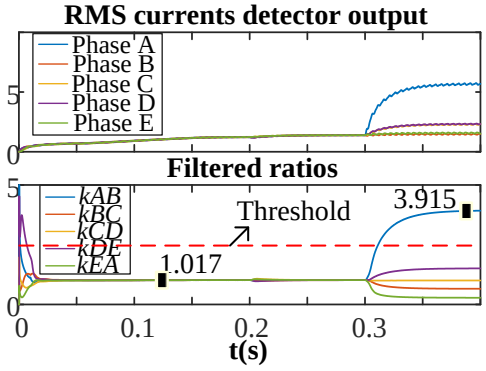

Fig. 3-13 RMS ripple current and fault indicator with balanced machine

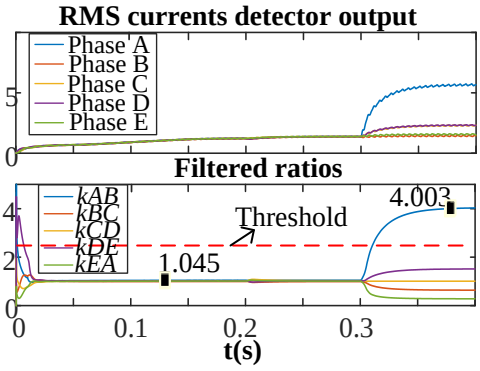

Fig. 3-14 RMS ripple current and fault indicator with unbalanced machine

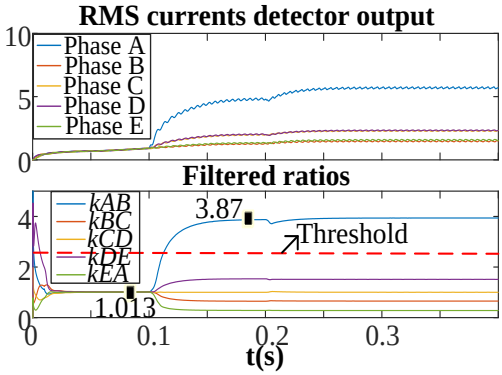

Fig. 3-15 Fault indicator when fault occur in non-stationary state

If the machine has an inherent unbalance, most detection methods published in literature are affected, and data map through extensive tests is usually the only solution.

The effect of phase unbalance on the proposed technique is also simulated. It should be noted that the unbalance in the back-EMFs will not have any effect on the proposed detection technique because they are of low frequency and filtered out. Hence, the simulation is performed by assuming the inductance and resistance in phase B are 3% and 5% larger than those in the other phases respectively. The simulation results are shown in Fig. 3-14 under the same operating conditions. As will be seen, the ratios associated with phase B under the healthy condition are slightly increased to 1.045 due to phase unbalance. However, the ratio under the fault condition is far greater. Thus, a few percent machine unbalance has little effect on this detection technique.

Fig. 3-15 shows the detector responses when the drive operates under the same speed and load profiles shown in Fig. 3-12 but the fault is injected at 0.1s during the speed transient. It is evident the detection is equally effective under the non-stationary conditions.

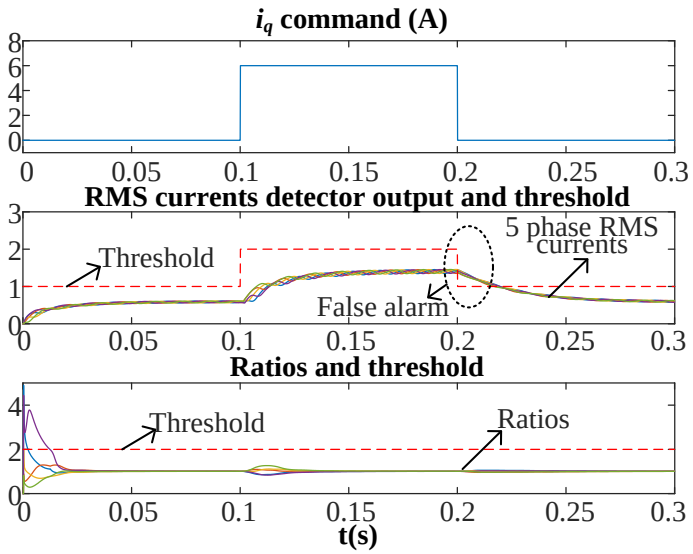

Fig. 3-16 Comparison of fault indicators obtained from the previous and proposed methods in transient state under healthy condition

The robustness of the proposed method is compared with that described in [61] where the detector signal proportional to RMS ripple current is used against pre-defined thresholds as fault indicator. Fig. 3-16 shows the simulated fault indicators of the two methods in response to step change in load current at 500 rpm in healthy condition. If the detector signals proportional to the RMS ripple currents are to compare with the pre-defined thresholds directly, false alarms are very likely to occur as shown in the second graph of Fig. 3-16. This is caused by the time delay of the RMS detection. Thus, reliable detection with the technique described in [61] is only feasible in steady state.

However, since the time delay for all the phases are equal, the effect on the ratio is greatly reduced. As a result, the ratio based method will not cause false alarms in transient state, enhancing the robustness and reliability of the fault detection.

3.5 Experiment Results

The proposed turn-fault detection technique has been tested on the 5-phase prototype machine described in section 3.2.1. The machine is mounted on the test rig shown in Fig. 3-17(a) and is controlled by the 5-phase MOSFET inverter shown in Fig. 3-17(b). A 2-turn fault for short time duration is injected by the relay shown in Fig. 3-17 (a). The test machine operates in torque control mode with an encoder feedback and the speed is adjusted by a dynamometer. The DC link voltage is set 60V. The 5-phase fault tolerant drive system is controlled at 10 kHz switching frequency using a digital signal processor (DSP) board (EzDSP F28335). A separate analogue BP filter circuit board is designed and installed to extract the high frequency components around 20 kHz from measured phase currents and obtain their RMS values through RMS converter chips. The outputs of the RMS converters are then sampled through the ADCs (Analog to Digital Converter) of the DSP, where the ratios are calculated in real time according to (3-18). The diagram of the signal processing chain of the detecting technique is shown in Fig. 3-18.

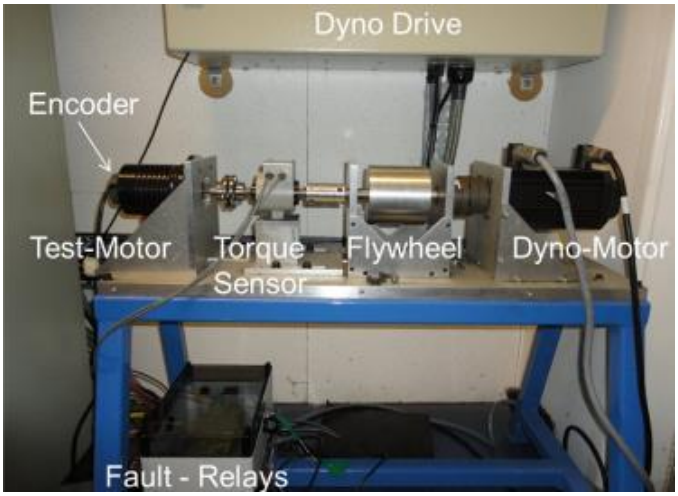

(a)

(b)

Fig. 3-17(a) Test rig with fault emulation set-up. (b) 5-Phase Inverter with HF detection board

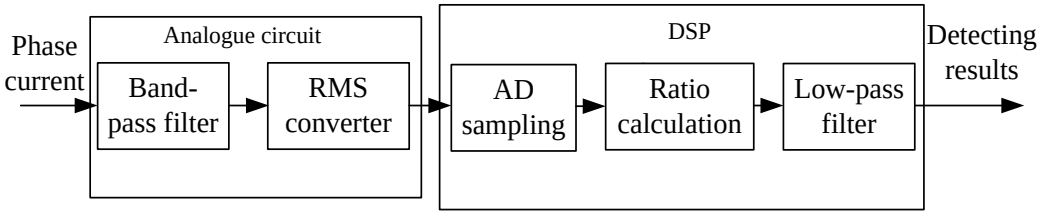

Fig. 3-18 Diagram of PWM ripple current based turn fault detection technique

Fig. 3-19 shows the detection results at i_q=3A and 500 r/min with 2-turn fault. The machine is operating in healthy conditions until 0.12s, when the 2-turn fault is injected. It can be seen that the RMS values for 5 phase HF currents are initially different in healthy conditions and the ratios are not equal to 1. This is due to a number of factors. First, a small phase unbalance is inevitable in a practical machine due to manufacturing tolerance. Second, the tolerance of capacitors used in the BP filter board is ±5% and small differences in filter gain also exist in different phases. Hence, the BP filter frequency responses in each phase are slightly different and the ratio in healthy conditions may not be 1 in an actual system. Despite of the deviation from the ideal conditions, the change of the ratios in the fault condition is still significant compared to that in healthy condition, thus the effectiveness of the ratios as fault indicator can be verified. The ripples of RMS currents are observed. To eliminate the ripples, a simple digital low-pass filter with adaptive corner frequency is applied in the DSP, and the filtered ratio is smoother and relatively constant, which will improve the robustness of the detection.

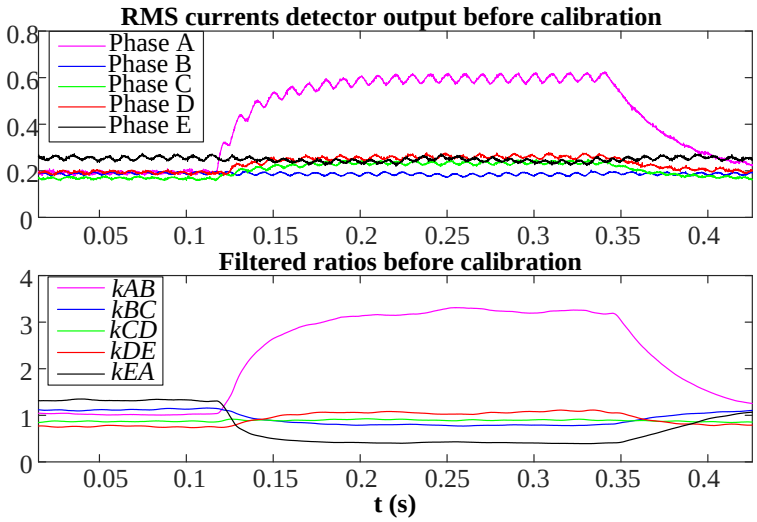

Fig. 3-19 Detector output with 2-turn fault in phase A before calibration, with iq=3A and at 500 r/min.

The ratio deviation from 1 under healthy conditions can be easily corrected by a simple calibration. By way of example, the ratio, k_{AB_h}, calculated from measured RMS currents in phases A and B in healthy conditions is recorded, and a calibration coefficient is defined in (3-19). The coefficient is applied to obtain the calibrated ratio k_{AB}' for both healthy and fault conditions, given in (3-20). The calibration processes for other ratios are applied in the same manner.

$$Cali_{AB} = \frac{1}{k_{AB\_h}} \tag{3-19}$$

$$k_{AB}' = Cali_{AB} \cdot k_{AB} \tag{3-20}$$

The results after the calibration are shown in Fig. 3-20. The ratios are 1 in healthy conditions, while they differ significantly from 1 when the 2-turn fault occurs in phase A. The ratio, k_{AB}, under the fault condition is the largest, which can be used to identify the faulted phase. These results are consistent with the foregoing analysis and simulations. The evident change in k_{AB} provides a very effective means for detecting fault.

The sensitivity of calibration to operating conditions is further assessed. Fig. 3-22 and Fig. 3-23 show k_{AB} ratio variations before calibration with respect to speed and load current and with modulation index, respectively. It is evident that the actual ratio is not exactly but close to 1, and is virtually constant in all operating conditions. Therefore, the calibration only needs to be performed at 1 operating point. In this case, the calibration coefficient for k_{AB} is 1.08. The ratios in faulted state are also very close and distinctive from 1 for a wide range of operating conditions. Although the ratio at low

speed and no load, i_q=0A, is smaller than the ratios in most operating conditions, which may be caused by machine unbalance and filter design tolerance, they have little effect on the fault detection. To compare with the technique proposed in [61], the detecting results from this technique is shown in Fig. 3-21. Before the detection can be effective, calibration for each phase is needed with at least 2 test operating points assuming that the RMS current is linearly proportional to modulation index. However, more data points are required if the relationship is no linear. Further, the detector outputs under the fault and healthy conditions at low speeds are so close that reliable fault detection is not possible with that method. However, these are not the problems in the ratio based detector as evident in Fig. 3-22.

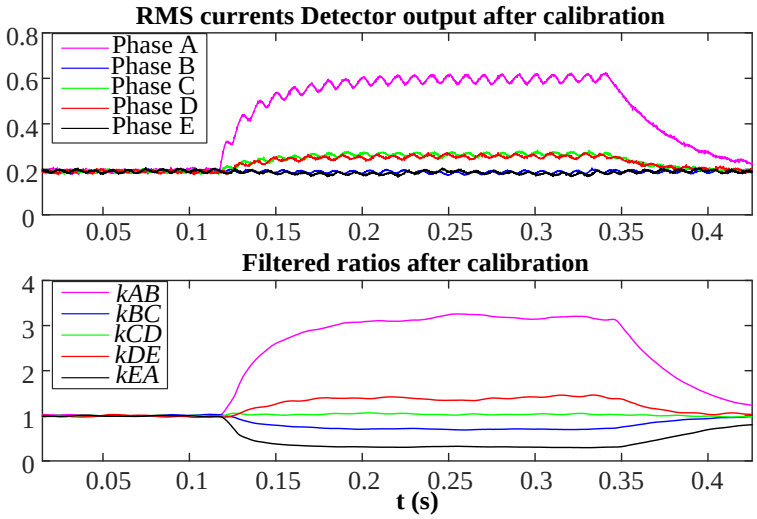

Fig. 3-20 Detector output with 2-turn fault in phase A after calibration, with iq=3A and at 500 r/min.

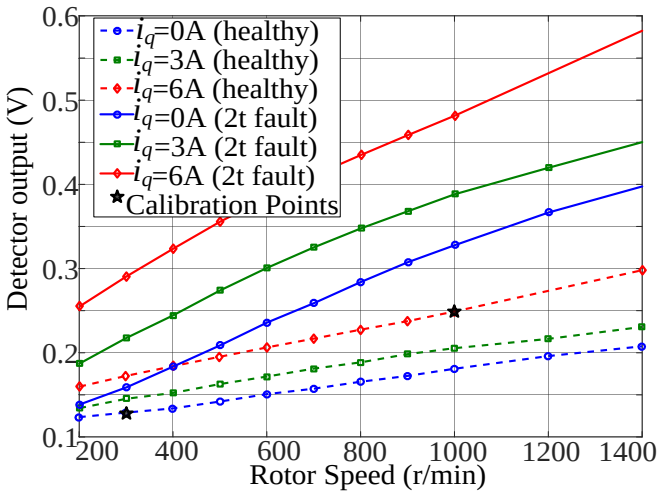

(a)

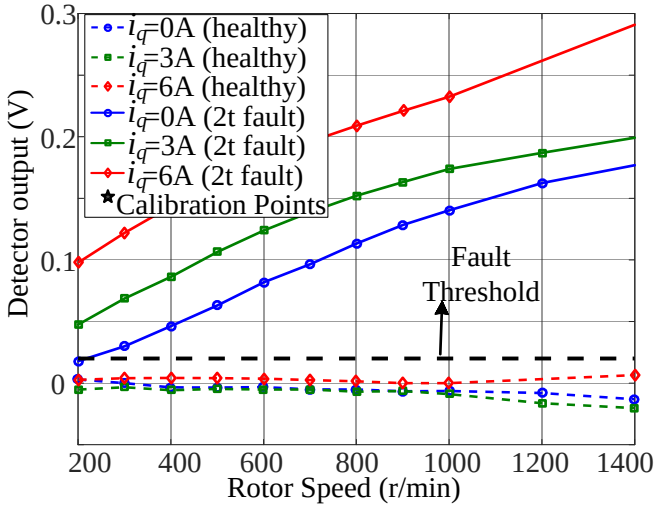

(b)

Fig. 3-21 Variations of detector output (ph-4) with load (0%,50%,100%) and speed (a) before and (b) after calibration. [61]

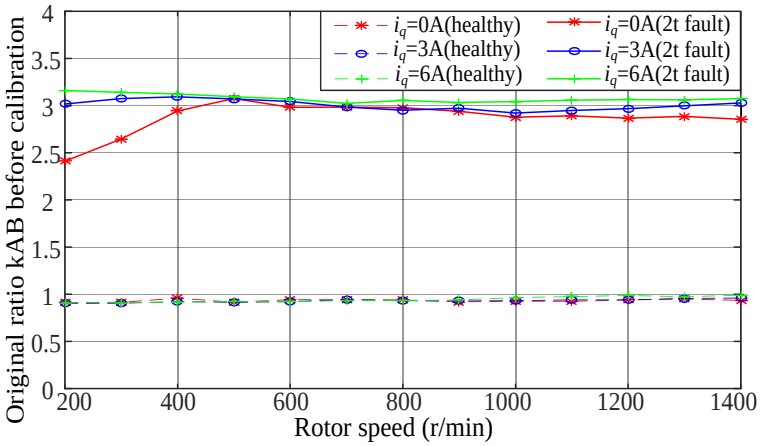

Fig. 3-22 Variations of ratio k_{AB} with load current and speed before calibration

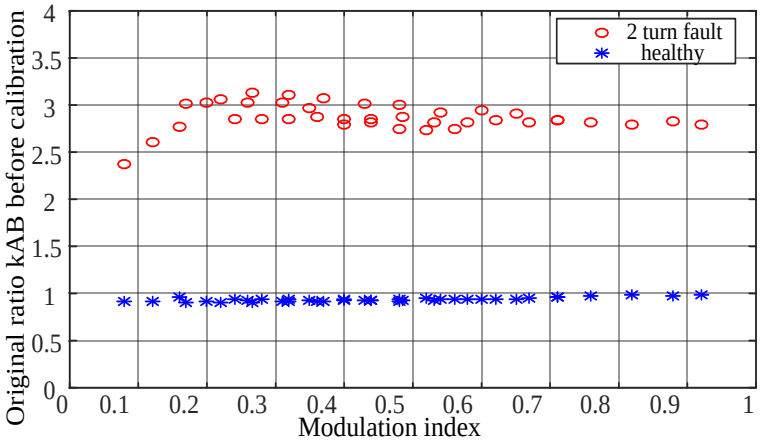

Fig. 3-23 Variations of ratio k_{AB} with modulation index before calibration

In contrast, the fact that ratio of RMS current ripples in two adjacent phases is 1 in the proposed technique provides a very simple means of auto-calibration. Fig. 3-24 shows the ratio variations with modulation index after calibration in both healthy and

fault conditions. As can been seen, a small difference in the ratio exists for a given modulation index. This is not seen from the theoretical analysis but can be explained. At the same modulation index with different combinations of i_q and speed, the effect of unbalance in phase impedance on the ripple current will be different. Further, the BP filter gains at the 4 side band frequencies are also different. These differences are ignored in the analysis, but will cause the actual ratio slightly affected by speed at a given modulation index. However, these differences are insignificant, and will not affect the detection. The experimental results verify the significant differences in the fault indicator in healthy and fault conditions, which implies that the proposed technique has a high signal-to-noise ratio, which enhances the robustness of the turn fault detection.

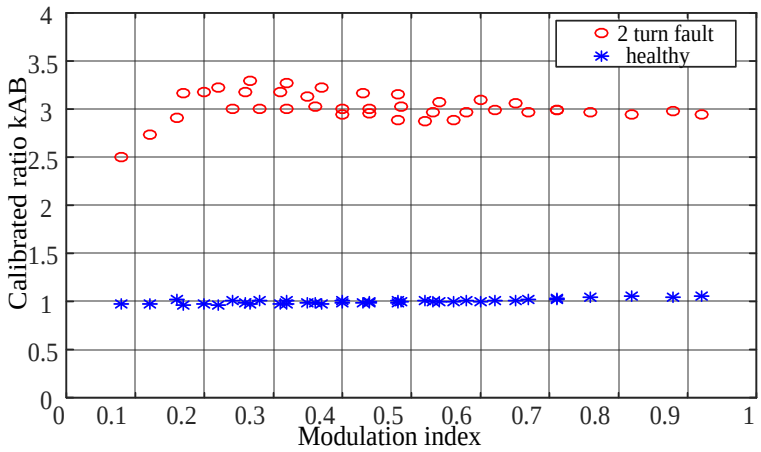

Fig. 3-24 Variations of calibrated ratio k_{AB} with modulation index under healthy and fault conditions

Fig. 3-25 shows the detector output during transient in healthy condition. At 500 r/min, a step change in load current from 0A to 3A is applied to i_q at 0.2s. A slight speed variation is witnessed from the waveform of phase current i_A due to limited disturbance rejection capacity of the dynamometer. Despite this, the ratio processed by the DSP is hardly affected. A similar test is performed with the machine operating at 500 r/min and i_q=1A, and the 2-turn fault is initiated at 0.2s and removed at 0.42s. The resultant phase current, fault current and fault indicator are shown in Fig. 3-26. The fault current increases from 0A to 10A, and the ratio changes immediately from 1 to 3 when the fault occurs. The effect of LPF to remove the ripple in the original ratio can also be seen. Although it will introduce additional delay, the effect is not significant as the fault can be detected within 0.05s with the threshold set at 2.

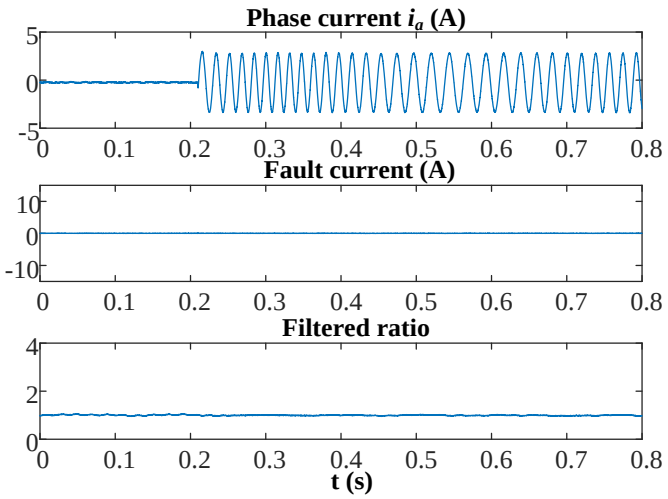

Fig. 3-25 Current waveforms and detector output with load step change of i_q from 0A to 3A at 0.2s in healthy conditions at 500 r/min

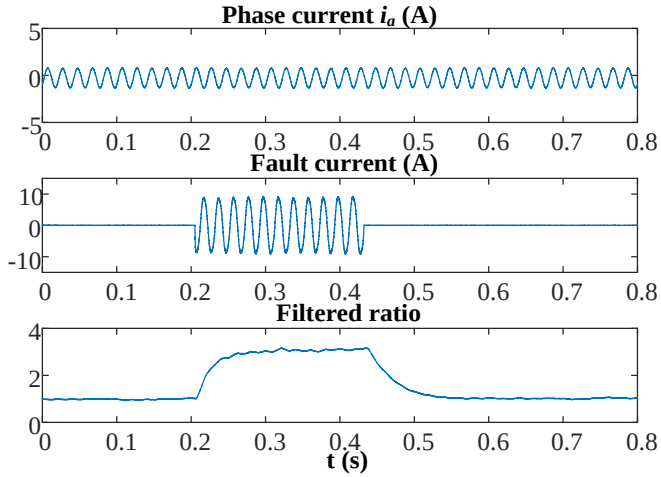

Fig. 3-26 Current waveforms and detector output with 2-turn fault at 0.2s at i_q=1A, 500 r/min

While the developed technique is verified on the 5-phase SPM machine which exhibits negligible effect of magnetic saturation, it should also be applicable to machines whose parameters are significantly affected by magnetic saturation, such as interior permanent magnet (IPM) machines. This is because under healthy conditions, the multi-phase machine is balanced and the ratios of PWM current ripples between two adjacent phases should be 1.0 regardless of operating (or saturation) conditions. If a turn fault occurs in one of its phases, the incremental inductance at a given operating condition in each phase becomes different and hence the ratios would deviate from 1.0, which provides an effective means of detecting the fault.

3.6 Extension to 3 phase SPM machines

The newly proposed PWM ripple current based turn fault detection has been validated successfully on a five-phase SPM fault tolerant machine, with a wide margin of the fault indicator in fault and healthy conditions. From the theoretical analysis, it can

be deduced that such big margin which helps to improve the fault detection performance and reliability is mainly because of the phase number and the unique spatial distribution of phase currents. However, for most applications, it is three-phase permanent magnet machine that is under use. Thus, it is necessary to analyse and evaluate the performance of this method on the widely used three phase machines with the consideration of the conventional topology and control strategy.

3.6.1 Machine Model in Turn Fault Conditions

For a three phase surface-mounted permanent magnet machine (SPM) with the topology shown in Fig. 3-27, the equivalent circuit in turn fault condition can be illustrated in Fig. 3-28 in the same way as the five phase machine assuming fault occurs in phase A. The machine under study has 12 slots and 7 pole pairs, and the circuit parameters under turn fault are shown in Table 3-3, after the extraction from the finite element analysis. With the assumption that the saturation effect in the SPM can be neglected, those parameters can be used for the further derivations. According to the parameters from the FE model, the relationship in (3-21) can be applied for the simplification, while the approximation of the relationship between the self- and mutual-inductances and μ in (3-5) cannot be used anymore, because each phase winding contains more than one coils.

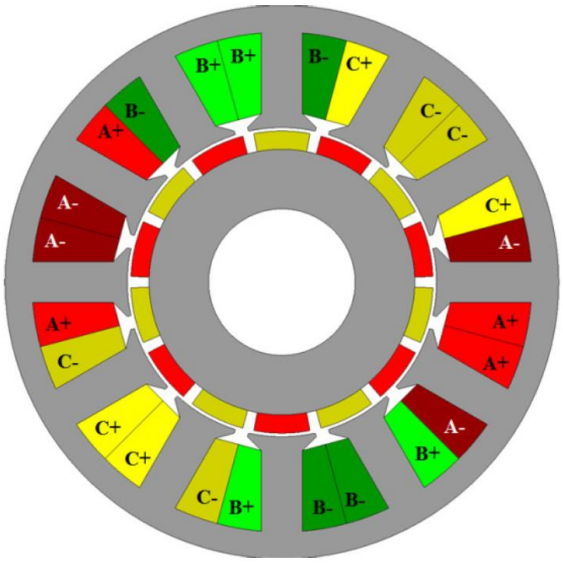

Fig. 3-27 SPM topology under study

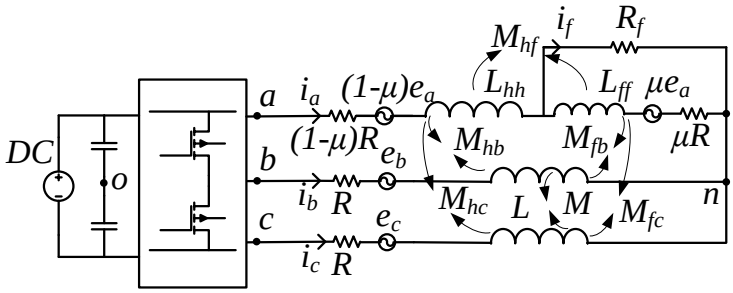

Fig. 3-28 Equivalent circuit and parameters with turn fault

Table 3-3 Parameters obtained from fea

	1-turn fault	4-turn fault
μ	0.03	0.12
$R\ (\Omega)$	0.0208	0.0208
$L(H)$	0.00031	0.00031
$M(H)$	2.8e-5	2.8e-5
$L_{hh}\ (H)$	0.0003	0.00025
$M_{hf}\ (H)$	9.3e-6	2.4e-5
$M_{hb}(H)$	2.8e-5	2.8e-5
$M_{hc}(H)$	2.7e-5	2.1e-5
$L_{ff}\ (H)$	1.2e-6	1.7e-5
$M_{fb}\ (H)$	4e-8	3e-8
$M_{fc}\ (H)$	2e-6	7.8e-6

$$\begin{cases} M \approx M_{hb} + M_{fb} \approx M_{hc} + M_{fc} \\ L \approx L_{hh} + 2M_{hf} + L_{ff} \end{cases} \tag{3-21}$$

With the same consideration of the floating and inaccessible neutral point, the common mode voltage u_{nN} (the voltage between the neutral point and ground or the negative DC supply) is also eliminated by (3-22). The final equations that represent the relations between the inverter output voltages and the phase currents can be expressed in (3-23). All the voltages in these equations are controllable and accessible, making it possible to predict the phase currents analytically with inverter output voltages in fault conditions.

$$\begin{cases} u_a = u_{aO} - \dfrac{u_{aO}+u_{bO}+u_{cO}}{3} = u_{an} - \dfrac{u_{an}+u_{bn}+u_{cn}}{3} \\ u_b = u_{bO} - \dfrac{u_{aO}+u_{bO}+u_{cO}}{3} = u_{an} - \dfrac{u_{an}+u_{bn}+u_{cn}}{3} \\ u_c = u_{cO} - \dfrac{u_{aO}+u_{bO}+u_{cO}}{3} = u_{an} - \dfrac{u_{an}+u_{bn}+u_{cn}}{3} \end{cases} \tag{3-22}$$

$$[u_{abc}] = [R_{abcf}][i_{abcf}] + [L_{abcf}]\frac{d}{dt}[i_{abcf}] + [e_{abc}] \tag{3-23}$$

where $[u_{abc}]=[u_a \quad u_b \quad u_c]^T$, $[i_{abcf}]=[i_a \quad i_b \quad i_c \quad i_f]^T$

$[e_{abc}]=[e_a-\bar{e} \quad e_b-\bar{e} \quad e_c-\bar{e}]^T$, $\bar{e}=\dfrac{e_a+e_b+e_c}{3}$,

$$L_{abcf}=\begin{bmatrix} L & M & M & -\frac{2}{3}(M_{hf}+L_{ff})+\frac{1}{3}(M_{fb}+M_{fc}) \\ M & L & M & \frac{1}{3}(M_{hf}+L_{ff})-\frac{2}{3}M_{fb}+\frac{1}{3}M_{fc} \\ M & M & L & \frac{1}{3}(M_{hf}+L_{ff})+\frac{1}{3}M_{fb}-\frac{2}{3}M_{fc} \end{bmatrix}, R_{abcf}=\begin{bmatrix} R & 0 & 0 & -\frac{2}{3}\mu R \\ 0 & R & 0 & \frac{1}{3}\mu R \\ 0 & 0 & R & \frac{1}{3}\mu R \end{bmatrix}$$

Considering the high frequency component in the voltages generated from the PWM control, the back EMFs can be ignored, leading to the voltage equations at high frequency domain, as shown in (3-24).

$$[u_{abc\_HF}]=[R_{abcf}][i_{abcf\_HF}]+[L_{abcf}]\frac{d}{dt}[i_{abcf\_HF}] \tag{3-24}$$

where $[u_{abc\_HF}]=[u_{a\_HF} \quad u_{b\_HF} \quad u_{c\_HF}]^T$, $[i_{abcf\_HF}]=[i_{a\_HF} \quad i_{b\_HF} \quad i_{c\_HF} \quad i_{f\_HF}]^T$.

In order to solve these equations and study the features of HF currents analytically, a state space equation is derived in (3-27), with the consideration of (3-25) based on Kirchhoff's Current Law (KCL) and the combination of the HF voltage equation in the faulted part shown in (3-26).

$$i_{a\_HF}+i_{b\_HF}+i_{c\_HF}=0 \tag{3-25}$$

$$\begin{aligned} 0=\mu R(i_{a\_HF}-i_{f\_HF})+M_{hf}\frac{di_{a\_HF}}{dt}+L_{ff}\frac{d(i_{a\_HF}-i_{f\_HF})}{dt} \\ +M_{fb}\frac{di_{b\_HF}}{dt}+M_{fc}\frac{di_{c\_HF}}{dt} \end{aligned} \tag{3-26}$$

$$s\begin{bmatrix} i_{a\_HF}(s) \\ i_{b\_HF}(s) \\ i_{f\_HF}(s) \end{bmatrix}=A\begin{bmatrix} i_{a\_HF}(s) \\ i_{b\_HF}(s) \\ i_{f\_HF}(s) \end{bmatrix}+B\begin{bmatrix} u_{a\_HF}(s) \\ u_{b\_HF}(s) \\ 0 \end{bmatrix} \tag{3-27}$$

where s is the Laplace operator, and matrices A, B are given below.

$$A=-\begin{bmatrix} L-M & 0 & -\frac{2}{3}(M_{hf}+L_{ff})+\frac{1}{3}(M_{fb}+M_{fc}) \\ 0 & L-M & \frac{1}{3}(M_{hf}+L_{ff})-\frac{2}{3}M_{fb}+\frac{1}{3}M_{fc} \\ M_{hf}+L_{ff}-M_{fc} & M_{fb}-M_{fc} & -L_{ff} \end{bmatrix}^{-1}\begin{bmatrix} R & 0 & -\frac{2}{3}\mu R \\ 0 & R & \frac{1}{3}\mu R \\ \mu R & 0 & -\mu R \end{bmatrix}$$

$$B=\begin{bmatrix} L-M & 0 & -\frac{2}{3}(M_{hf}+L_{ff})+\frac{1}{3}(M_{fb}+M_{fc}) \\ 0 & L-M & \frac{1}{3}(M_{hf}+L_{ff})-\frac{2}{3}M_{fb}+\frac{1}{3}M_{fc} \\ M_{hf}+L_{ff}-M_{fc} & M_{fb}-M_{fc} & -L_{ff} \end{bmatrix}^{-1}$$

As can be seen from (3-27), the inputs to the state space equation are the HF components of u_a, and u_b, whose spectra will be analysed in the following part. Based on this state space equation, the output HF currents can be predicted in (3-28) and the influence of a turn fault on the HF currents can be assessed once the parameters are obtained.

$$\begin{bmatrix} i_{a\_HF}(s) \\ i_{b\_HF}(s) \\ i_{f\_HF}(s) \end{bmatrix}=(sI-A)^{-1}B\begin{bmatrix} u_{a\_HF}(s) \\ u_{b\_HF}(s) \\ 0 \end{bmatrix} \tag{3-28}$$

3.6.2 Turn fault indicator

For the three phase machine control, the space vector PWM (SVPWM) is often employed in order to enhance the voltage utilization ratio, which is different from the SPWM control in the five phase SPM. Thus, the spectrum of the SVPWM needs to be analysed. The space vector modulating voltage is shown in Fig. 3-29, while the equivalent expression is written as (3-29). The Fourier expansion of the inverter output voltage is given in (3-30), where the first 2 items denote the dc offset, fundamental and its baseband harmonics, and the last 2 items denote the switching and its multiple frequency components with their sideband harmonics.

$$v_{sp}(t)=\begin{cases} M_m\cos(\omega_r t-\frac{\pi}{6}), & 0\le\omega_r t<\frac{\pi}{3},\pi\le\omega_r t<\frac{4\pi}{3} \\ \sqrt{3}M_m\cos\omega_r t, & \frac{\pi}{3}\le\omega_r t<\frac{2\pi}{3},\frac{4\pi}{3}\le\omega_r t<\frac{5\pi}{3} \\ M_m\cos(\omega_r t+\frac{\pi}{6}), & \frac{2\pi}{3}\le\omega_r t<\pi,\frac{5\pi}{3}\le\omega_r t<2\pi \end{cases} \tag{3-29}$$

$$F(t)=\frac{A_{00}}{2}+\sum_{n=1}^{\infty}(A_{0n}\cos n\omega_r t+B_{0n}\sin n\omega_r t)+$$
$$\sum_{m=1}^{\infty}(A_{m0}\cos m\omega_c t+B_{m0}\sin m\omega_c t)+ \tag{3-30}$$
$$\sum_{m=1}^{\infty}\sum_{\substack{n=-\infty\\ n\neq 0}}^{\infty}\{A_{mn}\cos[(m\omega_c+n\omega_r)t]+B_{mn}\sin[(m\omega_c+n\omega_r)t]\}$$

where M_m is the modulation, ω_r is the fundamental frequency, and ω_c is the switching frequency.

According to [116], the amplitude for each sideband harmonics can be expressed as (3-31), which is considerably different from the harmonics of SPWM.

$$A_{mn}=\frac{8V_{dc}}{q\pi^2}\times$$
$$\left\{\begin{aligned}
&\frac{\pi}{6}\sin\left[(m+n)\frac{\pi}{2}\right]\cdot\left[J_n\left(q\frac{\pi}{2}\frac{3}{2}M_m\right)+2\cos\left(n\frac{\pi}{6}\right)J_{nn}\left(q\frac{\pi}{2}\frac{\sqrt{3}}{2}M_m\right)\right]\\
&+\frac{1}{n}\sin\left(m\frac{\pi}{2}\right)\cos\left(n\frac{\pi}{2}\right)\sin\left(n\frac{\pi}{6}\right)\left[J_0\left(q\frac{\pi}{2}\frac{3}{2}M_m\right)-J_0\left(q\frac{\pi}{2}\frac{\sqrt{3}}{2}M_m\right)\right]\Bigg|_{n\neq 0}\\
&+\sum_{\substack{k=1\\ k\neq -n}}^{\infty}\left\{\begin{aligned}&\frac{1}{n+k}\sin\left[(m+k)\frac{\pi}{2}\right]\cos\left[(n+k)\frac{\pi}{2}\right]\sin\left[(n+k)\frac{\pi}{6}\right]\\&\times\left\{J_k\left(q\frac{\pi}{2}\frac{3}{2}M\right)+2\cos\left[(2n+3k)\frac{\pi}{6}\right]J_k\left(q\frac{\pi}{2}\frac{\sqrt{3}}{2}M_m\right)\right\}\end{aligned}\right\}\\
&+\sum_{\substack{k=1\\ k\neq n}}^{\infty}\left\{\begin{aligned}&\frac{1}{n-k}\sin\left[(m+k)\frac{\pi}{2}\right]\cos\left[(n-k)\frac{\pi}{2}\right]\sin\left[(n-k)\frac{\pi}{6}\right]\\&\times\left\{J_k\left(q\frac{\pi}{2}\frac{3}{2}M\right)+2\cos\left[(2n-3k)\frac{\pi}{6}\right]J_k\left(q\frac{\pi}{2}\frac{\sqrt{3}}{2}M_m\right)\right\}\end{aligned}\right\}
\end{aligned}\right\} \tag{3-31}$$

where $q=m+n\omega_c/\omega_r$, and J_k is the Bessel function of the k^{th} order.

The switching frequency of the inverter is still set at 10 kHz for the machine under study, and the spectrum of inverter output voltage u_{aN} with the modulation index of 0.6 is shown in Fig. 3-30(a) and can be predicted by (3-30) and (3-31).

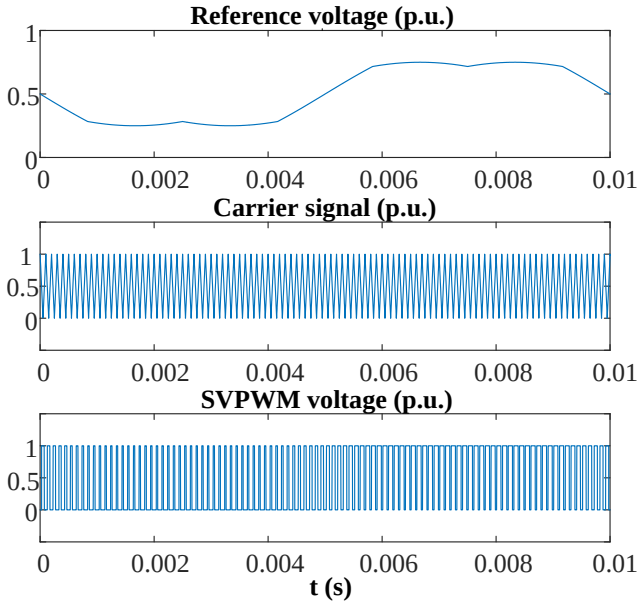

Fig. 3-29 Space vector pulse width modulation

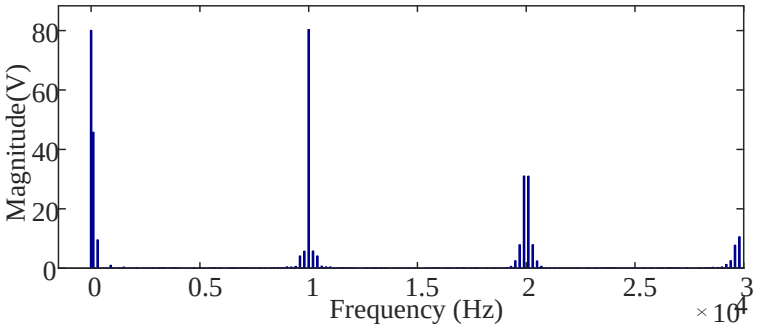

(a)

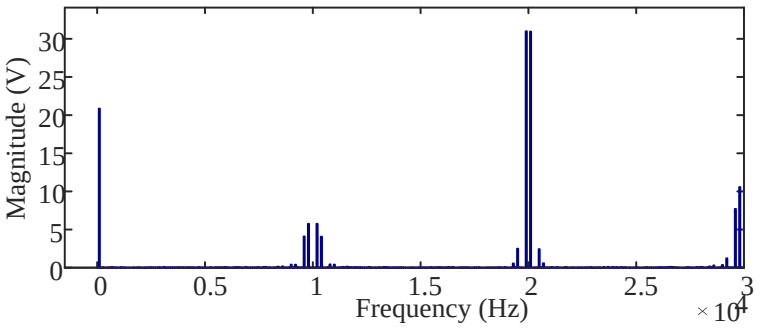

(b)

Fig. 3-30 (a) Spectrum of SVPWM voltage. (b) Spectrum of SVPWM voltage after elimination of zero sequence voltages

After the elimination of the common mode voltages, the spectrum of u_a defined in (3-22), is shown in Fig. 3-30(b). It can be seen that the spectrum is quite similar to that of the SPWM voltages generally that the sideband harmonics around the integer multiples of the switching frequency are symmetric, forming several sideband clusters. Thus, the same signal processing steps and devices are applied. A sideband cluster can be separated by a bandpass filter, while it is very difficult to separate the frequency

components within a sideband cluster. Thus, the frequency components around one cluster are processed as a whole. The cluster with the centre frequency at 20 kHz is selected since the energy is the strongest. The same 4th order bandpass filter with the centre frequency of 20 kHz, and the band width of 2kHz is also used to extract them from the measured currents.

After being filtered by the bandpass filter, the HF currents mainly contain 6 frequency components, $2f_c \pm f_r$, $2f_c \pm 5f_r$, $2f_c \pm 7f_r$. The composition of the voltage components is slightly different from that of the SPWM voltages, but it does not make any difference in the analysis and signal processing. The phasor diagrams of the frequency components at $2f_c \pm f_r$ are shown in Fig. 3-31(a) and (c) as an example, rotating in the same direction but at different speeds (frequencies). Note that although the phasor diagrams for the 2 frequency components are similar, the sequence and phase shift between the two phasors are different. The HF current at each frequency can be calculated by (3-28) as described in section 3.6.1, and the resultant current phasors are plotted in Fig. 3-31(b) and (d). For other harmonics, the current phasors can also be calculated in a similar manner. From the phasor diagram, It can be observed that in this three-phase SPM, the deviation of high frequency current caused by turn fault is not as significant as that in the five-phase SPM while the other merits such as robustness to transient state should be preserved.

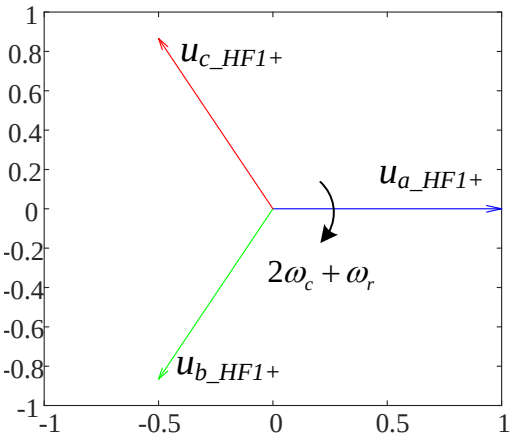

(a)

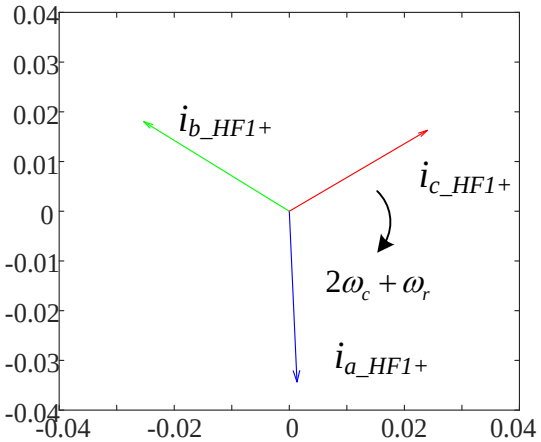

(b)

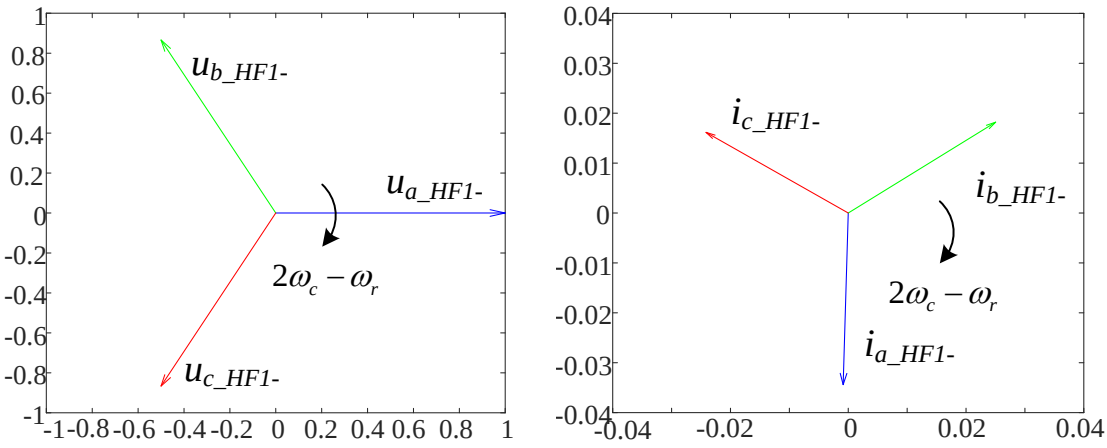

(c) (d)

Fig. 3-31 Phasor diagrams of HF (a)(c)voltages and (b)(d)currents

By applying the same processing procedure, the RMS value of the high frequency current is obtained through the RMS converter. Thereafter, the ratio between the high frequency currents from the two adjacent phases are calculated as the fault indicator, as shown in (3-32), which is the constant of 1 in healthy condition regardless of operating conditions. If the ratio is distinguishable from 1 in fault conditions, then it can be used to detect fault with a constant threshold. In this particular machine, the ratio in 1 turn fault is calculated as k_{ab}=1.108, k_{bc}=1.068, k_{ca}=0.845 with the parameters in Table 3-3. As can be seen, the ratio in 1 turn fault condition deviates from 1. However, the deviation is relatively small compared to that in the five phase machine. Despite of this, if the signal integrity is superior, and any inherent machine unbalance is reduced by the calibration described previously, the fault can still be detectable.

$$k_{ab} = \frac{i_{a\_rms}}{i_{b\_rms}},\ k_{bc} = \frac{i_{b\_rms}}{i_{c\_rms}},\ k_{ca} = \frac{i_{c\_rms}}{i_{a\_rms}} \tag{3-32}$$

The difference in the fault indicators between the two machines is due to the different phase numbers, winding distributions as well as winding configurations. In the 5-phase machine, each phase consists of one coil, and a turn fault has more significant influence on the inductance seen by the inverter. In the 3-phase machine, each phase comprises four coils, and a turn fault in one coil only affected the inductance of this fault. Consequently, the change in the total inductance seen by the inverter is much less.

To enhance fault detectability, a unified variable based on the standard deviation of the three ratios is proposed to indicate the occurrence of the turn fault. Its value is

calculated by (3-33) where the ratios are obtained from the measured outputs of the three RMS converter.

Since the deviation of all three ratios from their average is utilized, the abnormal changes in all three phase HF currents due to a fault are captured in the fault indicator, thus enhancing the detection effectiveness. It represents the unbalance on the high frequency currents caused by the turn fault. In ideal healthy conditions, all the ratios are equal, and the standard deviation is zero. In fault condition, the standard deviation becomes nonzero.

$$k_{ave} = \frac{k_{AB} + k_{BC} + k_{CA}}{3}$$
$$SD = \sqrt{\frac{(k_{AB} - k_{ave})^2 + (k_{BC} - k_{ave})^2 + (k_{CA} - k_{ave})^2}{3}} \quad (3\text{-}33)$$

3.6.3 Simulation Results

As has been stated before, the machine under study and simulation is a three-phase surface mounted permanent magnet (SPM) machine with 12 slots and 7 pole pairs. The main design and operational parameters are shown in Table 3-4. The machine is controlled by an outer speed loop and two inner current loops in the dq reference frame in a MATLAB/SIMULINK model. The control schematic block diagram is shown in Fig. 3-32. One turn short-circuit fault is injected in phase A in order to assess the feasibility of the proposed fault detection method.

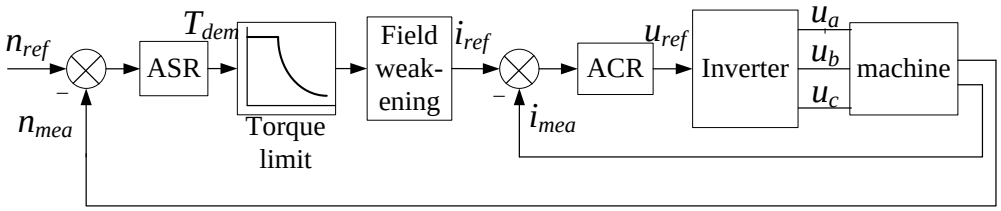

Fig. 3-32 Control diagram of the three phase SPM in the simulation

Table 3-4 Design and operational parameters

Machine topology: Surface mounted, fractional slot per pole	
Number of pole-pairs	7
Number of slots	12
Axial length (active, mm)	118
Outer diameter (excluding case, mm)	150
Number of turns per coil	8
Number of coils per phase	4

Maximum/base speeds (r/min)	5000/1350
Peak/continuous torques (Nm)	70/35
Continuous current (A peak/rms)	85/60.5
Maximum current (A peak/rms)	170/121
Phase resistance at 120 ℃ (mΩ)	20.8
Synchronous inductance (mH)	0.344
Flux linkage per phase (mWb)	39.6
Back-EMF constant (V peak s/rad)	0.277

The machine is simulated under low speed with speed and torque transients representative of the actual operation. The varying speed and load are shown in Fig. 3-33, and one-turn fault is injected at t= 0.55s. The sideband frequency components in phase currents around 20 kHz are processed by hardware analogue circuit to obtain their RMS values. Their ratios and standard deviation are shown in Fig. 3-34. It is seen that in the healthy condition, the RMS currents in each phase are the same and their ratios are 1, and they are also immune to speed variations. If a step change in torque is large, then the ratio is slightly affected, but the influence is insignificant and can be ignored. In the fault condition, all three ratios deviate from 1 but to different values. And the standard deviation which combines all the ratios becomes non-zero at 0.55s when the fault occurs while it stays at zero in the healthy condition. During the initial start-up period, RMS detector output is not correct due to the insufficient data, as has been explained in section 3.4, thus the ratios and standard deviation are all invalid. Except for this short period, the detection can be effective afterwards.

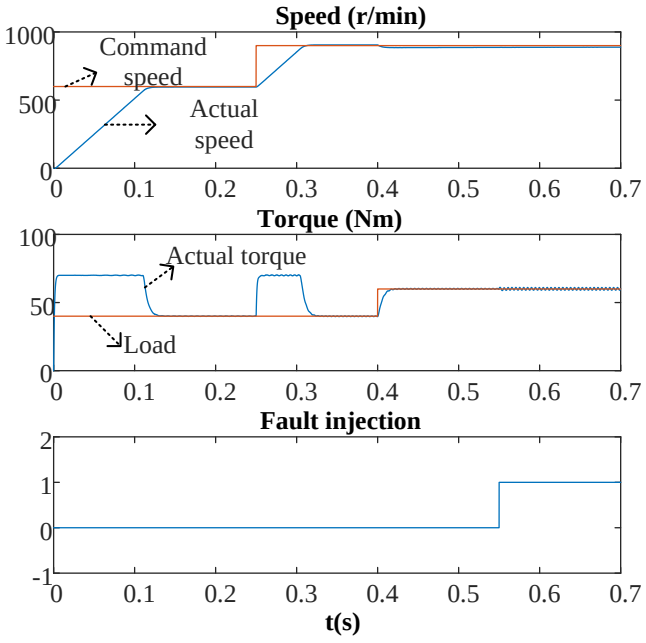

Fig. 3-33 Torque and speed variations, and fault injection in simulation study of proposed fault detection

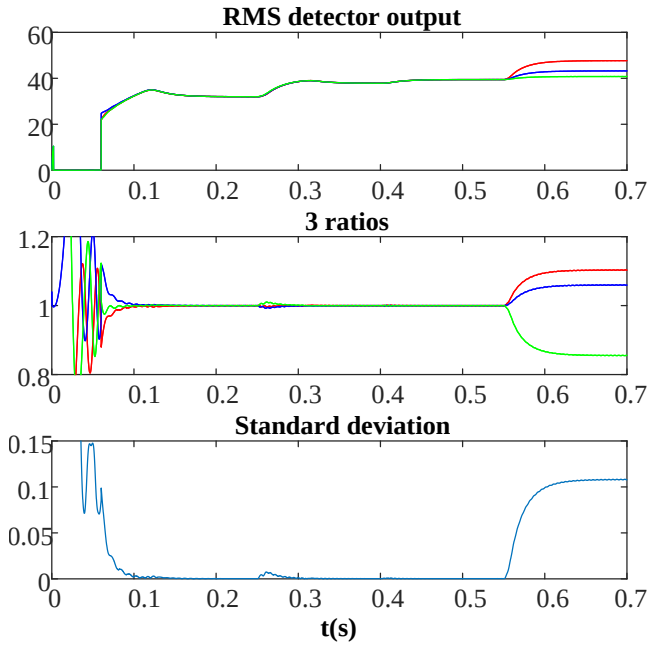

Fig. 3-34 Turn fault detection results for balanced machine. The RMS detector outputs are proportional to RMS HF current

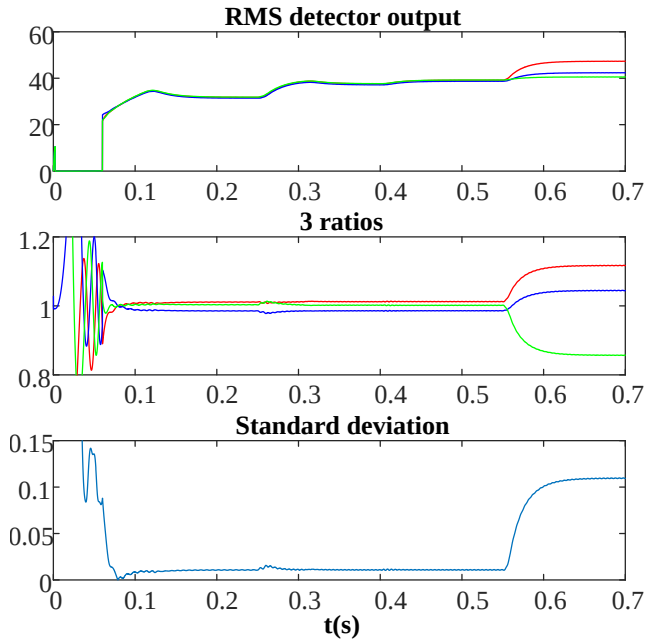

Fig. 3-35 Turn fault detection results for unbalanced machine

To study the influence of natural unbalance in a machine on the performance of the detection technique, it is assumed that the resistance and inductance in phase B are 5% and 3% higher than those in the other phases, respectively. The results are shown in Fig. 3-35. The ratios and standard deviation also deviate from nominal value even in healthy conditions. However, the fault indicators are far greater when the fault occurs. Thus, a few percent machine unbalance has little effect on this detection technique. In a practical application, it is possible to eliminate the effect of small unbalance and

differences in the RMS detectors for each phase by the calibration under healthy conditions as described previously.

3.7 Extension to 3 phase IPM machines

The PWM ripple current based turn fault detection method for the three-phase interior permanent magnet machine is also investigated. The machine under study is the nine phase permanent magnet assisted synchronous reluctance (PMA SynRM) machine with triple redundant 3-phase winding configuration as has been described in Chapter 2. Due to the physical and electrical isolation among the different 3-phase winding sets, each winding set can be treated as a 3-phase IPM machine system, and a single turn fault in phase B is emulated by switching the relay in Fig. 2-17(b).

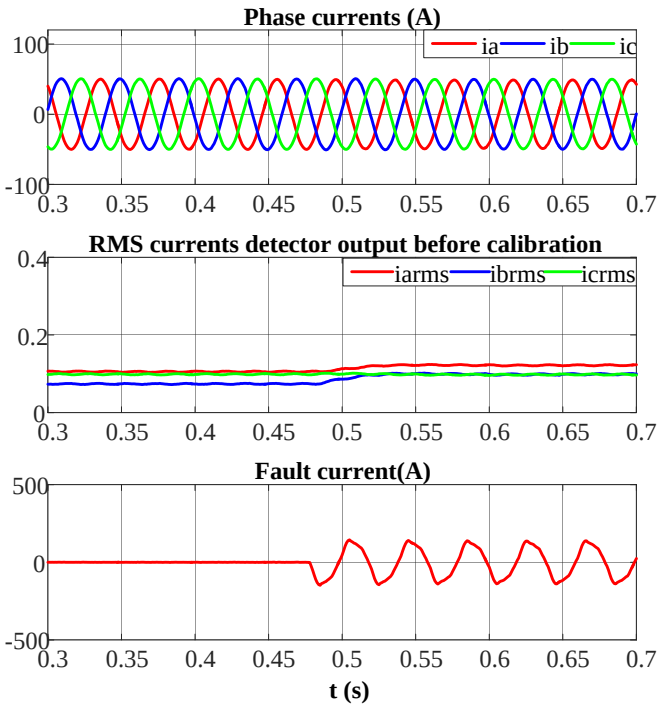

Fig. 3-36 Phase current, fault current and RMS current detector outputs before calibration when the machine operates at 500 rpm and 50A

As has been discussed in Chapter 2, due to the effect of rotor saliency, the phase inductances can no longer be seen as constant, but contains significant 2nd harmonic. By employing a classical IPM machine model, the high frequency current phasor can be obtained in the same way as those shown in section 3.6. However, apart from the saliency, magnetic saturation in the IPM machine also adds to the complexity of the mathematical analysis. The large current caused by fault also tends to distort the flux distribution, leading to uneven level of saturation. With all these considerations, it is

difficult to conduct a rigorous mathematical derivation for predicting the signals caused by a turn fault. However, qualitatively, it can be assumed that the IPM machine shares the similar feature in turn fault conditions that the high frequency component of phase currents deviate from each other because of the unbalance caused by fault. Thus, the same hardware signal processing circuit, the same calculation of the high frequency RMS current ratios and their standard deviations are applied to the detection of turn fault in the IPM machine. Extensive experiments are carried out to validate this method.

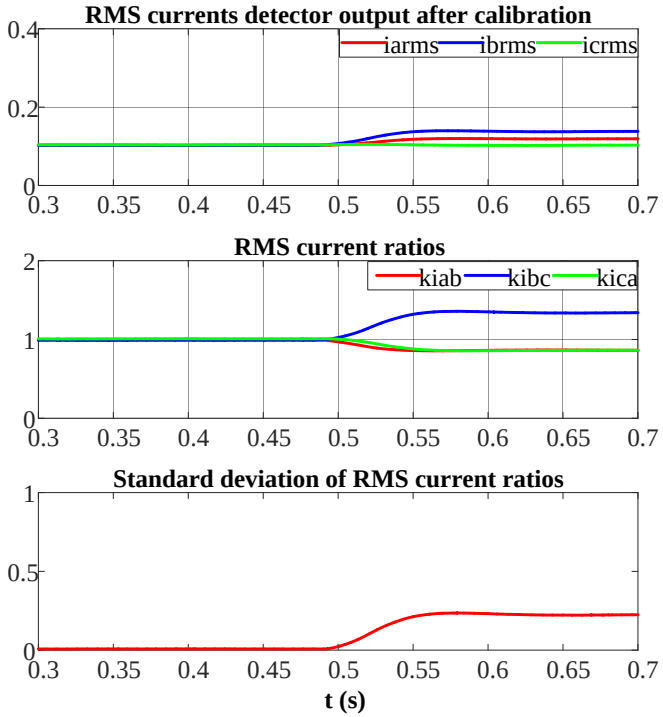

Fig. 3-37 RMS current detector outputs after calibration, RMS current ratios and standard deviation

The machine is first operating at 500rpm with 50A phase current when turn fault occurs at 0.48s. The three phase currents, RMS detector outputs, fault current are shown in Fig. 3-36. As can be seen, the RMS values of the high frequency current components are unequal to each other initially even in healthy condition. This is caused by the tolerance in all the components among the three signal processing channels for the three RMS high frequency currents, including winding impedances, current sensors, operational amplifiers, resistors, and capacitors, etc. A calibration is needed before further detection starts. The RMS current detector outputs after calibration and filtering are shown in Fig. 3-37, and the fault features can be revealed more clearly. It is obvious that phase B is the most affected where fault occurs, while the fault influences on the other two phases are much lower. This is due to the unbalanced inductances seen by the applied high frequency voltage phasors. As a result, the ratios deviates from 1 and their standard deviation increases significantly from 0 in the turn fault condition. Since the

fault occurs at 0.48s, while the standard deviation of the ratios varies immediately and reaches a stable value at about 0.55s, the fault detection can be accomplished within 0.1s. Such short diagnostic time is preferred for the minimization of further damages. Thus, this fault detection method is applicable to the IPM drive at this operating condition.

In order to understand the effectiveness of this fault detection method at various speed and load conditions, tests are performed in healthy and fault conditions with different speeds and load torques. The average detector outputs in the healthy (H) and turn fault (TF) conditions are compared in Fig. 3-38. While the fault current tends to increase with either the increase of current or speed, the speed range during the test is limited to 1000rpm and the current range is limited to 70A in order to ensure the fault current doesn't exceed the current limit of the relay and cause damage to the machine. The RMS detector outputs under various operating conditions have been calibrated with unified calibration coefficients and offsets. It can be seen that under all the operating conditions tested, the standard deviations of the RMS current ratios are always close to zero in the healthy condition but higher in the fault conditions. A good separation between the healthy and fault conditions can be achieved. Therefore, a simple threshold can be employed to classify the two conditions, thus detecting the fault successfully and reliably. The extremely high RMS value at 10 A in turn fault condition is due to the low high frequency components especially at lower speeds. It also can be seen that the standard deviation does not change much over the tested speed range, but decreases with the load current. For the tested operating conditions, it is obvious that turn fault can be easily detected by a single threshold. However, it is not practical to test the effectiveness of the method at higher speeds and currents as has been explained. Therefore, the simulation results on the high fidelity model developed in [27] is investigated for the trend and quality of the fault indicator. The fault indicators at higher currents under 1000 rpm are shown in Fig. 3-39. Although errors exist between the tested and simulated results, similar trend can be observed. The fault indicator is lower at higher load current, but still reserves a proper deviation from zero which is the reference value in healthy conditions. Even with the same level of noises and unbalances considered in the tests in Fig. 3-38, it can be deduced that the fault is still detectable at the rated current.

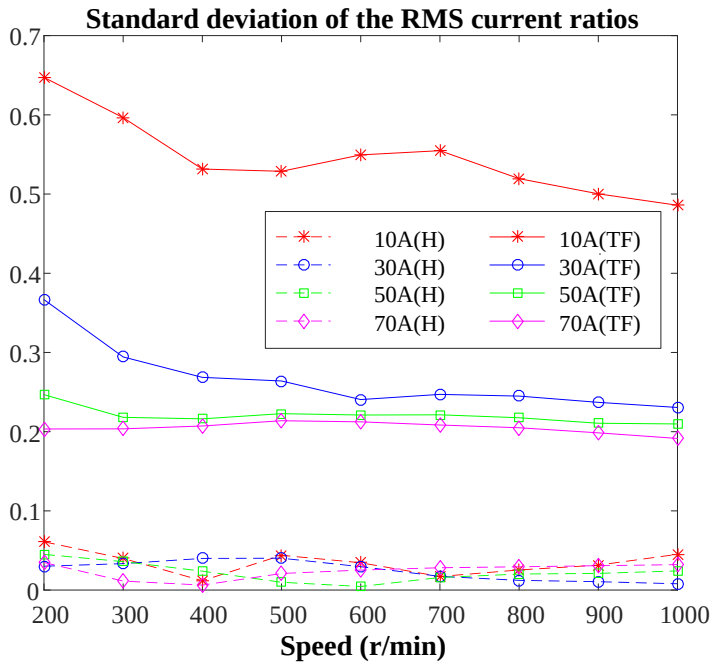

Fig. 3-38 Variations of the standard deviation as fault indicator with current and speed

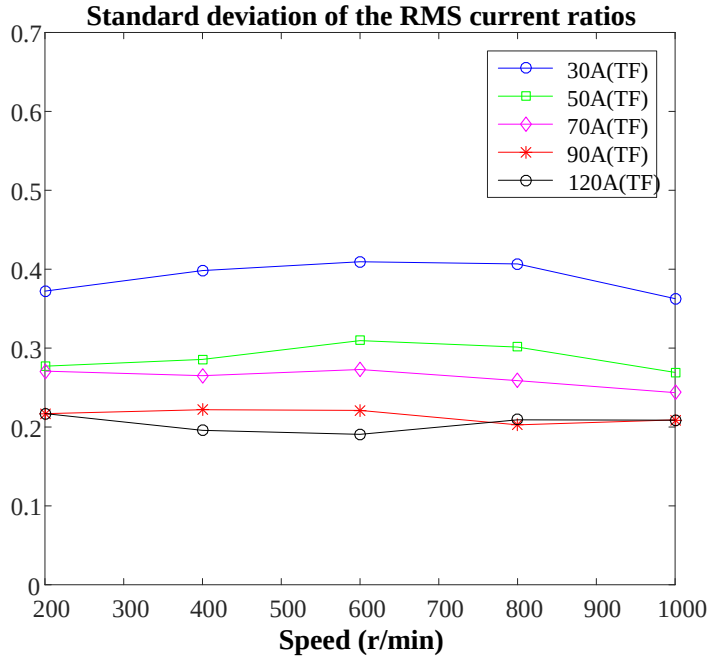

Fig. 3-39 Variations of the standard deviation as fault indicator with higher currents from simulation

The fault indicators at higher speeds are simulated and shown in Fig. 3-40. As can be seen, the trend of the fault indicator is not monotonous but is quite dependent on the speed. This is because the influence of the turn fault on the other two phases change oppositely with the increasing speed. The RMS value of the high frequency current in phase A is lower than that in phase C at lower speed but surpasses it when speed increases. As a result, the overall asymmetry level of the RMS current is non monotonous to the speed, and there exists a lowest point. If the noises and the initial

unbalance in the measurement can be minimized to guarantee the standard deviation in healthy condition smaller than that lowest point in turn fault conditions, then a proper threshold can still be determined to detect turn fault for a wider operating range.

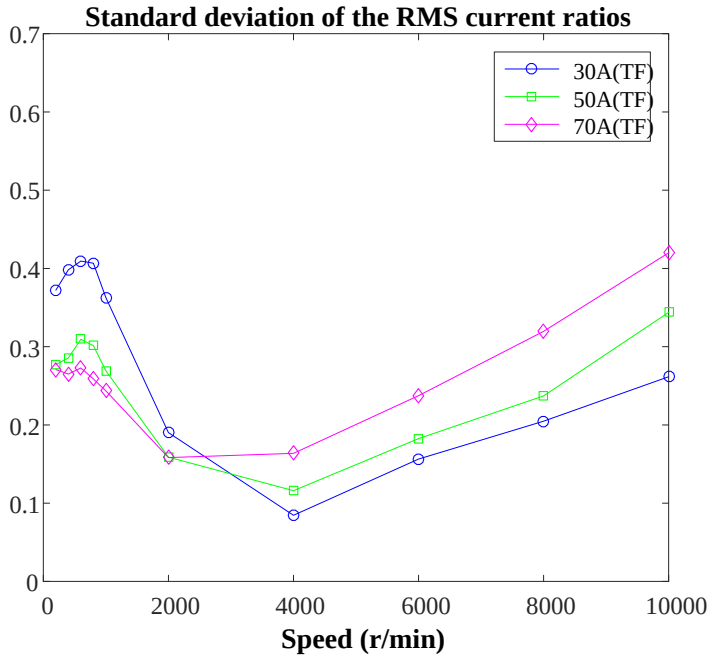

Fig. 3-40 Variations of the standard deviation as fault indicator with higher speeds from simulation

The fault detection performances during transient states have also been investigated. Fig. 3-41(a) and (b) show the RMS currents detector outputs and the fault indicators under the healthy condition when the speed increases from 550rpm to 1150rpm at the acceleration rate of 1000rpm/s. It shows that the RMS values of the high frequency currents increase with the speed increase, which is mainly caused by the change of the modulation index. While the RMS current is sensitive to both speed and fault, which is not suitable as the fault indicator, their ratios and the corresponding standard deviation tend to remain constant once the calibration has been implemented. Thus, no false alarm will be triggered. When turn fault occurs during the speed change as shown in Fig. 3-42(a) and (b), the standard deviation as the fault indicator is very sensitive to the turn fault, and hence it can be detected effectively.

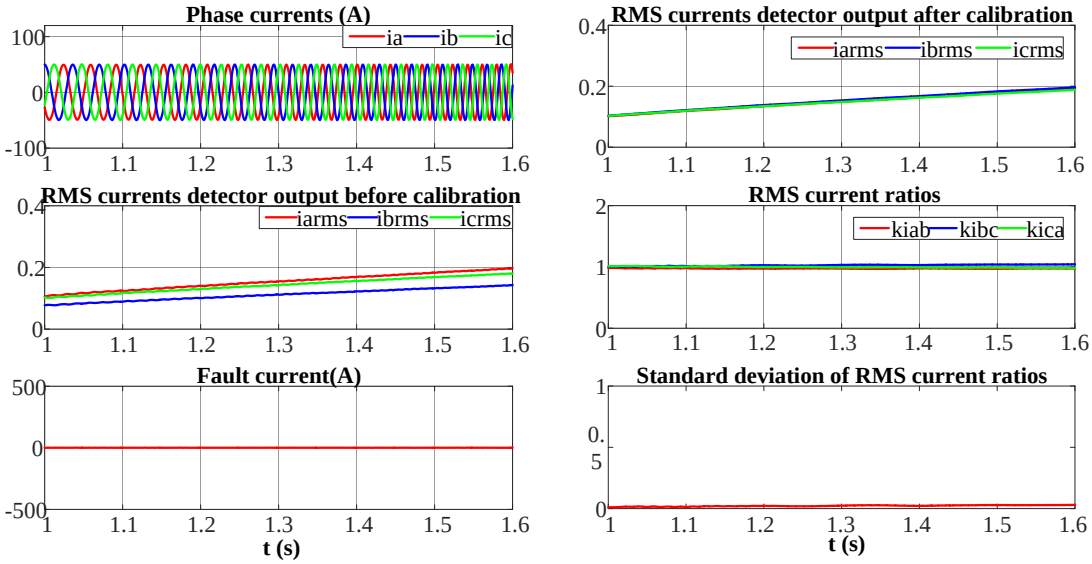

(a) (b)

Fig. 3-41 (a) Phase currents and RMS current detector outputs before calibration in healthy condition at 50 A with increasing speed. (b) RMS current detector outputs after calibration, RMS current ratios and standard deviation

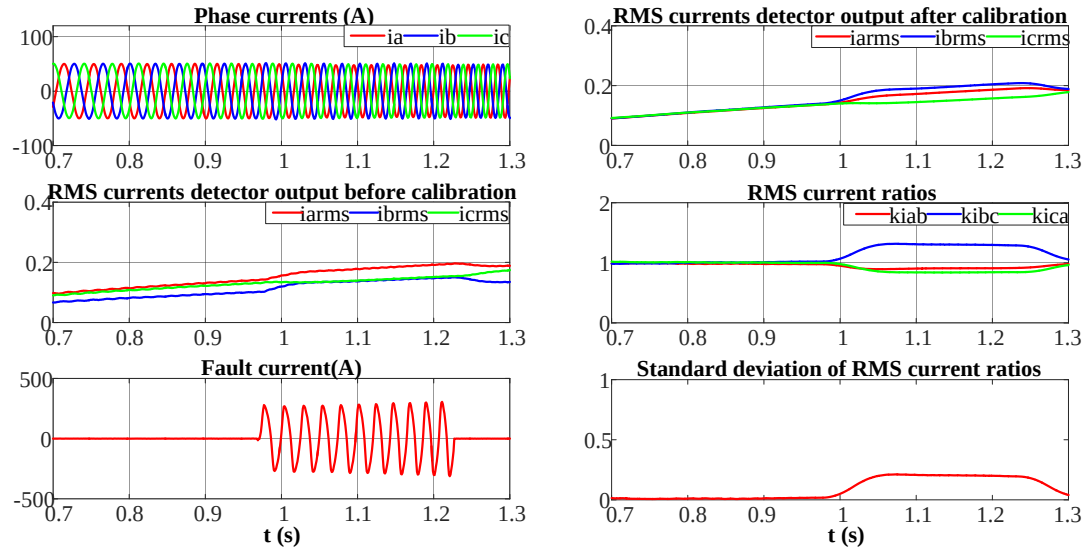

(a) (b)

Fig. 3-42 (a) Phase currents and RMS current detector outputs before calibration in fault condition at 50A with increasing speed. (b) RMS current detector outputs after calibration, RMS current ratios and standard deviation

Fig. 3-43(a) and (b) shows the fault detection results when a current step change from 50A to 80A at 500rpm takes place at 1.3s under healthy condition. As has been explained in Chapter 2, the speed also changes at the same time, due to limited speed control bandwidth of the dynamometer. With the abrupt change in both current and speed, the modulation index variation is very rapid. This results in a larger change in the RMS value of the high frequency currents, compared to the response of the fault condition in Fig. 3-37. The calculated ratios, however, are less sensitive to the changes

and quickly return to the initial values. Consequently, a small increase is seen in the standard deviation immediately after the current change, but it vanishes very quickly. Compared to the standard deviation in the fault condition in Fig. 3-37, the increase is very small, thus, it will not have any effect on the final diagnostic results. In Fig. 3-44(a) and (b), the turn fault is intended to be injected at the same time of the current step change, but due to the response delay of the relay, the onset of the turn fault is about 0.1s after the current change, when the speed has not reached its steady state. The sensitivity of the fault indicator to the transient states and to the turn fault condition can be observed clearly. The fault can be effectively detected while the disturbance to the standard deviation due to transient states can be discriminated, demonstrating the robustness of the proposed fault detection technique.

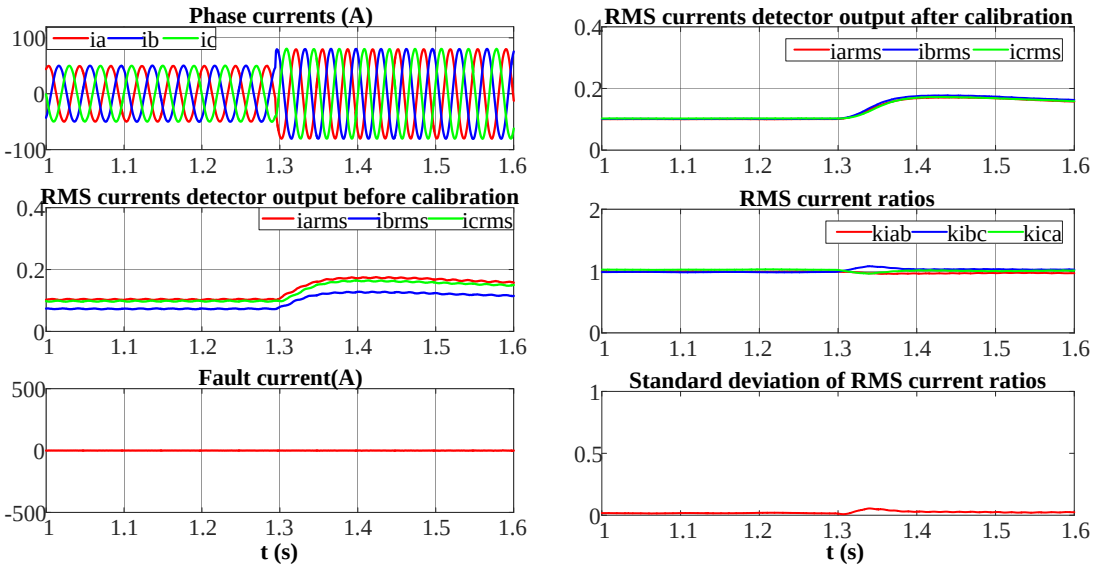

(a) (b)

Fig. 3-43 (a) Phase currents and RMS current detector outputs before calibration in healthy condition at 500rpm with current step change. (b) RMS current detector outputs after calibration, RMS current ratios and standard deviation

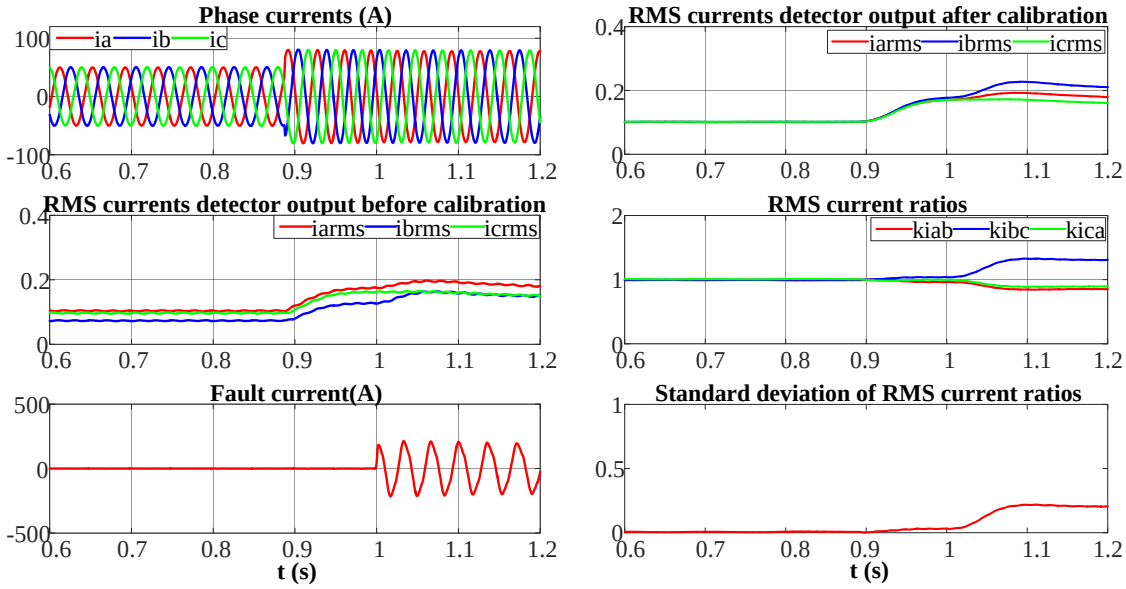

(a) (b)

Fig. 3-44 (a) Phase currents and RMS current detector outputs before calibration in fault condition at 500rpm with current step change. (b) RMS current detector outputs after calibration, RMS current ratios and standard deviation

The detectability of this method under no load conditions are also tested. The speed is 500rpm, and the three phase currents, RMS detector outputs, fault current are shown in Fig. 3-45. Since the phase currents are zero, the featured harmonics due to turn fault cannot be detected any more, thus the conventional MCSA based turn fault detection algorithms are no longer effective. However, since the driving voltages are equal to the back EMFs which are not zero when the machine is still rotating in this scenario, the PWM ripple current still exist. At such low speed, the modulation index is very small, so are the switching sideband harmonics in the phase currents. Although the signal to noise is low in the measurement of the RMS values of the PWM ripple currents, the change due to turn fault can still be observed. After the filtering and calibration, the ratios of the RMS values and the standard deviation are obtained, as illustrated in Fig. 3-46. The sensitivity of the fault indicator is not affected, and the fault can still be detected. The tests under no load conditions are then conducted at different speeds, and the standard deviation as the fault indicator in healthy and turn fault conditions are shown in Fig. 3-47. Compared with the results under other operating conditions in Fig. 3-38, it can be deduced that the turn fault under no load conditions at no lower than 400rpm are also detectable with a common threshold. When the speed is lower than 400rpm, the high frequency components are too small, making the measurement of their RMS values more vulnerable to the noises and errors, and the calculated ratios

unsuitable for the evaluation. Thus, the detection zone of this method can be obtained, as shown in (3-34).

$$\{(\omega_r, I) | 200rpm \le w_r \le 400rpm, I \ge 10A\} \cup \{(\omega_r, I) | w_r \ge 400rpm, I \ge 0A\} \quad (3\text{-}34)$$

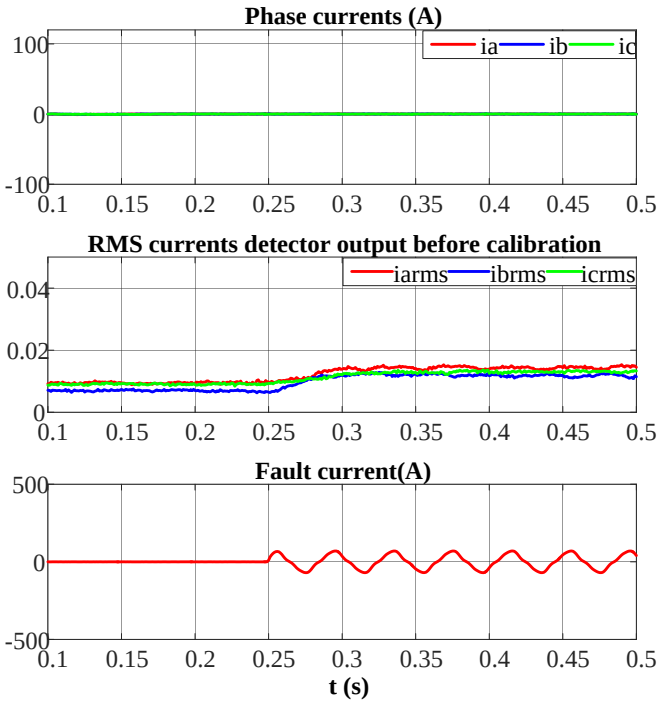

Fig. 3-45 Phase current, fault current and RMS current detector outputs before calibration when the machine operates at 500 rpm and 0A

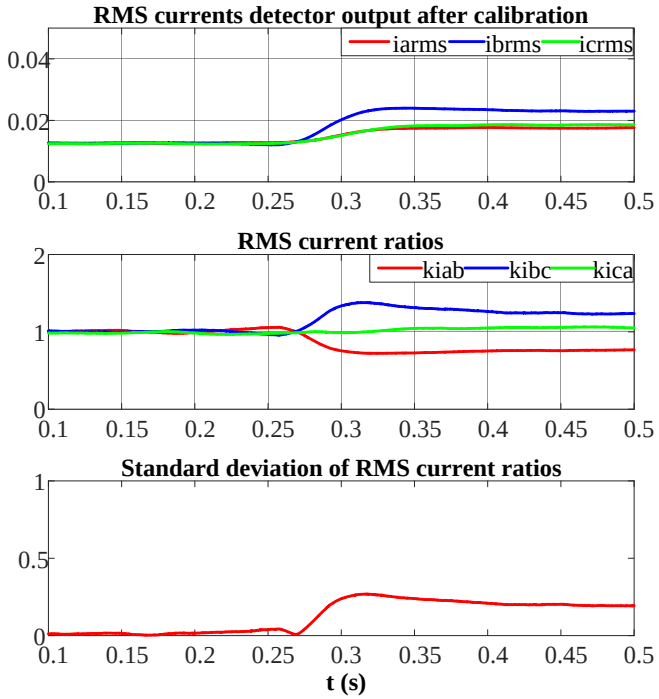

Fig. 3-46 RMS current detector outputs after calibration, RMS current ratios and standard deviation

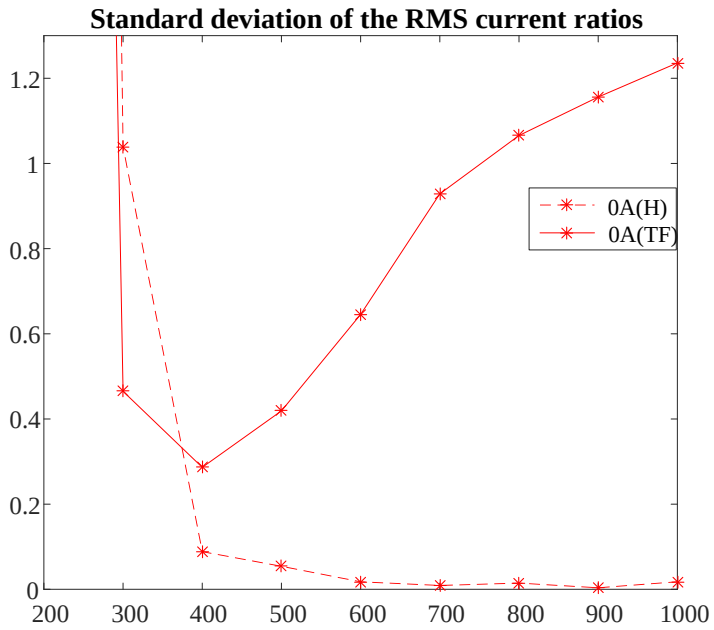

Fig. 3-47 Variations of the standard deviation as fault indicator under no load conditions with different speeds

3.8 Conclusions and discussions

An improved PWM ripple currents based turn fault detection technique has been described in this chapter. The change in the high frequency components of phase currents caused by a turn fault has been analysed through a simplified mathematical model. The analysis shows that the ratios of the RMS high frequency currents between two adjacent phases are not dependent on the operating conditions when the machine is in healthy state. They can be utilised as better fault indicators since the threshold can be determined more easily and extensive calibration based on test data is not necessary. By utilizing the switching sideband harmonics, no high frequency signal injection is needed, thus the machine operation is not affected. Only a simple analogue circuit board is needed for the bandpass filter and RMS converter of the PWM ripple currents. Since the high frequency components have been processed by the hardware board, low sampling frequency for the RMS value acquisition can be sufficient for the subsequent processing. Furthermore, due to the independence from the operating conditions and the utilization of high pass filter and RMS detector, the effect of transient states can be minimized, and risk of false alarm can be largely reduced.

This technique is first analysed, simulated and tested on the 5-phase fault tolerant machine controlled by SPWM strategy. The results show a good signal to noise ratio due to the large separation in fault conditions. For the 3-phase SPM with SVPWM

control, both the analytical and simulated results show that the deviation due to fault is relatively small. To enhance sensitivity and robustness of the detection, the standard deviation of the three ratios is introduced to represent the overall asymmetry caused by the turn fault. The detection scheme has been tested on one 3-phase winding set in a triple redundant 3x3-phase IPM drive. It has been shown that by employing initial simple calibration to remove the inherent unbalance of the machine and asymmetry caused by parameters disparities of the band-pass filters and RMS converters, the detection scheme is effective at the tested operating range.

Although this method only utilizes the high frequency components, it is still affected by the asymmetry of the fundamental frequency voltages through the modulation index. Thus, similar to the current residual based method, the HRC and static eccentricity faults that create constant asymmetry at fundamental frequency will produce similar symptoms, and requires classification. Other faults only produce additional harmonics on the switching sideband frequency components, while the fault indicator should be similar to the healthy conditions through the applied signal processing, which is unlikely to trigger false alarm of turn fault.

CHAPTER 4 Detection and Classification of Turn Fault and High Resistance Connection Fault based on High Frequency Signals

4.1 Introduction

The two foregoing chapters have proposed two effective techniques to detect the turn-to-turn short-circuit fault which is the worst failure case in the stator windings. They utilize the asymmetry in a multi-phase machine caused by a turn fault, reflected in the fundamental and high frequency (switching harmonics) components of voltages and currents, respectively. However, apart from the turn fault, another type of fault on the winding, i.e., the high resistance connection (HRC) fault, may also generate a similar asymmetry.

The high resistance connection fault can be caused by loose connection in any device between the inverter and the machine or damaged connectors and solder points. The actual contact area of a metal-to-metal connection at a joint is small because the surface may not be perfectly flat. Also, due to the oxidization, the real connections are only established where the non-conductive oxide film is fractured by the contact pressure. As the consequence, this cluster of micro-spots is the conducting part, and the possibility of high resistance connection is increased [117][118]. Other causes can be poor workmanship and loosening of connections.

This type of fault can cause local over-heating on the contact surface and subsequently break the connection [119]. The damage to the machine itself, however, is limited, which is different from that caused by the turn fault. In most cases, HRC only deteriorates the operating performance of the machine, such as the increase in torque ripple and the reduction in efficiency. The less severe consequences require no urgent measures. Therefore, appropriate remedy action depends not only on the prompt fault detection but also on correct fault classification.

Infrared thermography is a simple and straightforward way to detect the hot spots in the machine drive systems [120]. Thus, the HRC fault occurrence and its location may be identified. The evident disadvantage is the cost and installation of the infrared camera and those associated with post processing of the images.

The detection of high resistance connection asymmetries in inverter fed AC drive systems via the estimation of phase resistance by applying voltage phasor steps to machine terminals are proposed in [121][32]. It can identify both the already occurred and the incipient faults. However, it is only applicable while the machine is at standstill and not running. To conduct the detection of HRC while the machine is operating, additional dc currents are injected in the stationary (αβ) reference frame[122]. Further manipulation is applied to ensure that only a d-axis component is added to the current reference to avoid torque ripple in induction machines. The detection of HRC is successful in most operating conditions, but the side effect of the signal injection such as the increasing losses is the main concern. Other authors improved the field-oriented control scheme with additional PI controllers to cancel the negative-sequence component of the stator current vector caused by inherent asymmetries or the HRC faults, with the capability to detect them[34][123][124]. Zero sequence voltage in the star connected winding machine and the zero sequence current in the delta connected winding machine are also applied as the fault indicators of HRC in [125][62][126]. The faulty phases can also be identified according to the angle of the fault indicator. However, since both the turn fault and HRC fault introduce asymmetry into a three phase system, they will produce similar symptoms on the negative sequence component and zero sequence component of the interested signals, as has been pointed out in [127]. Thus, it is difficult to classify these two fault types based on the conventional fault detection methods.

An HRC fault detection method by utilizing both signal injection and the zero sequence voltage was proposed in [128], which is insensitive to inductance asymmetry and stator winding turn fault. Thus by combining with the methods for turn fault detection, an integrated winding fault diagnosis method can be achieved. A wavelet based index is proposed to discriminate the turn fault and resistive asymmetrical faults in stator windings in [129]. The normalised energy of the selected detail coefficients is compared to generate the fault indicator. The zero sequence voltage and negative sequence current in an induction machine are investigated in [119][33], where both the amplitude and phase angle of the signals are obtained and compared according to different patterns for the two fault types. In [130], the phase angle of both fundamental current and impedance are used to realize the fault classification. However, the impedance phase angle obtained by the prior measured machine parameters may change

under different operating conditions. In addition, the technique is only valid in steady-state conditions, and the feasibility in transient states is still a problem.

Apart from the phase differences caused by the turn fault and HRC fault, the difference in the phase impedances at high frequency is more significant, when the inductive effect is much more dominant than the resistive effect, making it possible to distinguish them. Therefore, a new method based on the high frequency impedance and PWM ripple current is proposed in this chapter, aiming to detect and classify the turn fault and HRC fault. The differentiating features between the two faults are analyzed and compared in a three phase surface-mounted permanent magnet (SPM) machine fed by an inverter with space vector pulse-width-modulation (SVPWM) voltages. The resultant high frequency components in both voltages and currents are utilized to calculate the apparent high frequency impedance. Together with the high frequency currents, the fault detection and classification strategy can be devised. Extensive simulations show that this method is capable of the fault detection and classification in both transient and steady-state operations. Further, the mathematical analysis and experiments on the three phase interior permanent magnet (IPM) machine with saliency are also conducted.

Since the switching sideband harmonics are determined by the reference signals, they are also affected by the fundamental components. Such effect can deteriorate the separation of the calculated the high frequency impedances in turn fault and HRC fault conditions in the IPM machine. Hence the reliability of this classification is reduced. In order to decouple the examined high frequency components and the fundamental components, a turn fault detection method based on the high frequency square wave signal injection is also proposed. Only the high frequency currents need to be extracted and compared as the injected voltages can be maintained invariant and immune to any conditions. Both the mathematical analysis and experimental tests in the IPM machine show that turn fault can be detected exclusively. The complete detection and classification of the two fault types can be achieved by the combination with a conventional winding fault detection techniques.

4.2 The effect of HRC fault on the turn fault detection method

Chapters 2 and 3 have developed new turn fault detection methods. However, it should be noted that they are under the assumption that turn fault is the only fault type which is more likely to occur while the possibility of the other faults such as HRC fault is very low. Thus, the interference of other faults on the fault detection is not considered. Consequently, whenever the fault indicator presents abnormal behavior, turn fault can be detected. However, in the scenario where the consideration of the HRC fault is necessary, the ability of the proposed methods to correctly classify a fault requires further evaluation.

4.2.1 The effect of HRC fault on the current residual based method

The current residual based turn fault detection method has been proposed in Chapter 2. It detects the difference in the negative sequence component between the measured and estimated currents. Like many other turn fault detection techniques, it makes use of the asymmetry or the unbalance introduced by the fault in the three phase system. However, if a high resistance connection fault occurs, the symmetry will also be broken. According to the phase voltage equations expressed in (2-4) in Chapter 2, the voltage drop on the resistance is only a small portion of the phase voltages, especially at high speed when the induced voltages are much higher. Thus, the influence of the unbalanced three phase resistance on the three phase voltages and currents is hardly seen at high speed. Also, if the level of the HRC fault is small, the turn fault indicator is also likely to be unaffected while stay at a normal value as in healthy condition. However, at lower speed and with an evident increase of the phase resistance, the turn fault indicator will be affected by or sensitive to an HRC fault. This condition is verified through experimental tests.

The same 9-phase triple redundant permanent magnet machine is operating at 500rpm with 30A phase current. At 0.12s, an additional 0.1 Ω resistor is connected in series with phase A winding to emulate an HRC fault. The resultant voltage and current waveforms, and the current residuals are shown in Fig. 4-1 and Fig. 4-2. The HRC also introduces 2nd harmonic significantly in the command dq voltages, measured and estimated dq currents, as shown in Fig. 4-3. It is evident that the negative sequence dq

current residuals also contain a significant dc component, and this feature is the same as that in the turn fault condition. Thus, the current residual based fault detection can detect both turn fault and HRC fault, but cannot classify the fault types.

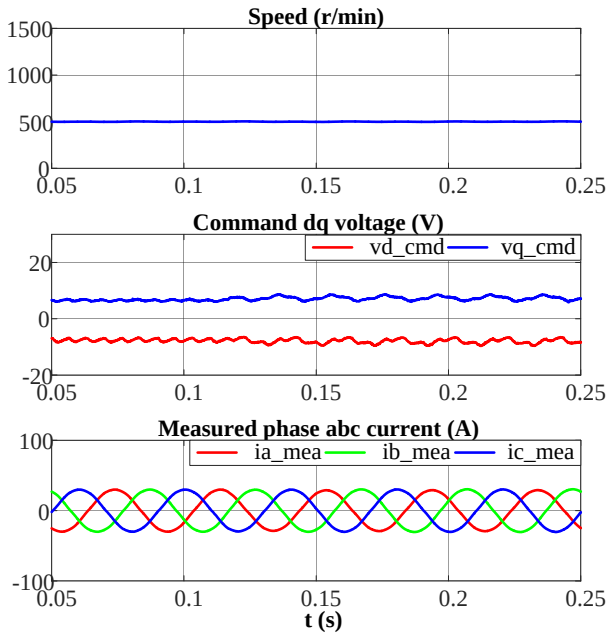

Fig. 4-1 Operating speed, command dq voltages and phase current at 500 rpm, 50A in HRC fault condition

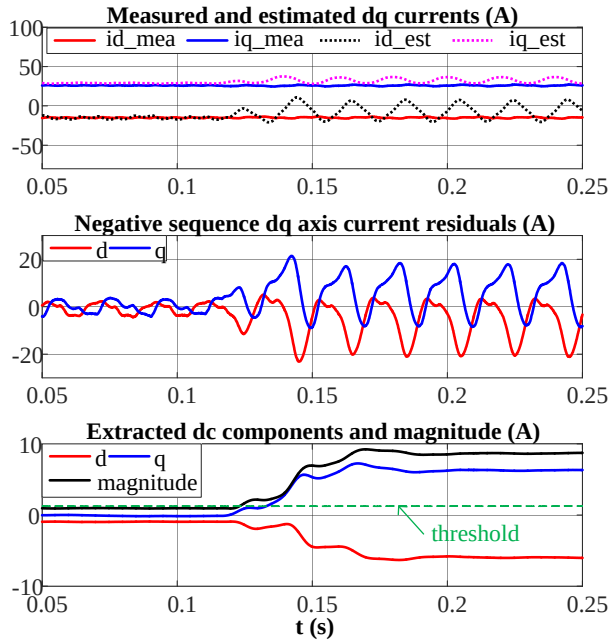

Fig. 4-2 Measured and estimated currents, current residuals and their DC components

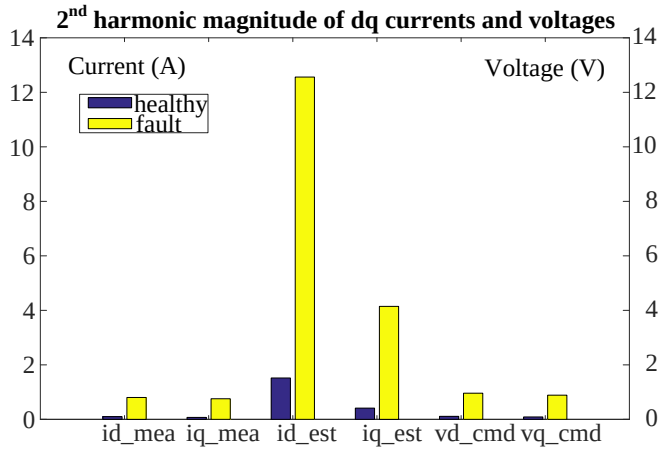

Fig. 4-3 The variations of the 2nd harmonic magnitude in dq currents and voltages

4.2.2 The effect of HRC on the PWM ripple current based method

The influence of the HRC on the fundamental frequency signals is evidently similar to the turn fault. Hence all fault detection methods based on fundamental components need further investigation in order to discriminate fault types. While the turn fault detection method described in Chapter 3 is based on the PWM ripple current which utilizes the high frequency switching sideband harmonics, the influence of an HRC fault on the high frequency signals also needs to be understood.

When an HRC fault or turn fault occurs, the 2nd harmonic in the dq command voltages caused by the asymmetry will lead to fluctuation in the modulation indexes, resulting in asymmetrical reference voltages in SVPWM. Consequently, the three phase high frequency components of the SVPWM voltages also differ from each other. Thus, the high frequency currents become asymmetrical under an HRC fault. As a result, the ratios of the RMS value of the high frequency currents in both turn and HRC fault conditions become unequal to each other, leading to a similar non-zero standard deviation. This analysis is also verified through the following experimental tests.

An additional 0.1 Ω resistor is similarly connected into the phase A winding to emulate the HRC fault condition when the machine is operating at 500rpm with 50A phase current, and the HRC fault is injected at 0.5s. The three phase currents, RMS detector outputs before and after calibration and filtering are shown in Fig. 4-4 and Fig. 4-5, respectively. As can be seen, after the calibration, the inequality emerges in the RMS currents when the HRC fault is triggered. Since the ratios also deviate from 1 and

the standard deviation deviates from 0, the same characteristic feature as the turn fault shown in Chapter 3, the detection techniques based on the high frequency currents also fail to distinguish these two fault types.

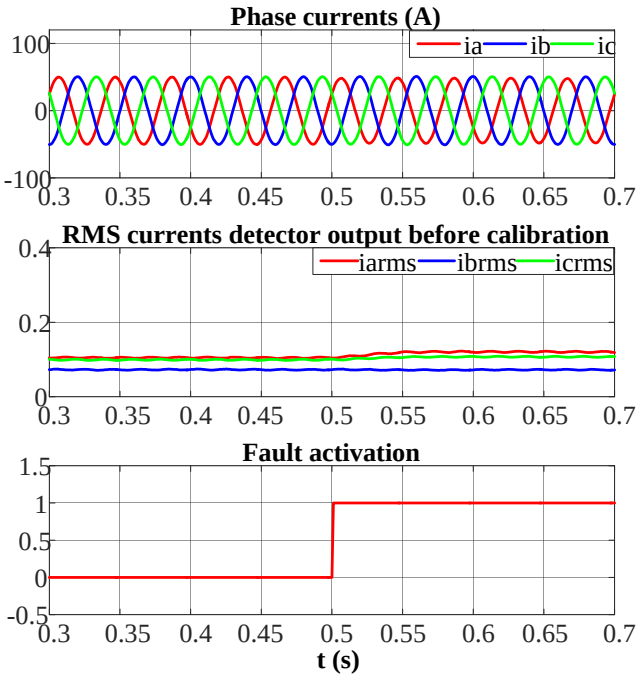

Fig. 4-4 Phase currents and RMS current detector outputs before calibration in HRC fault condition at 500 rpm and 50A

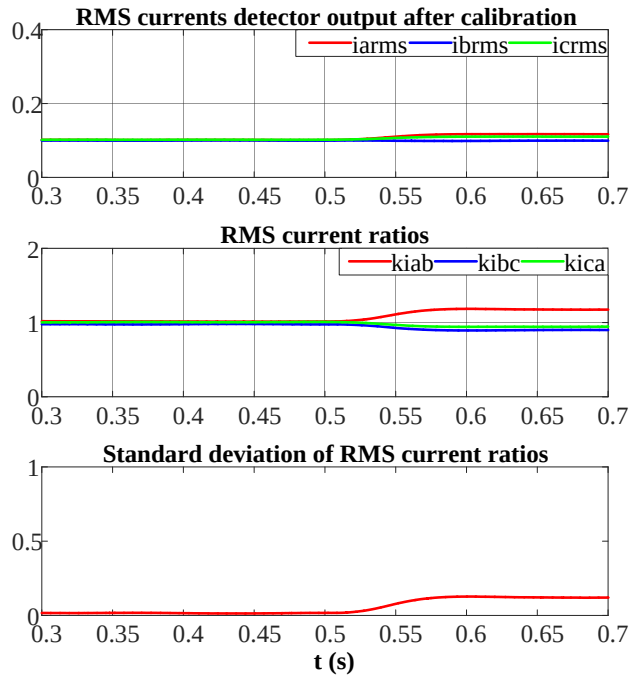

Fig. 4-5 RMS current detector outputs after calibration, RMS current ratios and standard deviation

4.3 Fault feature analysis

In order to develop fault detection and fault classification techniques, the terminal to neutral point voltage will be utilized to establish high frequency phase voltages and high frequency phase impedances under healthy and two fault conditions. The detailed analysis for the two faults is given subsequently.

4.3.1 Turn fault conditions

Similar to the analysis in Chapter 3, the equivalent circuit of the turn fault condition is illustrated in Fig. 4-6, where the parameters of the resistance and inductance in fault condition are denoted. Here, an extra resistors network is connected to the three phase winding terminals to form the artificial neutral point *m*. The resistance of the network should be identical and much larger than the impedance of the phase winding. According to the Kirchhoff's current law, the sum of currents through the balanced resistor network is zero, shown in (4-1). Thus, the voltage between the artificial neutral point *m* and the phase winding neutral point *n* can be obtained in (4-2). Therefore, the actual phase voltages can be transformed into the measurable voltages between the winding terminals and the point *m*, as shown in (4-3). In this way, the voltage equations based on u_{am}, u_{bm}, u_{cm} can be derived.

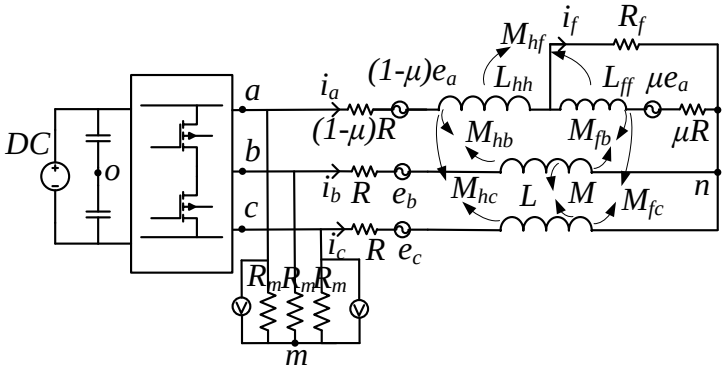

Fig. 4-6 Equivalent circuit and parameters with turn fault

$$\frac{u_{an}-u_{mn}}{R_m}+\frac{u_{bn}-u_{mn}}{R_m}+\frac{u_{cn}-u_{mn}}{R_m}=0 \tag{4-1}$$

$$u_{mn}=\frac{u_{an}+u_{bn}+u_{cn}}{3} \tag{4-2}$$

$$\begin{cases} u_{am} = u_{an} - u_{mn} = u_{an} - \dfrac{u_{an}+u_{bn}+u_{cn}}{3} \\ u_{bm} = u_{bn} - u_{mn} = u_{bn} - \dfrac{u_{an}+u_{bn}+u_{cn}}{3} \\ u_{cm} = u_{cn} - u_{mn} = u_{cn} - \dfrac{u_{an}+u_{bn}+u_{cn}}{3} \end{cases} \quad (4\text{-}3)$$

With the expressions of the phase voltages (3-23) in Chapter 3 and the relationships in (4-3), the measured phase voltage with respect to the artificial neutral voltage *m* can be expressed in (4-4), where the superscript 'TF' denotes the turn fault condition.

$$\mathbf{U}_m^{TF} = \mathbf{R}_{sm}^{TF}\mathbf{i}_s^{TF} + \mathbf{L}_{sm}^{TF} d\mathbf{i}_s^{TF} / dt + \mathbf{e}_m^{TF} \quad (4\text{-}4)$$

where $\mathbf{U}_m^{TF} = [u_{am} \quad u_{bm} \quad u_{cm}]^T$, $\mathbf{i}_s^{TF} = [i_a \quad i_b \quad i_c \quad i_f]^T$,

$\mathbf{e}_m^{TF} = [e_a - \bar{e} \quad e_b - \bar{e} \quad e_c - \bar{e}]^T$, $\bar{e} = \dfrac{e_a + e_b + e_c}{3}$,

$$\mathbf{L}_{sm}^{TF} = \begin{bmatrix} L & M & M & -\frac{2}{3}(M_{hf}+L_{ff}) + \frac{1}{3}(M_{fb}+M_{fc}) \\ M & L & M & \frac{1}{3}(M_{hf}+L_{ff}) - \frac{2}{3}M_{fb} + \frac{1}{3}M_{fc} \\ M & M & L & \frac{1}{3}(M_{hf}+L_{ff}) + \frac{1}{3}M_{fb} - \frac{2}{3}M_{fc} \end{bmatrix}, \mathbf{R}_{sm}^{TF} = \begin{bmatrix} R & 0 & 0 & -\frac{2}{3}\mu R \\ 0 & R & 0 & \frac{1}{3}\mu R \\ 0 & 0 & R & \frac{1}{3}\mu R \end{bmatrix}$$

Likewise, the high frequency switching sideband harmonics around 20kHz are of interest, and they are obtained by bandpass filters. At such high frequency and through bandpass filtering, the effect of the phase resistance and back EMF can be neglected. Thus, unified voltage equations at high frequency can be derived and written in (4-5), where the subscript 'HF' in voltages and currents denotes their high frequency components, and *s* denotes the Laplace operator.

$$\mathbf{U}_{m\_HF}^{TF} = \mathbf{L}_{sm}^{TF} d\mathbf{i}_{s\_HF}^{TF} / dt = s\mathbf{L}_{sm}^{TF}\mathbf{i}_{s\_HF}^{TF} \quad (4\text{-}5)$$

where $\mathbf{U}_{m\_HF}^{TF} = [u_{am\_HF} \quad u_{bm\_HF} \quad u_{cm\_HF}]^T$ $\mathbf{i}_{s\_HF}^{TF} = [i_{a\_HF} \quad i_{b\_HF} \quad i_{c\_HF} \quad i_{f\_HF}]^T$

The high frequency short circuit current due to the turn fault can be predicted using (4-6), and the relationship between the 3-phase high frequency currents and voltages is characterised by the operational impedance matrix $s\mathbf{L}_m^{TF}$ in (4-7).

$$\begin{aligned} L_{ff} i_{f\_HF} &= (L_{ff} + M_{hf}) i_{a\_HF} + M_{fb} i_{b\_HF} + M_{fc} i_{c\_HF} \\ &= (L_{ff} + M_{hf} - M_{fc}) i_{a\_HF} + (M_{fb} - M_{fc}) i_{b\_HF} \end{aligned} \tag{4-6}$$

$$\mathbf{U}_{m\_HF}^{TF} = s\mathbf{L}_{m}^{TF}\mathbf{i}_{m\_HF}^{TF} \tag{4-7}$$

Where $\mathbf{i}_{m\_HF}^{TF} = [i_{a\_HF} \quad i_{b\_HF} \quad i_{c\_HF}]^T$

$$\mathbf{L}_{m}^{TF} = \begin{bmatrix} L + A(L_{ff} + M_{hf}) & M + AM_{fb} & M + AM_{fc} \\ M + B(L_{ff} + M_{hf}) & L + BM_{fb} & M + BM_{fc} \\ M + C(L_{ff} + M_{hf}) & M + CM_{fb} & L + CM_{fc} \end{bmatrix},$$

$$A = \frac{-2(M_{hf} + L_{ff}) + (M_{fb} + M_{fc})}{3L_{ff}}$$

$$B = \frac{(M_{hf} + L_{ff}) - 2M_{fb} + M_{fc}}{3L_{ff}}$$

$$C = \frac{(M_{hf} + L_{ff}) + M_{fb} - 2M_{fc}}{3L_{ff}}$$

4.3.2 High resistance connection fault

The high resistance connection (HRC) fault can occur at the joints between any of the components connected between the source and machine winding. Therefore, when HRC fault occurs, the machine windings can be emulated with an additional resistor ΔR connected in series with the faulted phase winding, as shown in Fig. 4-7, assuming the fault occurs in phase A. The phase voltage equations in the HRC condition can be expressed as (4-8), where the superscript 'HRC' denotes the HRC fault condition.

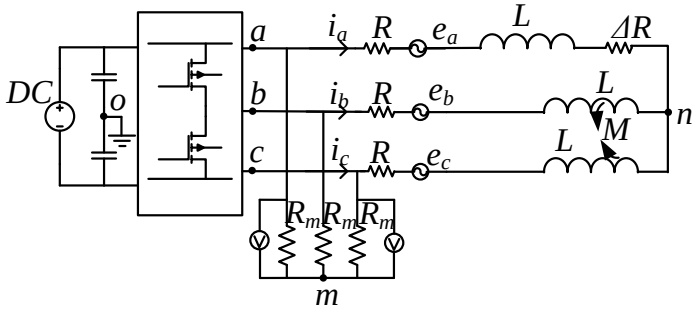

Fig. 4-7 Equivalent circuit and parameters with high resistance connection fault

$$\mathbf{U}_{s}^{HRC} = \mathbf{R}_{s}^{HRC}\mathbf{i}_{m}^{HRC} + \mathbf{L}_{s}^{HRC}d\mathbf{i}_{m}^{HRC}/dt + \mathbf{e}_{s}^{HRC} \tag{4-8}$$

where $\mathbf{U}_{s}^{HRC} = [u_{an} \quad u_{bn} \quad u_{cn}]^T$, $\mathbf{i}_{m}^{HRC} = [i_a \quad i_b \quad i_c]^T$, $\mathbf{e}_{s}^{HRC} = [e_a \quad e_b \quad e_c]^T$

$$\mathbf{L}_s^{HRC}=\begin{bmatrix} L & M & M \\ M & L & M \\ M & M & L \end{bmatrix}, \mathbf{R}_s^{HRC}=\begin{bmatrix} R+\Delta R & 0 & 0 \\ 0 & R & 0 \\ 0 & 0 & R \end{bmatrix}$$

With the same consideration and the same circuit configuration of the additional resistor network to generate the artificial neutral point *m* shown in Fig. 4-7, the expression of the measured phase voltages against *m* is shown in (4-9).

$$\mathbf{U}_m^{HRC}=\mathbf{R}_m^{HRC}\mathbf{i}_m^{HRC}+\mathbf{L}_m^{HRC}d\mathbf{i}_m^{HRC}/dt+\mathbf{e}_m^{HRC} \tag{4-9}$$

where $\mathbf{U}_m^{HRC}=[u_{am} \quad u_{bm} \quad u_{cm}]^T$, $\mathbf{e}_m^{HRC}=[e_a-\bar{e} \quad e_b-\bar{e} \quad e_c-\bar{e}]^T$,

$$\mathbf{R}_m^{HRC}=\begin{bmatrix} R+\frac{2}{3}\Delta R & 0 & 0 \\ 0 & R-\frac{1}{3}\Delta R & 0 \\ 0 & 0 & R-\frac{1}{3}\Delta R \end{bmatrix},$$

$$\mathbf{L}_m^{HRC}=\begin{bmatrix} L-M & 0 & 0 \\ 0 & L-M & 0 \\ 0 & 0 & L-M \end{bmatrix}=(L-M)\begin{bmatrix} 1 & 0 & 0 \\ 0 & 1 & 0 \\ 0 & 0 & 1 \end{bmatrix}$$

After the simplification and the neglect of back EMF and resistive impedance at high frequency, the relationship between the high frequency voltages and high frequency currents are expressed in (4-10).

$$\mathbf{U}_{m\_HF}^{HRC}=\mathbf{L}_m^{HRC}d\mathbf{i}_{m\_HF}^{HRC}/dt=s\mathbf{L}_m^{HRC}\mathbf{i}_{m\_HF}^{HRC} \tag{4-10}$$

where $\mathbf{U}_{m\_HF}^{HRC}=[u_{am\_HF} \quad u_{bm\_HF} \quad u_{cm\_HF}]^T$, $\mathbf{i}_{m\_HF}^{HRC}=[i_{a\_HF} \quad i_{b\_HF} \quad i_{c\_HF}]^T$

4.4 Fault detection and classification

Comparing the high frequency voltage equations (4-7) and (4-10), it is apparent that the difference lies in the inductance matrix. For the HRC fault condition, the inductance matrix is identical to that in healthy conditions, being symmetrical and characterised by the synchronous inductance. This implies that the relations between high frequency voltages and the corresponding high frequency currents are identical for three phases in terms of phase shift and magnitude ratio, regardless of the symmetrical or asymmetrical voltages. For the convenience of data processing, the ratio of the RMS values of the

high frequency voltage and high frequency current, i.e., the apparent high frequency impedance, is calculated, shown in (4-11), where *x*, *y* denote *a*, *b* and *c*, and *rms* denotes the RMS value. From the analysis, the three phase high frequency impedances should remain equal in the HRC fault condition as they are in healthy condition, shown in (4-12). However, since the symmetry at the fundamental frequency is broken due to the HRC fault, the SVPWM reference signals caused by fluctuating modulation index are different among the three phases. As the spectrum of the output PWM voltages are dependent on the reference signals, both the high frequency voltages and currents are no longer identical in the three phases.

$$Z_{x\_HF} = \frac{u_{x\_HF}^{rms}}{i_{x\_HF}^{rms}} \tag{4-11}$$

$$Z_{x\_HF} = Z_{y\_HF} \tag{4-12}$$

For turn fault conditions, the inductance matrix shown in (4-7) does not have the same characteristic. With the parameters obtained from finite element analysis (FEA), the relationship between the high frequency voltages and currents can be evaluated. Unlike the HRC fault conditions, the equivalent high frequency impedances in each phase calculated in the turn fault conditions are unequal to each other. Meanwhile, a turn fault introduces asymmetry into both the fundamental and high frequency components. Consequently, apart from the high frequency impedance, the high frequency voltages and currents also deviate from each other among the three phases due to the asymmetrical SVPWM reference signals.

Based on the foregoing analysis, the features of modulation indexes, reference voltages of SVPWM, high frequency voltages, high frequency currents, and high frequency impedances among the three phases are shown in Table 4-1.

Table 4-1 Features comparison in healthy and fault conditions

Healthy condition	**High resistance fault**	**Turn fault**
Constant modulation	Fluctuating modulation	Fluctuating modulation
Symmetrical reference	Asymmetrical reference	Asymmetrical reference
$u_{x\_HF}^{rms} = u_{y\_HF}^{rms}$	$u_{x\_HF}^{rms} \neq u_{y\_HF}^{rms}$	$u_{x\_HF}^{rms} \neq u_{y\_HF}^{rms}$
$i_{x\_HF}^{rms} = i_{y\_HF}^{rms}$	$i_{x\_HF}^{rms} \neq i_{y\_HF}^{rms}$	$i_{x\_HF}^{rms} \neq i_{y\_HF}^{rms}$
$Z_{x\_HF} = Z_{y\_HF}$	$Z_{x\_HF} = Z_{y\_HF}$	$Z_{x\_HF} \neq Z_{y\_HF}$

From Table 4-1, it is evident that by applying the features of high frequency currents, a turn fault or HRC fault can be detected but cannot be distinguished. By applying the features of the high frequency impedances, these two types of fault can be classified. To avoid dependency on the machine parameters and operating conditions, the fault indicators are defined as the ratios of the selected variables between two phases, shown in (4-13) and (4-14). With the same consideration as Chapter 3, a unified indicator based on the standard deviation of the three ratios is utilized. The standard deviation of the RMS current ratios is expressed in (4-15), while the standard deviation of the high frequency impedance is expressed in (4-16). Based on Table 4-1, the features of the ratios and their standard deviations in the healthy and two different fault conditions are shown in Table 4-2. By examining the two standard deviations, these two types of faults can be detected and classified with the flow chart shown in Fig. 4-8. Since a turn fault needs to be detected more swiftly to avoid significant damage, the standard deviation of impedance ratio is evaluated first. If it is a nonzero, then the turn fault can be diagnosed immediately. If not, then check the standard deviation of the high frequency currents ratios to determine whether the machine is still healthy or an HRC fault has occurred.

$$k_{i\_xy} = \frac{i_{x\_HF}^{rms}}{i_{y\_HF}^{rms}} \tag{4-13}$$

$$k_{Z\_xy} = \frac{Z_{x\_HF}}{Z_{y\_HF}} \tag{4-14}$$

$$\begin{cases} k_{i\_ave} = \dfrac{k_{i\_ab} + k_{i\_bc} + k_{i\_ca}}{3} \\ SD_i = \sqrt{\dfrac{\left(k_{i\_ab} - k_{i\_ave}\right)^2 + \left(k_{i\_bc} - k_{i\_ave}\right)^2 + \left(k_{i\_ca} - k_{i\_ave}\right)^2}{3}} \end{cases} \tag{4-15}$$

$$\begin{cases} k_{Z\_ave} = \dfrac{k_{Z\_ab} + k_{Z\_bc} + k_{i\_ca}}{3} \\ SD_Z = \sqrt{\dfrac{\left(k_{Z\_ab} - k_{Z\_ave}\right)^2 + \left(k_{Z\_bc} - k_{Z\_ave}\right)^2 + \left(k_{Z\_ca} - k_{Z\_ave}\right)^2}{3}} \end{cases} \tag{4-16}$$

Table 4-2 Ratios of RMS currents and high frequency impedance in healthy and fault conditions

Healthy condition	High resistance fault	Turn fault
$k_{i\_xy} = 1, SD_i = 0$	$k_{i\_xy} \neq 1, SD_i \neq 0$	$k_{i\_xy} \neq 1, SD_i \neq 0$
$k_{Z\_xy} = 1, SD_Z = 0$	$k_{Z\_xy} = 1, SD_Z = 0$	$k_{Z\_xy} \neq 1, SD_Z \neq 0$

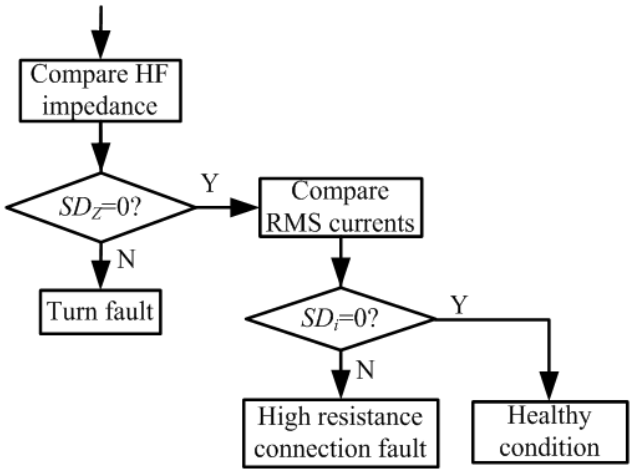

Fig. 4-8 Faults detection and classification steps

4.5 Simulation results

The three-phase SPM machine with 12 slots and 7 pole pairs which has been studied in Chapter 3 is also used for simulation to verify the proposed fault classification methods. The machine is controlled by an outer speed loop and two inner current loops in the dq reference frame. One turn short-circuit fault is injected in phase A to represent the turn fault condition, and 0.1Ω extra resistor is added to the winding of phase A to represent an HRC fault condition.

Fig. 4-9 shows the responses of the machine operating at 857 rpm with 100A phase current, when a single turn fault occurs at 0.2s.

Apparently, significant ripples which are mainly 2nd harmonics appear in both the dq currents and voltages. The behaviour of the RMS high frequency currents and voltages in three phases are shown in Fig. 4-10, together with their ratios. It is clear that both the RMS high frequency currents and voltages deviate from each other, and their ratios deviate from 1. The high frequency impedances of the three phases are calculated and compared in Fig. 4-11. As expected, their ratios are also different and deviate from 1. Finally, the fault indicators of the standard deviations of both the RMS current ratios and high frequency impedance ratios are examined. Both of them change from zero to a non-zero value once the turn fault occurs.

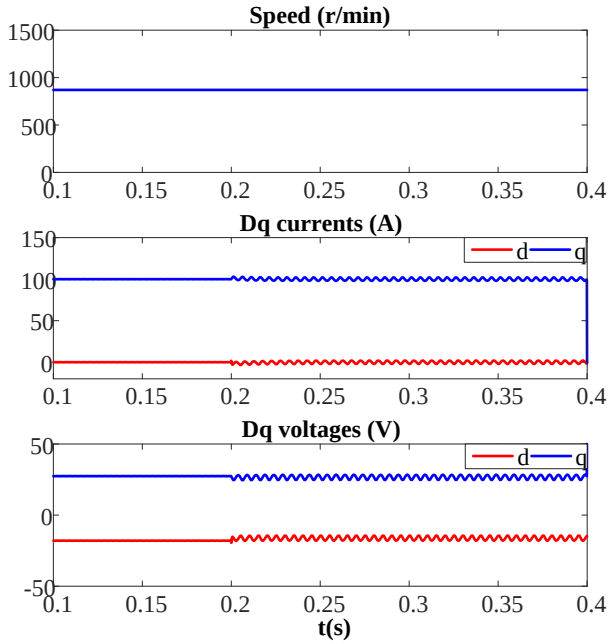

Fig. 4-9 Dq axis currents and voltages in healthy and turn fault condition at 875 rpm 100A

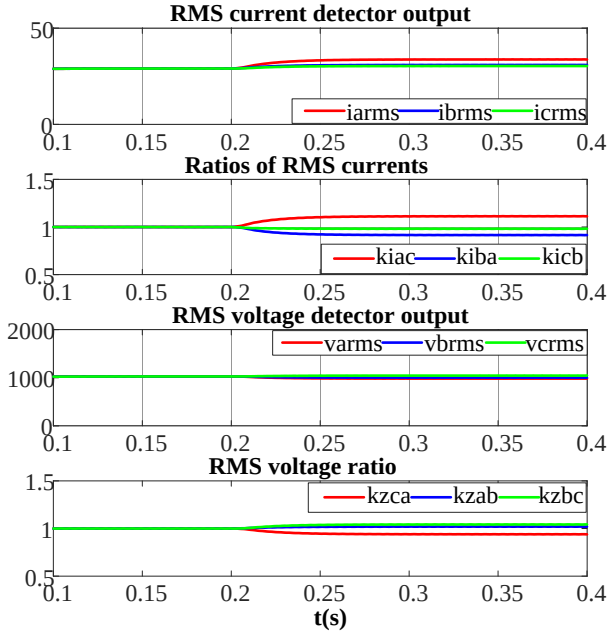

Fig. 4-10 RMS currents and voltages detectors output with their respective ratios in healthy and turn fault conditions

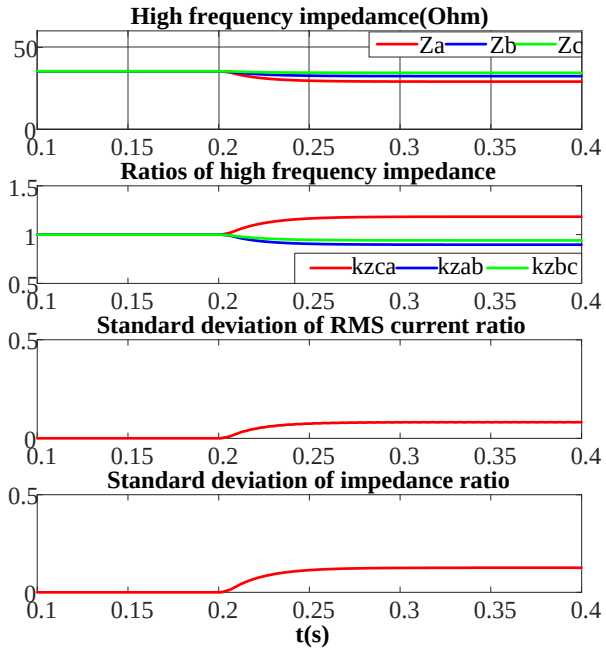

Fig. 4-11 High frequency impedance and the fault indicators in healthy and turn fault conditions

The responses of the machine operating at the same operating condition with a 0.1Ω HRC fault occurring at 0.2s are shown in Fig. 4-12. Quite similar to the turn fault case, both the dq currents and voltages contain a 2nd harmonic ripples in the fault condition. Thus, by examining the signals at the fundamental frequency, it is difficult to distinguish the fault types. The behaviour of the RMS high frequency currents and voltages in the three phases are shown in Fig. 4-13. It seems that the change in the high frequency currents and voltages are also similar to that in the turn fault condition. However, when the high frequency impedances are obtained in Fig. 4-14, a different feature can be observed. Unlike the behaviour in the turn fault condition, the high frequency impedance of the three phase windings are unchanged and remains identical to each other with the occurrence of HRC fault. These features are also reflected on the ratios and their standard deviations. In the HRC fault condition, the standard deviation of the RMS current ratios changes to a non-zero value as well, while that of the high frequency impedance ratios remains zero.

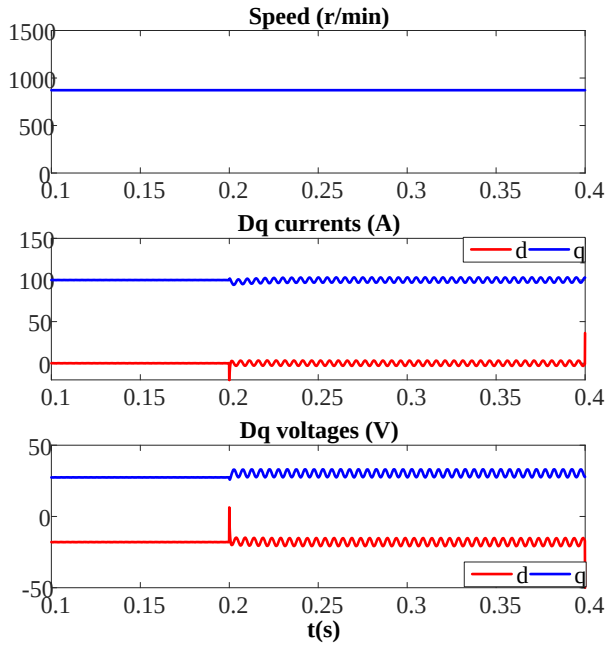

Fig. 4-12 Dq axis currents and voltages in healthy and HRC fault condition at 875 rpm 100A

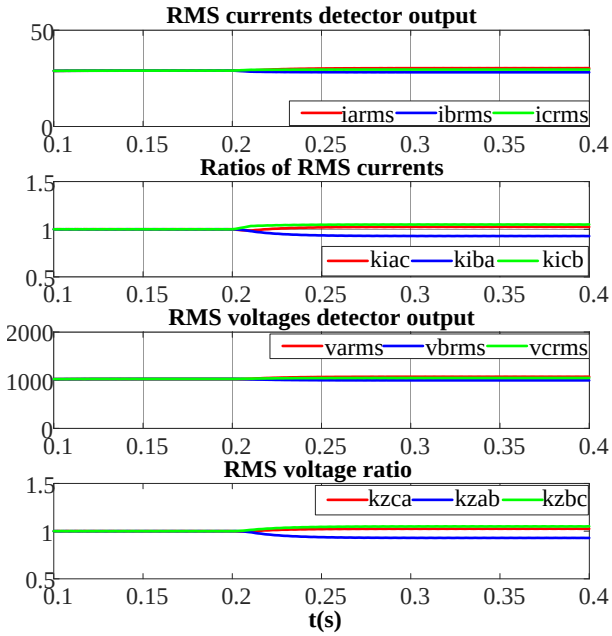

Fig. 4-13 RMS currents and voltages detectors output with their respective ratios in healthy and HRC fault conditions

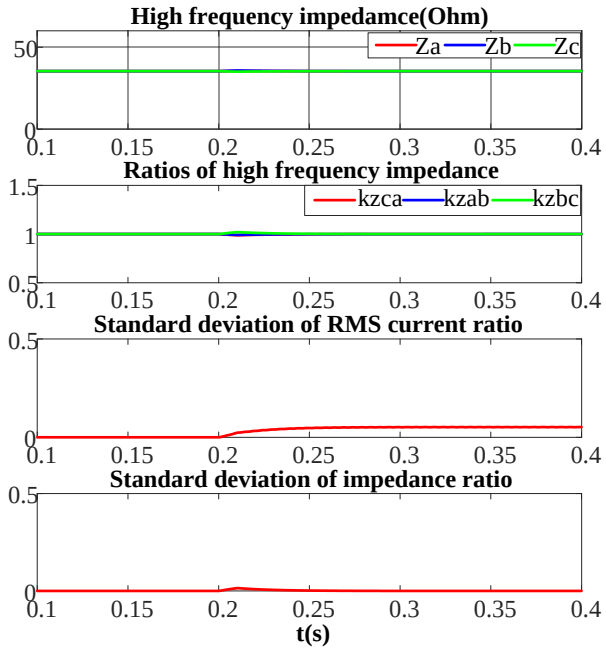

Fig. 4-14 High frequency impedance and the fault indicators in healthy and HRC fault conditions

The fault features in the simulation results have verified the theoretical comparison in Table 4-1 and Table 4-2. Thus, the fault detection and classification steps in Fig. 4-8 can be applied to diagnose whether a turn fault or an HRC fault has occurred. Also, since the ratios are calculated to eliminate the dependence on the operating condition in healthy states in the same way as the method in Chapter 3, the merits of immune and robust to transient states are also preserved. When a current step change and varying speed are applied separately in Fig. 4-15 and Fig. 4-16, the impact on the fault indicator is hardly seen, thus the false alarm will not be triggered by transient state.

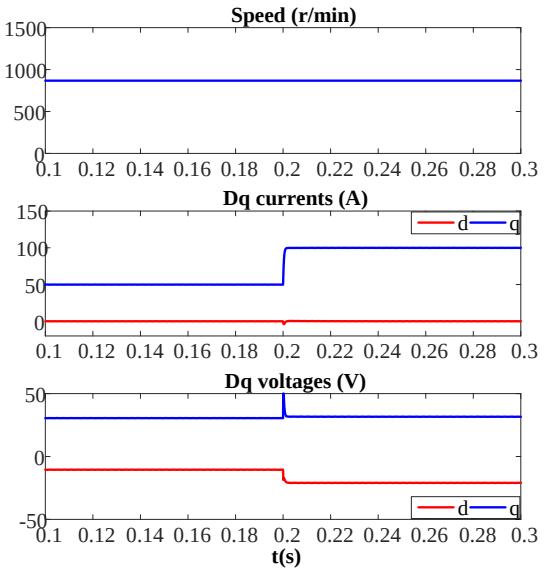

(a)

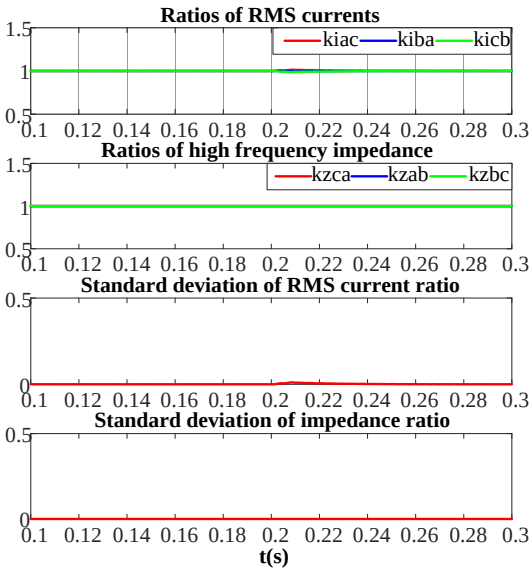

(b)

Fig. 4-15 Healthy condition with current step change (a) Dq axis currents and voltages (b) Ratios of RMS currents, high frequency impedances, and their respective standard deviations

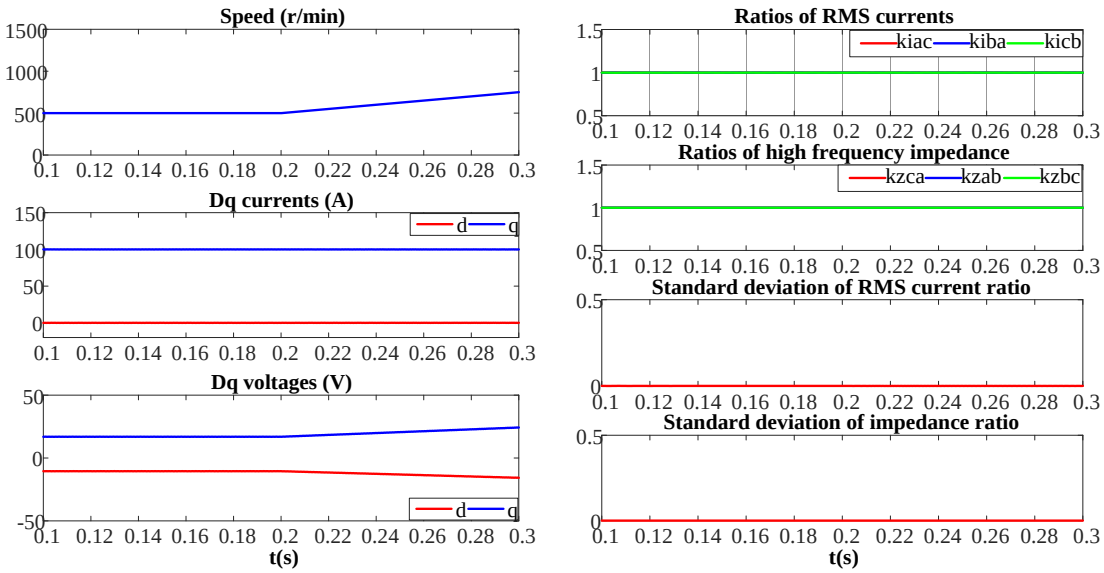

(a) (b)

Fig. 4-16 Healthy condition with varying speed (a) Dq axis currents and voltages (b) Ratios of RMS currents, high frequency impedances, and their respective standard deviations

4.6 High resistance connection fault features in IPM

The discrimination of the turn fault and HRC fault in SPM machine has been analyzed theoretically and validated through simulation. From the analysis, it is shown that the main principle for the successful classification is the feature of the identical three phase equivalent high frequency impedances in the case of the HRC fault. This is the case when the inductance is approximately constant in SPM machines. However, in the IPM machine, the prominent saliency effect leads to the 2nd space harmonic in the inductance, as has been expressed in (2-2) in Chapter 2. Thus, assuming that the high frequency impedances will still be unequal in a turn fault condition, the impedance behavior under an HRC fault needs to be investigated.

Supposing the high frequency voltages are expressed in (4-17), where V_a V_b V_c are the amplitudes and α β γ are the phase angles. It is evident that in a healthy condition of a balanced three phase system or in the case of the current open loop control, the amplitudes are equal while the phase angles differ 120° from each other.

$$\begin{cases} u_{ao\_HF} = V_a \sin(\omega_e t + \alpha)\sin\omega_c t \\ u_{bo\_HF} = V_b \sin(\omega_e t + \beta)\sin\omega_c t \\ u_{co\_HF} = V_c \sin(\omega_e t + \gamma)\sin\omega_c t \end{cases} \quad (4\text{-}17)$$

To ease the derivation of three phase high frequency currents, the voltages are first transformed into the *dq* rotating frame, as shown in (4-18).

$$\begin{cases} u_{d\_HF} = \frac{2}{3}\sin\omega_c t \left[\begin{array}{l} V_a \sin(\omega_e t + \alpha)\cos\omega_e t + V_b \sin(\omega_e t + \beta)\cos(\omega_e t - \frac{2}{3}\pi) \\ +V_c \sin(\omega_e t + \gamma)\cos(\omega_e t - \frac{4}{3}\pi) \end{array} \right] \\ u_{q\_HF} = -\frac{2}{3}\sin\omega_c t \left[\begin{array}{l} V_a \sin(\omega_e t + \alpha)\sin\omega_e t + V_b \sin(\omega_e t + \beta)\sin(\omega_e t - \frac{2}{3}\pi) \\ +V_c \sin(\omega_e t + \gamma)\sin(\omega_e t - \frac{4}{3}\pi) \end{array} \right] \end{cases} \quad (4\text{-}18)$$

With the voltage equations in the *dq* rotating frame shown in (4-19) derived from the three phase equations in (4-9), the relations between the high frequency *dq* axis currents and voltages can be expressed in (4-20), where the back-emf, the motion induced voltages and the voltage drops on the resistance are neglected. This is because the frequency ω_c under study is much higher than the machine's electrical angular speed frequency and a bandpass filter will be used.

$$\begin{cases} u_d = R_s i_d + L_d \frac{di_d}{dt} - \omega_e L_q i_q + \frac{2}{3}\Delta R i_a \cos\theta \\ u_q = R_s i_q + L_q \frac{di_q}{dt} + \omega_e (L_d i_d + \lambda_{pm}) - \frac{2}{3}\Delta R i_a \sin\theta \end{cases} \quad (4\text{-}19)$$

$$\begin{cases} i_{d\_HF} \approx \frac{u_{d\_HF}}{j\omega_c L_d} \\ i_{q\_HF} \approx \frac{u_{q\_HF}}{j\omega_c L_q} \end{cases} \quad (4\text{-}20)$$

Combining (4-18) and (4-20), and transforming the high frequency currents and voltages in the dq rotating frame back into the abc frame, one can obtain three phase high frequency currents in (4-21).

It is clear that to obtain the identical relationship between V_x and I_x (x=a,b,c), the second term on the right side of the equations which couples with the other phase voltages should be zero. This can be true in two scenarios. One is the SPM machine

where L_d=L_q, as has been demonstrated in the previous sections. The other one is the symmetrical high frequency voltages, where V_a=V_b=V_c, α=β+120=γ+240. This is actually the case of open loop current control where the three phase driving voltages are always symmetrical in any conditions. However, for an IPM machine with closed-loop current control in an HRC fault condition, those coupling items always exist. Consequently, if (4-11) is applied to calculate the apparent high frequency impedance, there is no guarantee that all the calculated HF impedances are equal. Thus, the application of the technique described in section 4.4 to IPM machines for classification of the two fault types cannot be theoretically demonstrated, but should be evaluated through experimental tests.

$$
\begin{aligned}
i_{a\_HF} \approx \frac{1}{4}\left(\frac{1}{L_d}+\frac{1}{L_d}\right)V_a\left\{\frac{1}{\omega_c-\omega_r}\sin\left[(\omega_c-\omega_r)t-\alpha\right]-\frac{1}{\omega_c+\omega_r}\sin\left[(\omega_c+\omega_r)t+\alpha\right]\right\} \\
+\frac{1}{12}\left(\frac{1}{L_q}-\frac{1}{L_d}\right)\left\{\begin{array}{l}
V_a\left\{\begin{array}{l}\frac{1}{\omega_c+\omega_r}\sin\left[(\omega_c-\omega_r)t+\alpha\right] \\ -\frac{1}{\omega_c-\omega_r}\sin\left[(\omega_c+\omega_r)t-\alpha\right]\end{array}\right. \\
+V_b\left\{\begin{array}{l}\frac{1}{\omega_c+\omega_r}\sin\left[(\omega_c-\omega_r)t+\beta+\frac{2\pi}{3}\right] \\ -\frac{1}{\omega_c-\omega_r}\sin\left[(\omega_c+\omega_r)t-\beta-\frac{2\pi}{3}\right]\end{array}\right. \\
+V_c\left\{\begin{array}{l}\frac{1}{\omega_c+\omega_r}\sin\left[(\omega_c-\omega_r)t+\gamma+\frac{4\pi}{3}\right] \\ -\frac{1}{\omega_c-\omega_r}\sin\left[(\omega_c+\omega_r)t-\gamma-\frac{4\pi}{3}\right]\end{array}\right.
\end{array}\right.
\end{aligned}
\tag{4-21}
$$

$$i_{b\_HF} \approx \frac{1}{4}\left(\frac{1}{L_d}+\frac{1}{L_d}\right)V_b\left\{\frac{1}{\omega_c-\omega_r}\sin\left[(\omega_c-\omega_r)t-\beta\right]-\frac{1}{\omega_c+\omega_r}\sin\left[(\omega_c+\omega_r)t+\beta\right]\right\}$$
$$+\frac{1}{12}\left(\frac{1}{L_q}-\frac{1}{L_d}\right)\left\{\begin{array}{l} V_a\left\{\begin{array}{l}\frac{1}{\omega_c+\omega_r}\sin\left[(\omega_c-\omega_r)t+\alpha+\frac{2\pi}{3}\right]\\ -\frac{1}{\omega_c-\omega_r}\sin\left[(\omega_c+\omega_r)t-\alpha-\frac{2\pi}{3}\right]\end{array}\right.\\ +V_b\left\{\begin{array}{l}\frac{1}{\omega_c+\omega_r}\sin\left[(\omega_c-\omega_r)t+\beta+\frac{4\pi}{3}\right]\\ -\frac{1}{\omega_c-\omega_r}\sin\left[(\omega_c+\omega_r)t-\beta-\frac{4\pi}{3}\right]\end{array}\right.\\ +V_c\left\{\begin{array}{l}\frac{1}{\omega_c+\omega_r}\sin\left[(\omega_c-\omega_r)t+\gamma\right]\\ -\frac{1}{\omega_c-\omega_r}\sin\left[(\omega_c+\omega_r)t-\gamma\right]\end{array}\right.\end{array}\right.$$

$$i_{c\_HF} \approx \frac{1}{4}\left(\frac{1}{L_d}+\frac{1}{L_d}\right)V_c\left\{\frac{1}{\omega_c-\omega_r}\sin\left[(\omega_c-\omega_r)t-\gamma\right]-\frac{1}{\omega_c+\omega_r}\sin\left[(\omega_c+\omega_r)t+\gamma\right]\right\}$$
$$+\frac{1}{12}\left(\frac{1}{L_q}-\frac{1}{L_d}\right)\left\{\begin{array}{l} V_a\left\{\begin{array}{l}\frac{1}{\omega_c+\omega_r}\sin\left[(\omega_c-\omega_r)t+\alpha+\frac{4\pi}{3}\right]\\ -\frac{1}{\omega_c-\omega_r}\sin\left[(\omega_c+\omega_r)t-\alpha-\frac{4\pi}{3}\right]\end{array}\right.\\ +V_b\left\{\begin{array}{l}\frac{1}{\omega_c+\omega_r}\sin\left[(\omega_c-\omega_r)t+\beta\right]\\ -\frac{1}{\omega_c-\omega_r}\sin\left[(\omega_c+\omega_r)t-\beta\right]\end{array}\right.\\ +V_c\left\{\begin{array}{l}\frac{1}{\omega_c+\omega_r}\sin\left[(\omega_c-\omega_r)t+\gamma+\frac{2\pi}{3}\right]\\ -\frac{1}{\omega_c-\omega_r}\sin\left[(\omega_c+\omega_r)t-\gamma-\frac{2\pi}{3}\right]\end{array}\right.\end{array}\right.$$

4.7 Experiments in IPM Drive

With the concerns of the ineffective classification based on the features of the impedance, experiments are carried out on the 9-phase triple redundant fault tolerant machine as has been introduced in Chapter 2. After the setup of the single turn fault in

phase B and 0.1 Ω HRC fault in phase A, the unbalance in the calculated impedances are compared quantitatively.

4.7.1 High resistance connection fault setup

The additional resistance is selected as 0.1 Ω, which is almost 4 times larger than the winding phase resistance. To cope with the power loss, the resistance is composed of 5 identical resistors in parallel connection. Each resistor is 0.5 Ω with the rated power 100W. Thus the RMS current in each resistor can be up to 14A, and the amplitude of the phase current should be limited to 99A. To avoid excessive heat, the phase current in the following tests is limited to 70A. The resistors are placed on a heat sink and inserted between the inverter terminal and the phase A winding. A relay is connected in parallel to the resistors and is controlled by the DSP controller. When the relay is closed, the resistors are by-passed, and the machine remains in healthy condition. When the relay is open, then the HRC fault is activated. A current sensor is attached to one of the resistors to measure the current in the branch. Therefore, in healthy condition, the measured current should be zero, while in HRC fault condition, the measured current should be 1/5 of the phase current. This current can be used to mark the occurrence of the HRC fault. The schematic and the practical implementation of the high resistance connection in the test rig are shown in Fig. 4-17 and Fig. 4-18.

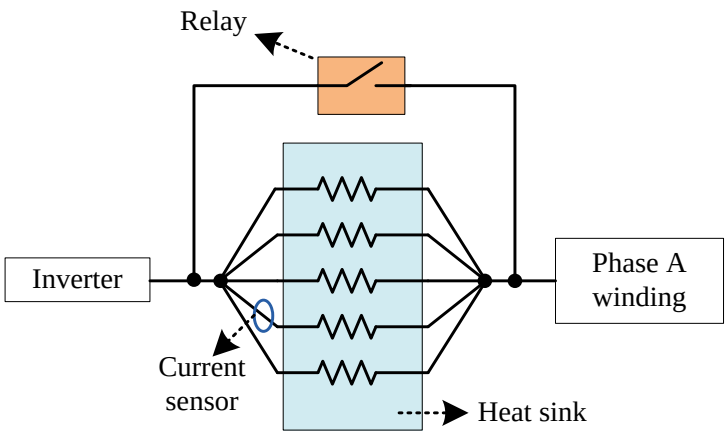

Fig. 4-17 Schematic of the high resistance connection in the test rig

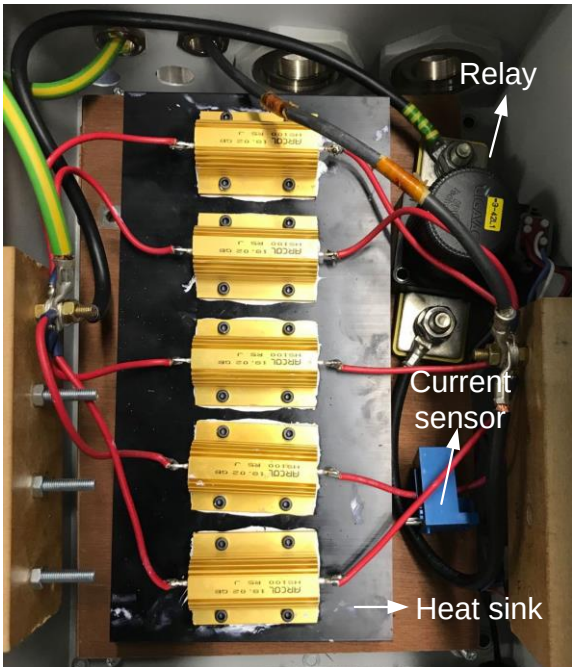

Fig. 4-18 High resistance connection in the test rig

4.7.2 Current and voltage measurement and RMS detection

Since the frequency of the components under investigation in the currents and voltages is 20k Hz, which is much higher than the DSP sampling frequency, the analogue circuit is designed to process the signal and produce the RMS value of the high frequency components, with the signal processing chain shown in Fig. 4-19 and the actual implementation board shown in Fig. 4-20.

The three phase currents are measured by the Hall-effect current transducer LEM LA200-P with a bandwidth of 100k Hz. The resistor network is mounted on the board and creates the artificial neutral point. The voltage between this point and the phase terminals are measured by Texas Instruments AMC1301 reinforced isolated amplifier with the output bandwidth 200k Hz. The amplitude of the measured currents and voltages signals are regulated accordingly and input into the two cascaded 2nd order active Butterworth bandpass filter. The Texas Instrument operational amplifier OPA364 is selected for the circuit due to its high performance, low cost and low voltage supply operation. The RMS detector is LTC1968 which is a precision wide bandwidth, RMS-to-DC converter from Linear Technology. Since the outputs of this circuit are almost DC signals, a low sampling rate is sufficient.

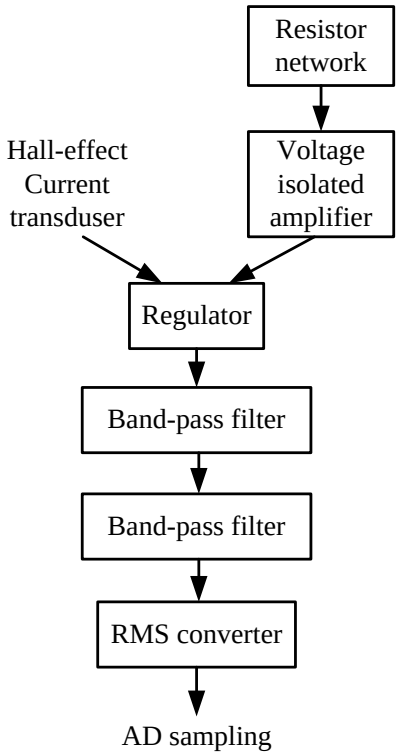

Fig. 4-19 Signal processing chain of the designed analogue circuit board

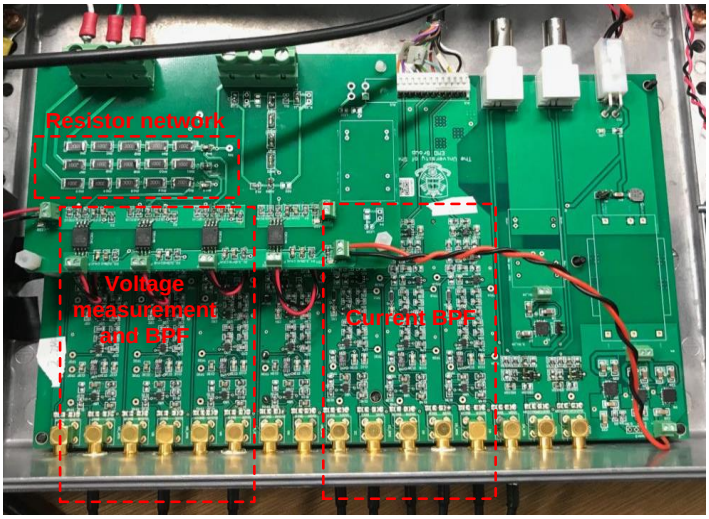

Fig. 4-20 The designed signal processing analogue circuit board

4.7.3 Experimental results

The machine is firstly operating at 500 rpm with 70A phase current, when a single turn fault occurs at 0.5s. The behaviours of the RMS high frequency currents and voltages in three phases are shown in Fig. 4-21, as well as their ratios, after the calibration and filter process have been implemented, as described in Chapter 3. It can be seen that the deviation of the three phase currents are significant, and is partially contributed by the unbalanced high frequency voltages. The major contribution lies in

the unequal high frequency impedances, which are calculated and shown in Fig. 4-22. This validates the previous assumption that the feature of the unequal high frequency impedance still remains in the turn fault condition in the IPM machine. The ratios of high frequency impedance are then obtained. The standard deviations of both the RMS current ratios and the high frequency impedance ratios are examined, and both of them stay at zero in healthy condition and become nonzero in the turn fault condition.

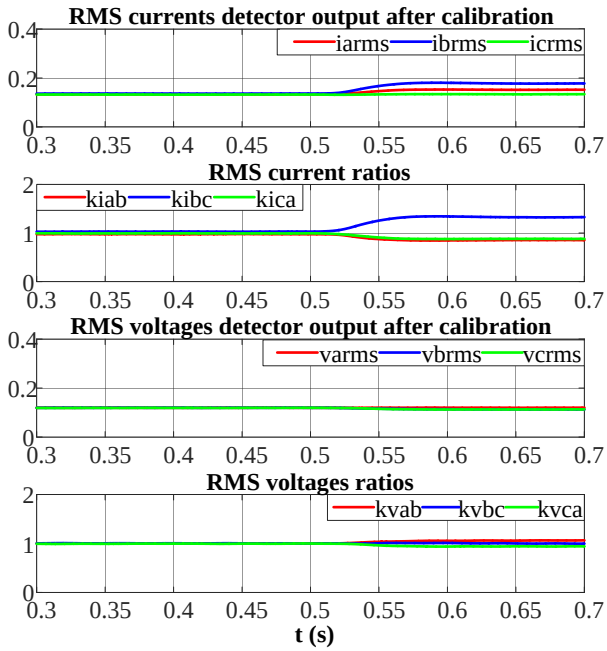

Fig. 4-21 RMS currents and voltages detectors output with their respective ratios in healthy and turn fault conditions

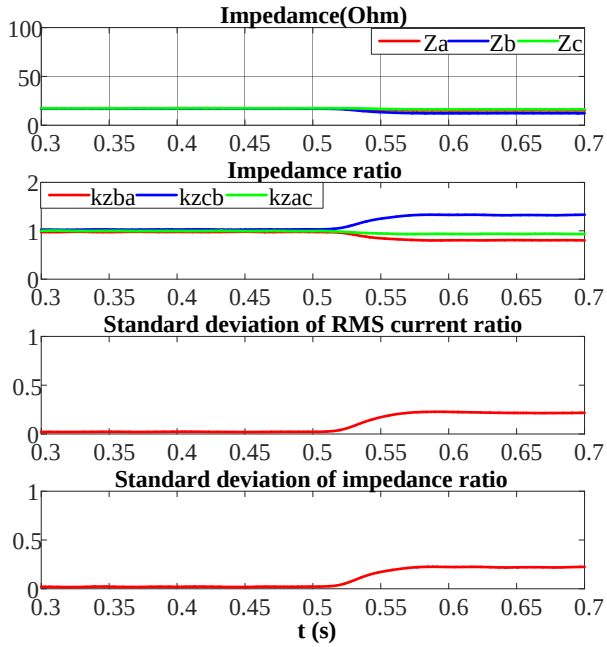

Fig. 4-22 High frequency impedance, their ratios and standard deviations in healthy and turn fault conditions

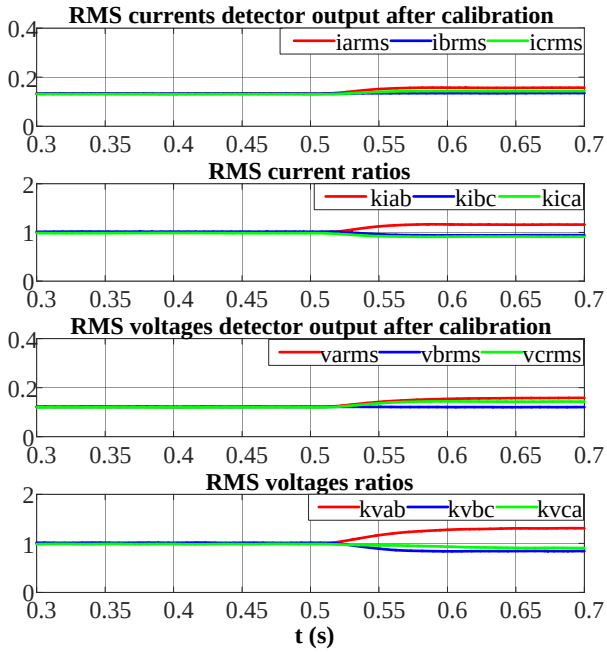

Fig. 4-23 RMS currents and voltages detectors output with their respective ratios in healthy and HRC fault conditions

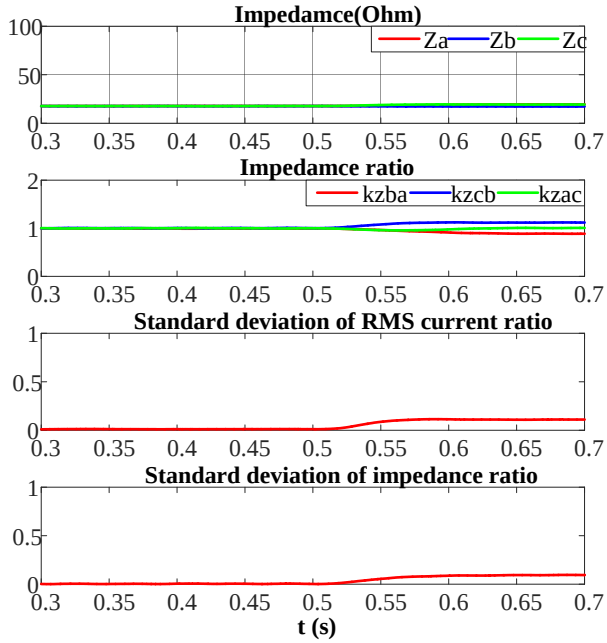

Fig. 4-24 High frequency impedance, their ratios and standard deviations in healthy and HRC fault conditions

At the same operating condition of 500 rpm speed and 70A phase current, the 0.1 Ω HRC fault is activated from the healthy condition at 0.5s. The RMS high frequency currents and voltages in three phases together with their ratios are shown in Fig. 4-23. It is seen that the deviation of high frequency voltages are more significant than that of the turn fault condition, and the changes of the high frequency currents and voltages are very similar. It indicates that the deviation of the high frequency currents is mainly caused by the high frequency voltages. After the calculation of three phase high

frequency impedances and their ratios in Fig. 4-24, the change due to the HRC fault can be observed although it is smaller compared with the turn fault condition. This validates the previous derivation that the calculated high frequency impedances are not equal in the HRC fault in the IPM machine due to saliency. As the consequence, the standard deviation of both the high frequency current ratios and impedance ratios deviate from zero.

Since it is difficult to classify the two fault conditions qualitatively based on the high frequency impedance feature in general, the standard deviations of the high frequency currents and impedances when a fault occurs at different operating conditions are also investigated. Firstly, the standard deviation of the RMS current ratios at different operating conditions are obtained and plotted in Fig. 4-25, where 'H' denotes healthy conditions, 'TF' denotes turn fault conditions, and 'HRC' denotes high resistance connection fault conditions. It can be seen that with the speed increasing, the fault indicator under the HRC fault decreases, approaching to that in healthy condition. This is because at higher speed under the same current level, the induced voltage becomes dominant in the voltage equations. Thus, the impact of the resistive unbalance is reduced largely. Because the three phase voltages tend to be less asymmetric as the speed increases, the high frequency components of the voltages also show the same characteristic. Consequently, the deviation of the resultant high frequency currents components is much smaller. Therefore, it is not sensitive to the HRC fault when the speed is close to and higher than 1000 rpm, where the turn fault can be more exclusively detected by the high frequency currents (denoted as PWM ripple currents in Chapter 3). However, for the speed below 400rpm, the features of a single turn fault and 0.1 Ω HRC fault are very close, and the fault detection results could be ambiguous.

As it is not possible to discriminate the two fault types purely based on the RMS high frequency currents, the standard deviation of the high frequency impedance ratios are compared against various currents and speeds, shown in Fig. 4-26. At low speed, the standard deviation of the high frequency impedance ratios in the HRC fault condition are decreased largely compared to that of the high frequency current ratios, but is still larger than the values in the healthy condition. Although the separation between the two fault types can still be seen, it is dependent on the fault severity and load current. If the fault resistance or the load current is higher in the HRC fault, the standard deviation of the high frequency impedance ratios increases, approaching to that in a single turn fault

condition. Hence, the fault detection and classification with a simple threshold is less reliable. In order to enhance that robustness of the detection and classification against various fault scenarios and operating conditions for the IPM machine, it is suggested to acquire the fault indicator values at various operating conditions with different possible fault severities, then apply data driven classification techniques such as k-means, Gaussian mixture model (GMM), support vector machine (SVM), etc., which will be studied in the future.

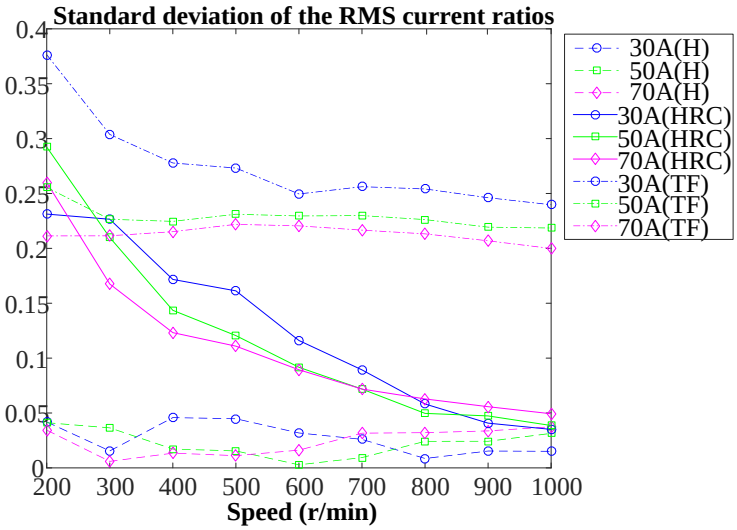

Fig. 4-25 Variation of the standard deviation of the RMS current ratios with current and speed.

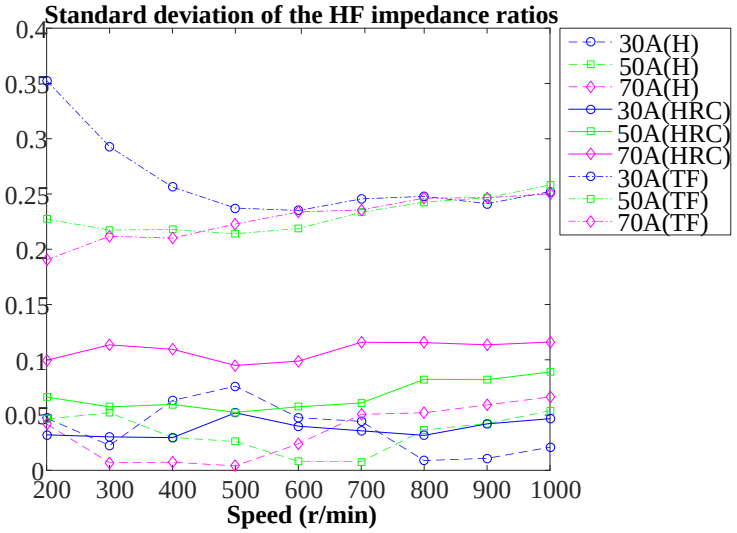

Fig. 4-26 Variation of the standard deviation of the high frequency impedance ratios with current and speed.

4.8 High frequency voltage injection based detection and classification

4.8.1 Injected high frequency signal

As can be concluded from the previous analysis and experiments, the classification based on the switching sideband high frequency currents and impedances is not ideal in an IPM machine in which the definition of a simple threshold is not possible. The asymmetry of the three phase high frequency voltages caused by the modulation index and their mutual couplings in contributing the high frequency currents makes it very difficult to extract a significantly different symptom in an HRC fault condition from that in a turn fault condition, as has been expressed in (4-21). If the high frequency voltages are not related to the fundamental components and always kept symmetric regardless of fault conditions, then the difference in the high frequency impedances is presented completely in the high frequency currents, which can be used for the effective discrimination of the two faults. This scenario can only be realized by extra high frequency voltage injection instead of the utilization of the PWM switching sideband harmonics.

The high frequency voltage injection techniques have already been extensively studied in the machines' sensorless control[131][132][133]. Rotating voltage signal injection in the stationary reference frame and pulsating voltage signal injection in the estimated rotor reference frame are the two main techniques reported in literature. Unlike the sensorless control which needs to extract the position angle estimation through the derivation of the high frequency equations, the concept of fault detection with the high frequency voltage injection is to analyse and compare the three phase high frequency currents. Thus, the rotating voltage signal injection is adopted so that the actual injected voltages on each phase can be kept to be a single high frequency component and symmetrical among the three phases.

It has been reported that the selection of the injected signal frequency is very essential[134]. In order to diminish the interference between the injected signal and the fundamental components of the current control, the frequency should be as high as possible. However, the concern of the aliasing effect on the PWM transformation process and the nonlinearity of the inverter place a lower restriction on the maximum frequency for the injected signal. Considering the fact that from the fault detection point

of view, the requirement for the injected signal's waveform is not very high, as long as there exit a dominant frequency component. Therefore, a rotating square wave voltage injection is preferred.

The rotating square waves for three phases should have 3-phase symmetry with 120 degree phase shift, thus only six states need to be produced, i.e. 101, 100, 110, 010, 011, 001, where 0 and 1 represent the lower and upper level of the square wave for each phase. The magnitude of the square wave is set to be 0.05 with respect to the normalised modulation index, and they are to be injected on the original modulating signals shown in Fig. 4-27 under the SVPWM control strategy. The newly modified modulating signals are compared with the triangle wave carrier signal to generate the gate signals for the inverter switches. The complete signal injection process is illustrated in Fig. 4-28. The original modulating signals generate the required three phase driving voltages with fundamental component as well as the switching harmonics and their sidebands, whose frequency are no lower than the switching frequency. The injected square wave voltages generate the three phase high frequency currents, which are separated from both the fundamental and switching frequency components.

In practice, the current sampling and modulation index updating frequency is equal to the switching frequency as 10k Hz. Thus, the configuration of the injected square wave's six states with the carrier signals is shown in Fig. 4-29 at the highest possible square wave frequency, being 1/6 of the carrier frequency. Considering the floating winding neutral point, and the transformation of the three phase voltages to eliminate the zero sequence voltage, the equivalent injected signals into the transformed voltage expressed in (4-3) and (4-4) can be calculated and is illustrated in Fig. 4-30. Compared with the original injected signal, the equivalent injected signal contains no 3^{rd} harmonic and its integer multiples, thus increasing the proportion of the sine wave fundamental component. The spectrum of the transformed phase voltage is shown in Fig. 4-31. It is clear that the injected signal is at 1666.7 Hz which is 1/6 of the switching frequency of 10k Hz. Also, it has a good separation from both the fundamental frequency component and the switching sideband harmonics. Thus, in a similar way, a band pass filter can be applied to acquire the frequency components of interest.

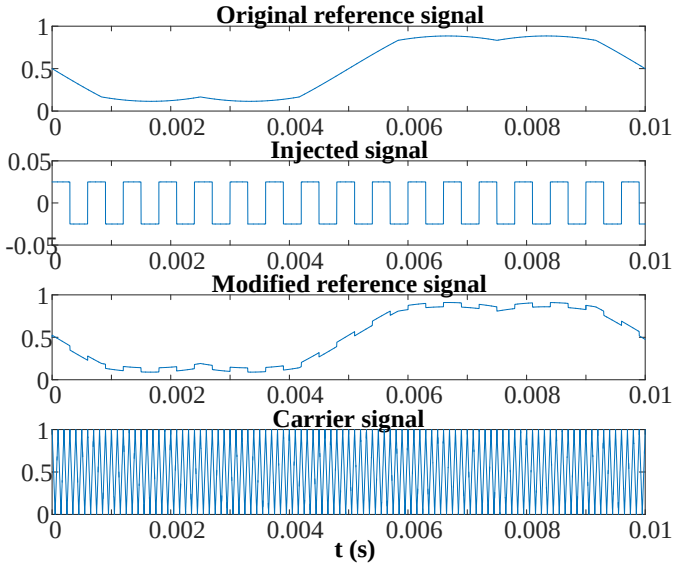

Fig. 4-27 Modified SVPWM modulating signal with square wave signal injection

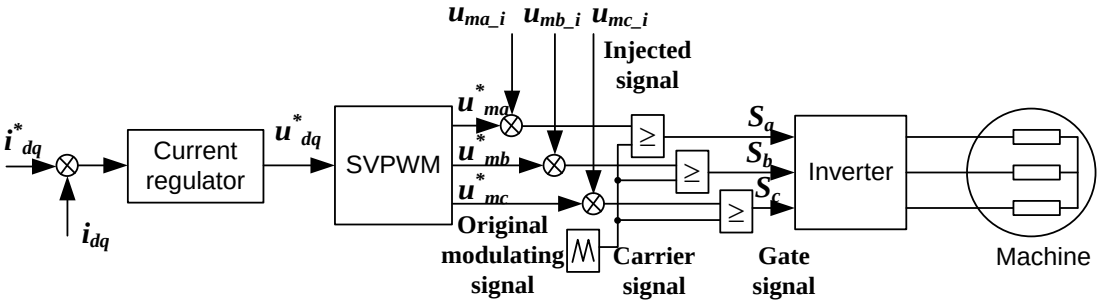

Fig. 4-28 Square wave signal injection implementation in the current control diagram

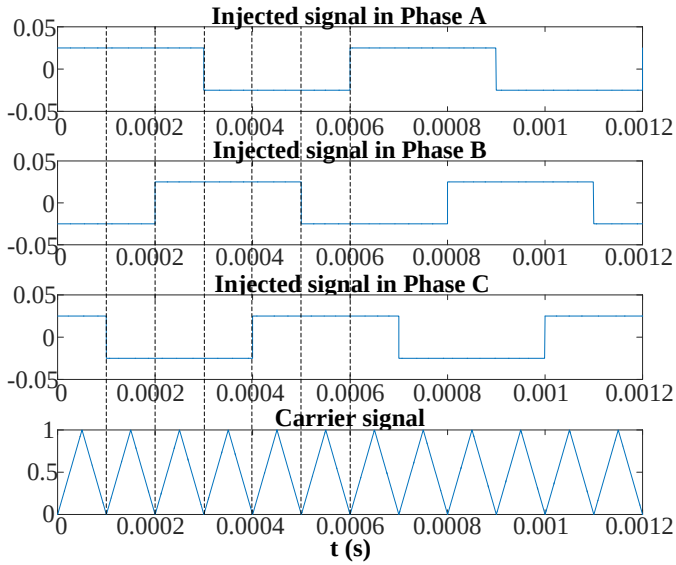

Fig. 4-29 The relationship between the injected square wave signals and the carrier signal

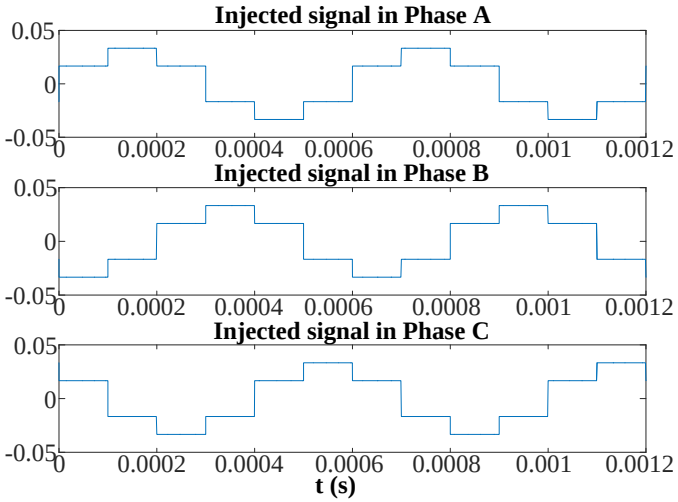

Fig. 4-30 The equivalent injected signal referred to the winding neutral point

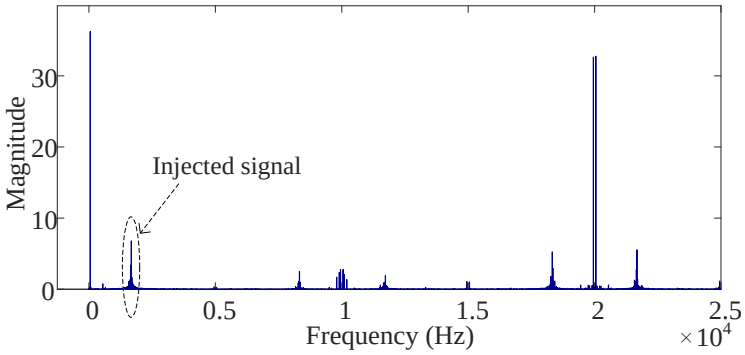

Fig. 4-31 Spectrum of the measurable transformed phase voltage with the resistor network

4.8.2 Theoretical analysis

The benefit of the signal injection is that the high frequency voltages can be applied independently from the fundamental frequency voltages. Thus, even in the fault conditions when the symmetry of the fundamental frequency voltages are broken, resulting in asymmetric SVPWM reference signals, the three phase injected frequency voltages are till symmetrical according to the balanced injected square wave signals. Because only one frequency component is to be examined, the injected voltages on the transformed phase voltages can be expressed as (4-22) with other frequency components neglected, where U_i and ω_i represent its amplitude and frequency.

$$\begin{cases} u_{am\_i} = U_i \sin \omega_i t \\ u_{bm\_i} = U_i \sin(\omega_i t - \dfrac{2\pi}{3}) \\ u_{cm\_i} = U_i \sin(\omega_i t - \dfrac{4\pi}{3}) \end{cases} \tag{4-22}$$

To analyse the three phase current signals in the IPM machine with saliency, the voltages are transformed into the rotating dq frame shown in (4-23) and applied to the voltage equations in the healthy condition given in (4-24). With the similar consideration for neglecting the resistive voltage drop and induced fundamental voltages, the current components at the injected frequency can be expressed as (4-25). Thereafter, the currents components are transformed back into the abc frame given in (4-26) which can be measured and compared directly in practice.

$$\begin{cases} u_{d\_i} = U_i \sin(\omega_i t - \omega_r t) \\ u_{q\_i} = -U_i \cos(\omega_i t - \omega_r t) \end{cases} \tag{4-23}$$

$$\begin{cases} u_d = R_s i_d + L_d \dfrac{di_d}{dt} - \omega_e L_q i_d \\ u_d = R_s i_d + L_q \dfrac{di_d}{dt} + \omega_e (L_d i_d + \lambda_{pm}) \end{cases} \tag{4-24}$$

$$\begin{cases} i_{d\_i} \approx \dfrac{u_{d\_i}}{j(\omega_i - \omega_r) L_d} \\ i_{q\_i} \approx \dfrac{u_{q\_i}}{j(\omega_i - \omega_r) L_q} \end{cases} \tag{4-25}$$

$$\begin{cases} i_{a\_i} = -\dfrac{U_i}{\omega_i - \omega_r} \left[\left(\dfrac{1}{2L_d} + \dfrac{1}{2L_q} \right) \cos \omega_i t + \left(\dfrac{1}{2L_d} - \dfrac{1}{2L_q} \right) \cos\left[(\omega_i - 2\omega_r) t \right] \right] \\ i_{b\_i} = -\dfrac{U_i}{\omega_i - \omega_r} \left[\left(\dfrac{1}{2L_d} + \dfrac{1}{2L_q} \right) \cos(\omega_i t - \dfrac{2\pi}{3}) + \left(\dfrac{1}{2L_d} - \dfrac{1}{2L_q} \right) \cos\left[(\omega_i - 2\omega_r) t + \dfrac{2\pi}{3} \right] \right] \\ i_{c\_i} = -\dfrac{U_i}{\omega_i - \omega_r} \left[\left(\dfrac{1}{2L_d} + \dfrac{1}{2L_q} \right) \cos(\omega_i t - \dfrac{4\pi}{3}) + \left(\dfrac{1}{2L_d} - \dfrac{1}{2L_q} \right) \cos\left[(\omega_i - 2\omega_r) t + \dfrac{4\pi}{3} \right] \right] \end{cases} \tag{4-26}$$

It should be noted that (4-26) also applies to the HRC fault condition, because the injected voltages remain symmetric and always satisfy (4-22). Hence, the corresponding

current components should be the same as that in the healthy condition, which should be symmetrical with identical amplitude and 120 degree phase difference to each other.

When a turn fault occurs, the dq axis voltage equations can be expressed in (4-27) according to the analysis in Chapter 2, assuming that the fault occurs in phase A. As the fault current also contains the injected frequency component, only the differential items are kept when rewriting the voltage equations at that frequency, shown in (4-28). The current components in the dq frames are solved in (4-29) and transformed back into the abc frame in (4-30). It can be seen that in addition to the symmetrical components shown in (4-26), the results also contain extra terms related to the fault current. It is evident that these extra terms are not symmetrical, so as the injected frequency current components in a turn fault condition.

$$\begin{cases} u_d^{TF} = R_s i_d^{TF} + L_d \dfrac{di_d^{TF}}{dt} - \omega_e L_q i_q^{TF} + \dfrac{2}{3}\mu\omega_e L_d i_f \sin\theta_e \\ \quad -\dfrac{2}{3}\mu\omega_e L_d \cos\theta_e \dfrac{di_f}{dt} - \dfrac{2}{3}\mu\omega_e L_q i_f \sin\theta_e - \dfrac{2}{3}\mu R i_f \cos\theta_e \\ u_q^{TF} = R_s i_q^{TF} + L_q \dfrac{di_q^{TF}}{dt} + \omega_e (L_d i_d^{TF} + \lambda_{pm}) + \dfrac{2}{3}\mu\omega_e L_q i_f \cos\theta_e \\ \quad +\dfrac{2}{3}\mu\omega_e L_q \sin\theta_e \dfrac{di_f}{dt} - \dfrac{2}{3}\mu\omega_e L_d i_f \sin\theta_e + \dfrac{2}{3}\mu R i_f \cos\theta_e \end{cases} \tag{4-27}$$

$$\begin{cases} u_{d\_i} = j\omega_i i_{d\_i}^{TF} L_d - \dfrac{2}{3} j\omega_i \mu\omega_e L_d \cos\theta_e i_{f\_i} \\ u_{q\_i} = j\omega_i i_{q\_i}^{TF} L_q + \dfrac{2}{3} j\omega_i \mu\omega_e L_q \sin\theta_e i_{f\_i} \end{cases} \tag{4-28}$$

$$\begin{cases} i_{d\_i}^{TF} = i_{d\_i} + \dfrac{2}{3}\mu\omega_e \cos\theta_e i_{f\_i} \\ i_{q\_i}^{TF} = i_{q\_i} - \dfrac{2}{3}\mu\omega_e \sin\theta_e i_{f\_i} \end{cases} \tag{4-29}$$

$$\begin{cases} i_{a\_i}^{TF} = i_{a\_i} + \mu\omega_e i_{f\_i} \\ i_{b\_i}^{TF} = i_{b\_i} - \dfrac{1}{2}\mu\omega_e i_{f\_i} \\ i_{c\_i}^{TF} = i_{c\_i} - \dfrac{1}{2}\mu\omega_e i_{f\_i} \end{cases} \tag{4-30}$$

Therefore, only by examining the three phase currents at the injected frequency, the turn fault can be exclusively detected out. Thus, the false turn fault alarm due to an

HRC fault should be avoided. However, since the currents at the injected frequency under an HRC fault are the same as those in healthy conditions, the detection of HRC fault cannot be realized. In order to detect the HRC fault, other winding fault detection techniques are needed, such as the current residual and the PWM ripple currents based methods.

It should be pointed out that the effectiveness of the method is limited by the maximum fundamental frequency. For the IPM machine under study, the fundamental frequency at the maximum speed of 19000 rpm is 950Hz, close to the injected frequency of 1.67 kHz. Fortunately, at high speeds the influence of an HRC fault on the standard deviation of the PWM ripple currents ratios diminishes as shown in Fig. 4-25, and hence the discrimination of the two faults with high frequency voltage injection is only required at low speeds, namely, below 1000 rpm for the machine under study.

4.8.3 Digital signal processing

Since the injected frequency is 1/6 of the sampling frequency of 10 kHz, the resultant frequency components can be extracted by a digital band pass filter. Considering the processing power in the micro controller, a digital infinite impulse response (IIR) filter is designed with the transfer function given in (4-31), and the filtered signal are obtained through (4-32), where z denotes the Z transformation operator, and n denotes the processing the n^{th} sampling time instant. The direct form II structure of the digital processing is shown in Fig. 4-32, where the transposed implementation can be represented clearly. The coefficients are calculated to yield the centre frequency at 1667Hz with a bandwidth 167Hz. The Bode plot of the filter is shown in Fig. 4-33.

The three identical digital filters are implemented for the three phase currents simultaneously, after which their RMS values are calculated separately according to (4-33). The interval of such discrete calculation is set to one electrical cycle, in order to minimize the ripples on the results. The whole signal processing is executed in the DSP controller, therefore there is no need of additional hardware, as long as the current transducers are available. Since the digital filters are more flexible to implement, it is more convenient to ensure their consistency, so the differences in three phase signal processing chains in healthy conditions are largely alleviated. Hence, the calibration

process is also simplified by the fact that only natural unbalance in the 3-phase windings and the tolerance in the current transducers needs to be considered.

$$\frac{Y(z)}{X(z)} = \frac{b(1)+b(2)z^{-1}+b(3)z^{-2}+b(4)z^{-3}+b(5)z^{-4}}{a(1)+a(2)z^{-1}+a(3)z^{-2}+a(4)z^{-3}+a(5)z^{-4}} \tag{4-31}$$

$$y(n) = \frac{1}{a(1)}\begin{bmatrix} b(1)x(n)+b(2)x(n-1)+b(3)x(n-2) \\ +b(4)x(n-3)+b(5)x(n-4)-a(2)y(n-1) \\ +a(3)y(n-2)+a(4)y(n-3)+a(5)y(n-4) \end{bmatrix} \tag{4-32}$$

where *x* and *X* denote the input, and *y* and *Y* denote the output of the digital IIR filter.

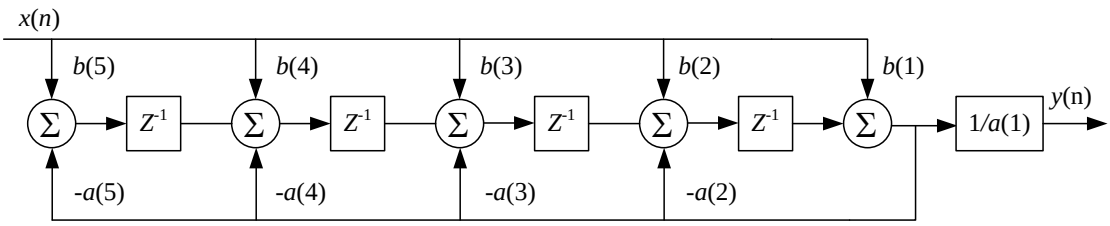

Fig. 4-32 Implementation diagram of the IIR filter

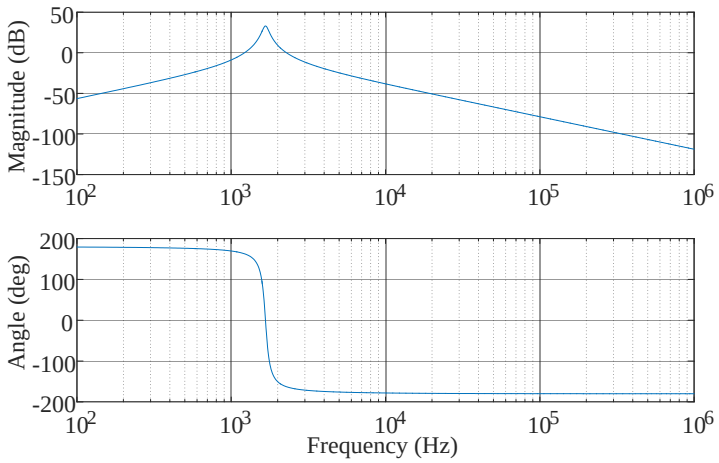

Fig. 4-33 The Bode plot of the digital bandpass filter

$$RMS(n) = \sqrt{\sum_{i=n-T_e}^{n}\left[y(i)\cdot y(i)\right]}$$
$$T_e = \left\lfloor \frac{2\pi}{\omega_e} \right\rfloor \tag{4-33}$$

4.8.4 Experimental results

The experiments are carried out on the 9-phase triple redundant fault tolerant machine as has been introduced in Chapter 2. The magnitude of the injected signal with

respect to the modulation index is set to be 0.05. Given the DC supply voltage is 270V, the magnitude of the actual injected voltage into the phase windings is approximately 8V. Since the injected high frequency voltages can be kept symmetrical, all the fault features will be reflected in the corresponding high frequency currents. As the consequence, only the high frequency components from the phase currents are examined, and no voltage transducers are needed in the tests. In the same way as the PWM ripple current based detection method, once the RMS values of the injected high frequency currents are obtained, their ratios and the standard deviation of the ratios are calculated for the fault detection.

The machine is firstly operating at 500rpm under the phase current of 50A with 1667Hz voltage signals injected when a single turn fault occurs at 0.11s. The responses of the relevant signals are shown in Fig. 4-34. The additional high frequency components can be seen in the dq voltages and phase currents. Because their amplitudes are very low, the machine operating performance is not affected significantly. After the occurrence of the turn fault in phase B, these high frequency components changes accordingly. The increase in the current ripples of phase B is illustrated in Fig. 4-34. The filtered high frequency components and their calculated RMS values are shown in Fig. 4-35. Since the sampling frequency is 6 times of the extracted signal frequency, the high frequency signals have a small distortion shown in the zoomed plot. However, this distortion does not affect the relationship among the three signals. It is evident that the magnitude of the high frequency current in phase B is the largest. This is due to the reduction of the high frequency impedance in the faulted phase being the largest. To avoid the dependence of the fault detection on operating conditions, the ratios and their standard deviation among the three RMS values are calculated, to determine the overall degree of asymmetry, shown in Fig. 4-35. The significant increase of the standard deviation can be used to detect the fault.

When the machine is operating at the same condition and the 0.1 Ω HRC fault is activated at 0.11s, similar features can be seen in the responses shown in Fig. 4-36 while the features in the high frequency components shown in Fig. 4-37 are quite different from those in the turn fault condition. When the HRC fault occurs, the high frequency currents remain the same as those in the healthy condition, so do their symmetrical property. This is because the invariance of the injected voltages and the high frequency impedance. As a result, the ratios stay at one, and the standard deviation

remains zero. Therefore, the standard deviation of the high frequency RMS current ratios is the exclusive indicator for the turn fault.

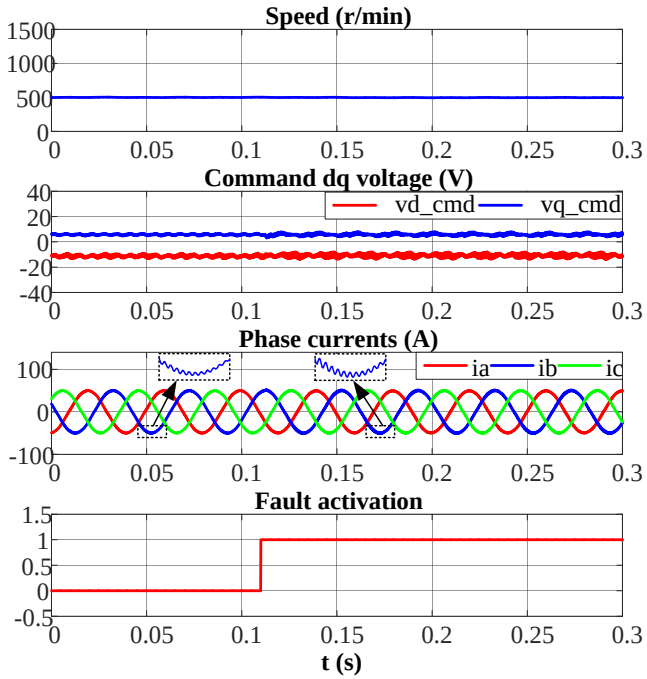

Fig. 4-34 Dq axis voltages and phase currents at 500rpm 50A in healthy and turn fault condition

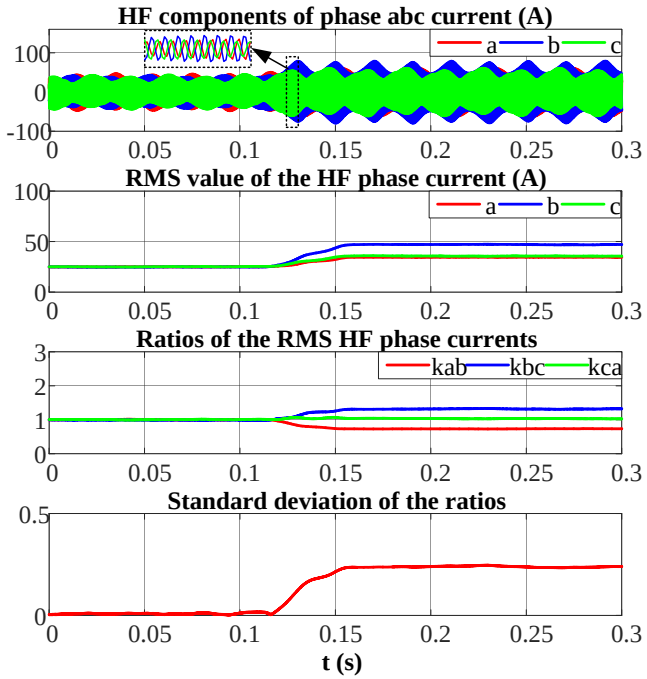

Fig. 4-35 The high frequency currents, RMS detector outputs, and their ratios and standard deviation in healthy and turn fault condition

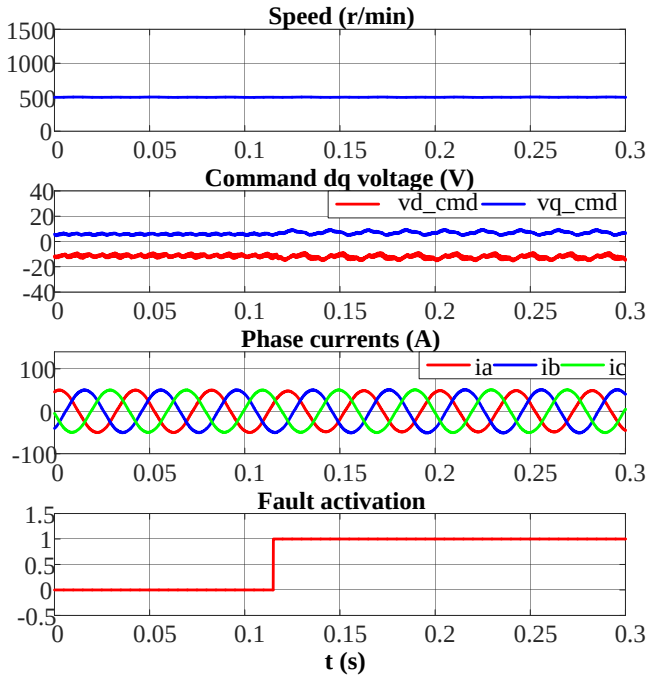

Fig. 4-36 Dq axis voltages and phase currents at 500rpm 50A in healthy and HRC fault condition

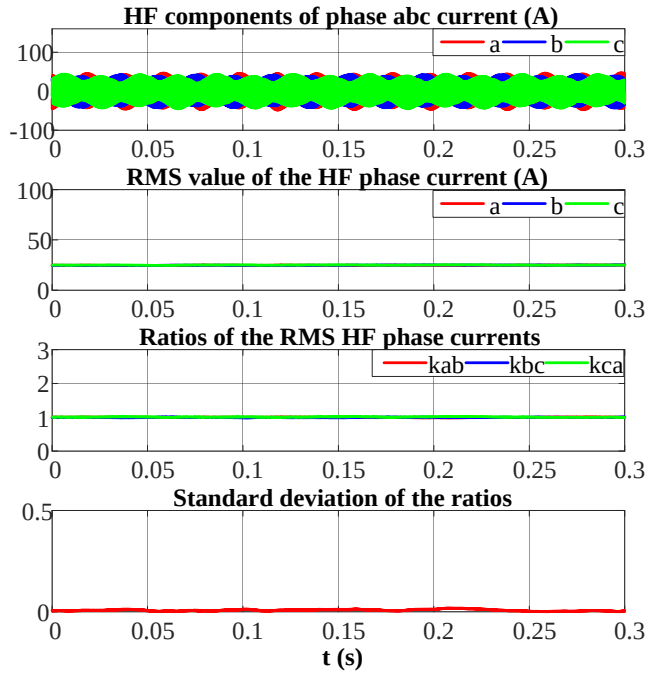

Fig. 4-37 The high frequency currents, RMS detector outputs, and their ratios and standard deviation in healthy and HRC fault condition

The variations of the fault indicator of the standard deviation under different operating speeds and currents in healthy and turn fault conditions are shown in Fig. 4-38. The fault indicators under these two conditions differ by large distance with great consistency independent of the operating conditions. Thus, a simple threshold can be defined to detect the turn fault exclusively.

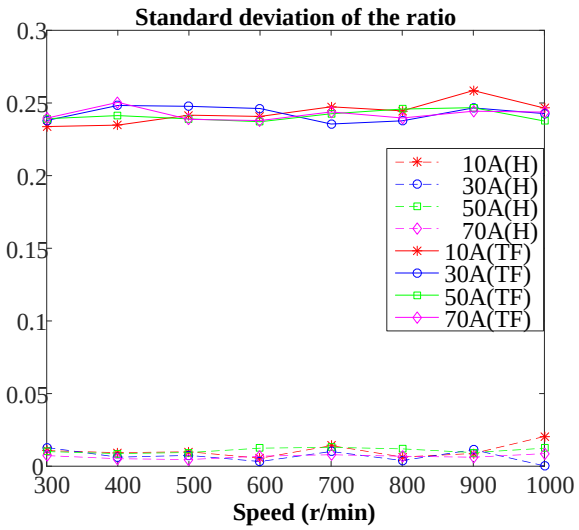

Fig. 4-38 Variations of fault indicators with speeds and currents in turn fault and healthy conditions

The impacts of current and speed changes on the fault indicator in healthy condition are tested and illustrated in Fig. 4-39 and Fig. 4-40, respectively. When the step change in current from 30A to 70A occurs at 0.2s, the high frequency components increase, because the inductance decreases due to the slight increase in saturation. Since the changes in the three phase high frequency currents are not exactly simultaneous, the ratios and standard deviation are slightly affected during the transient period. However, compared to the more significant increase of the indicator in the turn fault conditions in Fig. 4-35, such disturbance caused by the transient will not trigger false alarm if a proper threshold is determined. When the speed increases linearly with the acceleration of 1000 (r/min)/s in the healthy condition in Fig. 4-40, the results are not affected at all. A good isolation of the injected frequency signals from the fundamental signals guarantees that the fault indicator is immune to the transient states, avoiding any risk of false alarm. When the turn fault occurs at the same time when the operating condition changes as shown in Fig. 4-41 and Fig. 4-42, the fault detection is still effective. Thus, the reliability and robustness of the proposed fault indicator with the high frequency voltage injection for detecting the turn fault have been demonstrated.

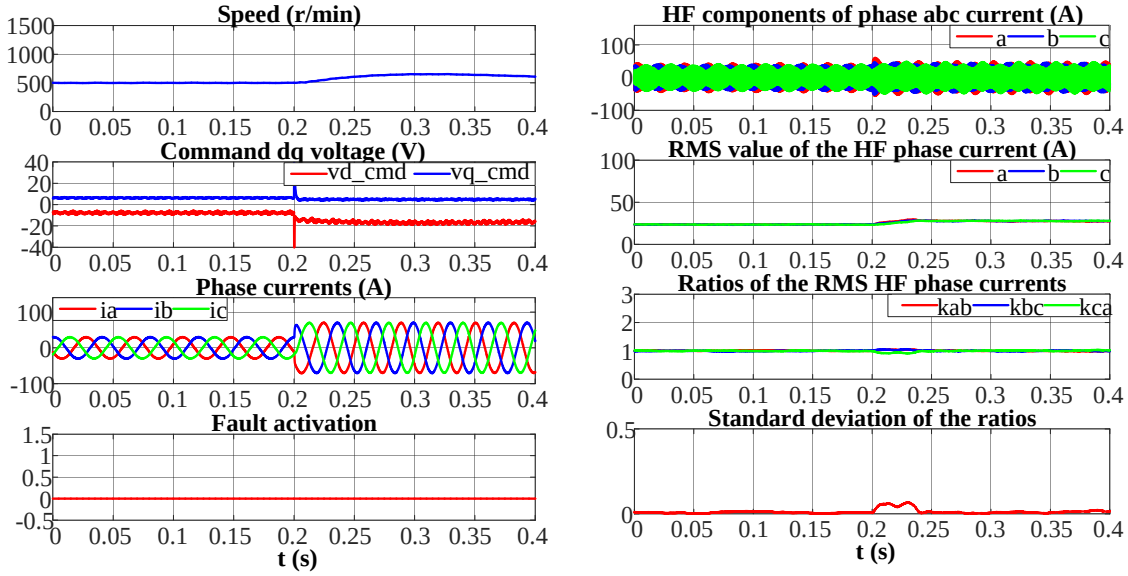

(a) (b)

Fig. 4-39 Healthy condition with current step change (a) speed, dq axis voltages and phase currents, (b) the high frequency currents, RMS detector outputs, and their ratios and standard deviation

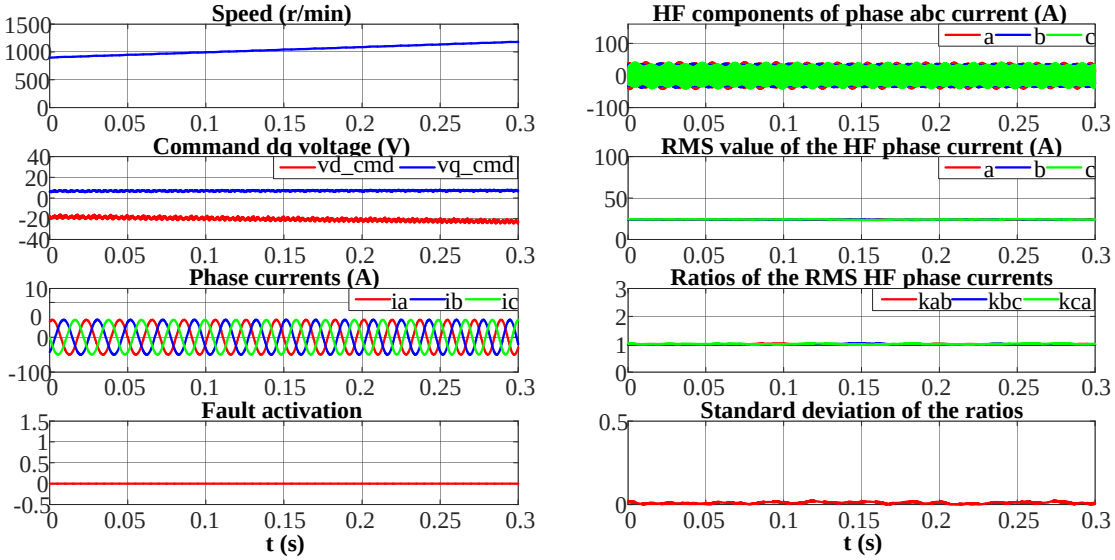

(a) (b)

Fig. 4-40 Healthy condition with increasing speed (a) speed, dq axis voltages and phase currents, (b) the high frequency currents, RMS detector outputs, and their ratios and standard deviation

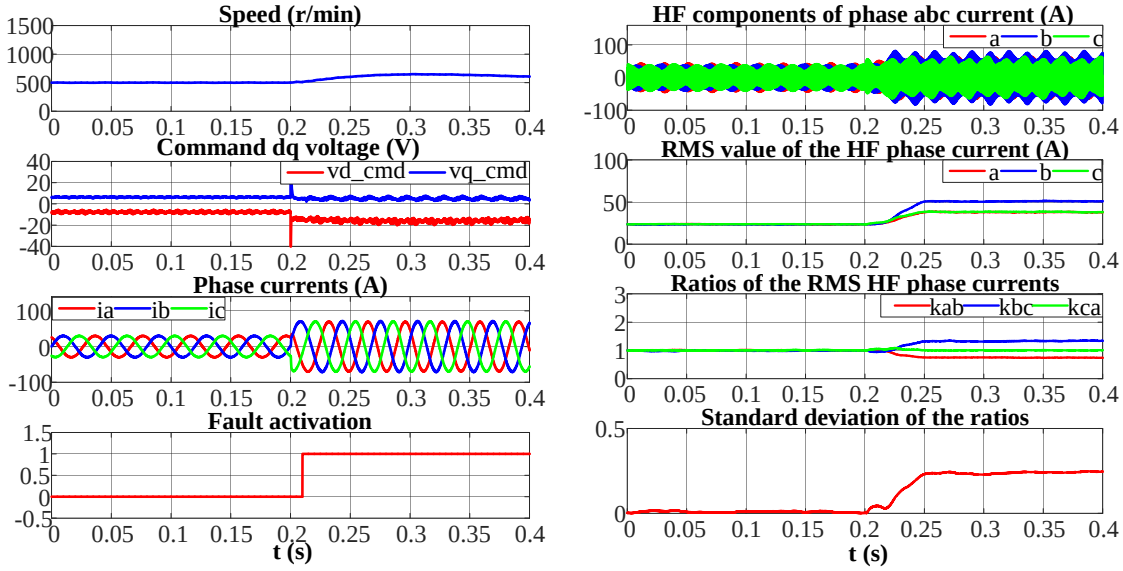

(a) (b)

Fig. 4-41 Turn fault condition with current step change (a) speed, dq axis voltages and phase currents, (b) the high frequency currents, RMS detector outputs, and their ratios and standard deviation

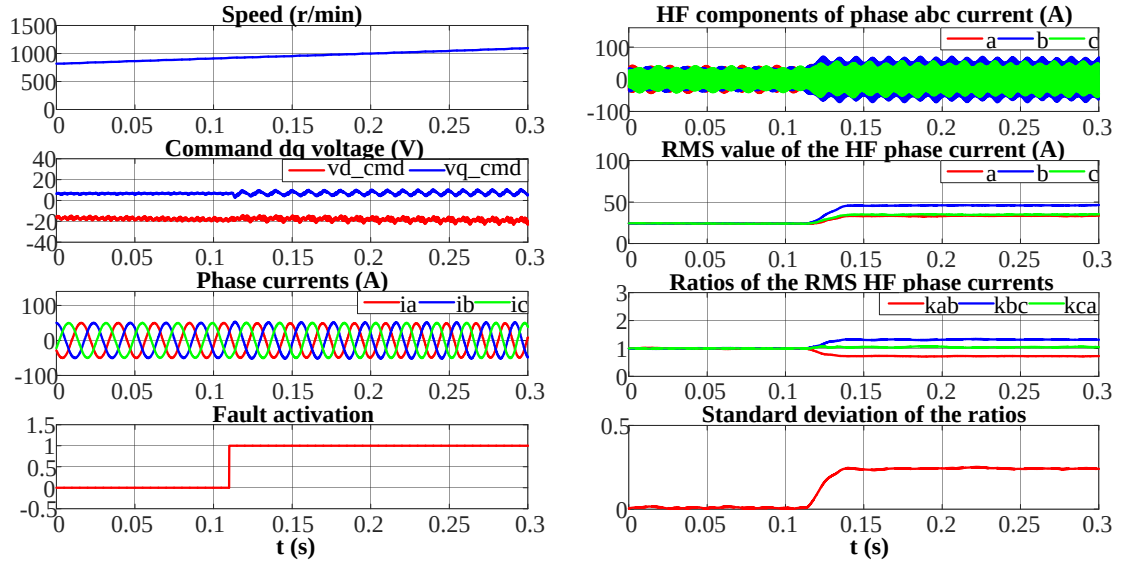

(a) (b)

Fig. 4-42 Turn fault condition with increasing speed (a) speed, dq axis voltages and phase currents, (b) the high frequency currents, RMS detector outputs, and their ratios and standard deviation

The turn fault detectability of this method at 500rpm under no load conditions are also tested. The speed, command dq voltages, three phase currents, together with the fault activation signal are shown in Fig. 4-43. The high frequency components in the phase currents, their RMS values, and the ratios among them are shown in Fig. 4-44. Since the injected high frequency voltages are independent from the operating conditions, the fault indicator of standard deviation of the RMS values ratios are also unaffected, and the turn fault can be detected successfully. The tests under no load

conditions are then conducted at different speeds, and the standard deviation as the fault indicator in healthy and turn fault conditions are shown in Fig. 4-45. Compared with the results under other operating conditions in Fig. 4-38, it is evident that the turn fault under no load conditions at all the tested speeds are also detectable with a common threshold.

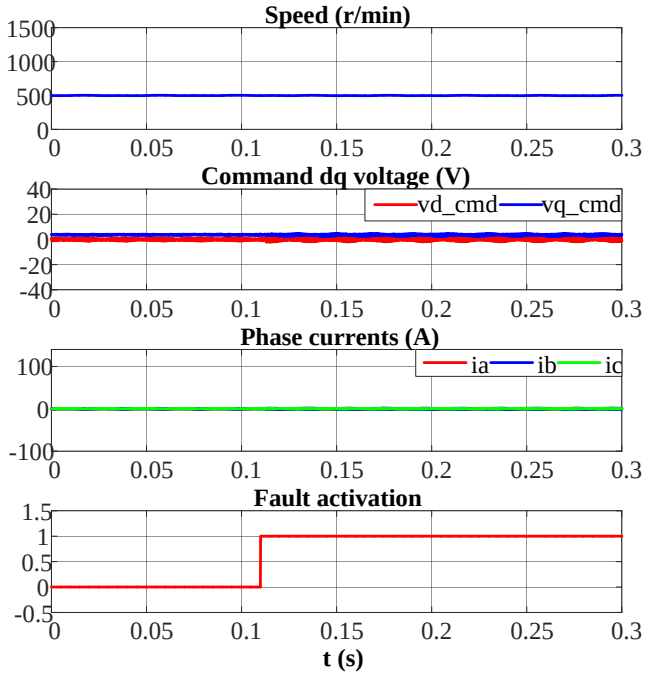

Fig. 4-43 Dq axis voltages and phase currents at 500rpm 0A in healthy and turn fault condition

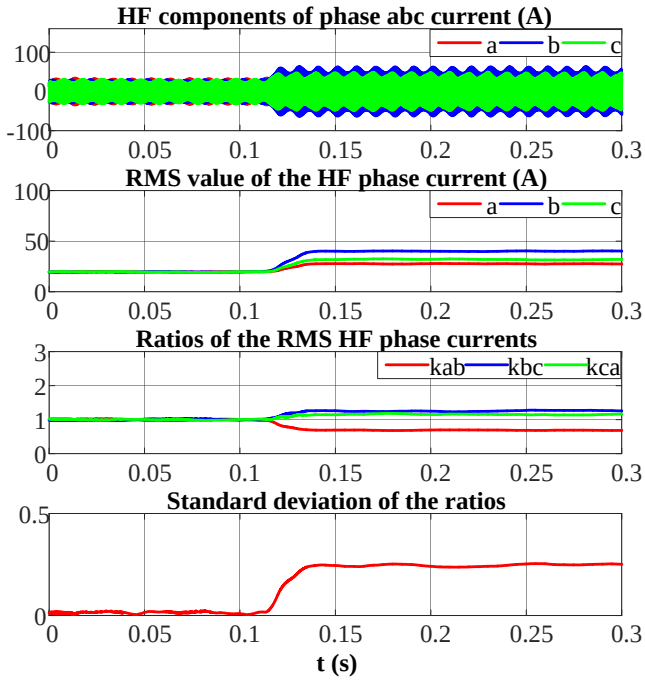

Fig. 4-44 The high frequency currents, RMS detector outputs, and their ratios and standard deviation in healthy and turn fault condition

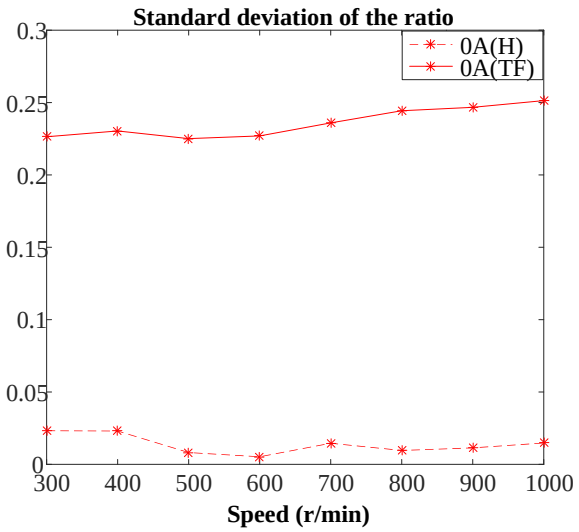

Fig. 4-45 Variations of fault indicators under no load conditions with different speeds

4.9 Conclusions and discussions

In this chapter, the impact of HRC faults on the turn fault detection techniques proposed in the previous chapters is firstly examined through experimental tests. It has been shown that when an HRC fault cannot be ruled out, these methods can only indicate the fault occurrence but fail to classify the fault types.

Therefore, the characteristic of the high frequency impedances are investigated. The analysis shows that due to the dominance of the inductance at high frequency, the high frequency impedance in each phase can be seen as identical in an HRC fault condition, which is significantly different from that in a turn fault. This feature is initially employed for the fault classification. The theoretical analysis and simulations have shown the validity on the SPM machine, with their mutual ratios and standard deviations calculated as the fault indicators. However, mathematical derivations also indicate that in the case of IPM machine, the difference between L_d and L_q results in the deviations among the calculated high frequency impedances due to the asymmetrical fundamental voltages caused by an HRC fault. The experiments on the 9-phase triple redundant IPM machine have shown such deviation of the fault indicator in an HRC fault condition. Although the two fault types may be separated under the tested fault severities and operating conditions, to guarantee the robust detection and classification, more sophisticated data-driven classification techniques need to be applied.

In addition to the investigation on the high frequency impedance, the high frequency voltage injection is also studied for fault detection. The high frequency voltages of the

square wave are injected into the modulating signals of the SVPWM control at 1667 Hz. The symmetry of the corresponding high frequency currents is examined, based on which a new turn fault indicator is proposed. The theoretical analysis and experiments have demonstrated the exclusivity for the detection of turn fault. However, if detection and classification of both faults are required in some applications, it should be combined with other winding fault detection methods. The fault indicator is insensitive to operating conditions due to its isolation from the fundamental components, which makes it easier to determine the threshold to separate the fault from health conditions. Similar to the PWM ripple current based method in Chapter 3, the robustness to the transient states is also preserved. The required 10 kHz sampling and data processing can be implemented in the DSP controller to extract the high frequency components and calculate the RMS values digitally with no additional hardware needed. Thus, this turn fault method is the most convenient to be implemented, although extra high frequency losses are introduced.

Both these methods can eliminate the impact of the HRC fault, through high frequency signal processing. They are also insensitive to the dynamic eccentricity, bearing fault and demagnetization which cause symmetric variations on the inductance and back EMF. However, the static eccentricity which also cause constant inductance asymmetry might also produce similar symptoms that the classification will be investigated in the future.

CHAPTER 5
Detection and Classification of Turn Fault and High Resistance Connection Fault based on Zero Sequence voltage

5.1 Introduction

The phase currents and voltages have been extensively analysed and explored for developing fault detection algorithms employing either the fundamental components as described in Chapter 2 or the high frequency components from PWM switching or signal injection in Chapter 4. All these methods are capable of detecting the asymmetry introduced by the winding faults, and are applicable in both transient and steady states. While it is difficult to distinguish the turn fault and the HRC fault by the fundamental components, it is much easier when high frequency components are utilized. However, the foregoing high frequency signals based detection and classification algorithms still have some limitations. On one hand, the high frequency impedance and currents from the switching harmonics based method is sensitive to the operating condition and fault severity in an IPM machine, thus it needs further data driven based classification techniques which increases the complexity of diagnosis. Also, the detection of HRC fault at higher speed is still a problem. On the other hand, the high frequency voltage injection based method is independent from the operating condition, but unable to detect the HRC fault. Thus, other fundamental components based methods are required to achieve both detection and classification.

In addition to the signatures extracted from the phase currents and voltages, those from zero sequence voltage or current have also been researched for winding fault detection. The asymmetries in the phase impedances of the machine can be caused by the faults in the stator windings, and increase the zero sequence voltage components. The zero sequence voltage is compared with stator currents in [135][58][127] for inter-turn fault detection, and it has shown that zero sequence voltage based methods usually yield more accurate and reliable results than those obtained by analysing the third harmonic amplitude of the stator currents. Different winding configurations are analysed and tested in [67], and the zero sequence voltage can be monitored for detecting the inter-turn faults in all the analysed winding configurations. The use of the

zero sequence voltage for fault detection in both line-fed and inverter-fed induction machines, has been discussed in [136]. It is shown that the measured zero sequence voltage contains reliable information independent of operating conditions or imbalances in the supply voltages. In [126], the fundamental component of zero sequence voltage is also effective for the diagnosis of HRC fault in a nine-phase flux-switching permanent-magnet (FSPM) machine. While most papers simply detect either a turn fault or an HRC fault separately, the classification of the fault types remains a problem since both of them give rise to the zero sequence voltage. The detection and classification of the two faults by using both zero sequence voltage and phase currents is proposed in [33]. The phase angle of the zero sequence voltage is compared in two fault conditions, but is not always sufficient for the fault classification.

From Chapter 4, it has been known that apart from the phase differences caused by the turn fault and HRC fault, the difference in the phase impedances at high frequency is more significant. Therefore, this chapter makes use of both the fundamental and high frequency components of the zero sequence voltage to realise the detection and classification of turn fault and HRC fault in permanent magnet machines. Fault indicators are defined and both simulations and experiments have been conducted to validate the effectiveness of this method.

5.2 Fault feature analysis

5.2.1 Zero sequence voltage measurement

The neutral point of machine's three phase windings is usually not connected to the reference ground, and its potential is floating when the machine is operating. In a healthy and balanced machine, the voltage between the neutral point *n* and the ground *o*, as shown in Fig. 5-1, only contains the 3rd harmonic and its integer multiples which come from the back electromagnetic force (EMF), and the high frequency components caused by the SVPWM switching in the inverter. In fault conditions, the symmetry is broken, thus, the 1st (fundamental) harmonic appears, and can be used for the detection. The high frequency components also change due to the parameters variation of the machine. To extract such variations only, the initial high frequency components from the inverter need to be eliminated, and an artificial neutral point *m* that provides the same potential as the neutral point in healthy conditions is created by a resistor network with identical resistance, as shown in Fig. 5-1.

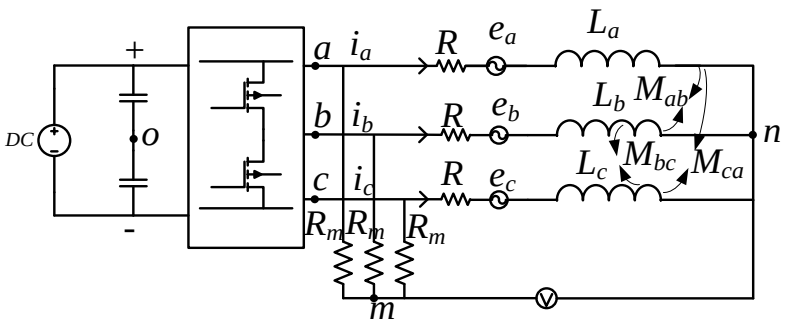

Fig. 5-1 Artificial neutral point and measurement of zero sequence voltage

According to the Kirchhoff's current law, the sum of currents through the wye-connected resistor network is zero, shown in (5-1). Thus, the voltage between the artificial neutral point *m* and the phase winding neutral point *n* can be obtained in (5-2). Therefore, the zero sequence voltage of the three phase windings can be measured by a voltage transducer over these two points.

$$\frac{u_{an}-u_{mn}}{R_m}+\frac{u_{bn}-u_{mn}}{R_m}+\frac{u_{cn}-u_{mn}}{R_m}=0 \tag{5-1}$$

$$u_{mn}=\frac{u_{an}+u_{bn}+u_{cn}}{3} \tag{5-2}$$

5.2.2 Healthy conditions

The equivalent circuit of a PM machine in healthy conditions is illustrated in Fig. 5-1. Thus, the three phase voltage equations can be expressed in (5-3).

$$\begin{cases} u_{an}=Ri_a+\dfrac{d(L_a i_a)}{dt}+\dfrac{d(M_{ab}i_b)}{dt}+\dfrac{d(M_{ac}i_c)}{dt}+e_a \\ u_{bn}=Ri_b+\dfrac{d(L_b i_b)}{dt}+\dfrac{d(M_{ab}i_a)}{dt}+\dfrac{d(M_{bc}i_c)}{dt}+e_b \\ u_{cn}=Ri_c+\dfrac{d(L_c i_c)}{dt}+\dfrac{d(M_{ac}i_a)}{dt}+\dfrac{d(M_{bc}i_b)}{dt}+e_c \end{cases} \tag{5-3}$$

where u_{an}, u_{bn}, u_{cn} are the phase voltages. i_a, i_b, i_c are the phase currents. e_a, e_b, e_c are the three phase back EMFs. R is the winding resistance. L_a, L_b, L_c, M_{ab}, M_{ac}, M_{bc} are the self- and mutual- inductances, and they can be expressed in (5-4) for interior permanent magnet (IPM) machines considering the rotor saliency, as has been explained in Chapter 2 for the purpose of analytical derivation. Thus, the relationships among the inductances can be written in (5-5).

$$\begin{cases} L_a = L_{ls} + L_{am} \approx L_{ls} + L_\Sigma - L_\Delta \cos(2\omega_e t) \\ L_b = L_{ls} + L_{bm} \approx L_{ls} + L_\Sigma - L_\Delta \cos(2\omega_e t - \frac{4\pi}{3}) \\ L_c = L_{ls} + L_{cm} \approx L_{ls} + L_\Sigma - L_\Delta \cos(2\omega_e t - \frac{2\pi}{3}) \\ M_{ab} = M_{ba} \approx -\frac{1}{2} L_\Sigma - L_\Delta \cos(2\omega_e t - \frac{2\pi}{3}) \\ M_{bc} = M_{cb} \approx -\frac{1}{2} L_\Sigma - L_\Delta \cos(2\omega_e t) \\ M_{ca} = M_{ac} \approx -\frac{1}{2} L_\Sigma - L_\Delta \cos(2\omega_e t - \frac{4\pi}{3}) \end{cases} \quad (5\text{-}4)$$

$$L_a + M_{ab} + M_{ac} \approx L_b + M_{ba} + M_{bc} \approx L_c + M_{ca} + M_{cb} \quad (5\text{-}5)$$

where ω_e is electrical angular speed. L_{ls} represents the leakage inductance, L_Σ the component of the inductances that is independent of rotor position and L_Δ the magnitude of a rotor position-dependent inductance resulting from rotor saliency. (5-4) and (5-5) are also applicable to surface-mounted PM machines when L_Δ=0.

In a wye-connected PMSM, (5-6) is satisfied according to the Kirchhoff's current law when the parasitic capacitance between the windings and the machine housing is neglected. This condition is generally valid because the leakage current through the parasitic capacitor is very small compared with the phase currents even at high frequency.

$$i_a + i_b + i_c = 0 \quad (5\text{-}6)$$

By adding the three phase voltages together and applying (5-4) and (5-6), then the zero sequence voltage, u_{mn}^H, in healthy operations can be obtained in (5-7), where the superscript 'H' denotes the healthy condition.

$$u_{mn}^H = e_0 = \frac{e_a + e_b + e_c}{3} = \sum_{v=3n, n=1,3,5} e_v \cos(v\theta - \theta_v) \quad (5\text{-}7)$$

It is shown that the zero sequence voltage in the healthy condition only contains the 3rd harmonic and its integer multiples of the permanent magnet back EMF. Since these harmonics are mainly at lower frequencies than the PWM switching frequency, the high frequency components can be assumed to be zero, as shown in (5-8), where the superscript 'HF' denotes the high frequency component.

$$u_{mn\_HF}^{H} \approx 0 \tag{5-8}$$

5.2.3 Turn fault conditions

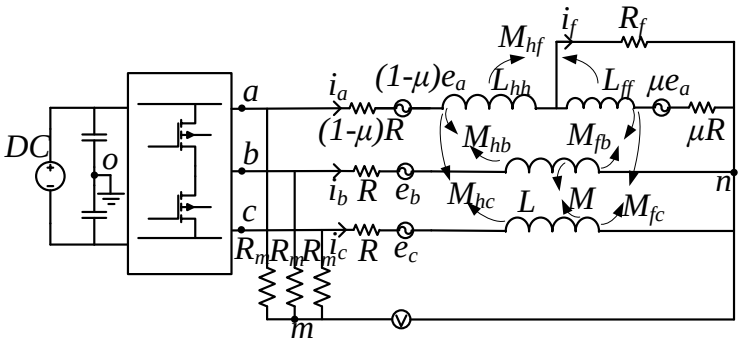

Fig. 5-2 Equivalent circuit in turn fault condition and the measurement of zero sequence voltage

The equivalent circuit of the phase windings in a turn fault condition is illustrated in Fig. 5-2 with all parameters defined, assuming that the fault occurs in phase A. Based on the detailed voltage equations in (2-11) and (2-12), the three phase voltages can be expressed in (5-9).

$$\begin{cases} u_{an} = Ri_a + \dfrac{d(L_a i_a)}{dt} + \dfrac{d(M_{ab} i_b)}{dt} + \dfrac{d(M_{ac} i_c)}{dt} + e_a - \dfrac{d\left[(M_{hf} + L_{ff})i_f\right]}{dt} - \mu R i_f \\ u_{bn} = Ri_b + \dfrac{d(L_b i_b)}{dt} + \dfrac{d(M_{ab} i_a)}{dt} + \dfrac{d(M_{bc} i_c)}{dt} + e_b - \dfrac{d(M_{fb} i_f)}{dt} \\ u_{cn} = Ri_c + \dfrac{d(L_c i_c)}{dt} + \dfrac{d(M_{ac} i_a)}{dt} + \dfrac{d(M_{bc} i_b)}{dt} + e_c - \dfrac{d(M_{fc} i_f)}{dt} \\ 0 = \mu R(i_a - i_f) + \dfrac{d(M_{hf} i_a)}{dt} + \dfrac{d\left[L_{ff}(i_a - i_f)\right]}{dt} + \dfrac{d(M_{fb} i_b)}{dt} + \dfrac{d(M_{fc} i_c)}{dt} + \mu e_a \end{cases} \tag{5-9}$$

Since the self-inductance is proportional to the square of the number of turns, and the mutual-inductance is to the product of the number of turns of both windings, the self- and mutual- inductances in turn fault conditions can be approximately expressed in (5-10) when the machine has one coil per phase [137]. For machines with more than one coil per phase, (5-10) is not strictly valid according to [106]. Nevertheless, for the sake of simplicity, the analysis of the fault behavior under such relation can still be useful for developing fault detection algorithm.

$$\begin{aligned} L_{hh} &= (1-\mu)^2 L_a \\ M_{hf} &= \mu(1-\mu)L_a \\ M_{hb} &= (1-\mu)M_{ab} \\ M_{hc} &= (1-\mu)M_{ac} \\ L_{ff} &= \mu^2 L_a \\ M_{fb} &= \mu M_{ab} \\ M_{fc} &= \mu M_{ac} \end{aligned} \tag{5-10}$$

In the same way, the zero sequence voltage can be solved by adding the three phase voltages in (5-9) together, and the result is given in (5-11), where the superscript 'TF' denotes turn fault condition. It is clear that apart from the same 3rd back- EMF harmonic and its integer multiples as those in the healthy condition the zero sequence voltage also contains additional term related to the fault current i_f. It can be inferred from the expressions in (5-9) that i_f is dependent on i_a, i_b, i_c, and the back EMF e_a. Thus, i_f mainly consists of the 1st (fundamental) and 3rd harmonics. Therefore, the zero sequence voltage in the turn fault contains a fundamental component, which constitutes the most significant difference from the healthy condition.

$$u_{mn}^{TF} = -\frac{1}{3}\mu(Ri_f + L_{ls}\frac{di_f}{dt}) + e_0 \tag{5-11}$$

The high frequency components in the phase currents due to SVPWM switching are also introduced to the fault current. Thus, the high frequency(switching) components of the zero sequence voltage are no longer zero, but can be expressed in (5-12), with the voltage across the resistance neglected.

$$u_{mn\_HF}^{TF} \approx \frac{1}{3}\mu L_{ls}\omega_{HF} i_{f\_HF} \tag{5-12}$$

5.2.4 High resistance connection fault conditions

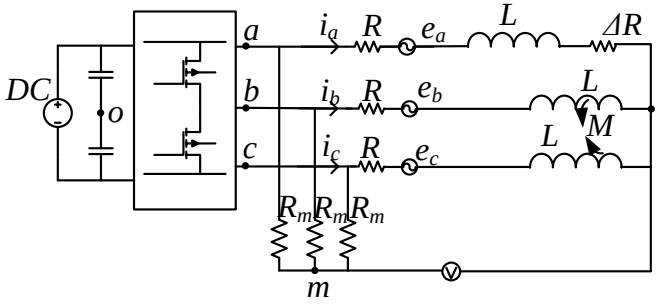

Fig. 5-3 Equivalent circuit in HRC fault condition and the measurement of zero sequence voltage

In an HRC fault condition, the machine windings can be emulated with an additional resistor ΔR connected to the faulted phase winding, as shown in Fig. 5-3, assuming the fault occurs in phase A. The phase voltage equations in the HRC condition can be expressed as (5-13).

$$\begin{cases} u_{an} = (R+\Delta R)i_a + \dfrac{d(L_a i_a)}{dt} + \dfrac{d(M_{ab} i_b)}{dt} + \dfrac{d(M_{ac} i_c)}{dt} + e_a \\ u_{bn} = Ri_b + \dfrac{d(L_b i_b)}{dt} + \dfrac{d(M_{ab} i_a)}{dt} + \dfrac{d(M_{bc} i_c)}{dt} + e_b \\ u_{cn} = Ri_c + \dfrac{d(L_c i_c)}{dt} + \dfrac{d(M_{ac} i_a)}{dt} + \dfrac{d(M_{bc} i_b)}{dt} + e_c \end{cases} \tag{5-13}$$

The zero sequence voltage can be derived and given in (5-14). Compared to the healthy condition, it contains an additional term related to the phase current and additional resistance. Further, the high frequency component of the zero sequence voltage can also be solved in (5-15).

$$u_{mn}^{HRC} = \frac{1}{3}\Delta R i_a + e_0 \tag{5-14}$$

$$u_{mo\_HF}^{HRC} \approx \frac{1}{3}\Delta R i_{a\_HF} \tag{5-15}$$

5.3 Fault detection and classification

From the above analysis, it follows that the fundamental and high frequency components of the zero sequence voltage do not exist theoretically in healthy conditions, but both appear in turn fault or HRC fault conditions. Thus, the faults can be detected by employing either the fundamental or high frequency zero sequence voltage as indicators. For the classification of the two fault types, the significance of the high frequency components is analysed further.

The high frequency components of the zero sequence voltages originally come from the high frequency components of the inverter output voltages in the SVPWM control. And they are selected as the sideband harmonics around 20k Hz due to the higher significance when the switching frequency is 10k Hz, according to the previous chapters,

In order to minimize the high frequency zero sequence voltage's dependence on the high frequency inverter voltages, the ratio between the RMS values of them is defined as the high frequency components based fault indicator (FI_{HF}), as shown in (5-16). The

level of high frequency components of the inverter output voltages is determined by the modulation index, with the relationship shown in Fig. 5-4. This relationship can be obtained through a SIMULINK simulation with various modulation indexes, and fitted by a 5 order polynomial, as given in (5-17), where m_i denotes the modulation index. Hence, the defined fault indicator can be obtained once the modulation index is approximately calculated by the dq axis reference voltage and the dc bus voltage. Since the modulation index is directly related to the operating conditions, the dependence of the fault indicator on the operating conditions can also be reduced. Ideally, this high frequency based fault indicator is zero in healthy conditions in theory, shown in (5-18). In the turn fault and HRC fault conditions, the fault indicators are expressed in (5-19) and (5-20) separately, according to (5-12) and (5-15).

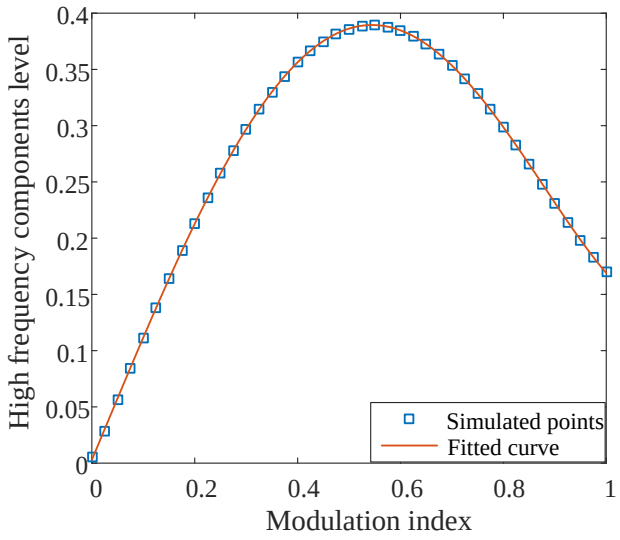

Fig. 5-4 The relationship between the high frequency components of the inverter output voltages and the modulation index

$$FI_{HF} = \frac{RMS(u_{mn\_HF})}{RMS(u_{inverter\_HF})} \tag{5-16}$$

$$RMS(u_{inverter\_HF}) = 0.5381m_i^{5} + 0.2165m_i^{4} - 1.8169m_i^{3} + 0.1364m_i^{2} + 1.092m_i + 0.003 \tag{5-17}$$

$$FI_{HF}^{H} = 0 \tag{5-18}$$

$$FI_{HF}^{TF} = \frac{1}{3}\mu L_{ls}\omega \frac{RMS(i_{f\_HF})}{RMS(u_{inverter\_HF})} \tag{5-19}$$

$$FI_{HF}^{HRC} = \frac{1}{3}\Delta R \frac{RMS(i_{a\_HF})}{RMS(u_{inverter\_HF})} \tag{5-20}$$

To roughly compare the fault indicators in the two fault conditions, the following representative assumptions are made with reference to the 9-phase triple redundant IPM machine described previously. In a turn fault condition, the leakage inductance L_{ls} is assumed to be 1.37e-5 H, the turn fault ratio μ is 0.0625 for a single turn fault, and the RMS value of the high frequency fault current is 8~10 times larger than that of the high frequency phase current based on initial experimental data. In an HRC fault condition, the additional resistance is assumed to be 0.1 Ω, which is 4 times the phase resistance. With these parameters, the fault indicator in the turn fault condition can be approximately 10 times larger than that in the HRC fault. As a result, this fault indicator is much more sensitive to the turn fault, which can be detected exclusively. Thus, the two faults can be distinguished. As for the detection of the HRC fault, the high frequency based fault indicator is not suitable any more due to very low sensitivity and potential susceptibility to noises.

In order to detect the HRC fault, the fundamental components of the zero sequence voltage and phase current are used. Their amplitudes are extracted, whose ratio is defined as the fundamental frequency based fault indicator (FI_{FUN}), given in (5-21). A number of methods, such as FFT, extended Kalman filter (EKF), or order tracking techniques can be used for the extraction of magnitudes. The fault indicator in healthy and the HRC fault conditions are expressed in (5-22) and (5-23) respectively, and by comparing with a predefined threshold, the HRC fault can be detected.

$$FI_{FUN} = \frac{\left|u_{mo\_FUN}\right|}{\left|i_{a\_FUN}\right|} \tag{5-21}$$

$$FI_{FUN}^{H} = 0 \tag{5-22}$$

$$FI_{FUN}^{HRC} = \frac{1}{3}\Delta R \tag{5-23}$$

In summary, the features of the zero sequence voltage are compared in Table 5-1, according to the above analysis. It is seen that only high frequency components are sensitive to turn fault. Thus, a turn fault can be detected exclusively by employing the indicator defined in (5-16). While the fundamental component is sensitive to both fault

types, the detection of HRC fault can also be done after the high frequency fault indicator is ruled out.

Table 5-1 Feature comparison of zero sequence voltage in healthy and fault conditions

Healthy condition	High resistance fault	Turn fault
No fundamental component	Fundamental component	Fundamental component
No high frequency components	Weak high frequency components	Strong high frequency components

With the two fault indicators defined in (5-16) and (5-21) to minimize the impact from the operating condition, the whole detection and classification procedure is illustrated in Fig. 5-5. First, the high frequency based fault indicator is used to diagnose whether a turn fault occurs with swift response. If that indicator is negative, the fundamental frequency based fault indicator is employed to judge whether high resistance fault occurs or the machine is operating in healthy condition.

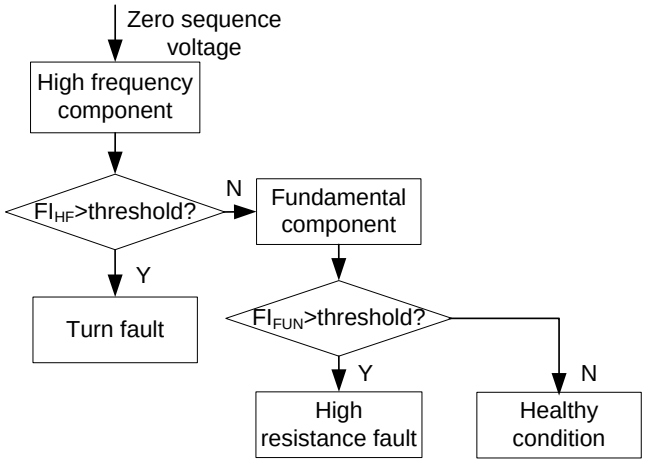

Fig. 5-5 Fault detection and classification steps

5.4 Simulation study

The machine model in the MATLAB/SIMULINK is established based the 4-D map depicting the relationships among the dq axis flux linkages, currents, fault flux linkages and fault current, which are extracted from the extensive finite element simulations, as has been proposed in [27]. The high-fidelity model can better represent the behaviour of the machine with the consideration of saturation and spatial harmonics.

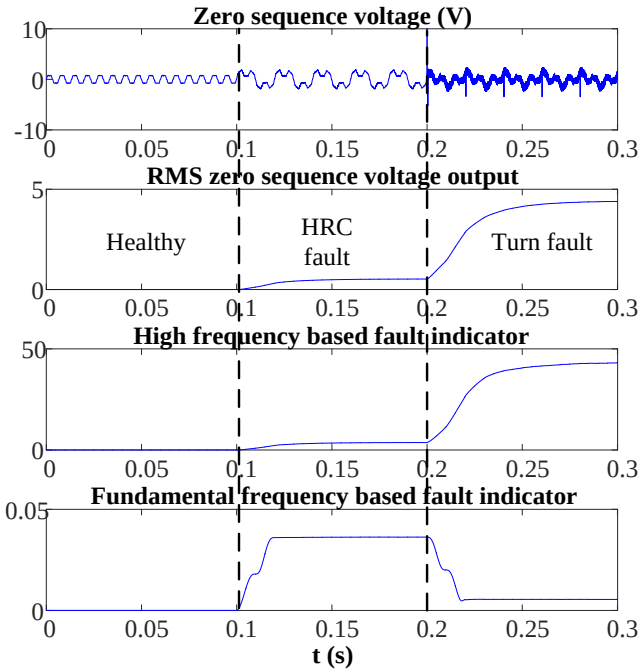

Fig. 5-6 Simulation result at steady state in healthy and fault conditions

The machine is operating at 1000rpm with 50A phase current. In order to better illustrate the difference of the two fault indicators in different fault conditions, both of them are examined in a single simulation. From 0s to 0.1s, the machine is operating in healthy condition. From 0.1s to 0.2s, it is operating in the 0.1Ω HRC fault condition. Then from 0.2s to 0.3s, the HRC fault is removed, and one turn short circuited fault is activated. The simulation results are shown in Fig. 5-6. It is clear that in healthy conditions, the zero sequence voltage only contains the 3rd and its integer multiple harmonics from the back EMF. When fault occurs after 0.1s, fundamental component appears in both fault conditions. Also, it is apparent that when turn fault occurs from 0.2s, a significant amount of high frequency components emerge due to the switching sideband harmonics. Thus, the utilization of these features should be competent for the fault detection and classification. The high frequency components are extracted by the band pass filter and an RMS detector is used to obtain the significance as have been explained before. The amplitude of the fundamental component is calculated by the angular integration with a 2π window length. After the high frequency voltages are estimated by the modulation index, the two indicators can be acquired shown in Fig. 5-6, according to (5-16) and (5-21). It is evident that the high frequency based fault indicator in turn fault condition is significantly larger than that in healthy and the HRC fault conditions. However, the deviation of that indicator in HRC fault condition from health condition is very small. Since the high frequency based fault indicator is much more

sensitive to the turn fault, it is only suitable for the turn fault detection. The fundamental frequency based fault indicator is also compared and both faults cause this indicator deviate from 0. Hence the HRC fault detection based on it should rest with the turn fault detection result.

5.5 Experimental results

Experiments are carried out on the 9-phase triple redundant fault tolerant permanent magnet machine as introduced in the previous chapters. The phase winding neutral point is led out, and the analogue circuit board shown in Fig. 5-7 is designed and built to realise the measurement and initial signal processing. The resistor network is mounted to create the artificial neutral point, so that the zero sequence voltage can be measured. The outputs of the circuit board for the tests of this method are the zero sequence voltage and the RMS value of its high frequency components around 20k Hz. The phase currents and their high frequency RMS values are also measured only for observation. The measurement results are captured and recorded by the multichannel YOKOGAWA oscilloscope.

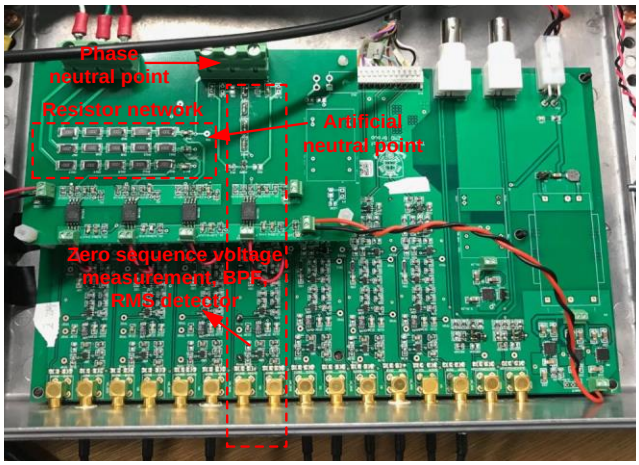

Fig. 5-7 The designed signal processing analogue circuit board for fault detection

5.5.1 Fault detection and classification

When a single turn fault occurs at the operating condition of 1000rpm with 50A phase current in steady state, the measurements are shown in Fig. 5-8. The fault current is measured to mark the fault occurrence. The distortion on the three phase current is hardly seen thanks to the PI regulated current control. The fundamental component emerges instantly in the measured zero sequence voltage when turn fault occurs. However, the increase of the examined high frequency components is not indicated

directly from the waveform due to the high frequency noises. The spectrum of the zero sequence voltage in healthy and fault conditions are obtained through FFT analysis and are shown in Fig. 5-9 and Fig. 5-10 respectively. It is clear that the switching sideband harmonics around 20k Hz which are extracted through the BPFs in this method stay low in healthy condition, but present prominent increase when turn fault occurs.

By exporting the measurement into MATLAB and apply the same transfer function of the bandpass filter in the analogue circuit, the switching sideband harmonics around 20k Hz are separated, shown in Fig. 5-11. It is evident that their magnitudes are low in the healthy condition, but rises significantly in the turn fault condition. Correspondingly, the measured RMS detector output of the high frequency components in Fig. 5-8 also increases largely. The lower frequency components can also be analysed through a low pass filter. It shows that the fundamental frequency component is hardly seen in healthy conditions, where only 3rd and higher order harmonics exist, but increases when turn fault occurs. The calculation process of the high frequency based fault indicator is shown in Fig. 5-12. The RMS detector output can be directly measured from the signal processing PCB board. The modulation index from the controller can be filtered digitally using the same transfer function of the low pass filter inside the RMS detector to synchronise their response. Then by applying the 5-order polynomial shown in (5-17) to estimate the high frequency components level of the inverter outputs. Finally, the high frequency based fault indicator is obtained.

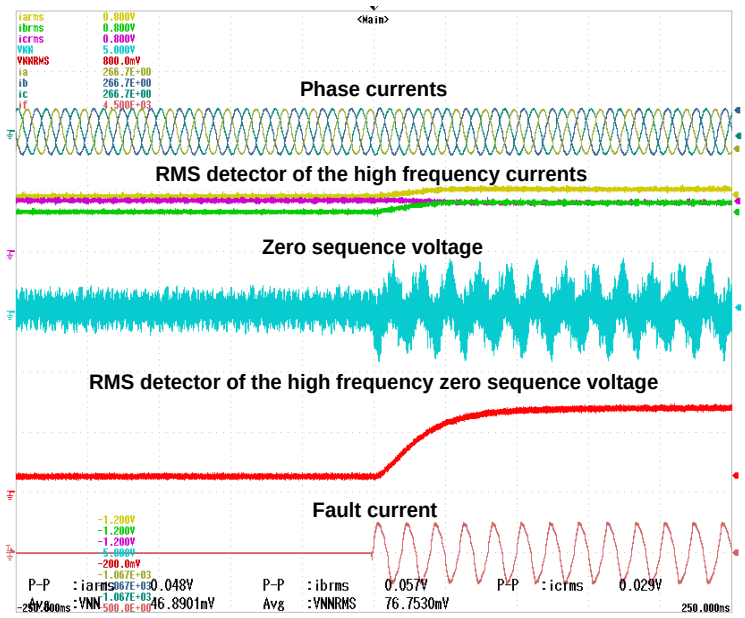

Fig. 5-8 Measured currents, zero sequence voltage and other outputs from the signal processing board when turn fault occurs

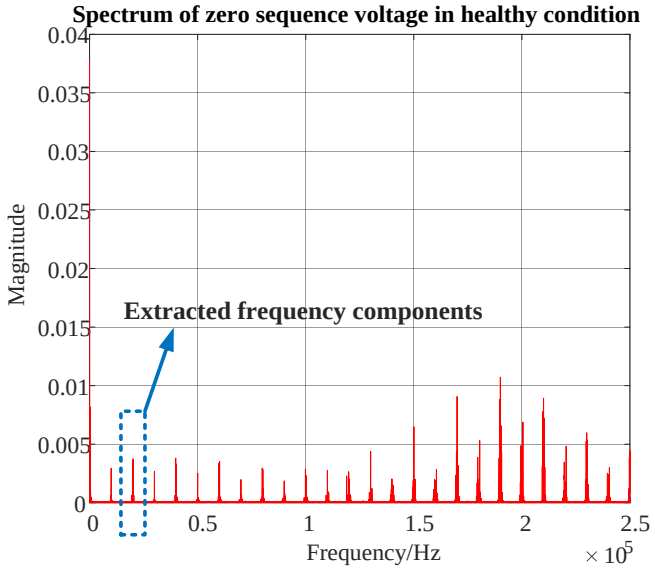

Fig. 5-9 Spectrum of zero sequence voltage in healthy condition

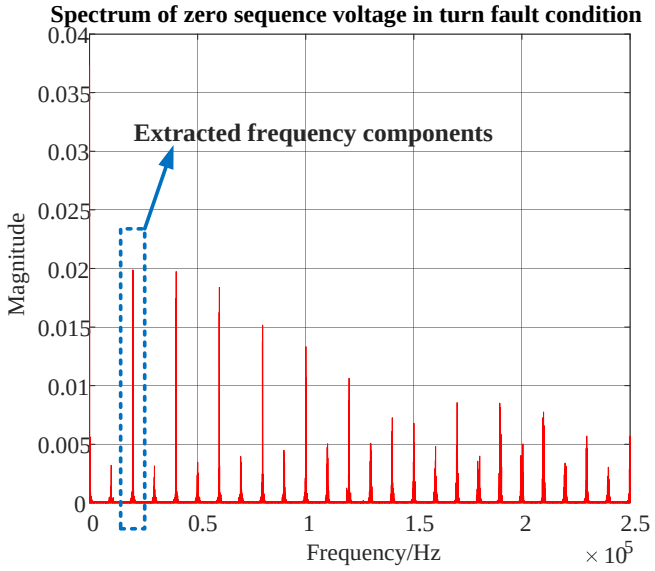

Fig. 5-10 Spectrum of zero sequence voltage in turn fault condition

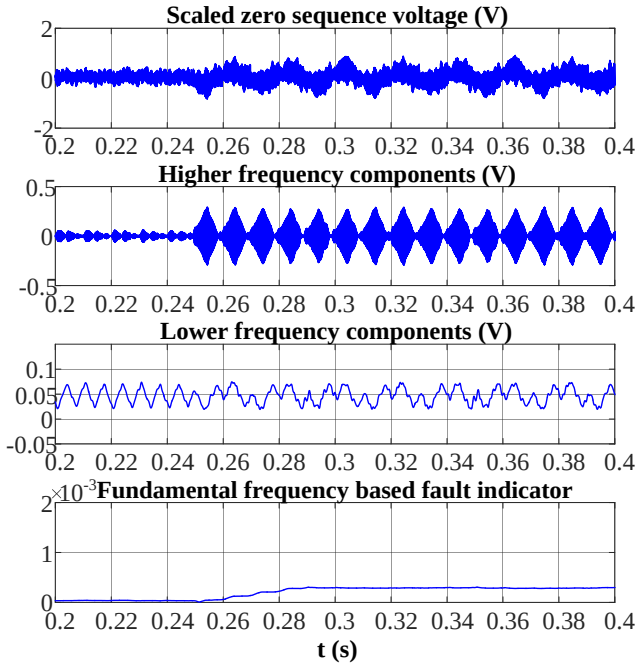

Fig. 5-11. The higher and lower frequency components of the zero sequence voltage when turn fault occurs

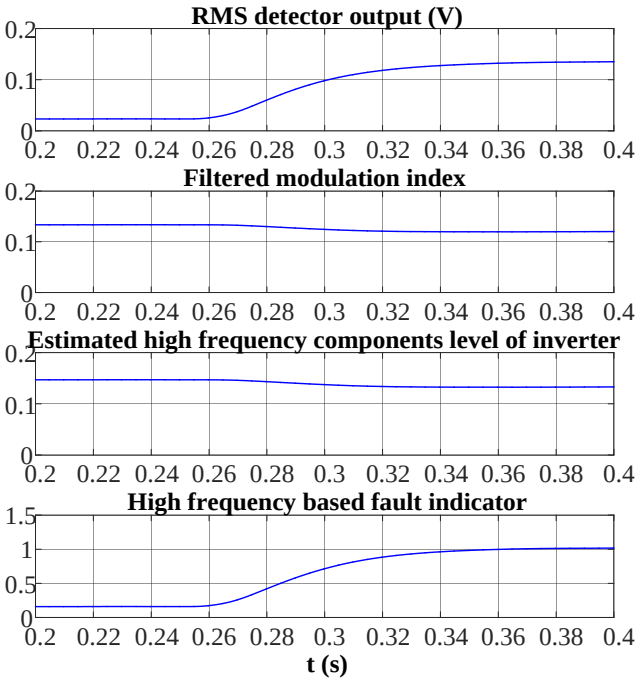

Fig. 5-12. The calculation of the high frequency based fault indicator when turn fault occurs

Under the same operating condition, a 0.1Ω additional resistor formed HRC fault is activated, with the measurements shown in Fig. 5-13. The fault current is the current flowing through one of the parallel connected resistor shown in Fig. 4-18 to denote the onset of the HRC fault, as explained in Chapter 4. Since the key features in the zero sequence voltage are contaminated by noise, the frequency components under evaluation are also examined through the MATLAB signal processing, shown in Fig.

5-14. As can be observed, the filtered high frequency components are very low and hardly increase in the HRC fault condition. As the result, the directly measured RMS value of the switching sideband harmonics around 20k Hz shown in Fig. 5-13 also presents little change. The high frequency based fault indicator is calculated in Fig. 5-15 after the modulation index is obtained. Comparing with the result in the turn fault condition, the high frequency components in the zero sequence voltage are much more sensitive to the turn fault, thus the high frequency based fault indicator can be employed for the exclusive turn fault detection. Since a steady increase also occurs on the fundamental frequency based fault indicator, it can be used for the HRC fault detection on condition that the detection result of the turn fault is negative. Due to gains and attenuations in both the analogue and digital signal processing chains, it is not equal but proportional to 1/3 of the additional resistance 0.1Ω as predicted in the theoretical analysis.

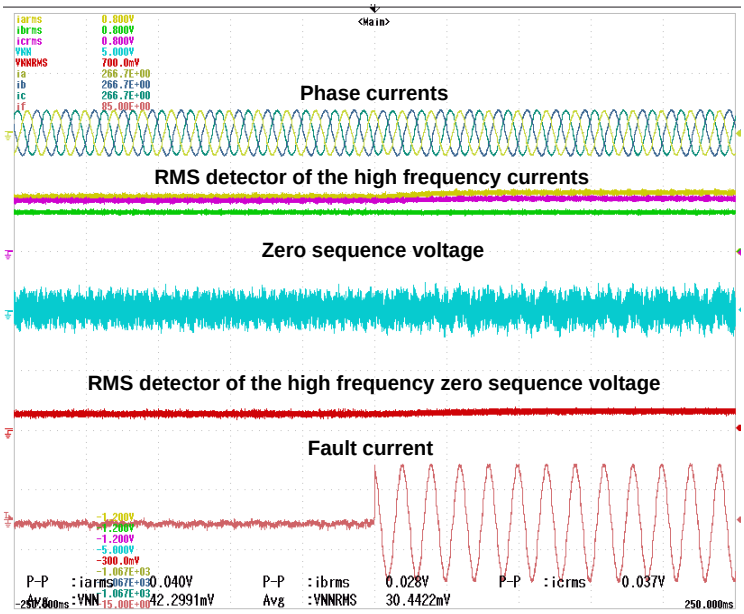

Fig. 5-13 Measured currents, zero sequence voltage and other outputs from the signal processing board when HRC fault occurs

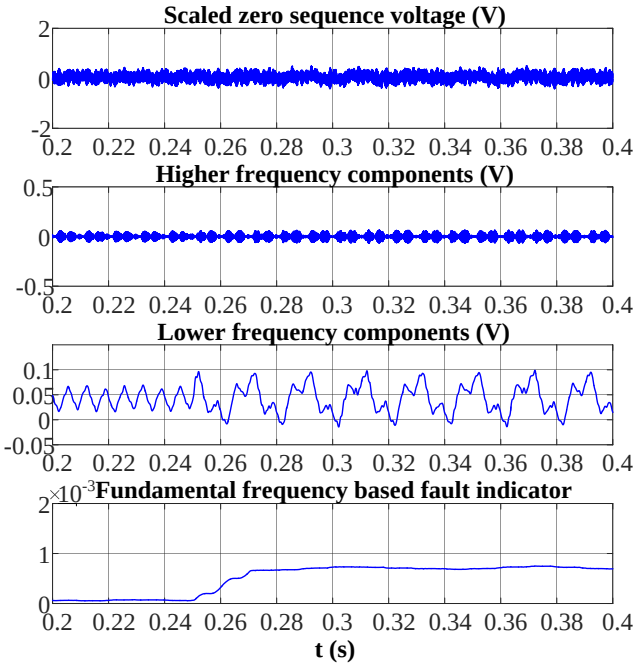

Fig. 5-14. The higher and lower frequency components of the zero sequence voltage when HRC fault occurs

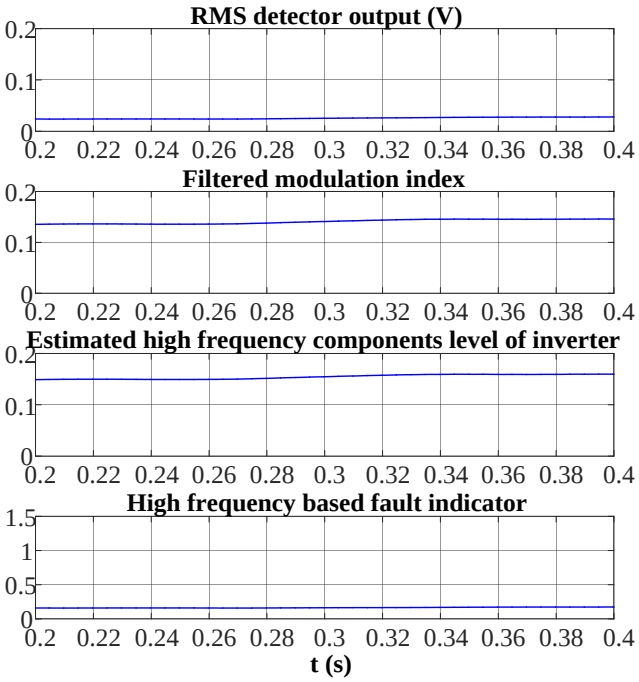

Fig. 5-15. The calculation of the high frequency based fault indicator when HRC fault occurs

5.5.2 Evaluation of the fault indicators

The RMS detector output of the measured high frequency zero sequence voltage in the healthy, turn fault and HRC fault conditions are compared at different speeds and currents in Fig. 5-16, which are denoted as ‘H’, ‘TF’, and ‘HRC’ respectively. It can be observed that the RMS detector output in healthy conditions is not zero but proportional

to the phase current and speed. This can be caused by the inherent small asymmetry in the high frequency phase impedances as well as unbalanced parasitic parameters in three phase inverter and PWM modulation process, which builds the connection between the high frequency components of zero sequence voltage and those of inverter output voltages. When the current or speed increases, the modulation indexes increase, then the high frequency components of inverter output voltages vary according to the relationship in Fig. 5-4, thereby, the high frequency zero sequence voltage also changes. Nevertheless the detector output in the HRC fault condition are very close to the values in the healthy conditions, both of which are much lower than those in the turn fault conditions. Although it is possible to define operating condition dependent thresholds to separate the turn fault condition by use this quantity alone, the process is not cost-effective in real applications.

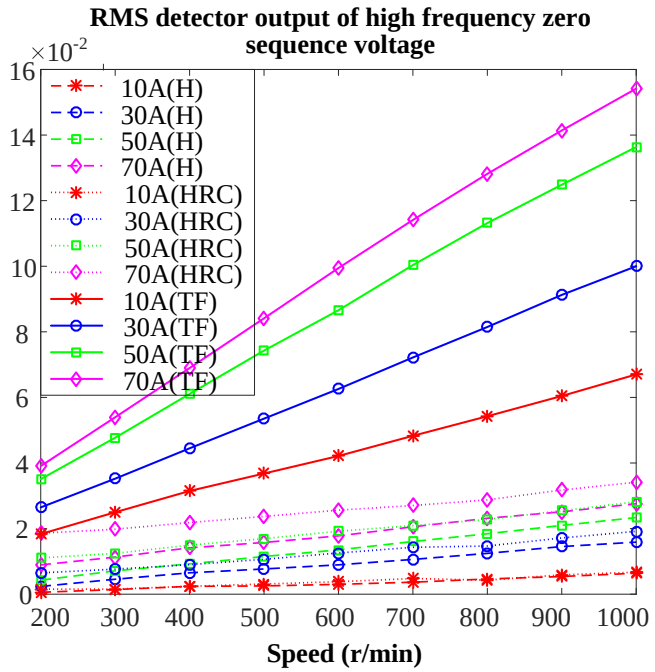

Fig. 5-16 Variations of RMS detector output of high frequency zero sequence voltage with speed and current in turn fault, HRC fault and healthy conditions

To minimize such dependency on the operating conditions, the high frequency based fault indicator expressed in (5-16) is obtained, and compared in Fig. 5-17. It can be observed that the variation of the fault indicator in healthy and HRC conditions due to speed and current has been reduced effectively, especially at higher current and speed conditions. The fault indicators in these states stay nearly constant at higher current and speed conditions, but deviate more from each other at lower speed and current conditions. The more deviations at lower speed and current conditions can be attributed

to the lower high frequency components due to the smaller modulation indexes, which makes the measurement more sensitive to the noise and error. For the turn fault conditions, although the dependence of the fault indicator on the speed and current still remains, a significant difference of the fault indicators between turn fault and other conditions can be achieved, where the smallest value lies at the lower speed. Thus, the determination of the threshold is more convenient, and the detectability of the turn fault is increased.

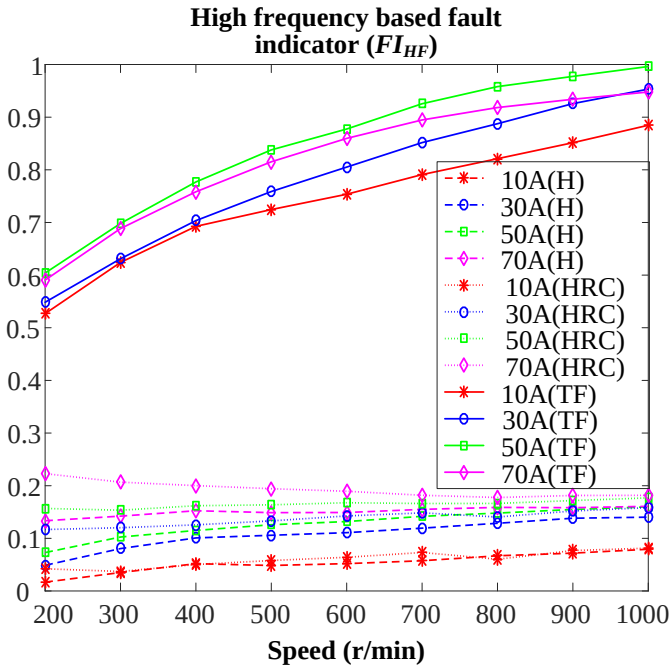

Fig. 5-17 Variation of high frequency based fault indicator with different speeds and currents in turn fault, HRC fault and healthy conditions

For the HRC fault detection, the fundamental component of the zero sequence voltage is extracted and compared with healthy conditions in various speeds and currents, as shown in Fig. 5-18. A strong dependency on the operating current can be observed, especially in the HRC fault conditions. This dependency can be explained indeed by the expression in (5-14). As a consequence, the detectability under lower current is degraded. The fundamental frequency based fault indicator introduced in (5-21) is compared in Fig. 5-19. The values in both healthy and the HRC fault conditions are almost constant for the specific fault severity. Therefore, a threshold to detect the HRC fault can also be defined.

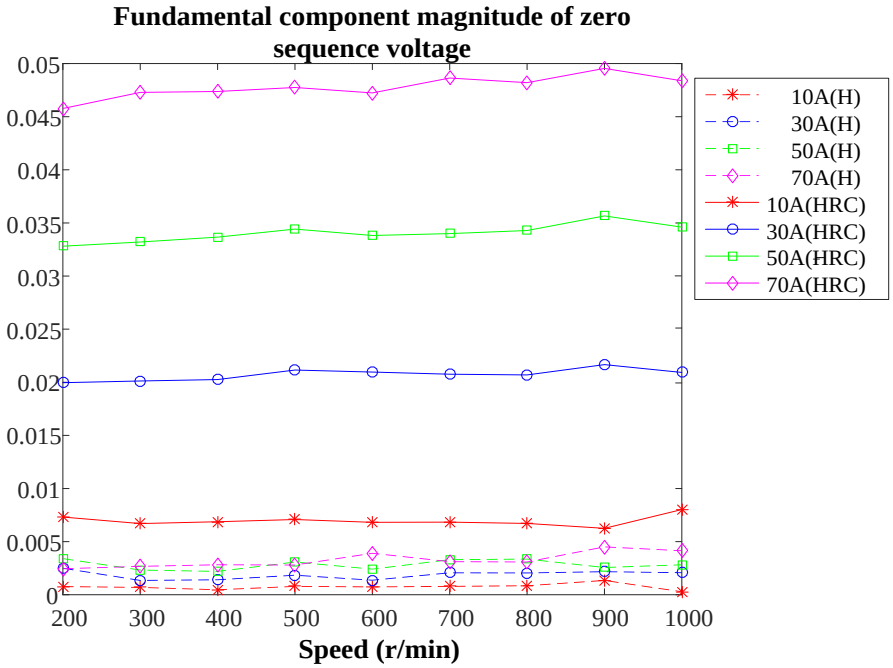

Fig. 5-18 Variations of fundamental component of zero sequence voltage with speed and current in healthy and HRC fault conditions

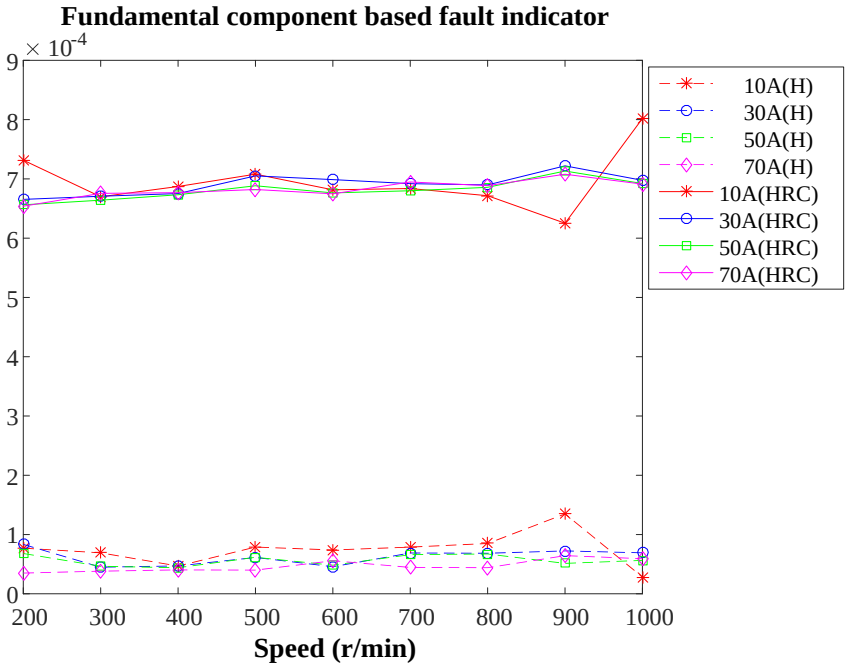

Fig. 5-19 Variations of fundamental frequency based fault indicator with speed and current in healthy and HRC fault conditions

5.5.3 Turn fault detection at no load conditions

The detection of turn fault under no load conditions is also investigated. At 500rpm, the phase currents, zero sequence voltage, and the RMS detector output of its high frequency components captured from the oscilloscope are shown in Fig. 5-20. The frequency components and the calculated high frequency based fault indicator are

shown in Fig. 5-21. Although the phase currents are zero when turn fault occurs, a significant increase in the high frequency components of the zero sequence voltage change can still be observed. This is attributed to the nonzero high frequency voltages which is introduced by the nonzero driving voltages, and the enhancement of the fault signature by measuring the zero sequence voltage through the artificial neutral point. The prominent and steady change of high frequency based turn fault indicator makes it still effective to detect the turn fault at such no load condition. The tests with no load are then conducted at different speeds, and the turn fault indicator in healthy and turn fault conditions are shown in Fig. 5-22. Compared with the results under other operating conditions in Fig. 5-17, it is evident that the turn fault can also be effectively detected under no load conditions with the same threshold. Thus, a wide detection zone of this technique can be achieved.

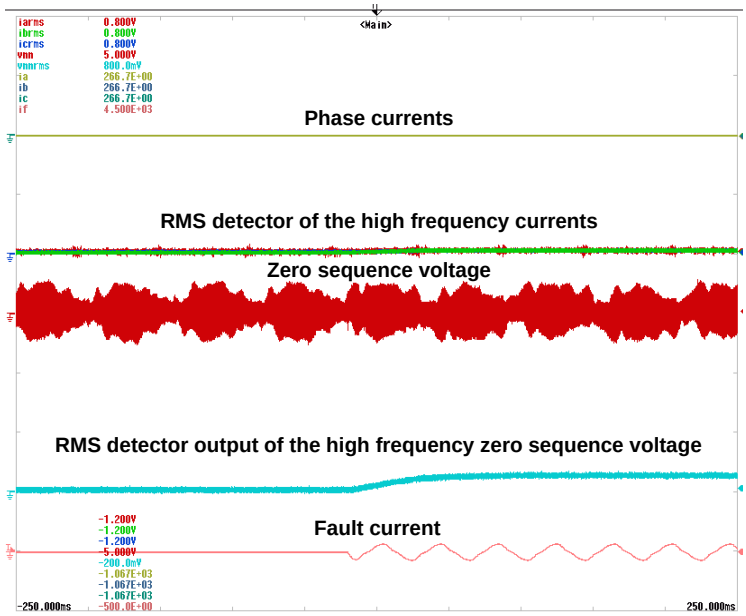

Fig. 5-20 Measured currents, zero sequence voltage and other outputs from the signal processing board when turn fault occurs at no load

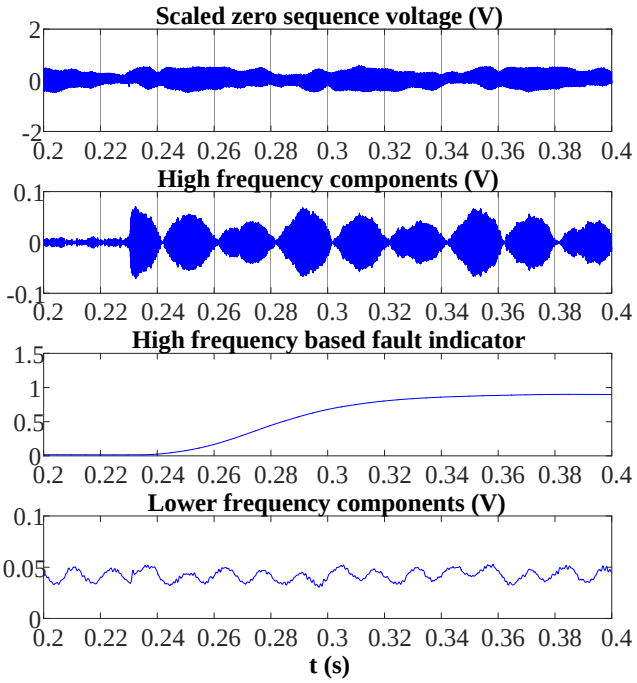

Fig. 5-21. The frequency components and high frequency based fault indicator when turn fault occurs at no load

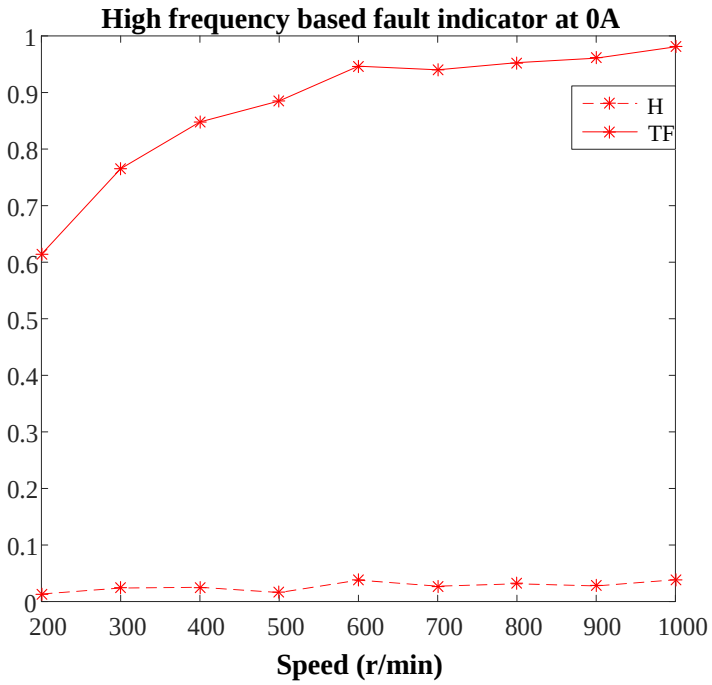

Fig. 5-22 Variation of high frequency based fault indicator at no load condition with different speeds in turn fault and healthy conditions

5.5.4 Turn fault detection at transient states

Since the high frequency based fault indicator is always monitored primarily, its robustness to transient states needs to be tested. When the machine is operating at 500rpm and a current step change from 30A to 70A occurs at 0.33s, the results are shown in Fig. 5-23. The RMS detector output of the high frequency zero sequence

voltage increases to a slight higher value, which accords with the results in Fig. 5-16. Because this dependency on the operating conditions is reduced according to (5-16) when the machine is healthy, the value of the fault indicator remains almost the same before and after the current change.

The results shown in Fig. 5-24 are under the varying speed condition, when the machine speed increases from 500 rpm to 900 rpm at the rate of 1000 rpm/s with phase current of 50A. The RMS detector of the high frequency zero sequence voltage increases with the speed increase, but the proposed high frequency fault indicator also presents little change. Therefore, the turn fault detection based on this fault indicator is immune and robust to the transient states of either current change or speed change, and no false alarm will be triggered.

When a turn fault occurs during the transient states, as shown in Fig. 5-25 and Fig. 5-26, the fault is effectively detectable, since the change due to the turn fault is much higher. To conclude, the effectiveness and robustness of this turn fault detection method in transient operating conditions have been validated.

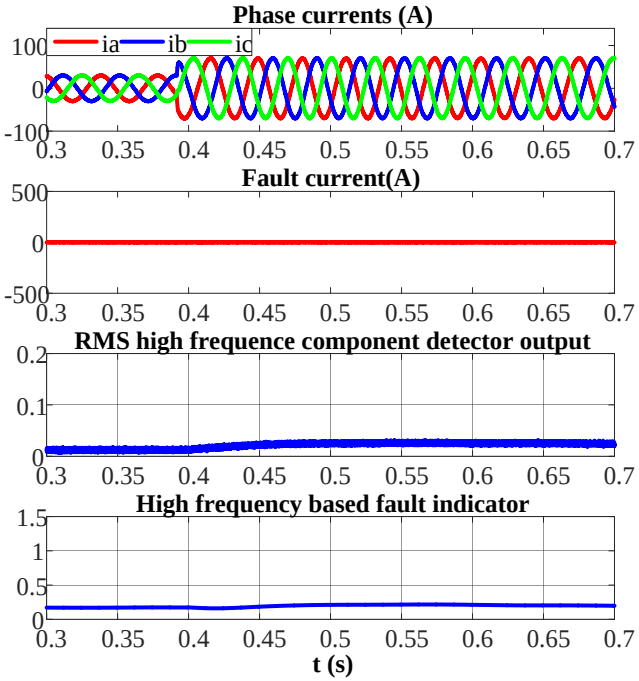

Fig. 5-23 Healthy condition with current step change

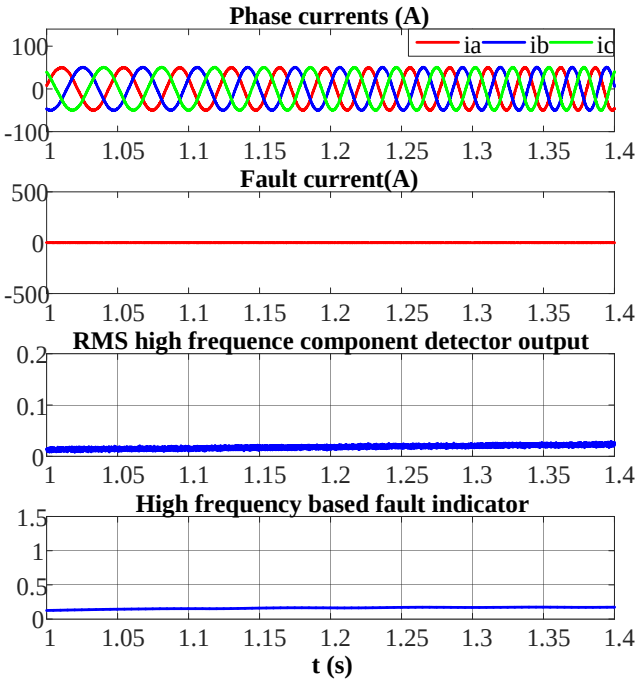

Fig. 5-24 Healthy condition with varying speed

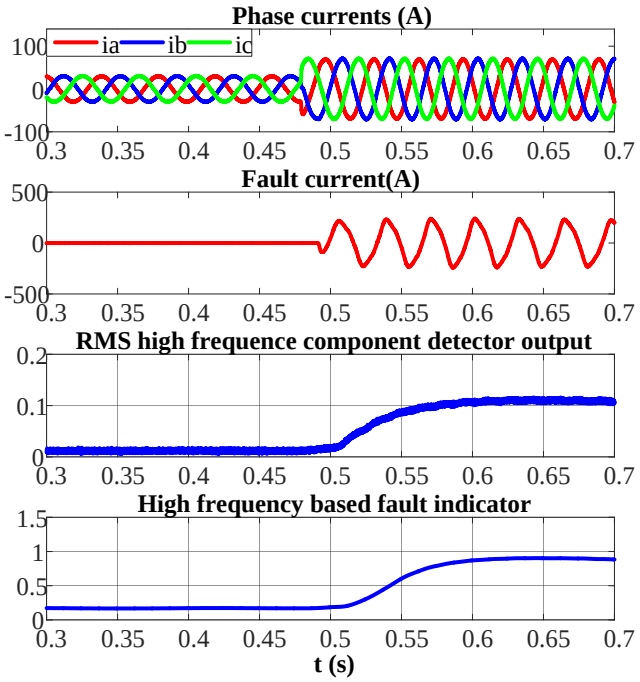

Fig. 5-25 Turn fault condition with current step change

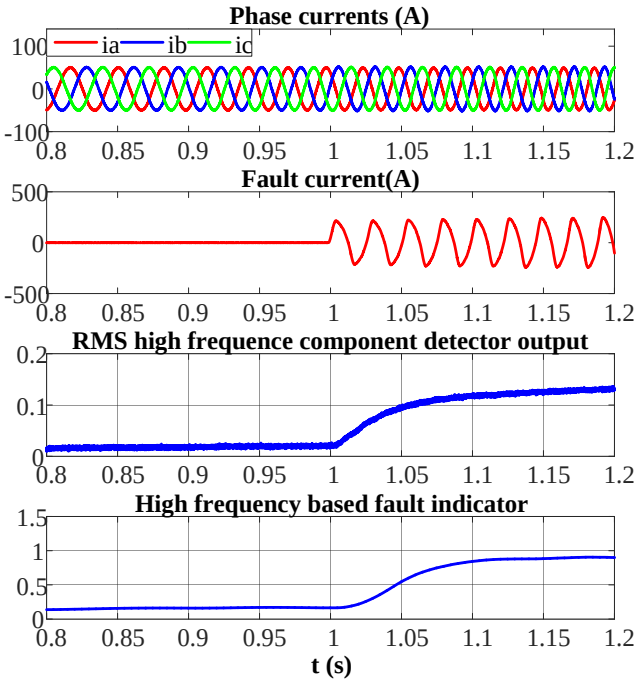

Fig. 5-26 Turn fault condition with varying speed

As for the HRC fault detection, the fundamental components of the zero sequence voltage and phase current is utilized. According to Fig. 5-19, the fundamental zero sequence voltage is hardly affected by the current or speed changes in healthy conditions. Thus, with appropriate frequency tracking algorithm applied to extract the magnitude of phase currents, the impact of the current or speed transient states on the fundamental frequency based fault indicator can also be eliminated. Thus, the reliability of the HRC fault detection can also be achieved albeit once a turn fault is ruled out HRC fault detection is not time-critical.

5.6 Conclusions and discussions

This chapter proposes a winding fault detection and classification technique based on both the high frequency and fundamental frequency components of the zero sequence voltage. Both turn fault and the HRC fault can be detected and classified successfully. The fault indicators are determined following the theoretical analysis on the zero sequence voltage measurement, with the aid of a resistor network when the phase neutral point is available. Simulations and experiments have testified its feasibility. The fault indicators in healthy and fault conditions are compared in different operating conditions, and simple threshold can be defined for fault detection with sufficient confidence. The turn fault detection in no load conditions and transient states are also tested and the effectiveness and robustness of this technique are verified.

It should be noted that the effectiveness of the exclusive turn fault detection is dependent on the condition that the relationships among three phase self- and mutual-inductances shown in (5-5) do not change in the HRC fault conditions. For demagnetization faults, inductance is not affected either, thus they do not produce similar signatures as turn fault. The classification of HRC fault and demagnetization can be done by investigating the harmonics at lower frequencies. Whether the proposed turn fault indicator will be triggered by eccentricity or bearing faults also depends on their impact on the inductance relationships, which needs further study on the specific machine structure and eccentricity or bearing fault severity.

CHAPTER 6
Experimental Testing of Fault Detection on a Permanent Magnet Alternator

6.1 Introduction

This chapter presents the Equipment Health Monitoring (EHM) of permanent magnet alternator (PMA). The project is sponsored by Rolls-Royce Electrical Capability Group (ECG) and Control Systems (CS), aimed at developing fault detection and insulation health monitoring techniques for the Trent 7000 PMA product that Rolls-Royce is currently developing. As will be seen, the PMA under study has a unique set of characteristics that are very different from conventional permanent magnet machines. Hence, the fault detection techniques developed in the previous chapters are not directly applicable. The fault behaviour under emulated turn-to-turn short circuit fault conditions as well as the assessment of the four fault detection algorithms based on monitoring zero sequence voltage and phase current harmonics are presented, and the key components, experimental setup and the test results are described and discussed in detail in this chapter.

6.2 Hardware components

The key hardware components implemented in the PMA test-assembly at Sheffield AEM UTC lab are introduced briefly in this section.

6.2.1 Prototype Trent 7000 PMA

The PMA under study is a prototype PMA designed by Rolls-Royce CS for Trent 7000 engine fleet. It has been designed, manufactured and tested initially. One of the main objectives for this project is to investigate the effect of turn-to-turn short circuit fault in this new PMA design and develop fault detection techniques for this type of fault as a most common type of electrical failure.

The PMA under study has 27 stator teeth and 9 pole-pairs. The PMA rotor is a permanent magnet rotor with Samarium Cobalt magnets bonded onto a stainless steel central hub. An Inconel sleeve is shrunk-fit around the rotor assembly to contain the bonded magnets. In the engine assembly, the PMA rotor is designed to be mounted onto

the drive shaft of a gearbox. It is spline driven and held in place by a locking nut. The manufactured bespoke rotor is shown in Fig. 6-1.

Fig. 6-1 PMA rotor

To provide a level of redundancy, two sets of independent 3-phase winding are employed on the stator, and each occupies 9-slots as shown in Fig. 6-2. The two 3-phase windings named as Channel A and Channel B are separated by unwound teeth at both ends that provide thermal and magnetic isolations. Each phase consists of three tooth wound coils with 71 turns connected in series. However, the coils next to the unwound teeth have different characteristics in the magnetic field from other coils and, hence, the 3-phase systems are unbalanced.

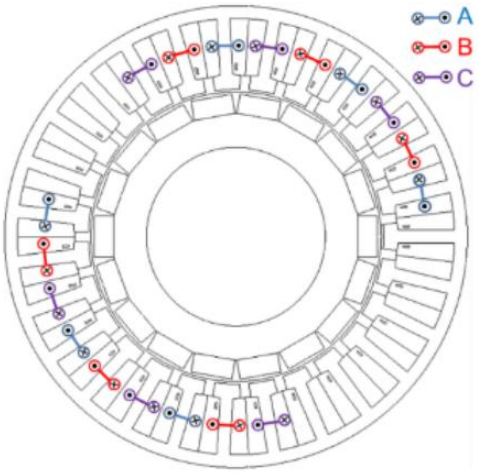

Fig. 6-2 Schematic of the PMA

To emulate the winding turn faults, a customized PMA stator winding configuration was proposed as shown in Fig. 6-3 for one set of the phase windings. As shown in the figure, one coil of the phase C winding is modified, which consists of four coils labelled as CF0 to CF3. The coils CF0 to CF3 are composed of 63 turns, 4 turns, 2 turns, and 2 turns respectively. These coils can then be re-arranged externally to create emulated

turn fault conditions with different number of faulted turns. For instance, to formulate a normal phase winding, external connections can be made between T0 and T2, T1 and T4, T3 and T5, respectively. To emulate a 2-turn shot circuit fault condition, the connection is made via an external relay, between T5 (or T3) and C. The application of this short circuit condition is controlled by the relay drive circuit with appropriate time trigger and duration. Similarly, fault conditions with 4-turns (T4-C), and 8-turn (T2-C) can also be created in a controlled manner.

The neutral point *n* of the phase windings is led out from the PMA stator for the sake of the measurement of the zero sequence voltage, which will be evaluated for the detection of turn fault.

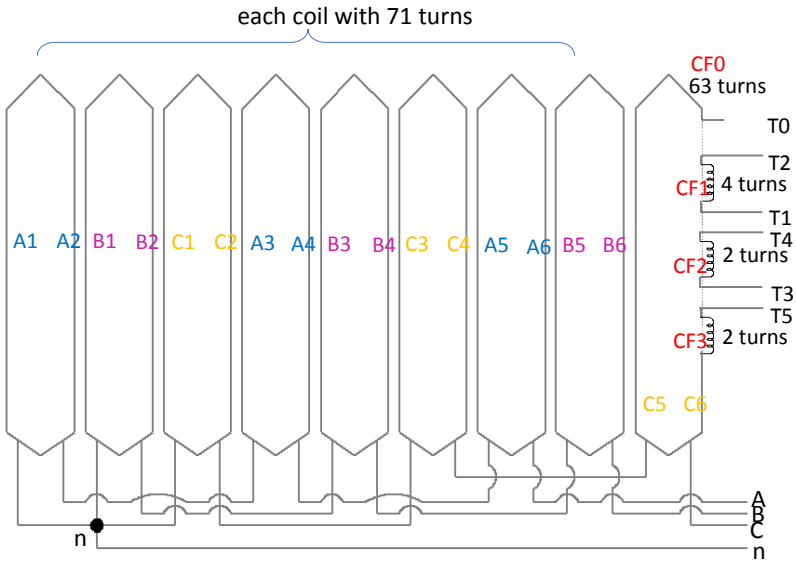

Fig. 6-3 Winding configuration of PMA stator

6.2.2 Power conditioning

In order to produce a fixed DC link voltage of 48V, an asymmetrical 3-phase power electronic converter as shown in Fig. 6-4 is used at the PMA output to regulate the rectifier output voltage which supplies to a nominal load 20Ω. The 3 active devices switch simultaneously at a constant frequency of 4.9 kHz while the duty ratio is controlled by a voltage regulator. When all the switches are off, the three phase currents generated by the PMA all pass through the diodes to charge the capacitor and the converter acts as a full-wave diode bridge rectifier. When all the three devices are switched on, the PMA output is effectively terminally short-circuited, and the capacitor discharges via the load. In this way, the PMA output power to the load is pulse-width

modulated with a filter capacitor to remove the ripples. An additional resistor network is implemented to create an artificial neutral point *m*, and the voltage between *m* and the phase winding neutral point *n* is measured as the zero sequence voltage for the further evaluation of fault indication.

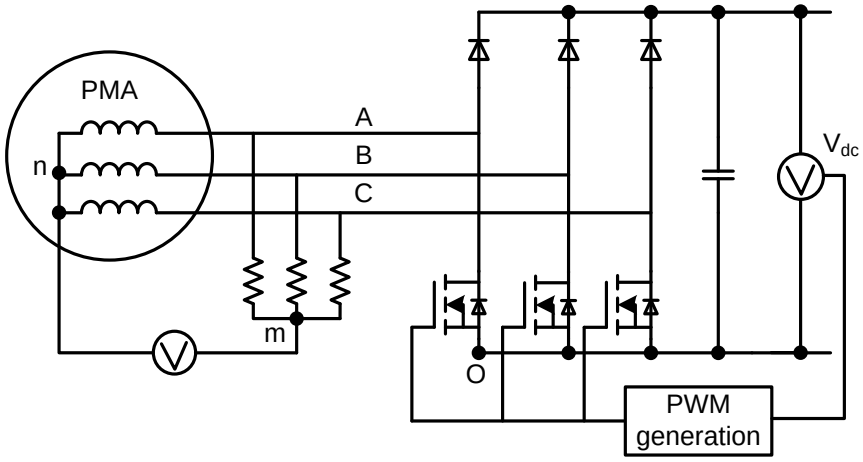

Fig. 6-4 Schematic of power converter and its control

The power conditioning PCB board is shown in Fig. 6-5. In addition to the function of AC-DC voltage converter, it also samples, isolates and scales the signals of interest for the fault detection and insulation health monitoring purposes.

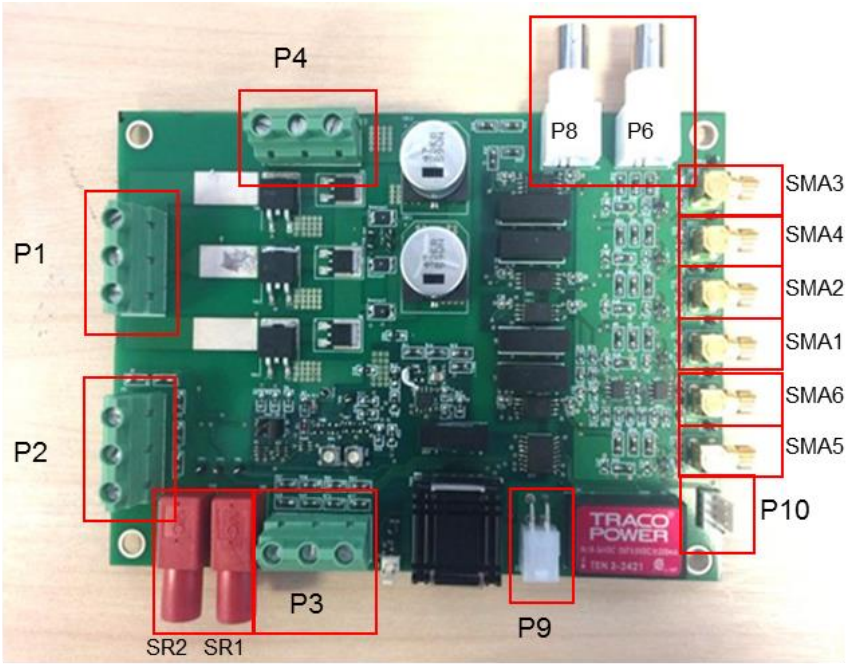

Fig. 6-5 Power conditioning PCB

6.2.3 Signal processing platform

Apart from the fault detection, the signal processing platform is also utilized for the insulation health monitoring techniques, although they are not covered in this thesis. The key features required are the acquisition and processing of the measured signals. In the cases of insulation health monitoring a high sampling frequency of 125 MHz is required. Once a sufficient buffer of 500,000 data points per channel is stored the processing will be performed with no strict time interval since insulation degradation is a very slow process. Conversely, for the tested fault detection methods, a much lower sampling rate of ~100 kHz is sufficient, but data must be constantly acquired and processed to give a prompt fault indication in real time. Both techniques perform similar FFT processing on the acquired data, albeit with vastly different sample sizes.

These differing requirements must be achieved on a common processing platform for the implementation of both techniques within the single system. The Xilinx Zynq-7000 SoC has been identified as the most suitable candidate. It comprises of dual core ARM A9 processors integrated with field programmable logic in a single IC. Although the capabilities demonstrated within EHM of PMA are not specific to a single processor and can be applied more generally to any suitable platform, the implementation of the embedded Linux system in the ARM core and integration with the FPGA provide more flexibilities and possibilities in the application.

To exploit the capability of the Zynq-7000 IC, the Red Pitaya STEM 125-14 shown in Fig. 6-6 has been considered to demonstrate the capacities within the timescale of the EHM of PMA activities. The Red Pitaya combines a Zynq7010 chip with a relatively limited number of similar performance input channels, which are 2 channels 14bit 125MS/s ADC and 4 channels 12bit 100 kS/s ADC, on a single PCB. The complete peripheral block diagram is shown in Fig. 6-7. The software supports low level access to the sample data and a clear mechanism to pass this to the on-board SRAM. To mitigate the time risk using the 4DSP card within the timescale of the EHM of PMA project, the Red Pitaya development board has been used.

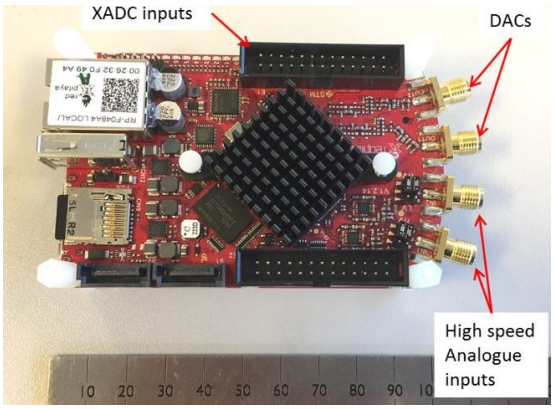

Fig. 6-6 Processing platform Red Pitaya

The Red Pitaya runs Debian, as a fully-fledged version of Linux, on the dual core ARM processing system. This allows experimental data to be saved on the internal SD card, with control and file access being possible through the Ethernet connection. The Fast Fourier transform computations, required by the detection techniques, are performed using the FFTW library on the ARM9 cores. The FPGA fabric implements the high-speed data sampling and processing, then transfers the data to the memory for the access by the ARM processors.

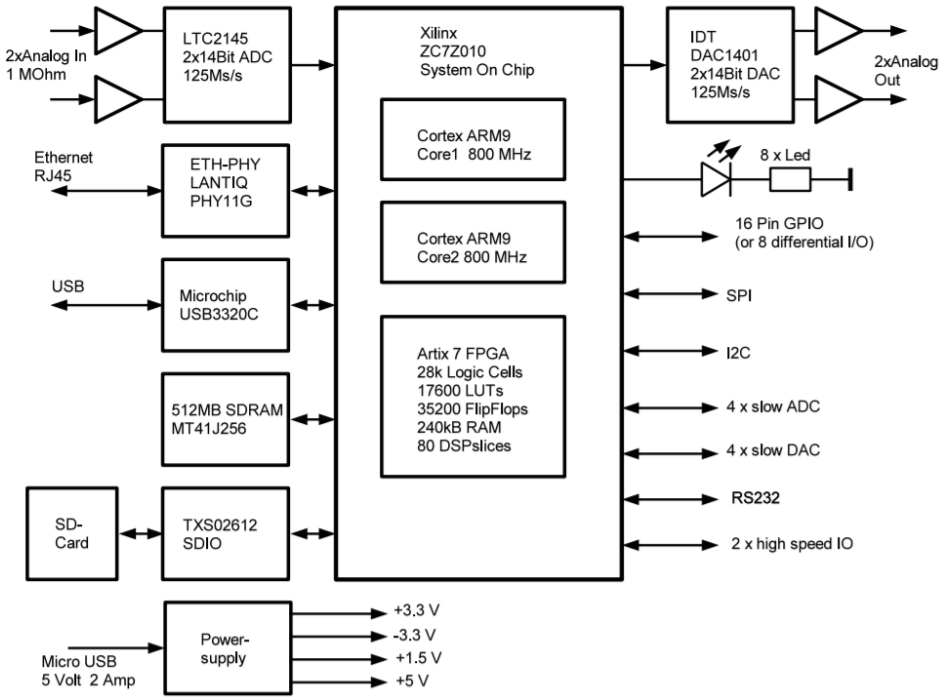

Fig. 6-7 Red Pitaya peripheral block diagram

6.2.3.1 Data acquisition and processing scheme

Two main signals need to be measured, i.e. zero sequence voltage and the phase currents, based on which several fault detection techniques are tested and evaluated. The

turn fault alters the inductance and back-EMF of the faulted phase, and the fault signature is reflected in spectrum change of these signals.

Zero sequence voltage is measured between the artificial neutral point of the extra resistor network and the neutral point of the 3-phase windings. Since the neutral point is not effectively connected to any other terminals, the sum of the 3 phase currents is zero according to the Kirchhoff's current law. Thus, only 2 phase currents need to be measured in order to obtain all the phase currents.

The data is first acquired by the FPGA, and subsequently read by the ARM after appropriate configuration in the FPGA. Two data configuration and reading schemes are designed for subsequent data processing.

6.2.3.2 Data packetizing and packet reading

The main data processing tasks for the fault detection are the execution of the FFT function in C code. Before the FFT function is performed, the data need to be saved into an array with the length of FFT window. Considering this requirement, the data can be buffered and packetized in the FPGA first with the fixed or flexible length, and saved into a memory space. The status of the packet (full or not) is also saved. If the packet is full, then the required FFT length has been met. The ARM reads the packet of data from the memory space, and executes the FFT function. At the same time, the buffer is reset and collects new data. The block configuration in the FPGA and the connection with ARM are shown in Fig. 6-8. The processing scheme is shown in Fig. 6-9.

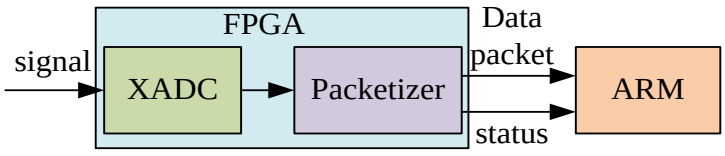

Fig. 6-8 Block configuration of FPGA and ARM

In this case, although the signal sampling rate can be guaranteed as 100 kS/s, the FFT results updating rate is dependent on the window length. The longer the window length, the lower the FFT updating rate is. For a more accurate result and a higher resolution, the window length is set to 0.2 s, containing 20000 points. Thus, the updating rate of the FFT result is 5 Hz.

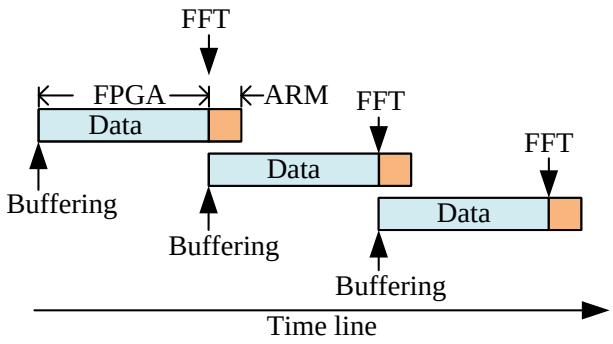

Fig. 6-9 Data acquisition and FFT execution scheme

6.2.3.3 Data reading at sampling rate

If only a few frequency components, such as 1st and 3rd harmonic are of concern, then the original Fourier calculation can be implemented without occupying too many of the resources. In this case, the data can be updated at the sampling rate. To realise this function, the configuration of the FGPA is designed as follows. A block RAM (BRAM) in FPGA is used to store data temporarily. Data are written into the BRAM through the BRAM writer which will also output the pointer of the data inside the BRAM space. Both the data and the pointer are read by the ARM. The writing speed or the updating speed of the data in FPGA is dependent on the sampling rate, while the rate of data reading by the ARM is dependent on the software design. To synchronize the writing and reading rates, the data pointer is used such that whenever the data pointer increases by 1, meaning the new data has been written into the BRAM, then the reading command is sent out to read the data. In this way, all the data measured can be transferred and processed in the ARM at the sampling rate. The block configuration in the FPGA and the connection with the ARM are shown in Fig. 6-10.

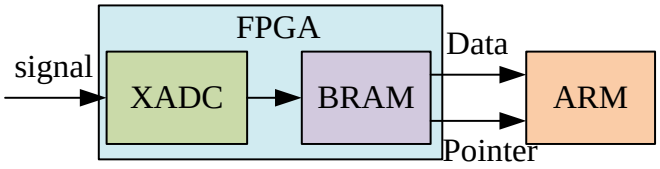

Fig. 6-10 Block configuration of FPGA and ARM

The expressions for the Fourier analysis implemented in the ARM are shown in (6-1), where the frequency ω or the machine rotating speed needs to be known. After calculating the coefficients a_k and b_k, the magnitude of the k^{th} frequency component can be obtained from $F(k)$. The integration interval for a_k and b_k can be one cycle or an integer multiple of cycles of the signal. To enhance the accuracy, the interval are set to be the maximum integer multiple (N) of cycle within 0.2s window.

$$
\begin{aligned}
&f(t)=\frac{a_0}{2}+\sum_{k=1}^{\infty}(a_k\cos k\omega t+b_k\sin k\omega t)\\
&\begin{cases}
a_k=\dfrac{2}{T}\displaystyle\int_{-\frac{T}{2}}^{+\frac{T}{2}} f(t)\cos k\omega t dt\\
b_k=\dfrac{2}{T}\displaystyle\int_{-\frac{T}{2}}^{+\frac{T}{2}} f(t)\sin k\omega t dt
\end{cases}\\
&F(k)=a_k-jb_k
\end{aligned}
\tag{6-1}
$$

Due to the limit of the memory, the data read by the ARM cannot be saved all the time. But at least 0.2s of data need to be saved for the integration. Thus, a space containing 20000 data array is allocated. Each time when a new data comes in, it is saved in that array, and the older data that has been saved the N cycles before is searched and identified. Then the most recent N cycles of the data are extracted and integrated. The searching and integrating scheme is shown in Fig. 6-11. In this way, the new harmonic component result can be obtained once a new data is read and saved into the array.

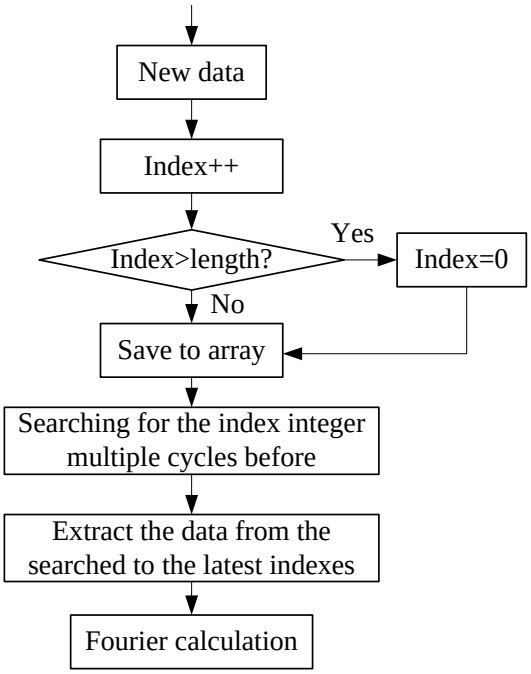

Fig. 6-11 The Fourier calculation scheme

6.3 Experimental setup

The PMA is mounted with AVL dynamometer shown in Fig. 6-12. The AVL dynamometer can operate in 4 quadrants with up to 20000rpm at 120 kW, which is

capable to achieve the PMA speed requirement. Throughout the testing it has been used as a speed controlled motor to drive the PMA, with a manually adjusted speed set point.

The DIN rail mounted terminals connecting the PMA output leads to the power conditioning enclosure and the fault emulation relay are contained in the plastic box next to the machine. Shorting links are used to create a normal phase C configuration for channel B with fault taps at 2-, 4- and 8-turns. Channel A is connected as a terminal short circuit while channel B is connected to the power conditioning PCB, and the position of these channel within the PMA is shown in Fig. 6-13. A large box is used to enclose the power conditioning and the signal processing hardware, including the power conditioning PCB, phase current sampling PCB, AC current transformer probe, differential voltage probe and the two Red Pitayas, as well as their required power supplies, as shown in Fig. 6-14. The inputs to this enclosure are the Channel B phase cables, casing ground point and 240 V supply. The measurement sensors included within the power conditioning enclosure are connected to the relevant Red Pitaya for on-line processing for fault detection. A complete set of the measured signals, including duplicates of the Red Pitaya are also passed to a Yokogawa DL850V oscilloscope for both on-line monitoring and recoding data for later offline processing. The resistive load bank is also provided for the output DC voltages of the power conditioning enclosure, as shown in Fig. 6-15.

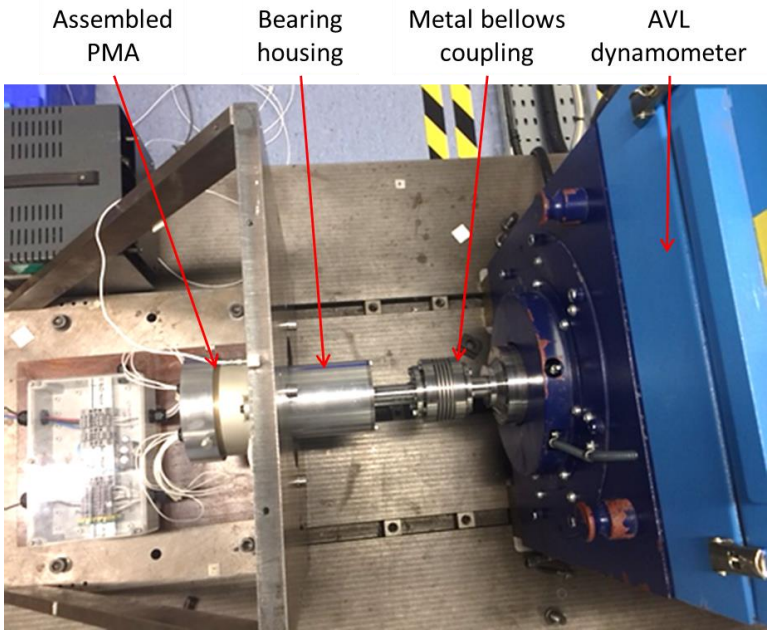

Fig. 6-12 PMA installation with AVL dynamometer

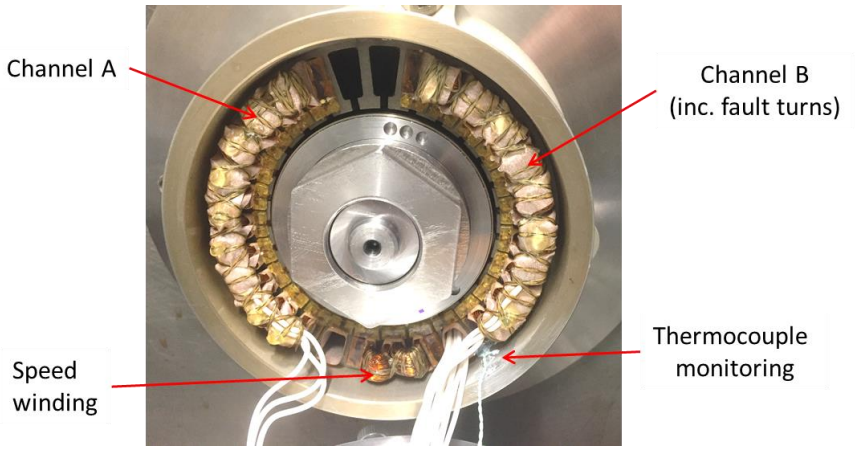

Fig. 6-13 PMA rear view showing output channels (rear cover removed)

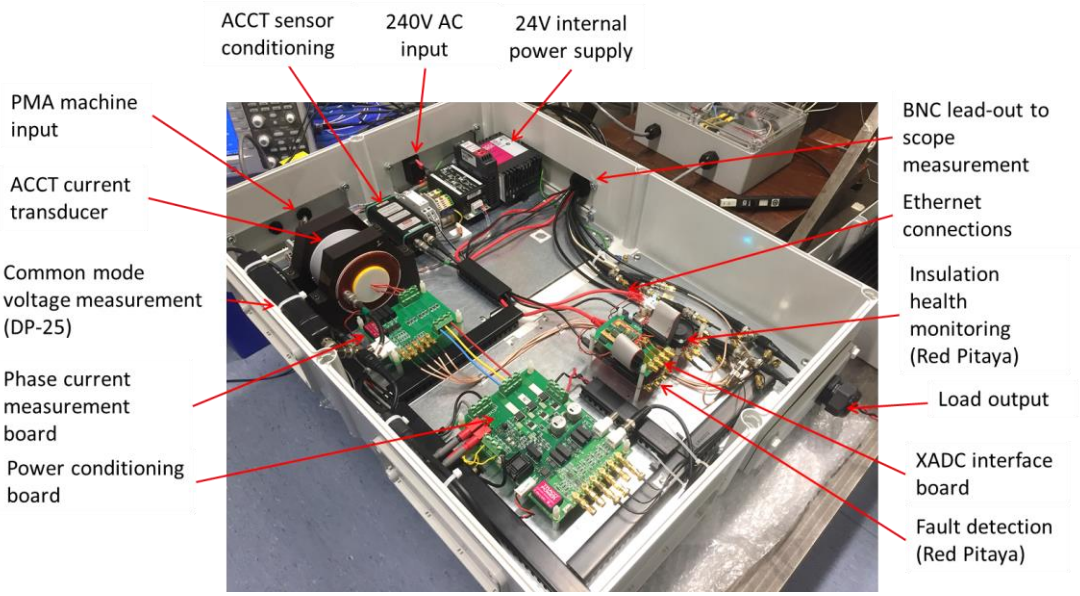

Fig. 6-14 Power conditioning enclosure internals

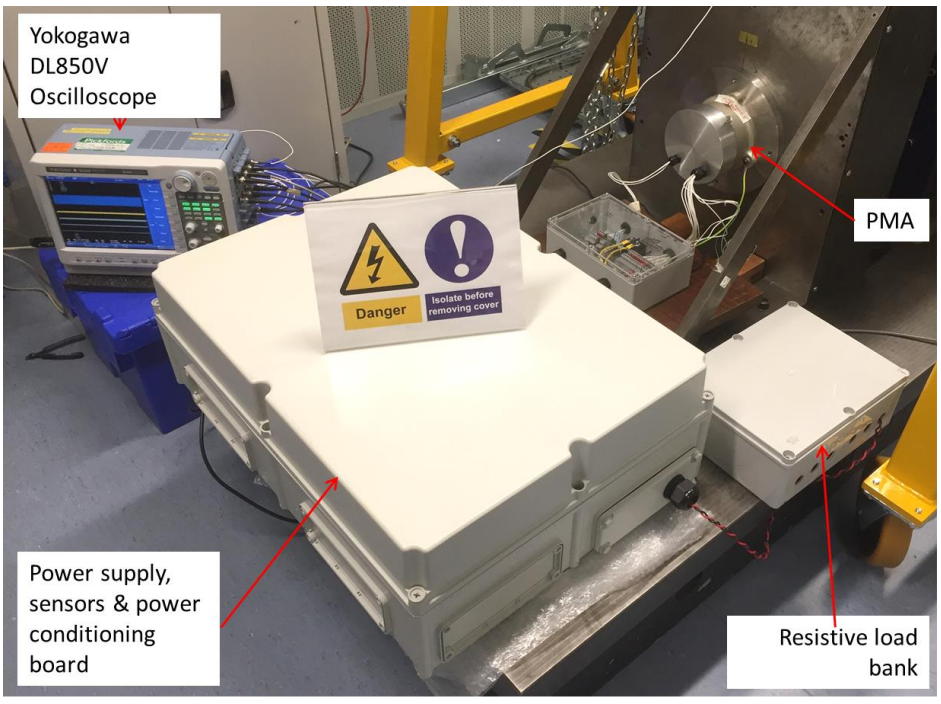

Fig. 6-15 PMA power conditioning and measurement system on-test

6.4 Experimental tests

6.4.1 Normal operations

In normal operation, the PMA machine is shunt regulated via the power conditioning board to control a fixed DC output voltage. The high impedance design of the PMA ensures the machine operate as a constant current source over a wide speed range. This design has the benefit of limiting the terminal short circuit current, while the corresponding drawback is a very high open circuit voltage at the maximum operating speed.

The gate signals for all three low-side MOSFETs are generated by the analogue controller based on the UC1843. When the resistive load is connected, the nominal DC link output is measured as 50.02V during testing.

The fixed load resistance connected to the power conditioning board DC output is a parallel connection of 82Ω resistors providing a load of 20.5Ω, which equates to a nominal load of 122W at 50.02 V. This is approximately equivalent to the minimum specification power output requirement (120W per channel) of the PMA from the 10% to 110% speed.

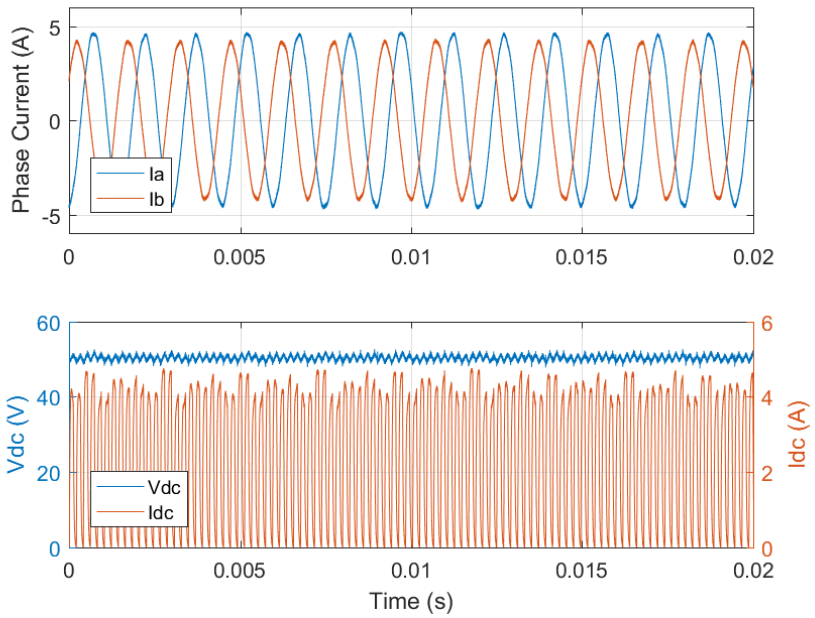

Fig. 6-16 Regulated output operation at 4446rpm

The normal operation of the power conditioning board is shown in Fig. 6-16 when the PMA operates at 4446 rpm (30 % of the maximum speed). It is seen that the magnitudes of the two phase currents are not the same due to inherent unbalance in the PMA. The average rms phase current is 3.3 A. The I_{DC} waveform visible in the lower trace is the current before the DC link capacitor. The discontinuous current is caused by the on-off switching of the MOSFETs, showing clearly the switching frequency of 4.9 kHz.

6.4.2 Inter-turn short circuit fault

To activate the fault conditions, a DC power relay is connected at the fault emulation terminals. The relay is an Omron G9EN-1, rated at 400V, 60 A with a maximum DC current switching capability up to 60 A. The relay is driven by 12 V pulse generator providing a pulse of 400ms duration. The application of the switching pulse and the resultant fault current is shown in Fig. 6-17(b), the operate time and release time have been measured as 8ms and 16.6ms respectively.

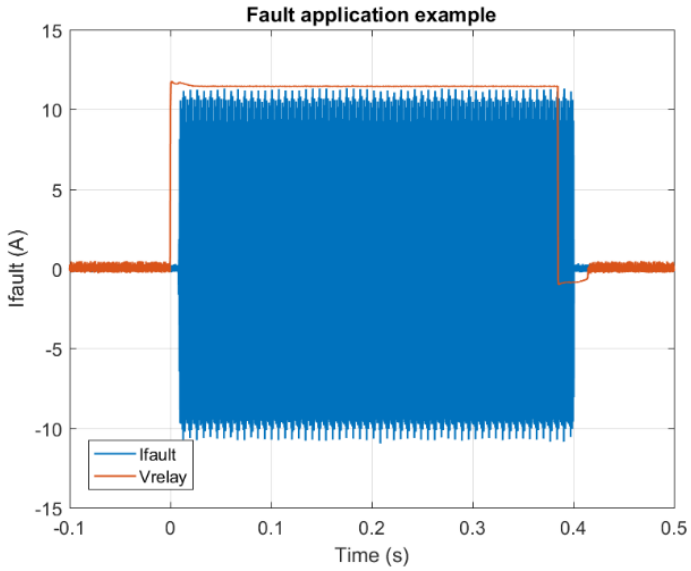

Fig. 6-17 Fault execution and fault current

In practice this external connection for fault emulation increases the fault turn resistance and impedance both by the length of cabling used and the relay's internal contact resistance. To minimise the effect as much as possible the relay is mounted at the machine lead-outs. The total resistance from the relay lead to the fault terminals (T3, T1, T0 for 2-turn, 4-turn, and 8-turn fault cases respectively) which includes the resistance of the relay, cable leads, and the shorted turns, is measured by micrometre.

The resistance of the shorted turns are estimated by the total resistance and the number of the turns in one phase winding. Thus, the additional resistance introduced into the shorted circuit in fault conditions can be estimated, as shown in Table 6-1. The additional resistance increases in the case of the 4 and 8 turn faults because these include the machine lead-outs of the 2-turn (T4 ,T3), 2- and 4-turn (T4, T3, T2, T1) respectively.

Table 6-1 Estimation of additional fault resistance

Fault configuration	Estimated shorted turns resistance (mΩ)	Measured total resistance from relay to fault terminals (mΩ)	Estimated additional fault resistance (mΩ)
2 - turn	15.7	66.7	51
4 - turn	31.4	109.95	78.55
8 - turn	62.9	168.65	105.75

A typical example of a waveform showing the application of a fault on the PMA, is presented in Fig. 6-18. An 8-turn fault is applied while the machine is operating at 8892rpm with a regulated DC output. As expected there is very little directly visible difference in the terminal phase currents and only a slight difference in the zero sequence voltage Vnn, before and after fault. The details of the techniques and processing performed to provide inter-turn fault detection capabilities are investigated in section 6.4.3.

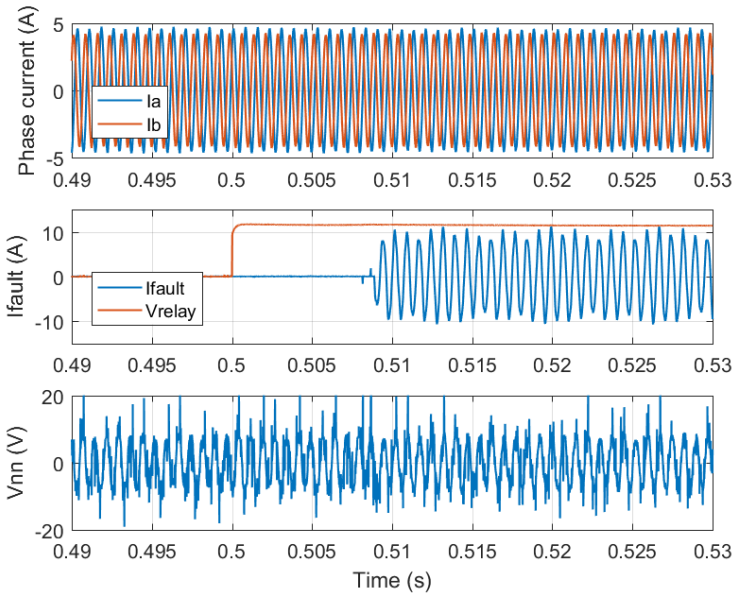

Fig. 6-18 Healthy and fault conditions example with an 8-turn fault at 8892 rpm

The fault currents have been recorded under fault conditions at 1482 rpm, 4446 rpm, and 8892 rpm with 2-, 4- and 8-turn faults, with the waveforms given in Fig. 6-19. Because of the introduced additional resistance in the turn fault emulation in Table 6-1, the fault currents are smaller than the actual turn fault conditions. The RMS values of the fundamental components are given in Table 6-2. In each fault case the fault current increases with the speed.

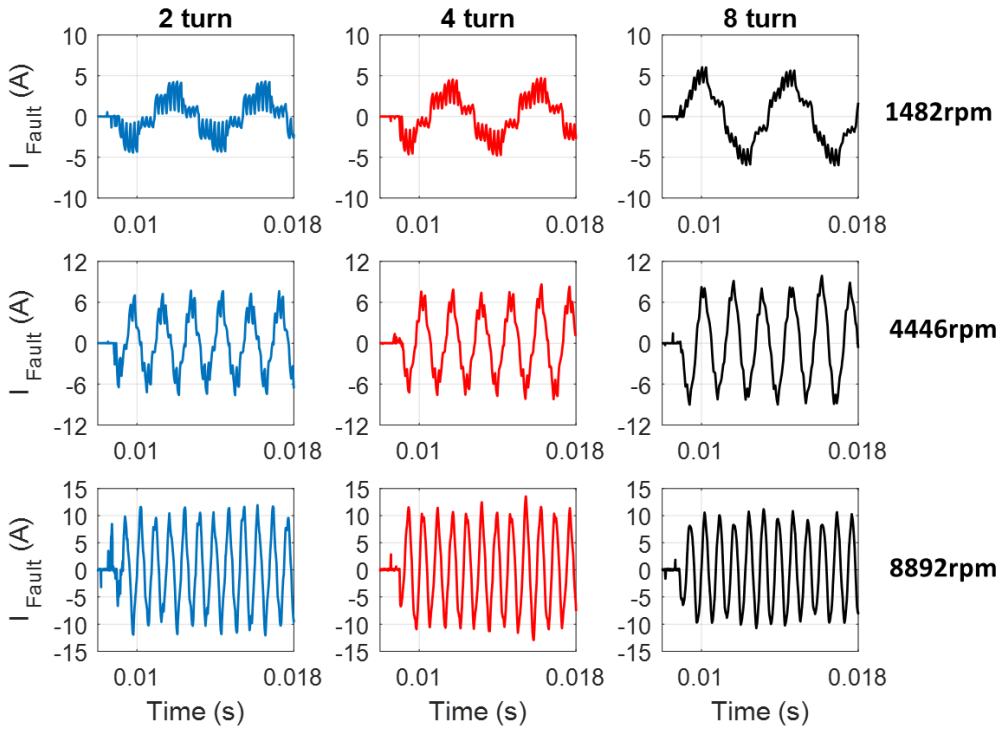

Fig. 6-19 Comparison of 2-, 4- and 8-turn faults at 1482, 4446 and 8892 rpm

Table 6-2 Fundamental RMS values for 2-, 4- and 8-turn faults currents at 1482, 4446 and 8892 rpm

Fault Current	2 Turn	4 Turn	8 Turn
1482 rpm RMS fault current	1.90	2.24	3.29
4446 rpm RMS fault current	4.08	4.38	5.34
8892 rpm RMS fault current	6.91	7.26	6.71

The fault currents are compared for 2- 4- and 8-turn faults under a both regulated DC output into a fixed resistive load and with a terminal short circuit applied. This comparison is shown in Fig. 6-20 and Fig. 6-21 for the 4446 rpm and 1482 rpm operating points respectively, the corresponding RMS values are given in Table 6-3 and Table 6-4. In all cases the terminal short circuit produces a clear reduction in the fault current. This is most significant in the 8-turn fault case where the reduction is 83 % at 1482 rpm and 59 % at 4446 rpm. The 2- and 4-turn cases both show a reduction of 66 %

and 45 % for 1482 and 4446 rpm respectively. This can provide a possible mitigation measure by shorting the winding terminals to reduce the fault current once a turn fault is detected.

It is clear from the above introduction and description that the PMA under study is unique and different from the conventional machine drives, the turn fault detection techniques developed in the previous chapters do not apply to this machine directly. Since it is intrinsically unbalanced, the 2nd harmonics in dq axis current or the negative sequence which is used as fault indicator in chapter 2 already exist in healthy condition in this PMA, which will be evaluated further. Due to the powerful data acquisition and processing ability of the signal processing platform, the zero sequence voltage can be analysed more detailedly, at both fundamental and switching frequencies.

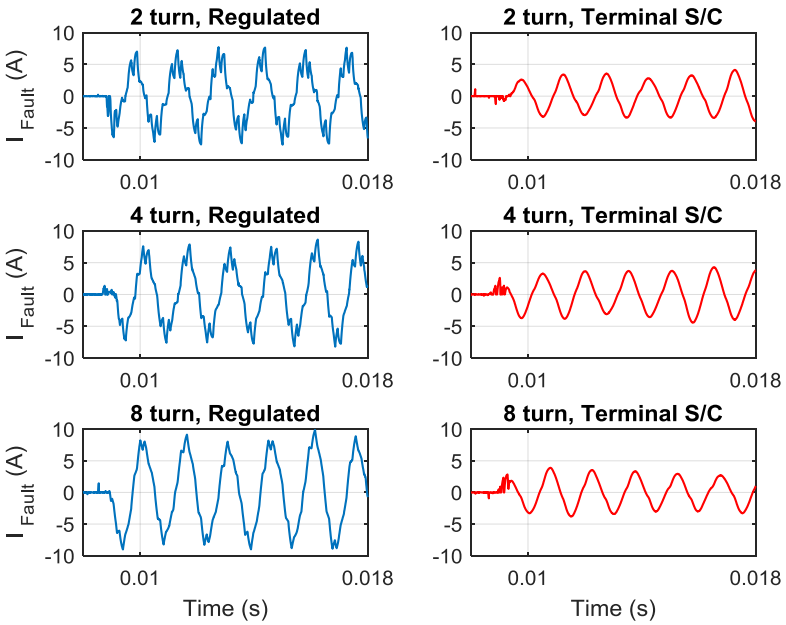

Fig. 6-20 Fault current comparison at 4446 rpm with regulated output and terminal S/C applied

Table 6-3 RMS values for 2-, 4- and 8-turn fault current with both regulated and terminal short circuit outputs at 4446 rpm

Fault current	**2 Turn**	**4 Turn**	**8 Turn**
Regulated RMS fault current	4.06	4.38	5.34
Terminal S/C RMS fault current	2.22	2.41	2.18

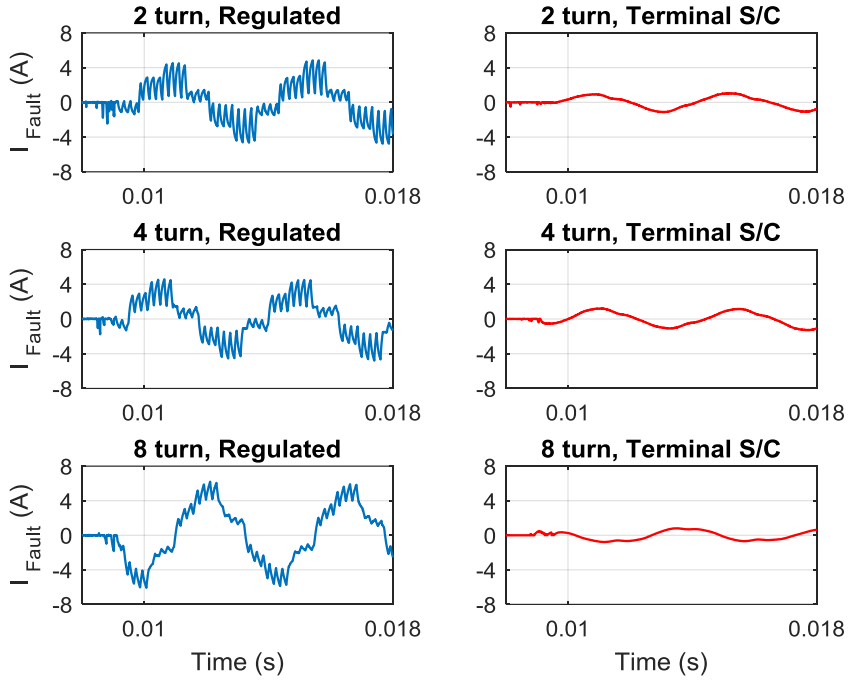

Fig. 6-21 Fault current comparison at 1482 rpm with regulated and terminal s/c applied

Table 6-4 Fundamental rms values for 2-, 4- & 8-turn fault current with both regulated and terminal short circuit outputs at 1482 rpm

Fault current	2 Turn	4 Turn	8 Turn
Regulated Fundamental (rms)	2.01	2.22	3.4
Terminal S/C Fundamental (rms)	0.68	0.75	0.58

6.4.3 Fault detection based on fundamental component or RMS value of zero sequence voltage

The turn faults result in changes in the measured zero sequence voltage v_{mn} shown in Fig. 6-4. Hence, the fault can be detected by monitoring the change of the fundamental component (also referred as 1st harmonic) in the form of magnitude or the RMS value.

Fig. 6-22 and Fig. 6-23 show the measured zero sequence voltage and the resultant fundamental and the RMS value under 2-, 4-, and 8- turn fault conditions at 8892 rpm and 1482 rpm, respectively. In each test, the fault is injected for a period of 0.4s and the resulting changes in zero sequence voltages can be observed from the measured waveforms. It should be noted that data processing window is set to 0.2s, and therefore, the outputs of the processing are available after 0.2s. At 8892 rpm, both the fundamental

and RMS value clearly show the change caused by the fault, except for the 8-turn fault. The sensitivity is, indeed, dependent on the number of the faulted turns and their location in a slot as well as speed. However, at 1482 rpm, which is 10 % of the maximum speed of the machine, the change can be rarely seen from either the calculated variables. As a result, it is not possible to detect a turn fault at this speed using this method. Fig. 6-24 and Fig. 6-25 compare the fundamentals and RMS values of the zero sequence voltage, respectively, under the health and fault conditions at different speeds. It is clear that for most of the test conditions, the differences between the health and fault conditions can be detectable. Thus, once the variations of the fundamental or the RMS value with speed are recorded in healthy conditions, they can be compared with on-line measured and processed data. A fault can be detected if the difference between the two is greater than a predefined threshold. The problem is that the change due to fault is very small. Therefore, the detection based on these two signals may not be robust against noise and other disturbances.

For example, the zero sequence voltage may also be affected by temperature variation since the remanence of the magnets is temperature dependent. Fig. 6-26 shows the measured zero sequence voltages and the resulting fundamental and RMS value at two different temperatures when the PMA operates at 1482 rpm under healthy conditions. The room temperature refers to 16° C and the higher temperature to 55° C. It is evident that the changes due to temperature are in the similar range to that caused by a fault.

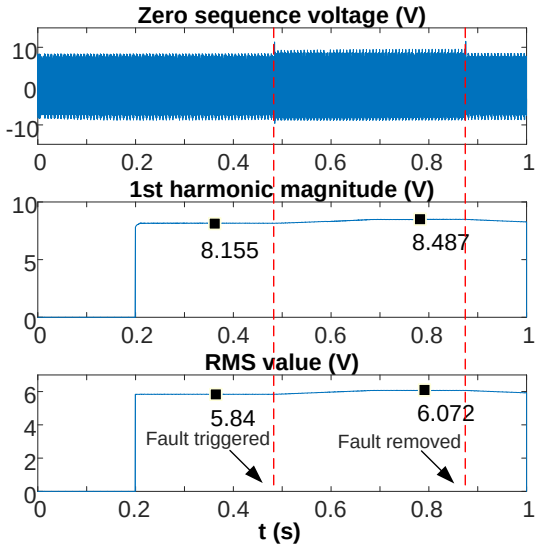

(a) 2-turn fault

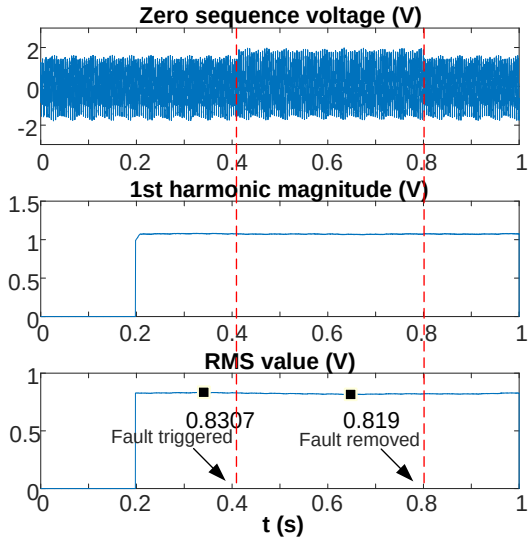

(a) 2-turn fault

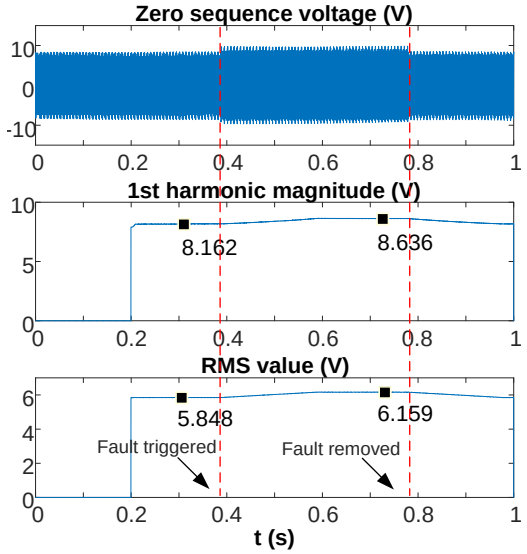

(b) 4-turn fault

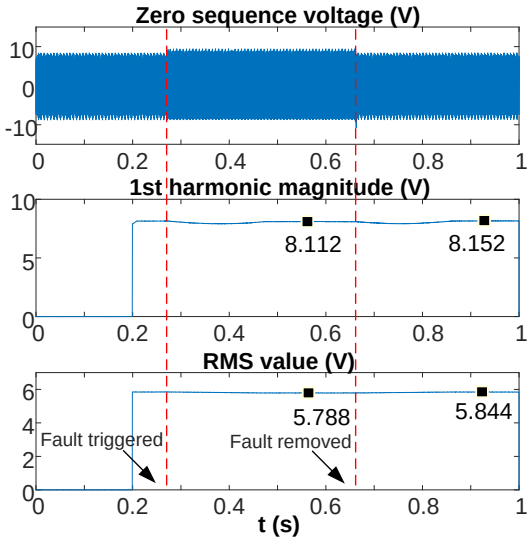

(c) 8-turn fault

Fig. 6-22 Zero sequence voltage and processed results at 8892 rpm

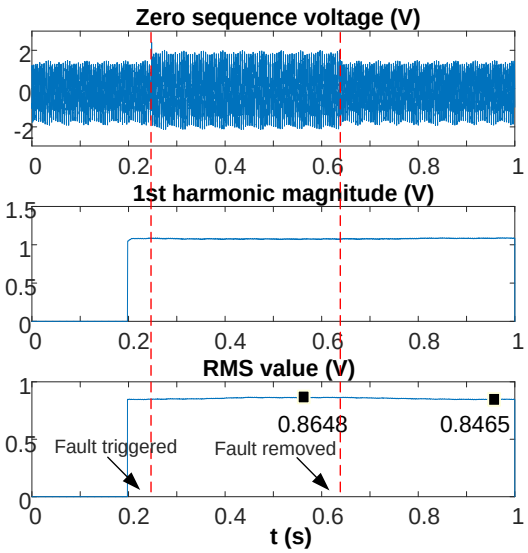

(b) 4-turn fault

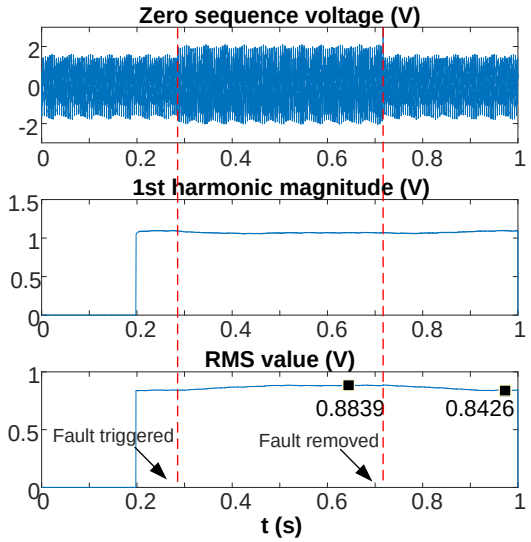

(c) 8-turn fault

Fig. 6-23 Zero sequence voltage and processed results at 1482 rpm

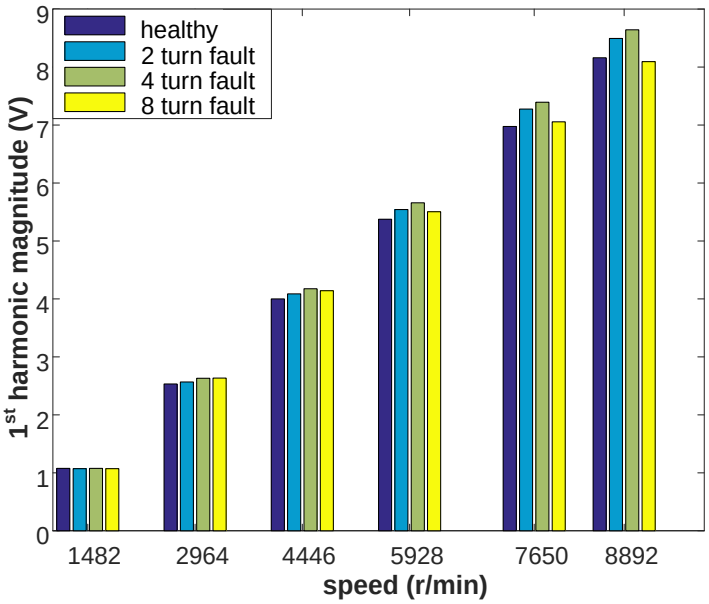

Fig. 6-24 The comparison of 1st harmonic of zero sequence voltage at different speeds

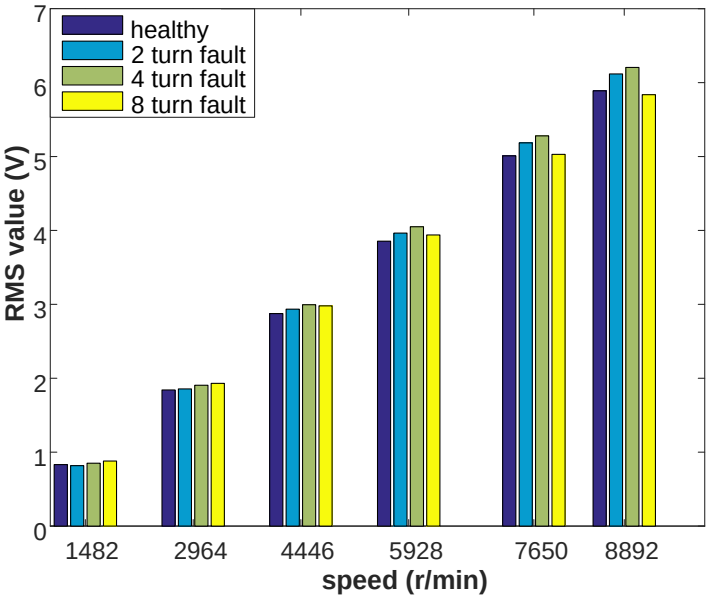

Fig. 6-25 Comparisons of RMS value of zero sequence voltage at different speeds

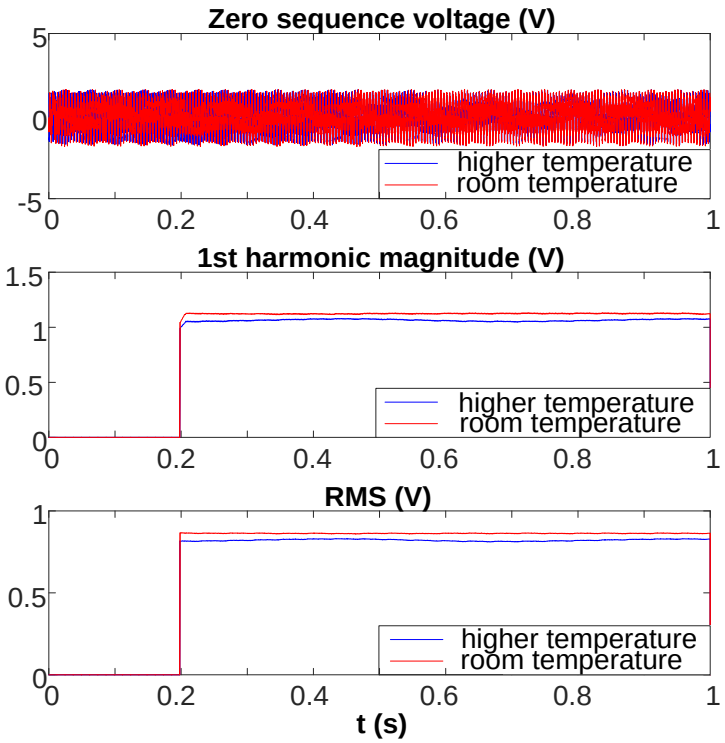

Fig. 6-26 Fundamental and RMS value of zero sequence voltage in healthy condition at 1482rpm at two different temperatures

6.4.4 Fault detection based on the ratio between the fundamental and 3rd harmonics of the zero sequence voltage

To improve the robustness of the fault detection, a different fault indicator based on the ratio of the fundamental to the 3rd harmonic of the zero sequence voltage is defined. Since the 3rd harmonic is also affected by temperature through the same physical cause, the ratio of the fundamental to the 3rd harmonic should be less dependent on temperature as shown in Fig. 6-27. In contrast, the changes in the fundamental and 3rd harmonic of the zero sequence voltage caused by the fault are different. Therefore, the defined indicator will be more sensitive to the fault. The fundamentals, 3rd harmonics and their ratios in 2-, 4-, and 8-turn fault conditions at 8892 rpm and 1482 rpm are shown in Fig. 6-29 and Fig. 6-30, respectively. It is seen that the changes in the ratios due to the faults are more significant at 8892 rpm, but less detectable at 1482 rpm. Fig. 6-28compares the variations of the ratios under the healthy and the 3 fault conditions with different speeds. It is evident that except for the faults at 1482 rpm and the 2-turn fault at 2964 rpm, all the faults at higher speeds can be detected with large differences in the ratios

between the healthy and fault conditions, especially for the 8-turn fault. Therefore, the robustness of the fault detection can be improved. The large differences in the fault indicator are attributed to the fact that a fault results in an increase in the fundamental but a decrease in the 3rd harmonic. The largest difference due to 8-turn fault can be 35% at 8892 rpm, while the difference in 2-turn fault condition at 4446 rpm is 6 %, which can still be distinguishable. Thus, the undetectable zone is limited to all turn faults at 1482 rpm and 2-turn fault at 2964 rpm.

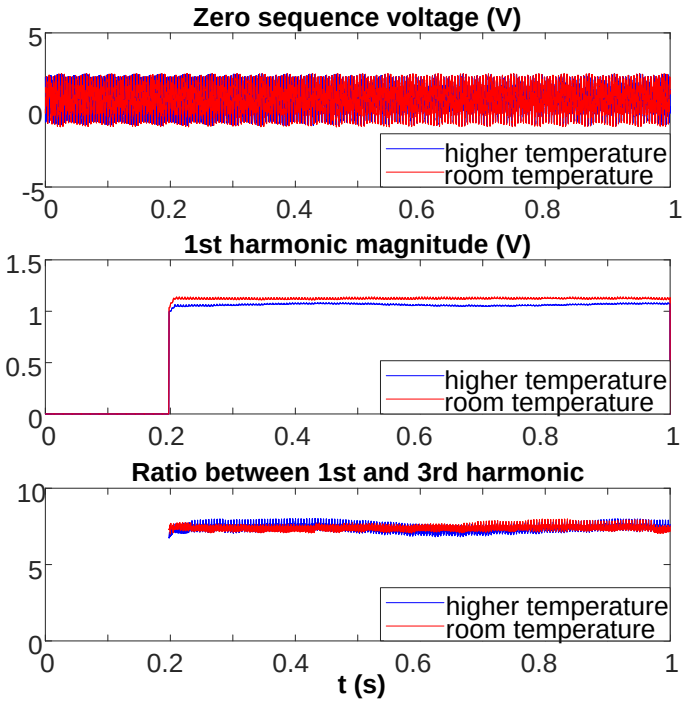

Fig. 6-27 Fundamental and its ratio to 3rd harmonic of zero sequence voltage at two different temperatures

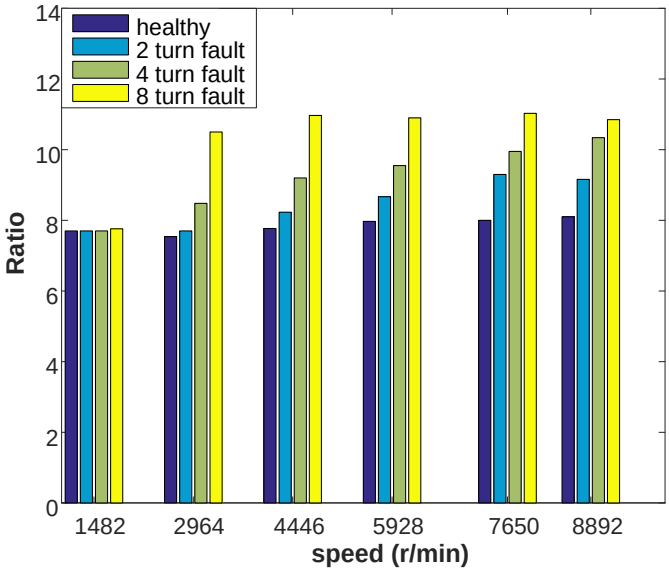

Fig. 6-28 Comparisons of the ratios between fundamental component and 3rd harmonics of zero sequence voltage at different speeds

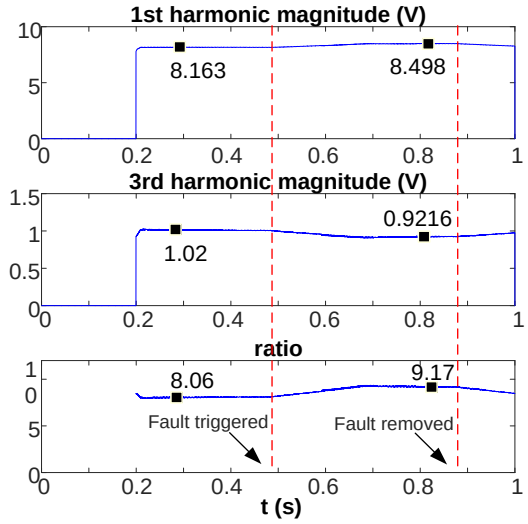

(a) 2-turn fault

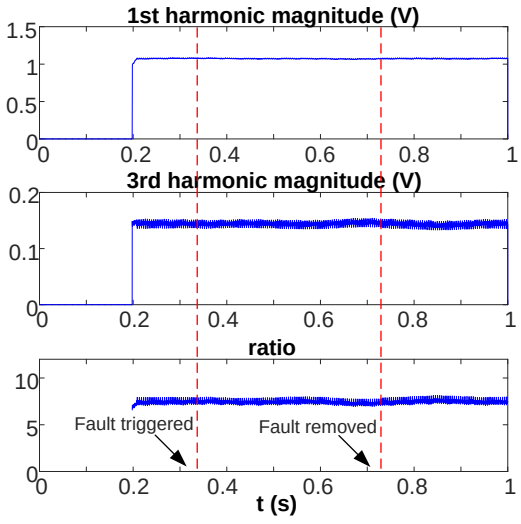

(a) 2-turn fault

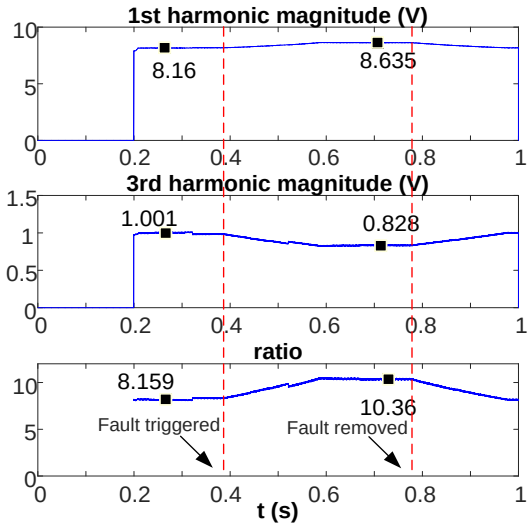

(b) 4-turn fault

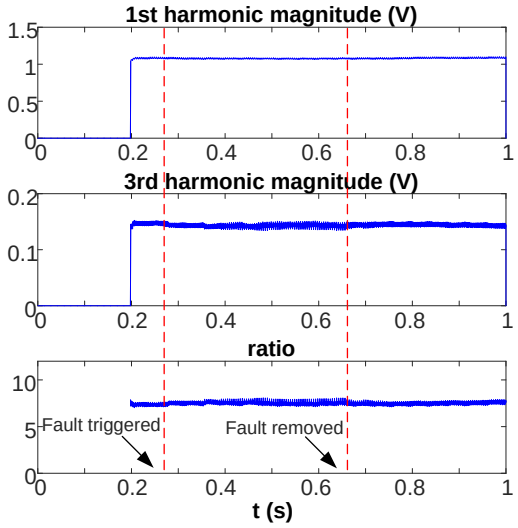

(b) 4-turn fault

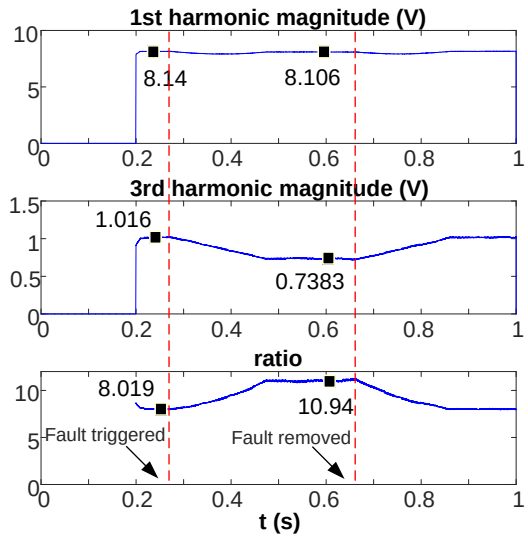

(c) 8-turn fault

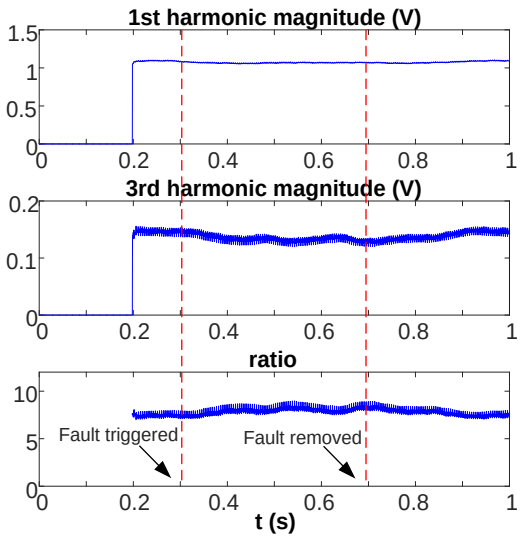

(c) 8-turn fault

Fig. 6-29 Fundamental and 3rd harmonic of zero sequence voltage and their ratio at 8892 rpm

Fig. 6-30 Fundamental and 3rd harmonic of zero sequence voltage and their ratio at 1482 rpm

6.4.5 Fault detection based on switching sideband harmonics in zero sequence voltage

Close examination of the zero sequence voltage waveforms reveals that more significant changes are present in the harmonics associated with the shunt PWM regulation of the output voltage. To illustrate this more clearly, Fig. 6-31 compares the zoomed waveforms of the zero sequence voltage under healthy and 2-turn fault conditions at 1482 rpm. It is evident that harmonic associated with the switching has visibly changed in shape and magnitude. The switching frequency of the shunt PWM regulation is at 4.9 kHz and its interaction with the fundamental produces two dominant sidebands at the frequency of (f_s+f_r) and (f_s-f_r), where f_s and f_r denote the switching frequency and fundamental frequency, respectively. The spectra of the zero sequence voltage under healthy and 2-turn fault conditions at 1482 rpm are compared in Fig. 6-32(a), with the zoomed views in Fig. 6-32(b). They are obtained by executing the FFT function, after reading the packetized data. At 1482 rpm, the fundamental frequency is 223 Hz, and hence the frequencies of interest are f_s-f_r = 4677 Hz and f_s+f_r=5123 Hz. The zoomed spectra show clearly that the changes at these two frequencies are significant, but in opposite direction. Thus, they are compared to the normal value in healthy condition separately, as shown in Fig. 6-33(a) and (b). As can be seen, for the lower sideband, the magnitude is always higher in fault conditions than that in healthy condition, all with larger differences than the previous methods. For the higher sideband, the magnitude can be higher or lower than the normal value in healthy condition, but is highly dependent on the faulted turn number. To enhance the sensitivity to the fault, the differences between the fault and healthy in both higher and lower sidebands are calculated and their absolute values are added, after the normal switching sidebands in healthy condition are recorded. Considering the limit of frequency resolution in the FFT calculation, and in order to minimize the effect of frequency leakage, the neighbouring frequencies around the 2 particular sidebands are also included, and their RMS value is calculated. The expression for the final fault indicator is defined in (6-2).

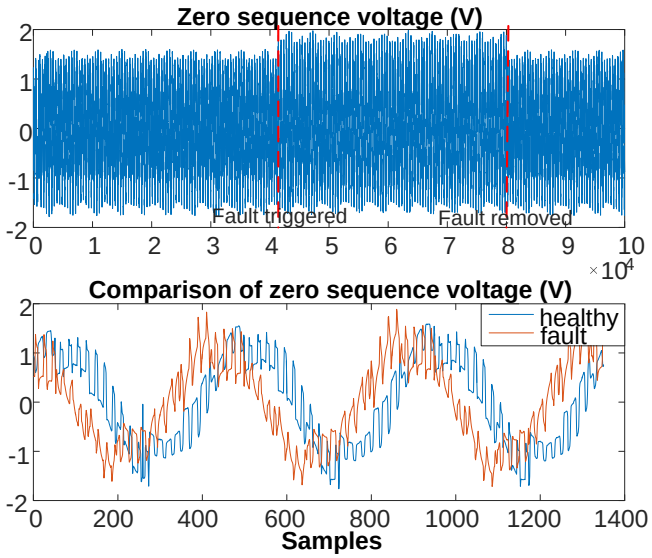

Fig. 6-31 Comparison of zero sequence voltages in healthy and 2-turn fault conditions at 1482 rpm

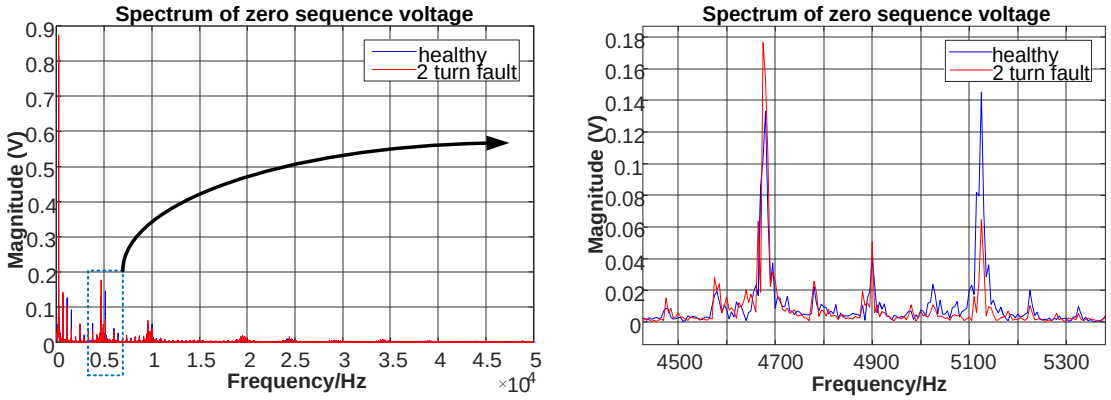

(a) Comparison of spectra (b) Zoomed spectra around switching frequency

Fig. 6-32 Comparison of spectra of zero sequence voltage under healthy and 2-turn fault conditions at 1482 rpm

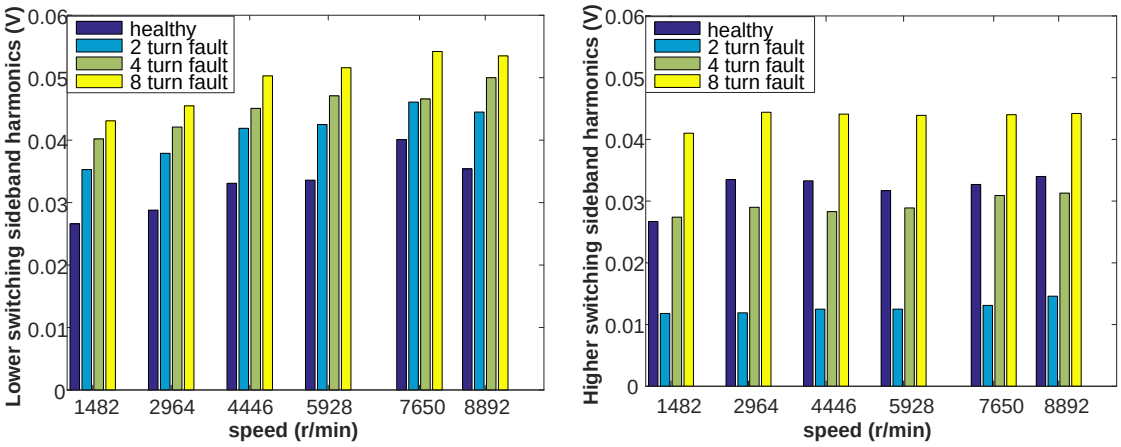

(a) (b)

Fig. 6-33 Comparisons of (a) lower and (b) higher switching sideband harmonics of zero sequence voltage at different speeds

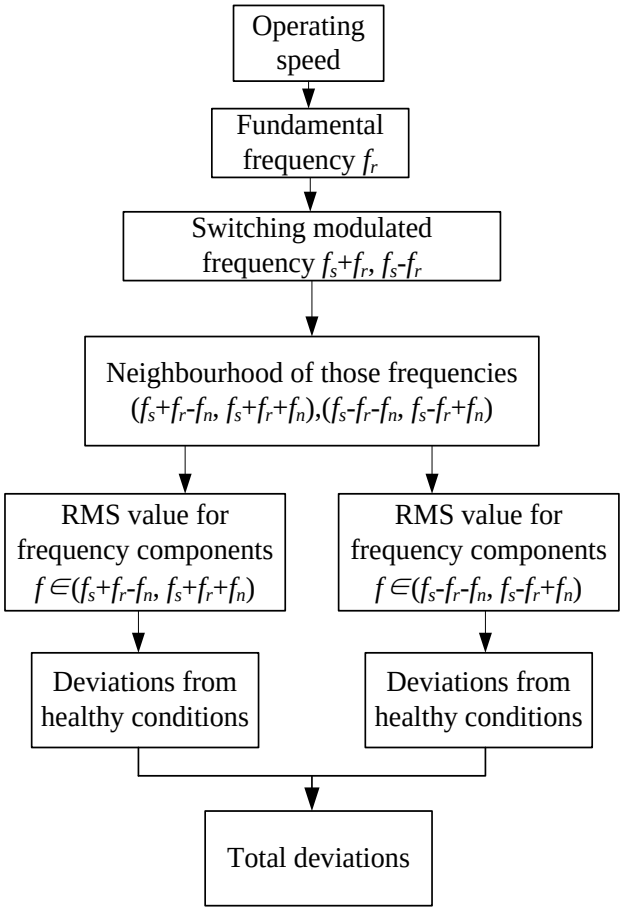

Fig. 6-34 Flow chart of evaluation of the switching sideband components in zero sequence voltage

$$FI = \left| RMS\left[f\big|_{f\in(fs-fr-fn,\,fs-fr+fn)} \right]\Big|_{fault} - RMS\left[f\big|_{f\in(fs-fr-fn,\,fs-fr+fn)} \right]\Big|_{healthy} \right| + \left| RMS\left[f\big|_{f\in(fs+fr-fn,\,fs+fr+fn)} \right]\Big|_{fault} - RMS\left[f\big|_{f\in(fs+fr-fn,\,fs+fr+fn)} \right]\Big|_{healthy} \right| \quad (6\text{-}2)$$

where f_s is the switching frequency, f_r is the fundamental frequency, f_n is the frequencies in the neighbourhood of the two sidebands. The flow chart of the evaluation of the switching sideband components is shown in Fig. 6-34.

Fig. 6-35 compares the variations of the defined fault indicator under the healthy and fault conditions with speed. For the healthy conditions the indicators are obtained from measured data at 2 different tests and they are very small which can be caused by measurement error. In contrast, the change due to the faults can be significant and is conducive to robust fault detection.

The difference in the healthy condition at 1482 rpm at the two different temperatures is also calculated, and the result is 0.0025. Compared to the difference in fault conditions, it will not cause any problems in the fault detection. This result is

expected because the sideband harmonics are mainly influenced by the inductance which is much less temperature dependent than the back-EMF and phase resistance.

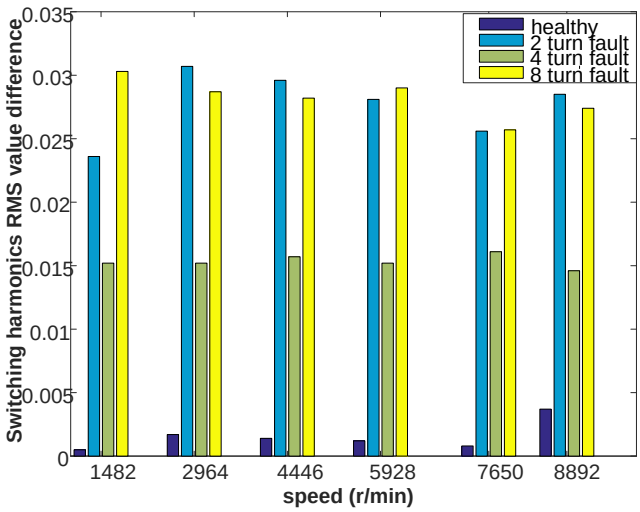

Fig. 6-35 Comparisons of the defined fault indicator based on switching sideband components in zero sequence voltage at different speeds

6.4.6 Fault detection based on 2nd harmonic of phase current vector

Another signal that can be possibly used to monitor the fault is the 2nd harmonic of the phase current vector, calculated in (6-3). It should be a pure dc signal in heathy conditions in a balanced three phase system but will contain the 2nd harmonic when a fault occurs. For the PMA under study, the cables and winding connectors must meet high reliability standard, and hence, a high resistance connection fault can be ruled out. However, with the intrinsic unbalance for this particular machine, the 2nd harmonic also exits in healthy condition. But the occurrence of a fault will deviate the magnitude of the 2nd harmonic from the reference value in healthy condition. Thus, once those reference magnitudes are recorded in different operating conditions, the actual magnitude of 2nd harmonic can be monitored and compared, and the turn fault detection can be achieved.

The current vector magnitude and its 2nd harmonic in 2-, 4-, and 8-turn fault conditions at 8892 rpm and 1482 rpm are shown in Fig. 6-36 and Fig. 6-37, respectively. It can be seen that all fault conditions can be easily detected at 8892 rpm, while both 4-turn and 8-turn faults are also detectable at 1482 rpm. This result is better than the detecting performance based on the fundamental or RMS zero sequence voltages, where all turn faults at 1482 rpm cannot be detected. Fig. 6-38 compares the variations of the

2nd harmonics under healthy and fault conditions with speed. It can be seen that the changes due to the 2-turn fault is relatively small, but the detectability increases with the faulted turn number.

The effect of temperature on the 2nd harmonic of the phase current magnitude is also assessed by experiments and the results at the two different temperatures are shown in Fig. 6-39. It is seen that the change due to temperature is in similar range caused by a 2-turn fault. Thus, the reliability of the fault detection using this indicator can also be degraded by the temperature variation.

$$
\begin{aligned}
i_\alpha &= i_a - \frac{1}{2}(i_b + i_c) \\
i_\beta &= \frac{\sqrt{3}}{2}(i_b - i_c) \\
i_{vector} &= \sqrt{i_\alpha{}^2 + i_\beta{}^2}
\end{aligned}
\tag{6-3}
$$

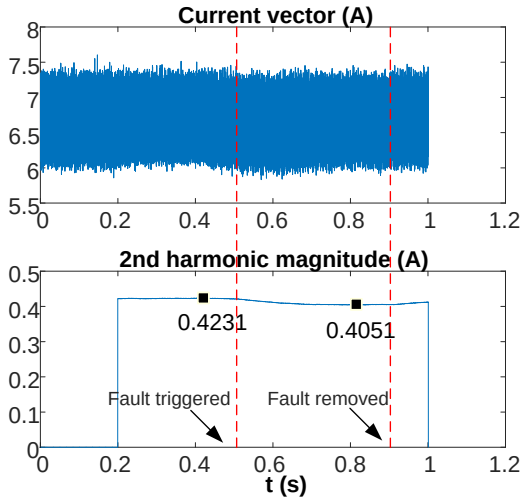

(a) 2-turn fault

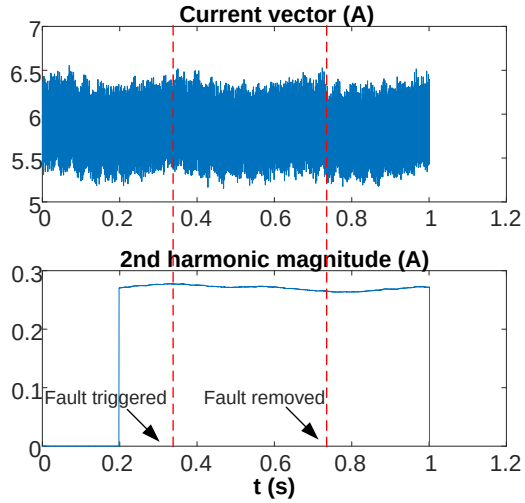

(a) 2-turn fault

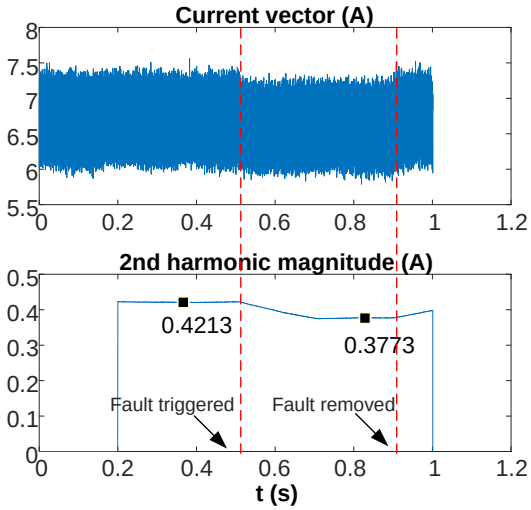

(b) 4-turn fault

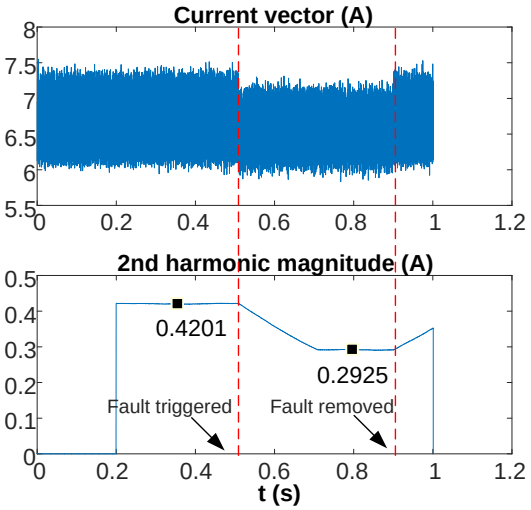

(c) 8-turn fault

Fig. 6-36 2nd harmonics of current vector at 8892 rpm

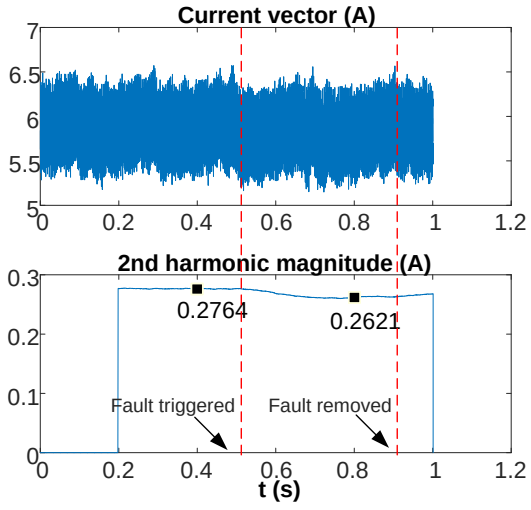

(b) 4-turn fault

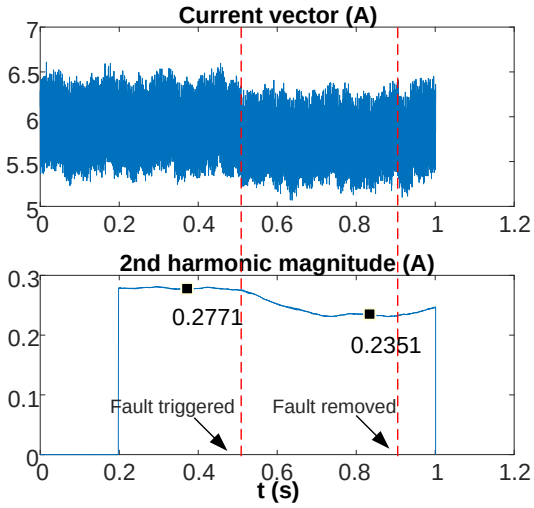

(c) 8-turn fault

Fig. 6-37 2nd harmonics of current vector at 1482 rpm

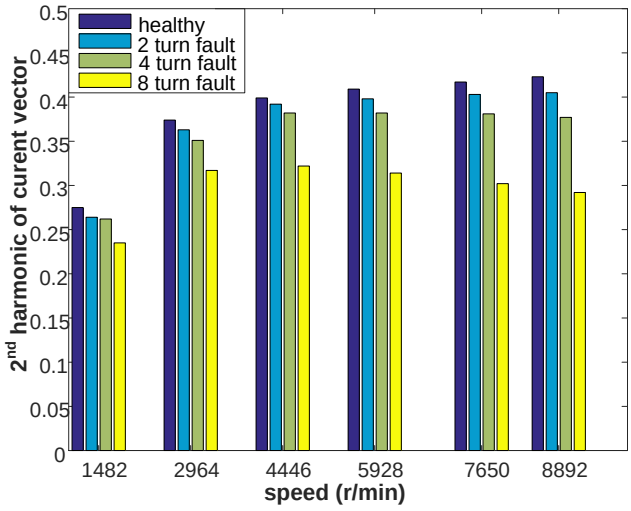

Fig. 6-38 Comparisons of 2nd harmonic of current vector at different speeds

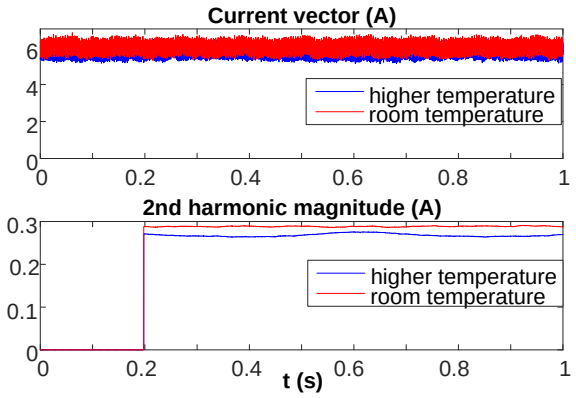

Fig. 6-39 Current vector and its 2nd harmonic in healthy condition at 1482rpm at two different temperatures

6.5 Conclusion

The testing process and results for health monitoring of a permanent magnet alternator are presented, as well as the essential hardware, software and the set-up of the test rig. Four methods are tested for the detection of turn fault. They are compared in different numbers of fault turns, different speeds and temperatures. The sensitivity to turn fault and the robustness of each method are evaluated. It has been shown that the turn fault detection method based on monitoring the ratio between the fundamental and the 3rd harmonic of the zero sequence voltage is effective in most operating conditions but fails to detect fault at speeds lower than 2000 rpm. The method based on the switching sideband harmonics of zero sequence voltage are more sensitive to turn fault, equally effective at low speed, and immune to the temperature variation, albeit the access to the neutral point of the PMA and the provision of an external neutral point are needed. The method based on monitoring of the 2nd harmonic of phase current vector is less intrusive but more susceptible to temperature variations. In conclusion, the switching sideband harmonics of zero sequence voltage are the best turn fault indicators for the permanent magnet alternator under study.

CHAPTER 7 Conclusions and Future Work

7.1 Conclusions

Since the permanent magnet machines can provide high torque density and high efficiency, they are being increasingly applied into areas such as electrical vehicle and "more electric" aircraft. However, the requirement for high availability or reliability in these safety critical applications necessitates the research into the health monitoring of the machine. Among all the possible faults in permanent magnet machines, the turn fault is the most severe and requires swift detection. This thesis has studied the techniques to detect the turn fault, mainly by improving fault feature extraction and classification and facilitating detection during transient states. The main contributions of the research are summarised as follows.

7.1.1 Turn fault detection based on current residual

The fault signatures manifested as the 2nd harmonic in the dq axis currents and voltages, including their variants such as the negative sequence components and the park's vector, have been used for the detection of turn fault in the existing techniques. However, the fault signature is relatively small compared to the fundamental, which compromise detection sensitivity. Also, since the fault feature essentially spreads in the dq axis currents and voltages, and influenced by the current controller bandwidth, the detection techniques based on the conventional motor current signature analysis are sensitive to noise and operating conditions.

The use of current residual can address these two problems. Although the fault feature in the current residual may be affected by the modelling error, the influence can be minimized through the improvement of the model accuracy. Thus, a more exclusive extraction of the fault signature can be achievable. Also, through the mathematical derivation of the current residual and the validation of the experimental tests, it has been shown that the influence of the current controller bandwidth on the fault signature is largely reduced, while the signal-to-noise ratio of the fault feature extraction is improved.

7.1.2 Angular integration of dc component

In order to analyse the frequency components for fault detection, FFT is usually applied. To cope with the transient states during speed or torque changes, more complex

time-frequency analysis techniques have to be used. However the required computational and data processing resources for online fault detection is a main concern. In the case of only one frequency component to be processed, its extraction can be more flexible, especially if the rotor position of the machine available as usually the case in a PM machine drive.

By transforming the current residual into the negative rotating dq frame, the fault signature becomes a dc component. With the angular integration, the dc component can be calculated more straightforward when the integral interval is set to one electrical cycle. Since the PM rotor position information is usually available for drive control, this angular integration can be practically realised. The effect of varying speed can be eliminated, while the effect of varying current can be tackled with a transient evaluation process. Consequently, the detection can be effective during transient operation and the risk of false alarm in transient state can be minimised.

7.1.3 Turn fault detection based on PWM ripple currents

Apart from the analysis of the fault feature in the fundamental frequency components, the high frequency components are also investigated. The intrinsic switching sideband voltage harmonics due to the PWM operation produce PWM ripple currents which can be exploited for fault detection. With extensive theoretical analysis, the behaviour of the PWM ripple currents are predicted. A specific cluster of the sideband harmonics of the phase PWM ripple currents is filtered and its magnitude is measured by a RMS detector on the designed circuit board. The relative strength or the asymmetry among the three phase ripple currents is used as the fault indicators. The technique has been validated in a 5-phase fault tolerant SPM, a 3-phase SPM, and a 9-phase triple redundant IPM. Although the magnitudes of the proposed fault indicators vary in different cases due to different machine structures and parameters, their immunity to transient states is validated in all the cases.

7.1.4 Turn fault detection and discrimination from HRC fault based on switching harmonic high frequency impedance

Both the fundamental frequency components and the high frequency components are investigated for turn fault detection initially. They both detect the emerging asymmetry in turn fault conditions. However, similar symptoms can also be triggered by a high resistance connection (HRC) fault. The impacts of the turn fault and HRC

fault on the voltage equations at both the fundamental and switching harmonic frequencies are analysed. It has shown that the symmetry of PWM ripple currents can be affected by the fundamental components through the modulation index. Thus, a very small asymmetry in the fundamental voltage caused by the high resistance fault would also affect the switching harmonics because they are dependent on modulation index.

The difference in the symmetry of the calculated high frequency impedance has been adopted as the indicator to differentiate the two fault types. This difference is more sensitive to the turn fault since the impedance is dominated by the inductance-driven reactance at high frequency. The fault indicator based on the high frequency impedance symmetry intends to eliminate the impact from the fundamental components, and works well in SPMs. For IPMs, however, the saliency causes the inductance variation with rotor position, and hence introduces another source of disturbance to the fault detection.

7.1.5 Turn fault detection and discrimination from HRC fault based on high frequency voltage injection

The disturbance brought by the saliency in the high frequency impedance based classification is essentially due to dependency of the high frequency switching harmonic voltages on the modulation index, and hence it varies with operating conditions. To solve this problem, additional high frequency voltage injection is applied. The injected high frequency square wave signal is specially designed and incorporated in the SVPWM generation. Since the symmetry of the injected high frequency voltages can be controlled properly, the different fault features in the high frequency impedance are fully reflected on the resultant high frequency currents. Thus, the exclusive detection of the turn fault can be fulfilled.

No extra hardware is needed, and the signal processing can be carried out in the conventional DSP controller and easily implemented. The detection technique also utilizes the dominance of the inductance at high frequency, and the inductance asymmetry introduced by a turn fault. Since the fault indicator is based on the frequency components of the injected signals, it is independent of the operating conditions in both healthy and fault states.

7.1.6 Turn fault and HRC fault detection base on zero sequence voltage

The resistor network connected to the three phase winding terminals creates an artificial point, which acts as the healthy reference point for the winding neutral point. Thus, the voltage between them is mainly the fault signatures that can be used for the fault diagnostics. Both the fundamental and switching sideband harmonic high frequency components are analysed in both turn fault and HRC fault conditions. And the significant difference in the high frequency zero sequence voltage is exploited for the detection of turn fault. The fault indicators for both fault types are specifically designed to minimise the effect from the operating conditions. It exhibits good capability to detect and classify these two fault types, and robustness to transient states, albeit the winding neutral point and the additional hardware are required.

7.1.7 Comparisons of all the proposed turn fault techniques

Since the turn fault detection is the primary focus of this thesis, all the proposed techniques are summarised and compared in Table 7-1. All the evaluations are based on test results on the same 9-phase triple redundant PM machine.

Initially, only turn fault is assumed to be the most likely to occur while other types of fault are not considered. Both the fundamental frequency components and the high frequency components are investigated, and the robustness to transient states can be achieved. The current residual based method requires a machine model while the other requires the additional circuit board to pre-process the PWM ripple currents before being sampled by the DSP. When the differentiation from the HRC fault is considered, the detection of turn fault is mainly focused on the asymmetry of the inductance and the detection at high frequency. The robustness to transient states is preserved, and no machine model is required. Except for the high frequency voltage injection method, the other two need additional hardware to process the signals in the similar way as that in the PWM ripple current based method. Also, the winding neutral point is required for the zero sequence voltage based method, but not necessary for the others.

Table 7-1 Summary and comparisons of all the proposed techniques

Proposed turn fault techniques	False alarm by HRC fault?	Applicable to no load condition?	Robust to transient states?	Machine model?	Additional hardware?
Current residual based	Yes	Yes	Yes	Yes	No

PWM ripple based	Yes	Yes	Yes	No	Yes
High frequency currents & impedance based	No	Yes	Yes	No	Yes
High frequency injection based	No	Yes	Yes	No	No
Zero sequence voltage based	No	Yes	Yes	No	Yes

7.2 Future work

Although several novel turn fault detection techniques are proposed and discussed in this thesis, further research is required in the following aspects.

7.2.1 Turn fault when fault resistance is not zero

The emulated turn fault conditions in thesis assume the fault resistance is zero. However, in fact it usually takes some time for the insulation resistance to degrade to zero from infinite. During that deterioration process, there might exist a point when the generated heat is the largest causing the most severe damage. This is the point where the fault detection should be able to detect the fault and mitigation measures should be activated. When the fault resistance is non zero, the fault signature will be even smaller, and this raises further challenges for the fault detection. Thus, further research to address this problem is required and the impact of non-zero fault resistance on the fault indicators should be assessed.

7.2.2 The prognostics for turn fault

The techniques in this thesis are all focused on the diagnostics when turn fault occurs, thus, a fast response is an essential requirement. Since the insulation degradation takes time, it is possible to estimate remaining useful life of insulation based on probability distribution model and operating conditions. The insulation degradation mechanism and model should be investigated together with appropriate data-driven approaches.

7.2.3 The classification from other fault types

As has been mentioned in Chapter 1, there exist many types of fault in PM machines. It is difficult to detect a type of fault exclusively. Some of these faults such as rotor eccentricity and partial demagnetisation result in similar harmonic patterns, thus the conventional techniques based on machine current signal analysis (MCSA) fail to classify them. As has been shown on the other hand, both turn fault and high resistance connection fault causes phase asymmetry. Therefore, a more in-depth and comprehensive research on the impact of different fault types on a specific machine is needed, in order to achieve a complete fault detection and classification for all possible faults.

A Appendix

A1 The DSP codes for the current residual detection

The DSP 28377D microchip is used primarily for the machine control in the all the experimental tests for the 9-phase machine in this thesis. The current residual based turn fault detection in Chapter 2 can be fully processed simultaneously in the DSP controller without any side effects. The following codes are specifically designed for this fault detection technique, and are inserted in the main control codes.

```
//*****************************//
//*****flux linkage calculation*****//
//*****************************//
theta_temp=(rotor.theta*180/PI-150)/3.000-5;
      if (theta_temp >= 0)
      {
         theta_lookup=theta_temp+5;
      }
      else
      {
         theta_lookup=theta_temp+125;
      }
psid_a=(vd_cmd-Rs*id_est+psiq_pre*rotor.we+Ll*iq_est*rotor.we)*Ts+psid_pre;
psiq_a=(vq_cmd-iq_est*Rs-psid_pre*rotor.we-Ll*id_est*rotor.we)*Ts+psiq_pre;
      psid_pre=psid_a;
      psiq_pre=psiq_a;
      psid=psid_a-Ll*id_est;
      psiq=psiq_a-Ll*iq_est;
/*****************************************************/
/*** estimate the current by interpolating in the lookup table.**/
/*****************************************************/
id_est=extrap3d(theta_vector, psiq_vector, psid_vector, id_table, 49, 16, 16, theta_lookup, psiq, psid);

iq_est=extrap3d(theta_vector, psiq_vector, psid_vector, iq_table, 49, 16, 16, theta_lookup, psiq, psid);

        Cpu2toCpu1.id_est = id_est; // send id_est to cpu1
        Cpu2toCpu1.iq_est = iq_est; // send iq_est to cpu1

/*********************************/
/********residual calculation********/
/*********************************/
            id_mea = current.q;
            iq_mea = current.q;
            id_re=id_mea-id_est;
            iq_re=iq_mea-iq_est;
```

```
        k=k+1;
        if (k>max-1)
            k=k-max;

        kk=k-1;
        if (kk<0)
             kk=max-1;

            angle = rotor.theta;

            id_re_nega = id_re*cos(2*angle)-iq_re*sin(2*angle);
            iq_re_nega = id_re*sin(2*angle)+iq_re*cos(2*angle);

            angle_d=angle-angle_pre;

            if (angle_d<0)
            {
                    angle_d=angle_d+2*PI;
            }

             angle_a[k]=angle_a[kk]+angle_d;          //angle accumulation
             if  (angle_a[k]>=angle_max)
             {
                    angle_a[k]=angle_a[k]-angle_max;
  }
/*************************************/
/***********angular integration**********/
/*************************************/
            integ_iqn_re[k]=iq_re_nega*angle_d+integ_iqn_re[kk];
            integ_idn_re[k]=id_re_nega*angle_d+integ_idn_re[kk];

            j=kk;
            interval=1;

            if (integ_iqn_re[k]>=integ_max)
            {
                     integ_iqn_re[k]=integ_iqn_re[k]-integ_max;
             }
            else if (integ_iqn_re[k]<=-integ_max)
            {
                    integ_iqn_re[k]=integ_iqn_re[k]+integ_max;
            }
            if (integ_idn_re[k]>=integ_max)
            {
                     integ_idn_re[k]= integ_idn_re[k]-integ_max;
            }
            else if (integ_idn_re[k]<=-integ_max)
            {
```

```
                    integ_idn_re[k]= integ_idn_re[k]+integ_max;
            }

/************************************/
/********looking for 2pi interval*********/
/************************************/

            j=k;
            n=0;
            interval=1;
            step_index=fs*(2*PI)/rotor.we-5;
        j=j-step_index;
        j=(j<0)?(j+max):j;
        interval=angle_a[k]-angle_a[j];
         while((n<15)&&(interval<2*PI))
         {
                    n+=1;
                    j-=1;
                    j=(j<0)?(j+max):j;
                    interval=angle_a[k]-angle_a[j];
                    interval=(interval<0)?(interval+angle_max):interval;

        }

            delta_index=k-j;
            sum_iqn_re=integ_iqn_re[k]-integ_iqn_re[j];
            if (sum_iqn_re<-9000)
            {
                    sum_iqn_re=sum_iqn_re+integ_max;
            }
            else if (sum_iqn_re>9000)
            {
                    sum_iqn_re=sum_iqn_re-integ_max;
            }
            sum_idn_re=integ_idn_re[k]-integ_idn_re[j];
            if (sum_idn_re<-9000)
            {
                    sum_idn_re=sum_idn_re+integ_max;
            }
            else if (sum_idn_re>9000)
            {
                    sum_idn_re=sum_idn_re-integ_max;
            }

            iqn_re_dc = sum_iqn_re/interval;
            idn_re_dc = sum_idn_re/interval;

            in_re_vector=sqrt(idn_re_dc* idn_re_dc+ iqn_re_dc* iqn_re_dc);
```

```
/*********************************/
/********decision making **********/
/*********************************/
            if (in_re_vector <fault_threshold)
              {
                    fault_count=0;
              }
              else
             {
                    fault_count= fault_count +angle_d;
             }

            if (fault_count>2*PI)
                  fault_detected=1;
            else
                  fault_detected=0;

            angle_pre=angle;
```

A2 The DSP codes for the high frequency voltage injection

The high frequency voltage injection based turn fault detection are also fully implemented in the DSP controller. The codes for the voltage injection, the digital bandpass filter, and the RMS calculation are listed below.

```
//************************************//
//**********pulse injection*************//
//************************************//
            Modu_counter++;
            if (Modu_counter>=7)
            {
                  Modu_counter=1;
            }
            if (Modu_counter==1)
               {
                  Modu_pulse_a=1;
                  Modu_pulse_b=0;
                  Modu_pulse_c=1;
               }
            else if (Modu_counter==2)
               {
                  Modu_pulse_a=1;
                  Modu_pulse_b=0;
                  Modu_pulse_c=0;
               }
```

```
        else if (Modu_counter==3)
            {
               Modu_pulse_a=1;
               Modu_pulse_b=1;
               Modu_pulse_c=0;
            }
        else if (Modu_counter==4)
            {
               Modu_pulse_a=0;
               Modu_pulse_b=1;
               Modu_pulse_c=0;
            }
        else if (Modu_counter==5)
            {
               Modu_pulse_a=0;
               Modu_pulse_b=1;
               Modu_pulse_c=1;
            }
        else
            {
               Modu_pulse_a=0;
               Modu_pulse_b=0;
               Modu_pulse_c=1;
            }

             Modu_injection=0.05;
             Modu_a=Modu_injection*(Modu_pulse_a-0.5);
             Modu_b=Modu_injection*(Modu_pulse_b-0.5);
             Modu_c=Modu_injection*(Modu_pulse_c-0.5);

EPwm1Regs.CMPA.bit.CMPA = HALFPERIOD_10kHz
+(int)((HALFPERIOD_10kHz)*(Ta+Modu_a));
EPwm2Regs.CMPA.bit.CMPA = HALFPERIOD_10kHz
+(int)((HALFPERIOD_10kHz)*(Tb+Modu_b));
EPwm3Regs.CMPA.bit.CMPA = HALFPERIOD_10kHz
+(int)((HALFPERIOD_10kHz)*(Tc+Modu_c));


    /*************************************************************/
    /***********digital band pass filter centre frequency 1667Hz.*********/
    /*************************************************************/
    ia=current.u1;
    ib=current.u2;
    ic=current.u3;

ia_x1=ia*bz[0]+ia_p1*bz[1]+ia_p2*bz[2]+ia_p3*bz[3]+ia_p4*bz[4];
ia_x2=ia_BPF_p1*az[1]+ia_BPF_p2*az[2]+ia_BPF_p3*az[3]+ia_BPF_p4*az[4];
ia_BPF=(ia_x1-ia_x2)/az[0];
```

```
    ia_p4=ia_p3;
    ia_p3=ia_p2;
    ia_p2=ia_p1;
    ia_p1=ia;

    ia_BPF_p4=ia_BPF_p3;
    ia_BPF_p3=ia_BPF_p2;
    ia_BPF_p2=ia_BPF_p1;
    ia_BPF_p1=ia_BPF;

ib_x1=ib*bz[0]+ib_p1*bz[1]+ib_p2*bz[2]+ib_p3*bz[3]+ib_p4*bz[4];
ib_x2=ib_BPF_p1*az[1]+ib_BPF_p2*az[2]+ib_BPF_p3*az[3]+ib_BPF_p4*az[4];
ib_BPF=(ib_x1-ib_x2)/az[0];
    ib_p4=ib_p3;
    ib_p3=ib_p2;
    ib_p2=ib_p1;
    ib_p1=ib;

    ib_BPF_p4=ib_BPF_p3;
    ib_BPF_p3=ib_BPF_p2;
    ib_BPF_p2=ib_BPF_p1;
    ib_BPF_p1=ib_BPF;

ic_x1=ic*bz[0]+ic_p1*bz[1]+ic_p2*bz[2]+ic_p3*bz[3]+ic_p4*bz[4];
ic_x2=ic_BPF_p1*az[1]+ic_BPF_p2*az[2]+ic_BPF_p3*az[3]+ic_BPF_p4*az[4];
ic_BPF=(ic_x1-ic_x2)/az[0];

    ic_p4=ic_p3;
    ic_p3=ic_p2;
    ic_p2=ic_p1;
    ic_p1=ic;

    ic_BPF_p4=ic_BPF_p3;
    ic_BPF_p3=ic_BPF_p2;
    ic_BPF_p2=ic_BPF_p1;
    ic_BPF_p1=ic_BPF;

    /*************************************/
    /*****RMS calculation within one cycle****/
    /*************************************/
            k=k+1;
            if (k>max-1)
                k=k-max;

            kk=k-1;
            if (kk<0)
                kk=max-1;

            angle=rotor.theta;
```

```
                angle_d=angle-angle_pre;
                if (angle_d<0)
                {
                        angle_d=angle_d+2*PI;
                }

                angle_a[k]=angle_a[kk]+angle_d;
                if  (angle_a[k]>=angle_max)
                {     angle_a[k]=angle_a[k]-angle_max;}

        integ_ia_BPF[k]=ia_BPF*ia_BPF+integ_ia_BPF[kk];
        integ_ib_BPF[k]=ib_BPF*ib_BPF+integ_ib_BPF[kk];
        integ_ic_BPF[k]=ic_BPF*ic_BPF+integ_ic_BPF[kk];

                if (integ_ia_BPF[k]>=integ_max)
                {
                        integ_ia_BPF[k]=integ_ia_BPF[k]-integ_max;
                }
                else if (integ_ia_BPF[k]<=-integ_max)
                {
                        integ_ia_BPF[k]=integ_ia_BPF[k]+integ_max;
                }

                if (integ_ib_BPF[k]>=integ_max)
                {
                        integ_ib_BPF[k]=integ_ib_BPF[k]-integ_max;
                }
                else if (integ_ib_BPF[k]<=-integ_max)
                {
                        integ_ib_BPF[k]=integ_ib_BPF[k]+integ_max;
                }

                if (integ_ic_BPF[k]>=integ_max)
                {
                        integ_ic_BPF[k]=integ_ic_BPF[k]-integ_max;
                }
                else if (integ_ic_BPF[k]<=-integ_max)
                {
                         integ_ic_BPF[k]=integ_ic_BPF[k]+integ_max;
                 }

        /************************************/
        /********looking for 2pi interval*********/
        /************************************/
                j=k;
                n=0;
                interval=1;
                step_index=fs*(2*PI)/rotor.we-5;
```

```
j=j-step_index;
j=(j<0)?(j+max):j;
interval=angle_a[k]-angle_a[j];
while((n<15)&&(interval<2*PI))
{
        n+=1;
         j-=1;
        j=(j<0)?(j+max):j;
        interval=angle_a[k]-angle_a[j];
        interval=(interval<0)?(interval+angle_max):interval;
 }
 delta_index=k-j;
 if(delta_index<0)
 {
         delta_index=delta_index+max;
  }
        sum_ia_BPF=integ_ia_BPF[k]-integ_ia_BPF[j];
        sum_ib_BPF=integ_ib_BPF[k]-integ_ib_BPF[j];
        sum_ic_BPF=integ_ic_BPF[k]-integ_ic_BPF[j];

  if (sum_ia_BPF<-(integ_max-2000))
  {
        sum_ia_BPF=sum_ia_BPF+integ_max;
   }
        else if (sum_ia_BPF>(integ_max-2000))
   {
        sum_ia_BPF=sum_ia_BPF-integ_max;
    }
   if (sum_ib_BPF<-(integ_max-2000))
    {
        sum_ib_BPF=sum_ib_BPF+integ_max;
    }
   else if (sum_ib_BPF>(integ_max-2000))
    {
        sum_ib_BPF=sum_ib_BPF-integ_max;
    }
    if (sum_ic_BPF<-(integ_max-2000))
    {
        sum_ic_BPF=sum_ic_BPF+integ_max;
    }
   else if (sum_ic_BPF>(integ_max-2000))
    {
        sum_ic_BPF=sum_ic_BPF-integ_max;
    }
    ia_HF_RMS = sqrt(sum_ia_BPF/delta_index);
    ib_HF_RMS = sqrt(sum_ib_BPF/delta_index);
    ic_HF_RMS = sqrt(sum_ic_BPF/delta_index);
    angle_pre=angle;
```

A3 The signal measurement and conditioning circuit design

A PCB board is designed for the measurement and conditioning of phase currents, voltages, and zero sequence voltages. The bandpass filters and RMS detectors are also contained for the pre-processing of these signals before their RMS values are sampled by the DSP controller. The block diagram and the schematics of the signal conditioning circuit board are listed below.

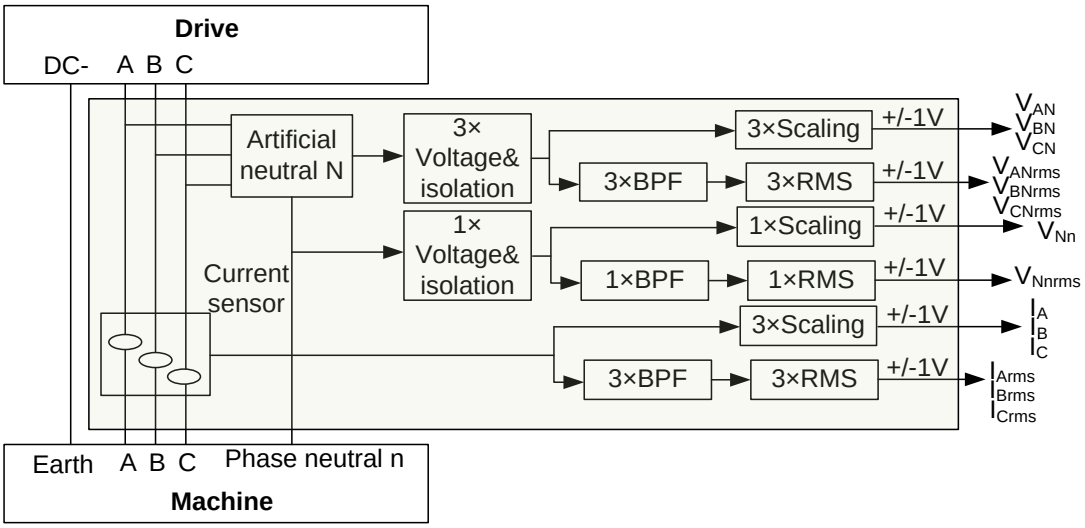

Fig. A-1.The block diagram of the signal conditioning circuit board

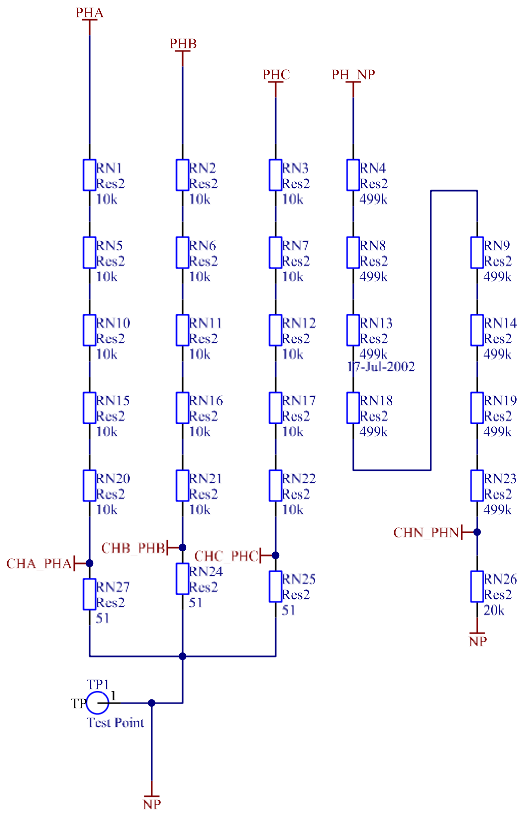

Fig. A-2. The creation of artificial neutral point, and the dividing resistors between it and the phase neutral point

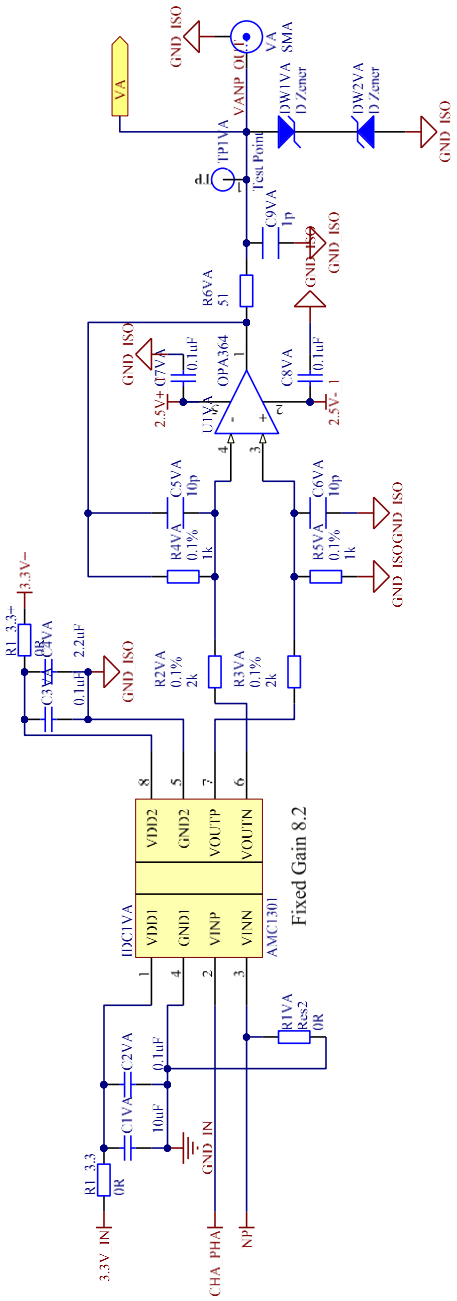

Fig. A-3. Phase voltage measurement

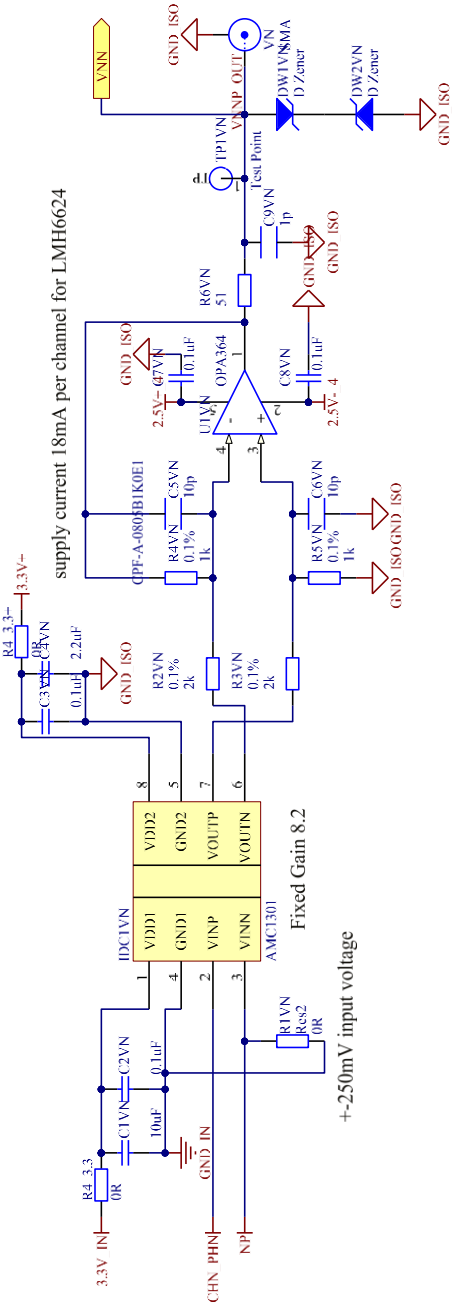

Fig. A-4. Zero sequence voltage measurement

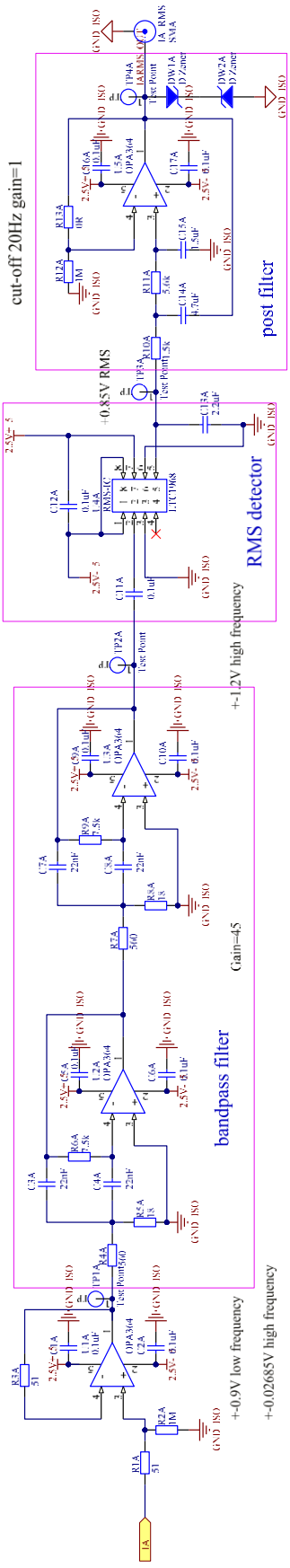

Fig. A-5. High frequency phase current processing

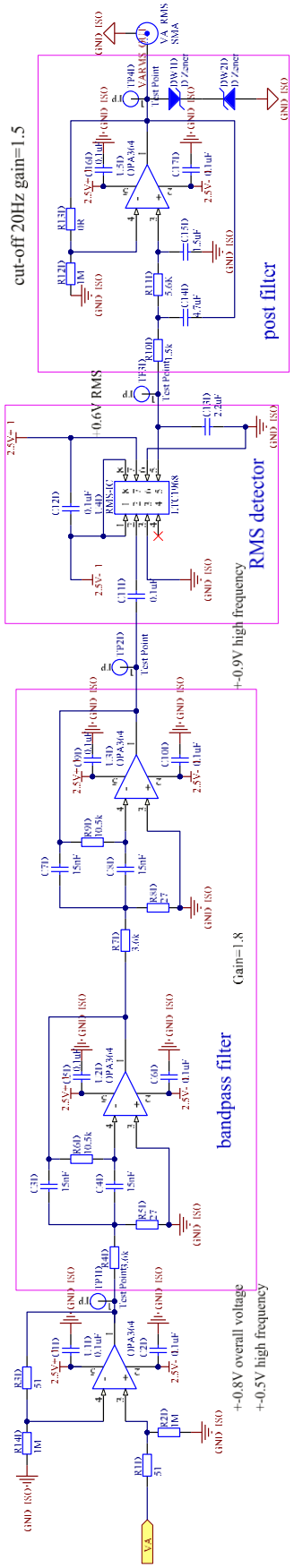

Fig. A-6. High frequency phase voltage processing

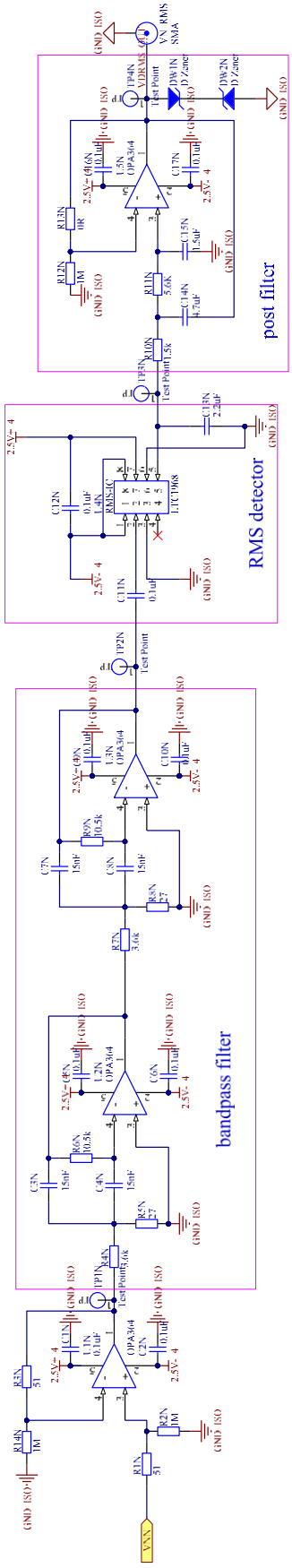

Fig. A-7. High frequency zero sequence voltage processing

The assembled PCB board together with the connections of the ports are shown in Fig. A-8. The outputs of the signal conditioning board are connected to the Xilinx Zynq-7000 SoC ZC702 Evaluation Kit for the signal processing or the oscilloscope for the signal sampling and monitoring.

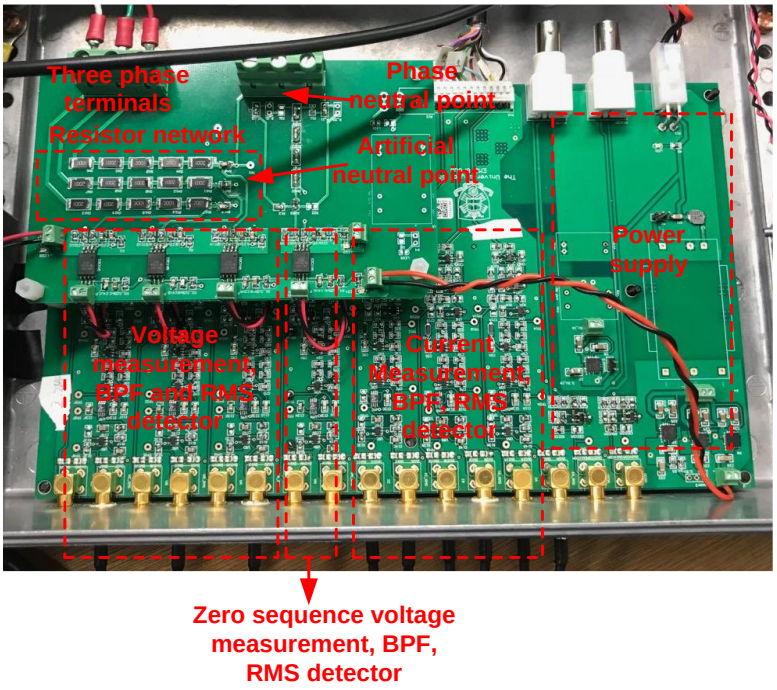

Fig. A-8. The assembled PCB board for the signal conditioning circuit

A4 The data acquisition and digital signal processing of Xilinx Zynq-7000 SoC ZC702 Evaluation Kit

The tests of the PWM ripple current and high frequency impedance based turn fault detection methods on the 9-phase machine are conducted using a Xilinx Zynq-7000 SoC ZC702 evaluation board.

The ZC702 evaluation board for the XC7Z020 SoC provides a hardware environment for developing and evaluating designs targeting the Zynq® XC7Z020-1CLG484C device, which combines programmable logic modules (FPGA) and a 2-core ARM processing system. The ZC702 board provides features common to many embedded processing systems, including DDR3 component memory, a tri-mode Ethernet PHY, general purpose I/O, and two UART interfaces. Other features can be supported using VITA-57 FPGA mezzanine cards (FMC) attached to either of two low pin count (LPC) FMC connectors. The XC7Z020 SoC consists of an SoC-style integrated processing system (PS) and programmable logic (PL) on a single die, as shown in Fig. A-9. The PS integrates two Arm® Cortex™-A9 MPCore™ application

processors, AMBA® interconnect, internal memories, external memory interfaces, and peripherals including USB, Ethernet, SPI, SD/SDIO, I2C, CAN, UART, and GPIO. The PS runs independently of the PL and boots at power-up or reset. An FMC112 Mezzanine Card which provides 12 A/D 14-bit 125 MSPS channels samples all the required signals from the signal conditioning PCB for the specific method, and is plugged onto the ZC702 board, as shown in Fig. A-10, and Fig. A-11.

The FPGA unit on the XC7Z020 SoC is programmed graphically by configuring different functional blocks in Vivado software, to down sample the signals at the rate of 100 KS/s and save into a memory. The PS is running Debian Linux system, through which many software and libraries can be installed directly in order to fulfil a particular task. The reading and processing of the data are programmed using C code, and run under the Linux environment. The processing C program for the PWM ripple current method on the 9-phase machine is given below.

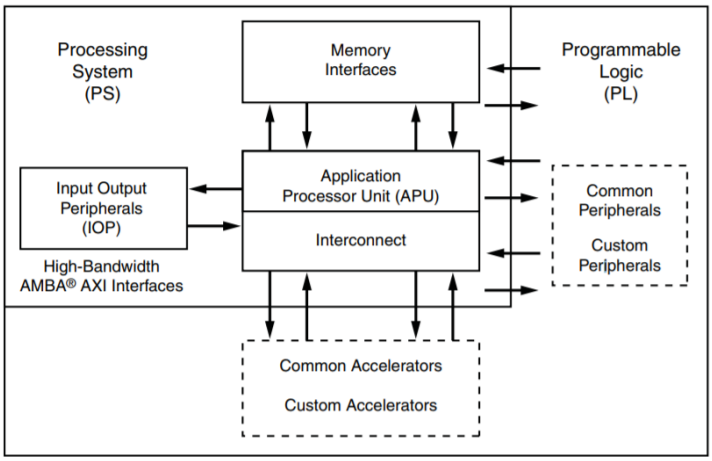

Fig. A-9. High-level block diagram of XC7Z020

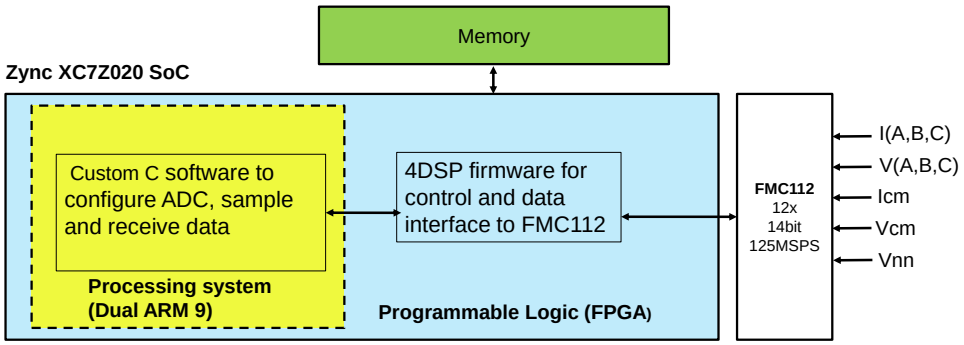

Fig. A-10. Block diagram of the signal processing system

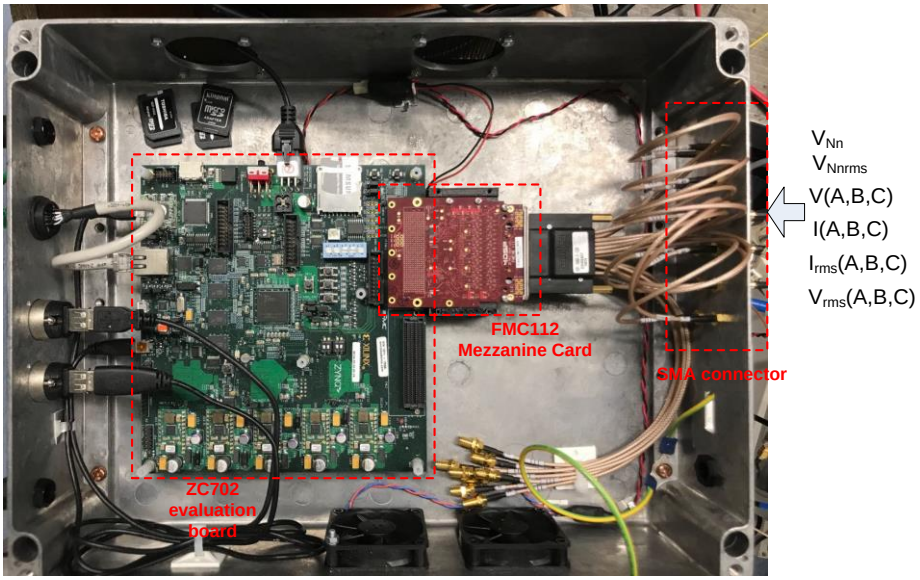

Fig. A-11. The assembled signal processing system

```
/*****************************************************************/
/**********************main.c in Zynq PS**************************/
/**************PWM ripple current based turn fault detection*********/
/*****************************************************************/
printf("starting reading loop\n");
total_count=0;
tfConfigure();
while(!tfCheckADCRunning())
{
        tfStopADC();
        tfStartADC();
}

    while(times<times_limit)
    {
        times++;
        printf("reading times = %d\n", times);
        /*****************************************/
        rowCount = tfReadNData(DATA_LENGTH);
        printf("rowcount = %d\n", rowCount);
        /*****************************************/
        printf("getting ia_rms \n");
        ia_rms_raw = tfChannelX(0);
        ib_rms_raw = tfChannelX(1);
        ic_rms_raw = tfChannelX(2);

        if (rowCount > 0)
        {
            for (b = 1; a < rowCount ; a++)
            {
```

```
                        ia_rms_real[a]=-1*(double)ia_rms_raw[a]/16384.000;
                        ib_rms_real[a]=-1*(double)ib_rms_raw[a]/16384.000;
                        ic_rms_real[a]=-1*(double)ic_rms_raw[a]/16384.000;
                        total_count++;
                        x++;
                        ia_rms_integ[a]=ia_rms_integ[a-1]+ia_rms_real[a];
                        ib_rms_integ[a]=ib_rms_integ[a-1]+ib_rms_real[a];
                        ic_rms_integ[a]=ic_rms_integ[a-1]+ic_rms_real[a];

                    if (a>interval)
                    {
                        sum_ia_rms=ia_rms_integ[a]-ia_rms_integ[a-interval];
                        sum_ib_rms=ib_rms_integ[a]-ib_rms_integ[a-interval];
                        sum_ic_rms=ic_rms_integ[a]-ic_rms_integ[a-interval];
                        ia_rms_filter[a]=sum_ia_rms/interval;
                        ib_rms_filter[a]=sum_ib_rms/interval;
                        ic_rms_filter[a]=sum_ic_rms/interval;

                        ia_rms_net[a]=ia_rms_filter[a]-ia_rms_offset;
                        ib_rms_net[a]=ib_rms_filter[a]-ib_rms_offset;
                        ic_rms_net[a]=ic_rms_filter[a]-ic_rms_offset;

                        kiab_net[a]=(ia_rms_net[a])/(ib_rms_net[a]);
                        kibc_net[a]=(ib_rms_net[a])/(ic_rms_net[a]);
                        kica_net[a]=(ic_rms_net[a])/(ia_rms_net[a]);

                        ia_rms_cali[a]=ia_rms_net[a];
                        ib_rms_cali[a]=ib_rms_net[a]*kiab_cali;
                        ic_rms_cali[a]=ic_rms_net[a]/kica_cali;
                        kiab_net_cali[a]=kiab_net[a]/kiab_cali;
                        kibc_net_cali[a]=kibc_net[a]/kibc_cali;
                        kica_net_cali[a]=kica_net[a]/kica_cali;

    ki_mean=(kiab_net_cali[a]+kibc_net_cali[a]+kica_net_cali[a])/3;
    i_SD[a]=sqrt(((kiab_net_cali[a]-ki_mean)*(kiab_net_cali[a]-
    ki_mean)+(kibc_net_cali[a]-ki_mean)*(kibc_net_cali[a]-
    ki_mean)+(kica_net_cali[a]-ki_mean)*(kica_net_cali[a]-ki_mean))/3);

                    }
                    a++;

                    }
            }
              else
              {
                    printf("data error, please try again\n\n");
              }
}
```

List of Figures

Fig. 1-1 Failure progress in time line 4

Fig. 1-2 Diagnostic program 5

Fig. 1-3 Distribution of faults in [21] 7

Fig. 1-4 Distribution of faults in [22] 7

Fig. 1-5 Fault types in permanent magnet machines 7

Fig. 1-6 Equivalent circuits of (a) turn-to-turn fault and (b)HRC fault 9

Fig. 1-7 Static and dynamic eccentricity 11

Fig. 2-1 Equivalent circuit of a three phase machine driving system 25

Fig. 2-2 Self- and mutual- inductances of phase A 26

Fig. 2-3 Permanent magnet flux linkages 27

Fig. 2-4 Back EMF at 4000 rpm 27

Fig. 2-5 Equivalent circuit and parameters in turn fault condition 29

Fig. 2-6 Permanent magnet machine current control diagram 32

Fig. 2-7 Equivalent transfer function block diagrams to the 2nd harmonic disturbances due to a turn fault in (a) d-axis and (b) q-axis. 33

Fig. 2-8 The amplitude frequency curve of the control diagram with 2nd harmonic disturbances 34

Fig. 2-9 Voltage residual generation structure 35

Fig. 2-10 Flux linkage maps versus d- and q-axis currents at rotor position = 0°. (a) d-axis flux linkage. (b) q-axis flux linkage. 36

Fig. 2-11 Current maps versus d- and q-axis flux linkages at rotor position =0°. (a) d-axis current. (b) q-axis current. 37

Fig. 2-12 Current residual generation structure 38

Fig. 2-13 Fault detection flow chart 40

Fig. 2-14 Triple redundant PMA SynRM with segregated windings 41

Fig. 2-15 The nine phase PMA SynRM test rig 43

Fig. 2-16 DSP based nine phase inverter 43

Fig. 2-17 Turn fault test setup (a) cable leads (b) turn fault relay. 44

Fig. 2-18 The LABVIEW interface for machine monitoring based on CAN bus communication 44

Fig. 2-19 The LABVIEW interface for machine controlling and data transferring.....45

Fig. 2-20 The performance of current estimation by machine model at 80A (i_d = -53.5A, i_q = 59.5A) at different speeds of (a)250 rpm (b) 500 rpm (c)1000 rpm 46

Fig. 2-21 Comparisons of the positive sequence (a) measured dq currents (b) command dq voltages (c) dq residual currents at 1000rpm 50A with different current controller bandwidths 48

Fig. 2-22 Operating condition of 500 rpm, 50A (i_d = -28.7A, i_q = 41A) 50

Fig. 2-23 Fault detection process and result 50

Fig. 2-24 The variations of the 2nd harmonic magnitude in dq currents and voltages 51

Fig. 2-25 Fault features extraction in dq current residuals at 1000rpm, 50A 51

Fig. 2-26. Variations of negative sequence dq current residuals vector magnitude with speed and current in healthy and turn fault conditions 52

Fig. 2-27 Healthy condition with increasing speed (a) operating condition, (b) fault detection process and result 53

Fig. 2-28 Turn fault condition with increasing speed (a) operating condition, (b) fault detection process and result 54

Fig. 2-29 Healthy condition with current step change (a) operating condition, (b) fault detection process and result 54

Fig. 2-30 Turn fault condition with current step change (a) operating condition, (b) fault detection process and result 55

Fig. 3-1 Geometry of 10-slot, 12-pole SPM machine [61] 58

Fig. 3-2 Schematic of winding under turn fault [61] 58

Fig. 3-3 Comparison of admittance magnitude in healthy and 2 turn fault condition 59

Fig. 3-4 Equivalent circuit under turn fault condition in phase A 59

Fig. 3-5 Phasor plot in fault conditions.....63

Fig. 3-6 (a) Spectrum of SPWM voltage. (b) Spectrum of SPWM voltage after elimination of zero sequence voltages 65

Fig. 3-7 Variations in sideband frequency magnitudes with modulation index 65

Fig. 3-8 Signal processing block diagram of RMS converter.....66

Fig. 3-9 Normalized RMS current variations in phase A under healthy and 2-turn fault conditions with modulation index,.....67

Fig. 3-10 Variations of RMS current ratios with modulation index under healthy and 2-turn fault conditions. 68

Fig. 3-11 HF and RMS currents in both healthy and 2-turn fault conditions 69

Fig. 3-12 Operating conditions 70

Fig. 3-13 RMS ripple current and fault indicator with balanced machine 70

Fig. 3-14 RMS ripple current and fault indicator with unbalanced machine 70

Fig. 3-15 Fault indicator when fault occur in non-stationary state 70

Fig. 3-16 Comparison of fault indicators obtained from the previous and proposed methods in transient state under healthy condition 71

Fig. 3-17(a) Test rig with fault emulation set-up. (b) 5-Phase Inverter with HF detection board 73

Fig. 3-18 Diagram of PWM ripple current based turn fault detection technique 73

Fig. 3-19 Detector output with 2-turn fault in phase A before calibration, with iq=3A and at 500 r/min. 74

Fig. 3-20 Detector output with 2-turn fault in phase A after calibration, with iq=3A and at 500 r/min. 75

Fig. 3-21 Variations of detector output (ph-4) with load (0%,50%,100%) and speed (a) before and (b) after calibration. [61] 76

Fig. 3-22 Variations of ratio k_{AB} with load current and speed before calibration 76

Fig. 3-23 Variations of ratio k_{AB} with modulation index before calibration 76

Fig. 3-24 Variations of calibrated ratio k_{AB} with modulation index under healthy and fault conditions 77

Fig. 3-25 Current waveforms and detector output with load step change of i_q from 0A to 3A at 0.2s in healthy conditions at 500 r/min 78

Fig. 3-26 Current waveforms and detector output with 2-turn fault at 0.2s at i_q=1A, 500 r/min 78

Fig. 3-27 SPM topology under study 79

Fig. 3-28 Equivalent circuit and parameters with turn fault 80

Fig. 3-29 Space vector pulse width modulation 84

Fig. 3-30 (a) Spectrum of SVPWM voltage. (b) Spectrum of SVPWM voltage after elimination of zero sequence voltages 84

Fig. 3-31 Phasor diagrams of HF (a)(c)voltages and (b)(d)currents 86

Fig. 3-32 Control diagram of the three phase SPM in the simulation 87

Fig. 3-33 Torque and speed variations, and fault injection in simulation study of proposed fault detection 88

Fig. 3-34 Turn fault detection results for balanced machine. The RMS detector outputs are proportional to RMS HF current 89

Fig. 3-35 Turn fault detection results for unbalanced machine 89

Fig. 3-36 Phase current, fault current and RMS current detector outputs before calibration when the machine operates at 500 rpm and 50A 90

Fig. 3-37 RMS current detector outputs after calibration, RMS current ratios and standard deviation 91

Fig. 3-38 Variations of the standard deviation as fault indicator with current and speed 93

Fig. 3-39 Variations of the standard deviation as fault indicator with higher currents from simulation 93

Fig. 3-40 Variations of the standard deviation as fault indicator with higher speeds from simulation 94

Fig. 3-41 (a) Phase currents and RMS current detector outputs before calibration in healthy condition at 50 A with increasing speed. (b) RMS current detector outputs after calibration, RMS current ratios and standard deviation 95

Fig. 3-42 (a) Phase currents and RMS current detector outputs before calibration in fault condition at 50A with increasing speed. (b) RMS current detector outputs after calibration, RMS current ratios and standard deviation 95

Fig. 3-43 (a) Phase currents and RMS current detector outputs before calibration in healthy condition at 500rpm with current step change. (b) RMS current detector outputs after calibration, RMS current ratios and standard deviation 96

Fig. 3-44 (a) Phase currents and RMS current detector outputs before calibration in fault condition at 500rpm with current step change. (b) RMS current detector outputs after calibration, RMS current ratios and standard deviation 97

Fig. 3-45 Phase current, fault current and RMS current detector outputs before calibration when the machine operates at 500 rpm and 0A 98

Fig. 3-46 RMS current detector outputs after calibration, RMS current ratios and standard deviation 98

Fig. 3-47 Variations of the standard deviation as fault indicator under no load conditions with different speeds 99

Fig. 4-1 Operating speed, command dq voltages and phase current at 500 rpm, 50A in HRC fault condition 105

Fig. 4-2 Measured and estimated currents, current residuals and their DC components 105

Fig. 4-3 The variations of the 2nd harmonic magnitude in dq currents and voltages 106

Fig. 4-4 Phase currents and RMS current detector outputs before calibration in HRC fault condition at 500 rpm and 50A 107

Fig. 4-5 RMS current detector outputs after calibration, RMS current ratios and standard deviation 107

Fig. 4-6 Equivalent circuit and parameters with turn fault 108

Fig. 4-7 Equivalent circuit and parameters with high resistance connection fault 110

Fig. 4-8 Faults detection and classification steps 114

Fig. 4-9 Dq axis currents and voltages in healthy and turn fault condition at 875 rpm 100A 115

Fig. 4-10 RMS currents and voltages detectors output with their respective ratios in healthy and turn fault conditions 115

Fig. 4-11 High frequency impedance and the fault indicators in healthy and turn fault conditions 116

Fig. 4-12 Dq axis currents and voltages in healthy and HRC fault condition at 875 rpm 100A 117

Fig. 4-13 RMS currents and voltages detectors output with their respective ratios in healthy and HRC fault conditions 117

Fig. 4-14 High frequency impedance and the fault indicators in healthy and HRC fault conditions 118

Fig. 4-15 Healthy condition with current step change (a) Dq axis currents and voltages (b) Ratios of RMS currents, high frequency impedances, and their respective standard deviations 119

Fig. 4-16 Healthy condition with varying speed (a) Dq axis currents and voltages (b) Ratios of RMS currents, high frequency impedances, and their respective standard deviations 119

Fig. 4-17 Schematic of the high resistance connection in the test rig 123

Fig. 4-18 High resistance connection in the test rig 124

Fig. 4-19 Signal processing chain of the designed analogue circuit board 125

Fig. 4-20 The designed signal processing analogue circuit board 125

Fig. 4-21 RMS currents and voltages detectors output with their respective ratios in healthy and turn fault conditions 126

Fig. 4-22 High frequency impedance, their ratios and standard deviations in healthy and turn fault conditions 126

Fig. 4-23 RMS currents and voltages detectors output with their respective ratios in healthy and HRC fault conditions 127

Fig. 4-24 High frequency impedance, their ratios and standard deviations in healthy and HRC fault conditions 127

Fig. 4-25 Variation of the standard deviation of the RMS current ratios with current and speed. 129

Fig. 4-26 Variation of the standard deviation of the high frequency impedance ratios with current and speed. 129

Fig. 4-27 Modified SVPWM modulating signal with square wave signal injection 132

Fig. 4-28 Square wave signal injection implementation in the current control diagram 132

Fig. 4-29 The relationship between the injected square wave signals and the carrier signal 132

Fig. 4-30 The equivalent injected signal referred to the winding neutral point 133

Fig. 4-31 Spectrum of the measurable transformed phase voltage with the resistor network 133

Fig. 4-32 Implementation diagram of the IIR filter 137

Fig. 4-33 The Bode plot of the digital bandpass filter 137

Fig. 4-34 Dq axis voltages and phase currents at 500rpm 50A in healthy and turn fault condition 139

Fig. 4-35 The high frequency currents, RMS detector outputs, and their ratios and standard deviation in healthy and turn fault condition 139

Fig. 4-36 Dq axis voltages and phase currents at 500rpm 50A in healthy and HRC fault condition 140

Fig. 4-37 The high frequency currents, RMS detector outputs, and their ratios and standard deviation in healthy and HRC fault condition 140

Fig. 4-38 Variations of fault indicators with speeds and currents in turn fault and healthy conditions 141

Fig. 4-39 Healthy condition with current step change (a) speed, dq axis voltages and phase currents, (b) the high frequency currents, RMS detector outputs, and their ratios and standard deviation 142

Fig. 4-40 Healthy condition with increasing speed (a) speed, dq axis voltages and phase currents, (b) the high frequency currents, RMS detector outputs, and their ratios and standard deviation 142

Fig. 4-41 Turn fault condition with current step change (a) speed, dq axis voltages and phase currents, (b) the high frequency currents, RMS detector outputs, and their ratios and standard deviation.....143

Fig. 4-42 Turn fault condition with increasing speed (a) speed, dq axis voltages and phase currents, (b) the high frequency currents, RMS detector outputs, and their ratios and standard deviation.....143

Fig. 4-43 Dq axis voltages and phase currents at 500rpm 0A in healthy and turn fault condition.....144

Fig. 4-44 The high frequency currents, RMS detector outputs, and their ratios and standard deviation in healthy and turn fault condition.....144

Fig. 4-45 Variations of fault indicators under no load conditions with different speeds 145

Fig. 5-1 Artificial neutral point and measurement of zero sequence voltage 149

Fig. 5-2 Equivalent circuit in turn fault condition and the measurement of zero sequence voltage.....151

Fig. 5-3 Equivalent circuit in HRC fault condition and the measurement of zero sequence voltage 152

Fig. 5-4 The relationship between the high frequency components of the inverter output voltages and the modulation index.....154

Fig. 5-5 Fault detection and classification steps 156

Fig. 5-6 Simulation result at steady state in healthy and fault conditions.....157

Fig. 5-7 The designed signal processing analogue circuit board for fault detection.....158

Fig. 5-8 Measured currents, zero sequence voltage and other outputs from the signal processing board when turn fault occurs.....159

Fig. 5-9 Spectrum of zero sequence voltage in healthy condition 160

Fig. 5-10 Spectrum of zero sequence voltage in turn fault condition 160

Fig. 5-11. The higher and lower frequency components of the zero sequence voltage when turn fault occurs.....161

Fig. 5-12. The calculation of the high frequency based fault indicator when turn fault occurs 161

Fig. 5-13 Measured currents, zero sequence voltage and other outputs from the signal processing board when HRC fault occurs.....162

Fig. 5-14. The higher and lower frequency components of the zero sequence voltage when HRC fault occurs 163

Fig. 5-15. The calculation of the high frequency based fault indicator when HRC fault occurs 163

Fig. 5-16 Variations of RMS detector output of high frequency zero sequence voltage with speed and current in turn fault, HRC fault and healthy conditions 164

Fig. 5-17 Variation of high frequency based fault indicator with different speeds and currents in turn fault, HRC fault and healthy conditions 165

Fig. 5-18 Variations of fundamental component of zero sequence voltage with speed and current in healthy and HRC fault conditions 166

Fig. 5-19 Variations of fundamental frequency based fault indicator with speed and current in healthy and HRC fault conditions 166

Fig. 5-20 Measured currents, zero sequence voltage and other outputs from the signal processing board when turn fault occurs at no load 167

Fig. 5-21. The frequency components and high frequency based fault indicator when turn fault occurs at no load 168

Fig. 5-22 Variation of high frequency based fault indicator at no load condition with different speeds in turn fault and healthy conditions 168

Fig. 5-23 Healthy condition with current step change 169

Fig. 5-24 Healthy condition with varying speed 170

Fig. 5-25 Turn fault condition with current step change 170

Fig. 5-26 Turn fault condition with varying speed 171

Fig. 6-1 PMA rotor 174

Fig. 6-2 Schematic of the PMA 174

Fig. 6-3 Winding configuration of PMA stator 175

Fig. 6-4 Schematic of power converter and its control 176

Fig. 6-5 Power conditioning PCB 176

Fig. 6-6 Processing platform Red Pitaya 178

Fig. 6-7 Red Pitaya peripheral block diagram 178

Fig. 6-8 Block configuration of FPGA and ARM 179

Fig. 6-9 Data acquisition and FFT execution scheme 180

Fig. 6-10 Block configuration of FPGA and ARM 180

Fig. 6-11 The Fourier calculation scheme 181

Fig. 6-12 PMA installation with AVL dynamometer 182

Fig. 6-13 PMA rear view showing output channels (rear cover removed) 183

Fig. 6-14 Power conditioning enclosure internals 183

Fig. 6-15 PMA power conditioning and measurement system on-test 184

Fig. 6-16 Regulated output operation at 4446rpm 184

Fig. 6-17 Fault execution and fault current 185

Fig. 6-18 Healthy and fault conditions example with an 8-turn fault at 8892 rpm 186

Fig. 6-19 Comparison of 2-, 4- and 8-turn faults at 1482, 4446 and 8892 rpm 187

Fig. 6-20 Fault current comparison at 4446 rpm with regulated output and terminal S/C applied 188

Fig. 6-21 Fault current comparison at 1482 rpm with regulated and terminal s/c applied 189

Fig. 6-22 Zero sequence voltage and processed results at 8892 rpm 191

Fig. 6-23 Zero sequence voltage and processed results at 1482 rpm 191

Fig. 6-24 The comparison of 1st harmonic of zero sequence voltage at different speeds 192

Fig. 6-25 Comparisons of RMS value of zero sequence voltage at different speeds ... 192

Fig. 6-26 Fundamental and RMS value of zero sequence voltage in healthy condition at 1482rpm at two different temperatures 193

Fig. 6-27 Fundamental and its ratio to 3rd harmonic of zero sequence voltage at two different temperatures 194

Fig. 6-28 Comparisons of the ratios between fundamental component and 3rd harmonics of zero sequence voltage at different speeds 194

Fig. 6-29 Fundamental and 3rd harmonic of zero sequence voltage and their ratio at 8892 rpm 196

Fig. 6-30 Fundamental and 3rd harmonic of zero sequence voltage and their ratio at 1482 rpm 196

Fig. 6-31 Comparison of zero sequence voltages in healthy and 2-turn fault conditions at 1482 rpm 197

Fig. 6-32 Comparison of spectra of zero sequence voltage under healthy and 2-turn fault conditions at 1482 rpm 197

Fig. 6-33 Comparisons of (a) lower and (b) higher switching sideband harmonics of zero sequence voltage at different speeds 197

Fig. 6-34 Flow chart of evaluation of the switching sideband components in zero sequence voltage 198

Fig. 6-35 Comparisons of the defined fault indicator based on switching sideband components in zero sequence voltage at different speeds 199

Fig. 6-36 2nd harmonics of current vector at 8892 rpm 201

Fig. 6-37 2nd harmonics of current vector at 1482 rpm 201

Fig. 6-38 Comparisons of 2nd harmonic of current vector at different speeds 201

Fig. 6-39 Current vector and its 2nd harmonic in healthy condition at 1482rpm at two different temperatures 202

Fig. A-1.The block diagram of the signal conditioning circuit board 217

Fig. A-2. The creation of artificial neutral point, and the dividing resistors between it and the phase neutral point 217

Fig. A-3. Phase voltage measurement 218

Fig. A-4. Zero sequence voltage measurement 218

Fig. A-5. High frequency phase current processing 219

Fig. A-6. High frequency phase voltage processing 219

Fig. A-7. High frequency zero sequence voltage processing 219

Fig. A-8. The assembled PCB board for the signal conditioning circuit 220

Fig. A-9. High-level block diagram of XC7Z020 221

Fig. A-10. Block diagram of the signal processing system 221

Fig. A-11. The assembled signal processing system 222

List of Tables

Table 1-1 Comparisons of different machine types 2

Table 1-2 The effects of different faults on the parameters in voltage equations 13

Table 2-1 Machine Specifications 43

Table 3-1 Machine data 61

Table 3-2 Machine parameters under fault conditions 62

Table 3-3 Parameters obtained from fea 80

Table 3-4 Design and operational parameters 87

Table 4-1 Features comparison in healthy and fault conditions 112

Table 4-2 Ratios of RMS currents and high frequency impedance in healthy and fault conditions 113

Table 5-1 Feature comparison of zero sequence voltage in healthy and fault conditions 156

Table 6-1 Estimation of additional fault resistance 186

Table 6-2 Fundamental RMS values for 2-, 4- and 8-turn faults currents at 1482, 4446 and 8892 rpm 187

Table 6-3 RMS values for 2-, 4- and 8-turn fault current with both regulated and terminal short circuit outputs at 4446 rpm 188

Table 6-4 Fundamental rms values for 2-, 4- & 8-turn fault current with both regulated and terminal short circuit outputs at 1482 rpm 189

Table 7-1 Summary and comparisons of all the proposed techniques 206

Bibliography

[1] Z. Q. Zhu and D. Howe, “Electrical Machines and Drives for Electric, Hybrid, and Fuel Cell Vehicles,” *Proc. IEEE*, vol. 95, no. 4, pp. 746–765, 2007.

[2] K. T. Chau, C. C. Chan, and C. Liu, “Overview of permanent-magnet brushless drives for electric and hybrid electric vehicles,” *IEEE Trans. Ind. Electron.*, vol. 55, no. 6, pp. 2246–2257, 2008.

[3] W. Cao, B. C. Mecrow, G. J. Atkinson, J. W. Bennett, and D. J. Atkinson, “Overview of electric motor technologies used for more electric aircraft (MEA),” *IEEE Trans. Ind. Electron.*, vol. 59, no. 9, pp. 3523–3531, 2012.

[4] B. P. Wheeler and S. Bozhko, “The More Electric Aircraft: Technology and challenges,” *IEEE Electrif. Mag.*, vol. 2, no. 4, pp. 6–12, 2014.

[5] B. E. Ganev, “Selecting the Best Electric Machines for Electrical Power-Generation Systems: High-performance solutions for aerospace More electric architectures,” *IEEE Electrif. Mag.*, vol. 2, no. 4, pp. 13–22, 2014.

[6] A. Boglietti, A. Cavagnino, A. Tenconi, S. Vaschetto, P. Torino, I. Elettrica, and C. Duca, “The Safety Critical Electric Machines and Drives in the More Electric Aircraft : a Survey,” *35th Annu. Conf. IEEE Ind. Electron.*, pp. 2587–2594, 2009.

[7] B. Bilgin, P. Magne, P. Malysz, Y. Yang, V. Pantelic, M. Preindl, A. Korobkine, W. Jiang, M. Lawford, and A. Emadi, “Making the Case for Electrified Transportation,” *IEEE Trans. Transp. Electrif.*, vol. 1, no. 1, pp. 4–17, 2015.

[8] M. Zeraoulia, M. El, and H. Benbouzid, “Electric Motor Drive Selection Issues for HEV Propulsion Systems : A Comparative Study,” *IEEE Trans. Veh. Technol.*, vol. 55, no. 6, pp. 1756–1764, 2006.

[9] J. De Santiago, H. Bernhoff, B. Ekergard, S. Eriksson, S. Ferhatovic, R. Waters, and M. Leijon, “Electrical motor drivelines in commercial all-electric vehicles: A review,” *IEEE Trans. Veh. Technol.*, vol. 61, no. 2, pp. 475–484, 2012.

[10] G. Vachtsevanos, F. Lewis, A. Hess, and B. Wu, *Intelligent fault diagnosis and prognosis for engineering systems*. Hoboken: Wiley, 2006.

[11] J. Lee, F. Wu, W. Zhao, M. Ghaffari, L. Liao, and D. Siegel, “Prognostics and

health management design for rotary machinery systems - Reviews , methodology and applications," *Mech. Syst. Signal Process.*, vol. 42, no. 1–2, pp. 314–334, 2014.

[12] S. J. Qin, "Survey on data-driven industrial process monitoring and diagnosis," *Annu. Rev. Control*, vol. 36, no. 2, pp. 220–234, 2012.

[13] M. Shan, A. C. C. Tan, and J. Mathew, "A review on prognostic techniques for non-stationary and non-linear rotating systems," *Mech. Syst. Signal Process.*, vol. 62–63, pp. 1–20, 2015.

[14] A. K. S. J. Ã, D. Lin, and D. Banjevic, "A review on machinery diagnostics and prognostics implementing condition-based maintenance," *Mech. Syst. Signal Process.*, vol. 20, pp. 1483–1510, 2006.

[15] S. Rajagopalan, W. le Roux, T. G. Habetler, and R. G. Harley, "Dynamic eccentricity and demagnetized rotor magnet detection in trapezoidal flux (Brushless DC) motors operating under different load conditions," *IEEE Trans. Power Electron.*, vol. 22, no. 5, pp. 2061–2069, 2007.

[16] E. G. Strangas, S. Aviyente, and S. S. H. Zaidi, "Time-frequency analysis for efficient fault diagnosis and failure prognosis for interior permanent-magnet AC motors," *IEEE Trans. Ind. Electron.*, vol. 55, no. 12, pp. 4191–4199, 2008.

[17] V. Choqueuse, M. E. H. Benbouzid, Y. Amirat, and S. Turri, "Diagnosis of three-phase electrical machines using multidimensional demodulation techniques," *IEEE Trans. Ind. Electron.*, vol. 59, no. 4, pp. 2014–2023, 2012.

[18] N. Daroogheh, N. Meskin, and K. Khorasani, "A novel particle filter parameter prediction scheme for failure prognosis," *Proc. Am. Control Conf.*, pp. 1735–1742, 2014.

[19] R. K. Singleton, E. G. Strangas, and S. Aviyente, "Extended kalman filtering for remaining-useful-life estimation of bearings," *IEEE Trans. Ind. Electron.*, vol. 62, no. 3, pp. 1781–1790, 2015.

[20] P. Boškoski, M. Gašperin, and D. Petelin, "Bearing fault prognostics based on signal complexity and Gaussian process models," *PHM 2012 - 2012 IEEE Int. Conf.on Progn. Heal. Manag. Enhancing Safety, Effic. Availability, Eff. Syst.*

Through PHM Technol. Appl. Conf. Progr., 2012.

[21] IEEE, "Report of Large Motor Reliability Survey of Industrial and Commercial Installations, Part I," *IEEE Trans. Ind. Appl.*, vol. IA-21, no. 4, pp. 853–864, 1985.

[22] A. H. Bonnett and C. Yung, "INCREASED EFFICIENCY VERSUS INCREASED RELIABILITY: A comparison of pre-EPAct, EPAct, and premium-efficient motros," *IEEE Ind. Appl. Mag.*, vol. 14, no. 1, pp. 29–36, 2008.

[23] M. Cheng, J. Hang, and J. Zhang, "Overview of Fault Diagnosis Theory and Method for Permanent Magnet Machine," *Chinese J. Electr. Eng.*, vol. 1, no. 1, pp. 21–36, 2015.

[24] A. H. Bonnett and G. C. Soukup, "Cause and Analysis of Stator and Rotor Failures in Three-phase Squirrel-Cage Induction Motors," *IEEE Trans. Ind. Appl.*, vol. 28, no. 4, pp. 921–937, 1992.

[25] A. Gandhi, T. Corrigan, and L. Parsa, "Recent advances in modeling and online detection of stator interturn faults in electrical motors," *IEEE Trans. Ind. Electron.*, vol. 58, no. 5, pp. 1564–1575, 2011.

[26] B. Vaseghi, N. Takorabet, B. Nahid-Mobarakeh, and F. Meibody-Tabar, "Modelling and study of PM machines with inter-turn fault dynamic model-FEM model," *Electr. Power Syst. Res.*, vol. 81, no. 8, pp. 1715–1722, 2011.

[27] B. Sen and J. Wang, "A High-Fidelity Computationally Efficient Transient Model of Interior Permanent-Magnet Machine With Stator Turn Fault," *IEEE Trans. Ind. Electron.*, vol. 63, no. 2, pp. 773–783, 2016.

[28] M. Zafarani, E. Bostanci, Y. Qi, T. Goktas, and B. Akin, "Inter-turn Short Circuit Faults in Permanent Magnet Synchronous Machines : An Extended Review and Comprehensive Analysis," *IEEE J. Emerg. Sel. Top. Power Electron.*, vol. Early Acce, no. 1, pp. 1–19, 2018.

[29] B. M. Ebrahimi and J. Faiz, "Feature Extraction for Short-Circuit Fault Detection in Permanent-Magnet Synchronous Motors Using Stator-Current Monitoring," *IEEE Trans. Power Electron.*, vol. 25, no. 10, pp. 2673–2682, 2010.

[30] K. H. Kim, "Simple online fault detecting scheme for short-circuited turn in a

PMSM through current harmonic monitoring," *IEEE Trans. Ind. Electron.*, vol. 58, no. 6, pp. 2565–2568, 2011.

[31] H. Jeong, S. Moon, and S. W. Kim, "An Early Stage Interturn Fault Diagnosis of PMSMs by Using Negative-Sequence Components," *IEEE Trans. Ind. Electron.*, vol. 64, no. 7, pp. 5701–5708, 2017.

[32] P. M. De La Barrera, G. R. Bossio, and J. A. Solsona, "High-resistance connection detection in induction motor drives using signal injection," *IEEE Trans. Ind. Electron.*, vol. 61, no. 7, pp. 3563–3573, 2014.

[33] J. Yun, K. Lee, K. W. Lee, S. Bin Lee, and J. Y. Yoo, "Detection and classification of stator turn faults and high-resistance electrical connections for induction machines," *IEEE Trans. Ind. Appl.*, vol. 45, no. 2, pp. 666–675, 2009.

[34] L. Zarri, M. Mengoni, Y. Gritli, A. Tani, F. Filippetti, and S. Bin Lee, "On-line detection of high resistance connections with negative-sequence regulators in three phase induction motor drives," *IEEE Trans. Ind. Appl.*, vol. 51, no. 2, pp. 1579–1586, 2015.

[35] J. Hong, S. Bin Lee, C. Kral, and A. Haumer, "Detection of Airgap Eccentricity for Permanent Magnet Synchronous Motors Based on the d -Axis Inductance," *IEEE Trans. Power Electron.*, vol. 27, no. 5, pp. 2605–2612, 2012.

[36] W. le Roux, R. G. Harley, and T. G. Habetler, "Detecting rotor faults in low power permanent magnet synchronous machines," *IEEE Trans. Power Electron.*, vol. 22, no. 1, pp. 322–328, 2007.

[37] B. M. Ebrahimi, J. Faiz, and B. N. Araabi, "Pattern identification for eccentricity fault diagnosis in permanent magnet synchronous motors using stator current monitoring," *IET Electr. Power Appl.*, vol. 4, no. 6, pp. 418–430, 2010.

[38] B. M. Ebrahimi, J. Faiz, M. Javan-Roshtkhari, and A. Zargham Nejhad, "Static Eccentricity Fault Diagnosis in Permanent Magnet Synchronous Motor Using Time Stepping Finite Element Method," *IEEE Trans. Magn.*, vol. 44, no. 11, pp. 4297–4300, 2008.

[39] B. M. Ebrahimi, J. Faiz, and M. J. Roshtkhari, "Static-, dynamic-, and mixed-eccentricity fault diagnoses in permanent-magnet synchronous motors," *IEEE*

Trans. Ind. Electron., vol. 56, no. 11, pp. 4727–4739, 2009.

[40] P. Zhang, Y. Du, T. G. Habetler, and B. Lu, "A survey of condition monitoring and protection methods for medium-voltage induction motors," *IEEE Trans. Ind. Appl.*, vol. 47, no. 1, pp. 34–46, 2011.

[41] C. Piantsop Mbo'o and K. Hameyer, "Fault diagnosis of bearing damage by means of the linear discriminant analysis of stator current features from the frequency selection," *IEEE Trans. Ind. Appl.*, vol. 9994, no. c, pp. 1–1, 2016.

[42] R. R. Schoen, T. G. Habetler, F. Kamran, and R. G. Bartheld, "Motor bearing damage detection using stator current monitoring," vol. 31, no. 6, pp. 1274–1279, 1995.

[43] J. Faiz and E. Mazaheri-tehrani, "Demagnetization Modeling and Fault Diagnosing Techniques in Permanent Magnet Machines Under Stationary and Nonstationary Conditions : An Overview," *IEEE Trans. Ind. Appl.*, vol. 53, no. 3, pp. 2772–2785, 2017.

[44] J. C. Urresty, J. R. Riba, M. Delgado, and L. Romeral, "Detection of demagnetization faults in surface-mounted permanent magnet synchronous motors by means of the zero-sequence voltage component," *IEEE Trans. Energy Convers.*, vol. 27, no. 1, pp. 42–51, 2012.

[45] J. R. R. Ruiz, A. Garcia Espinosa, L. Romeral, and J. Cusidó, "Demagnetization diagnosis in permanent magnet synchronous motors under non-stationary speed conditions," *Electr. Power Syst. Res.*, vol. 80, no. 10, pp. 1277–1285, 2010.

[46] J. Faiz and H. Nejadi-Koti, "Demagnetization Fault Indexes in Permanent Magnet Synchronous Motors - An Overview," *IEEE Trans. Magn.*, vol. 52, no. 4, pp. 1–11, 2016.

[47] Y. Da, X. Shi, and M. Krishnamurthy, "Health monitoring, fault diagnosis and failure prognosis techniques for brushless permanent magnet machines," *2011 IEEE Veh. Power Propuls. Conf. VPPC 2011*, 2011.

[48] V. Garg, D. Ionel, and M. A. Masrur, "Fault Diagnosis Techniques for Permanent Magnet AC Machine and Drives– A Review of Current State of the Art," *IEEE Trans. Transp. Electrif.*, 2018.

[49] C. Wang, M. D. Prieto, L. Romeral, and Z. Chen, "Detection of Partial Demagnetization Fault in PMSMs Operating Under Nonstationary Conditions," *IEEE Trans. Magn.*, vol. 52, no. 7, pp. 1–4, 2016.

[50] J. Cusido, L. Romeral, J. a. Ortega, J. a. Rosero, and A. Garcia Espinosa, "Fault Detection in Induction Machines Using Power Spectral Density in Wavelet Decomposition," *IEEE Trans. Ind. Electron.*, vol. 55, no. 2, pp. 633–643, 2008.

[51] Z. Gao, C. Cecati, and S. X. Ding, "A Survey of Fault Diagnosis and Fault-Tolerant Techniques Part I: Fault Diagnosis," *IEEE Trans. Ind. Electron.*, vol. 62, no. 6, pp. 3768–3774, 2015.

[52] J. A. Rosero, L. Romeral, J. A. Ortega, and E. Rosero, "Short-circuit detection by means of empirical mode decomposition and Wigner-Ville distribution for PMSM running under dynamic condition," *IEEE Trans. Ind. Electron.*, vol. 56, no. 11, pp. 4534–4547, 2009.

[53] Y. Zhao, L. E. Atlas, and R. J. Marks, "The Use of Cone-Shaped Kernels for Generalized Time-Frequency Representations of Nonstationary Signals," *IEEE Trans. Acoust.*, vol. 38, no. 7, pp. 1084–1091, 1990.

[54] J.-C. Urresty, J.-R. Riba, H. Saavedra, and L. Romeral, "Detection of inter-turns short circuits in permanent magnet synchronous motors operating under transient conditions by means of the zero sequence voltage," *Proc. 14th Eur. Conf. Power Electron. Appl.*, pp. 1–9, 2011.

[55] Y. Mollet, X. Kestelyn, F. Meinguet, E. Semail, and J. Gyselinck, "Change-detection algorithm for short-circuit fault detection in closed-loop AC drives," *IET Electr. Power Appl.*, vol. 8, no. 5, pp. 165–177, 2014.

[56] J. Hang, J. Zhang, M. Cheng, and J. Huang, "Online Inter-turn Fault Diagnosis of Permanent Magnet Synchronous Machine Using Zero Sequence Components," *IEEE Trans. Power Electron.*, vol. 30, no. 12, pp. 6731–6741, 2015.

[57] Z. Sun, J. Wang, D. Howe, and G. W. Jewell, "An online winding fault detection technique for fault-tolerant PM machines," *Int. J. Syst. Sci.*, vol. 40, no. 3, pp. 289–296, 2009.

[58] J. C. Urresty, J. R. Riba, and L. Romeral, "Diagnosis of interturn faults in pmsms

operating under nonstationary conditions by applying order tracking filtering," *IEEE Trans. Power Electron.*, vol. 28, no. 1, pp. 507–515, 2013.

[59] M. S. Islam, S. Cho, and U. Chong, "Bearing Fault Detection and Identification using Adaptive Filter and Computed Order Tracking," *5th Int. Conf. Informatics, Electron. Vis.*, pp. 322–327, 2016.

[60] F. Briz, M. W. Degner, A. Zamarron, and J. M. Guerrero, "Online Stator Winding Fault Diagnosis in Inverter-Fed AC Machines Using High-Frequency Signal Injection," *IEEE Trans. Ind. Appl.*, vol. 39, no. 4, pp. 1109–1117, 2003.

[61] B. Sen and J. Wang, "Stator Interturn Fault Detection in Permanent-Magnet Machines Using PWM Ripple Current Measurement," *IEEE Trans. Ind. Electron.*, vol. 63, no. 5, pp. 3148–3157, 2016.

[62] J. Zhang, J. Hang, S. Ding, and M. Cheng, "Online Diagnosis and Localization of High-Resistance Connection in PMSM With Improved Fault Indicator," *IEEE Trans. Power Electron.*, vol. 32, no. 5, pp. 3585–3594, 2017.

[63] S. Grubic, J. M. Aller, B. Lu, and T. G. Habetler, "A survey on testing and monitoring methods for stator insulation systems of low-voltage induction machines focusing on turn insulation problems," *IEEE Trans. Ind. Electron.*, vol. 55, no. 12, pp. 4127–4136, 2008.

[64] R. Z. Haddad and E. G. Strangas, "On the Accuracy of Fault Detection and Separation in Permanent Magnet Synchronous Machines using MCSA/MVSA and LDA," *IEEE Trans. Energy Convers.*, vol. 31, no. 3, pp. 924–934, 2015.

[65] W. T. Thomson and M. Fenger, "Current signature analysis to detect induction motor faults," *IEEE Ind. Appl. Mag.*, vol. 7, no. 4, pp. 26–34, 2001.

[66] N. H. Obeid, T. Boileau, and B. Nahid-Mobarakeh, "Modeling and diagnostic of incipient inter-turn faults for a three phase permanent magnet synchronous motor," *2014 IEEE Ind. Appl. Soc. Annu. Meet. IAS 2014*, pp. 1–8, 2014.

[67] H. Saavedra, J. C. Urresty, J. R. Riba, and L. Romeral, "Detection of interturn faults in PMSMs with different winding configurations," *Energy Convers. Manag.*, vol. 79, pp. 534–542, 2014.

[68] A. Bellini, "Closed-loop control impact on the diagnosis of induction motors

faults," *IEEE Trans. Ind. Appl.*, vol. 36, no. 5, pp. 1318–1339, 2000.

[69] W. Le Roux, R. G. Harley, and T. G. Habetler, "Detecting faults in rotors of PM drives: Effects of the speed-controller bandwidth in permanent magnet synchronous machines," *IEEE Ind. Appl. Mag.*, vol. 14, no. 2, pp. 23–31, 2008.

[70] T. Boileau, N. Leboeuf, B. Nahid-Mobarakeh, and F. Meibody-Tabar, "Stator winding inter-turn fault detection using control voltages demodulation," *2012 IEEE Transp. Electrif. Conf. Expo, ITEC 2012*, vol. 1, 2012.

[71] K.-H. Kim, D.-U. Choi, B.-G. Gu, and I.-S. Jung, "Online fault-detecting scheme of an inverter-fed permanent magnet synchronous motor under stator winding shorted turn and inverter switch open," *IET Electr. Power Appl.*, vol. 4, no. 4, p. 214, 2010.

[72] M. Drif and A. J. M. Cardoso, "Stator Fault Diagnostics in Squirrel Cage Three-Phase Induction Motor Drives Using the Instantaneous Active and Reactive Power Signature Analyses," *IEEE Trans. Ind. Informatics*, vol. 10, no. 2, pp. 1348–1360, 2014.

[73] B. Wang, J. Wang, A. Griffo, and B. Sen, "Stator Turn Fault Detection by Second Harmonic in Instantaneous Power for a Triple-Redundant Fault-Tolerant PM Drive," *IEEE Trans. Ind. Electron.*, vol. 65, no. 9, pp. 7279–7289, 2018.

[74] S. M. A. Cruz and A. J. Marques Cardoso, "Stator winding fault diagnosis in three-phase synchronous and asynchronous motors, by the extended park's vector approach," *IEEE Trans. Ind. Appl.*, vol. 37, no. 5, pp. 1227–1233, 2001.

[75] A. J. Marques Cardoso, S. M. A. Cruz, and D. S. B. Fonseca, "Inter-turn stator winding fault diagnosis in three-phase induction motors, by Park's vector approach," *IEEE Trans. Energy Convers.*, vol. 14, no. 3, pp. 595–598, 1999.

[76] S. Das, P. Purkait, D. Dey, and S. Chakravorti, "Monitoring of inter-turn insulation failure in induction motor using advanced signal and data processing tools," *IEEE Trans. Dielectr. Electr. Insul.*, vol. 18, no. 5, pp. 746–751, 2002.

[77] R. M. Tallam, T. G. Habetler, and R. G. Harley, "Stator winding turn-fault detection for closed-loop induction motor drives," *IEEE Trans. Ind. Appl.*, vol. 39, no. 3, pp. 720–724, 2003.

[78] S. Bin Lee, R. M. Tallam, and T. G. Habetler, "A robust, on-line turn-fault detection technique for induction machines based on monitoring the sequence component impedance matrix," *IEEE Trans. Power Electron.*, vol. 18, no. 3, pp. 865–872, 2003.

[79] S. Cheng, P. Zhang, and T. G. Habetler, "An impedance identification approach to sensitive detection and location of stator turn-to-turn faults in a closed-loop multiple-motor drive," *IEEE Trans. Ind. Electron.*, vol. 58, no. 5, pp. 1545–1554, 2011.

[80] P. Neti and S. Nandi, "Stator interturn fault detection of synchronous machines using field current and rotor search-coil voltage signature analysis," *IEEE Trans. Ind. Appl.*, vol. 45, no. 3, pp. 911–920, 2009.

[81] G. N. Surya, Z. J. Khan, M. S. Ballal, and H. M. Suryawanshi, "A Simplified Frequency-Domain Detection of Stator Turn Fault in Squirrel-Cage Induction Motors Using an Observer Coil Technique," *IEEE Trans. Ind. Electron.*, vol. 64, no. 2, pp. 1495–1506, 2017.

[82] Y. Da, X. Shi, and M. Krishnamurthy, "A new approach to fault diagnostics for permanent magnet synchronous machines using electromagnetic signature analysis," *IEEE Trans. Power Electron.*, vol. 28, no. 8, pp. 4104–4112, 2013.

[83] H. Henao, C. Demian, and G. A. Capolino, "A frequency-domain detection of stator winding faults in induction machines using an external flux sensor," *IEEE Trans. Ind. Appl.*, vol. 39, no. 5, pp. 1272–1279, 2003.

[84] M. A. Awadallah, M. M. Morcos, S. Gopalakrishnan, and T. W. Nehl, "Detection of Stator Short Circuits in VSI-Fed Brushless DC Motors Using Wavelet Transform," *IEEE Trans. Energy Convers.*, vol. 21, no. 1, pp. 1–8, 2006.

[85] M. A. Awadallah, M. M. Morcos, S. Gopalakrishnan, and T. W. Nehl, "A Neuro-Fuzzy Approach to Automatic Diagnosis and Location of Stator Inter-Turn Faults in CSI-Fed PM Brushless DC Motors," *IEEE Trans. Energy Convers.*, vol. 20, no. 2, pp. 253–259, 2005.

[86] W. G. Zanardelli, E. G. Strangas, and S. Aviyente, "Identification of Intermittent Electrical and Mechanical Faults in Permanent Magnet AC Drives Based on Time-Frequency Analysis," *IEEE Trans. Ind. Appl.*, vol. 43, no. 4, pp. 1–10,

2007.

[87] O. A. Mohammed, Z. Liu, S. Liu, and N. Y. Abed, “Internal short circuit fault diagnosis for PM machines using FE-based phase variable model and wavelets analysis,” *IEEE Trans. Magn.*, vol. 43, no. 4, pp. 1729–1732, 2007.

[88] J. Rosero, A. G. Espinosa, J. Cusido, J. A. Ortega, and L. Romeral, “Simulation and fault detection of short circuit winding in a permanent magnet synchronous machine (PMSM) by means of fourier and wavelet transform,” *IEEE Instrum. Meas. Technol. Conf.*, pp. 411–416, 2008.

[89] M. Youse, M. Khedri, H. Reza, M. Ali, and S. Nejad, “Hybrid modelling of doubly fed induction generators with inter-turn stator fault and its detection method using wavelet analysis,” *IET Gener. Transm. Distrib.*, vol. 7, no. 9, pp. 982–990, 2013.

[90] J. Seshadrinath, B. Singh, and B. K. Panigrahi, “Incipient turn fault detection and condition monitoring of induction machine using analytical wavelet transform,” *IEEE Trans. Ind. Appl.*, vol. 50, no. 3, pp. 2235–2242, 2012.

[91] J. Seshadrinath, B. Singh, and B. K. Panigrahi, “Single-Turn Fault Detection in Induction Machine Using Complex-Wavelet-Based Method,” *IEEE Trans. Ind. Appl.*, vol. 48, no. 6, pp. 1846–1854, 2012.

[92] D. Bayram and S. Serhat, “Redundancy-Based Predictive Fault Detection on Electric Motors by Stationary Wavelet Transform,” *IEEE Trans. Ind. Appl.*, vol. 53, no. 3, pp. 2997–3004, 2017.

[93] M. Khan and M. a. Rahman, “Development and Implementation of a Novel Fault Diagnostic and Protection Technique for IPM Motor Drives,” *IEEE Trans. Ind. Electron.*, vol. 56, no. 1, pp. 85–92, 2009.

[94] H.-I. Choi and W. J. Williams, “Improved Time-Frequency Representations of Multicomponent Signals Using Exponential Kernels,” *IEEE Trans. Acoust. speech and, signal Process.*, vol. 37, no. 6, pp. 862–870, 1989.

[95] S. Rajagopalan, J. M. Aller, J. A. Restrepo, T. G. Habetler, and R. G. Harley, “Detection of rotor faults in brushless DC motors operating under nonstationary conditions,” *IEEE Trans. Ind. Appl.*, vol. 42, no. 6, pp. 1464–1477, 2006.

[96] S. Rajagopalan, J. A. Restrepo, J. M. Aller, T. G. Habetler, and R. G. Harley, "Selecting time-frequency representations for detecting rotor faults in BLDC motors operating under rapidly varying operating conditions," *IECON Proc. (Industrial Electron. Conf.*, vol. 2005, pp. 2585–2590, 2005.

[97] S. Rajagopalan, J. A. Restrepo, J. M. Aller, T. G. Habetler, and R. G. Harley, "Nonstationary motor fault detection using recent quadratic time-frequency representations," *IEEE Trans. Ind. Appl.*, vol. 44, no. 3, pp. 735–744, 2008.

[98] K. R. Fyfe and E. D. S.Munck, "Analysis of computed order tracking," *Mech. Syst. Signal Process.*, vol. 11, no. 2, pp. 187–205, 1997.

[99] M. Akar, "Detection of a static eccentricity fault in a closed loop driven induction motor by using the angular domain order tracking analysis method," *Mech. Syst. Signal Process.*, vol. 34, no. 1–2, pp. 173–182, 2013.

[100] A. Brandt and A. E. Ab, "Main Principles and Limitations of Current Order Tracking Methods," *Sound Vib.*, no. March, pp. 19–22, 2005.

[101] K. Wang, "A Comparison between Two Conventional Order Tracking Techniques in Rotating Machine Diagnostics," *2011 Int. Conf. Qual. Reliab. Risk, Maintenance, Saf. Eng.*, no. 1, pp. 1–4, 2011.

[102] N. Leboeuf, T. Boileau, B. Nahid-Mobarakeh, G. Clerc, and F. Meibody-Tabar, "Real-time detection of interturn faults in PM drives using back-EMF estimation and residual analysis," *IEEE Trans. Ind. Appl.*, vol. 47, no. 6, pp. 2402–2412, 2011.

[103] B. Sen and J. Wang, "A Fast Detection Technique for Stator Inter-turn Fault in Multi- Phase Permanent Magnet Machines using Model Based Approach," in *IET International Conference on Power Electronics, machines and Drive*, 2014, pp. 1–6.

[104] C. H. De Angelo, G. R. Bossio, S. J. Giaccone, and Etc, "Online model-based stator-fault detection and identification in induction motors," *IEEE Trans. Ind. Electron.*, vol. 56, no. 11, pp. 4671–4680, 2009.

[105] S. Moon, H. Jeong, H. Lee, and S. W. Kim, "Interturn Short Fault Diagnosis in a PMSM by Voltage and Current Residual Analysis With the Faulty Winding

Model," *IEEE Trans. Energy Convers.*, vol. 33, no. 1, pp. 190–198, 2018.

[106] B. Vaseghi, B. Nahid-Mobarakh, N. Takorabet, and F. Meibody-Tabar, "Inductance identification and study of PM motor with winding turn short circuit fault," *IEEE Trans. Magn.*, vol. 47, no. 5, pp. 978–981, 2011.

[107] B. Wang, J. Wang, B. Sen, A. Griffo, Z. Sun, and E. Chong, "A Fault-Tolerant Machine Drive Based on Permanent Magnet-Assisted Synchronous Reluctance Machine," *IEEE Trans. Ind. Appl.*, vol. 54, no. 2, pp. 1349–1359, 2018.

[108] F. Briz, M. Degner, a. B. Diez, and J. M. Guerrero, "Online Diagnostics in Inverter-Fed Induction Machines Using High-Frequency Signal Injection," *IEEE Trans. Ind. Appl.*, vol. 40, no. 4, pp. 1153–1161, 2004.

[109] F. Briz, M. W. Degner, P. García, and A. B. Diez, "High-frequency carrier-signal voltage selection for stator winding fault diagnosis in inverter-fed AC machines," *IEEE Trans. Ind. Electron.*, vol. 55, no. 12, pp. 4181–4190, 2008.

[110] J. Arellano-padilla, M. Sumner, and C. Gerada, "Winding condition monitoring scheme for a permanent magnet machine using high-frequency injection," *IET Electr. Power Appl.*, vol. 5, no. 1, pp. 89–99, 2011.

[111] N. Teske, G. M. Asher, K. J. Bradley, and M. Sumner, "Analysis and Suppression of Inverter Clamping Saliency in Sensorless Position Controlled Induction Machine Drives," *Proc. IEEE- IAS Annu. Meet. Chicago, Sept.*, 2001.

[112] S. C. Yang, "Online Turn Fault Detection of Interior Permanent-Magnet Machines Using the Pulsating-Type Voltage Injection," *IEEE Trans. Ind. Appl.*, vol. 52, no. 3, pp. 2340–2349, 2016.

[113] S. Kim, J. Ha, and S. Sul, "PWM Switching Frequency Signal Injection Sensorless Method in IPMSM," *IEEE Trans. Ind. Appl.*, vol. 48, no. 5, pp. 1576–1587, 2012.

[114] A. A. Khan and O. Mohammed, "Neural Network based Modeling of Audible Noise for High Frequency Injection based Position Estimation for PM Synchronous Motors at Low and Zero speed," *IEEE Electr. Sh. Technol. Symp. 2009, ESTS*, pp. 119–122, 2009.

[115] T. Lipo and D. G. Holmes, "Pulse Width Modulation for Power Converters," no.

Wiley-IEEE Press, 2003.

[116] D. G. Holmes, "A general analytical method for determining the theoretical harmonic components of carrier based PWM strategies," *Conf. Rec. 1998 IEEE Ind. Appl. Conf. Thirty-Third IAS Annu. Meet.*, vol. 2, no. 2, pp. 1207–1214, 1998.

[117] R. D. Naybour and T. Farrell, "Degradation mechanisms of mechanical connectors on aluminium conductors," *Proc. Inst. Electr. Eng.*, vol. 120, no. 2, pp. 273–280, 1973.

[118] M. Braunovic, "Effect of Connection Design on the Contact Resistance of High Power Overlapping Bolted Joints," *IEEE Trans. Components Packag. Technol.*, vol. 25, no. 4, pp. 642–650, 2002.

[119] J. Yun, J. Cho, S. Bin Lee, and J. Y. Yoo, "Online detection of high-resistance connections in the incoming electrical circuit for induction motors," *IEEE Trans. Ind. Appl.*, vol. 45, no. 2, pp. 694–702, 2009.

[120] M. Bara and A. Polak, "Thermographic diagnostic of Electrical Machines," *Electr. Mach. (ICEM), 2010 XIX Int. Conf.*, pp. 42–44, 2010.

[121] G. Stojcic and T. M. Wolbank, "Detecting high-resistance connection asymmetries in inverter fed AC drive systems," *Proc. - 2013 9th IEEE Int. Symp. Diagnostics Electr. Mach. Power Electron. Drives, SDEMPED 2013*, pp. 227–232, 2013.

[122] P. M. De Barrera, G. R. Bossio, and R. Leidhold, "On Line Voltage Sensorless High-Resistance Connection Diagnosis in Induction Motor Drives," *IEEE Trans. Ind. Electron.*, vol. 62, no. 7, pp. 4374–4384, 2015.

[123] M. Mengoni, L. Zarri, A. Tani, Y. Gritli, G. Serra, F. Filippetti, and D. Casadei, "Online Detection of High-Resistance Connections in Multiphase Induction Machines," *IEEE Trans. Power Electron.*, vol. 30, no. 8, pp. 4505–4513, 2015.

[124] L. Zarri, M. Mengoni, Y. Gritli, A. Tani, F. Filippetti, G. Serra, and D. Casadei, "Detection and localization of stator resistance dissymmetry based on multiple reference frame controllers in multiphase induction motor drives," *IEEE Trans. Ind. Electron.*, vol. 60, no. 8, pp. 3506–3518, 2013.

[125] J. Hang, J. Zhang, M. Cheng, B. Zhang, and S. Ding, "High-Resistance

Connection Detection in Permanent Magnet Synchronous Machine Using Zero-Sequence Current Component," *IEEE Trans. Power Electron.*, vol. 31, no. 7, pp. 4710–4719, 2016.

[126] J. Hang, J. Zhang, S. Ding, and M. Cheng, "Fault Diagnosis of High-Resistance Connection in a Machine Considering the Neutral-Point Connection Model," *IEEE Trans. Power Electron.*, vol. 32, no. 8, pp. 6444–6454, 2017.

[127] J. U. J. Riba, L. Romeral, and J. Antonio, "Mixed resistive unbalance and winding inter-turn faults model of permanent magnet synchronous motors," *Electr. Eng.*, no. 97, pp. 75–85, 2015.

[128] P. M. De Barrera, R. Leidhold, and G. R. Bossio, "On-Line Diagnosis of High-Resistance Connection for Inverter Fed Induction Motors," *Power Electron. Mach. Drives (PEMD 2014), 7th IET Int. Conf.*, 2014.

[129] R. Roshanfekr and A. Jalilian, "Wavelet-based index to discriminate between minor inter-turn short-circuit and resistive asymmetrical faults in stator windings of doubly fed induction generators : a simulation study," *IET Gener. Transm. Distrib.*, vol. 10, no. 2, pp. 374–381, 2016.

[130] B. Sen, "Modelling , Fault Detection and Control of Fault Tolerant Permanent Magnet Machine Drives," *PhD thesis, Univ. Sheff.*, no. September, 2015.

[131] M. W. Degner and R. D. Lorenz, "Using Multiple Saliencies for the Estimation of Flux , Position , and Velocity in AC Machines," *IEEE Trans. Ind. Appl.*, vol. 34, no. 5, pp. 1097–1104, 1998.

[132] J. M. Liu and Z. Q. Zhu, "Novel Sensorless Control Strategy With Injection of High-Frequency Pulsating Carrier Signal Into Stationary Reference Frame," *IEEE Trans. Ind. Appl.*, vol. 50, no. 4, pp. 2574–2583, 2014.

[133] S.-I. Kim, J.-H. Im, E.-Y. Song, and R.-Y. Kim, "A New Rotor Position Estimation Method of IPMSM Using All-Pass Filter on High-Frequency Rotating Voltage Signal Injection," *IEEE Trans. Ind. Electron.*, vol. 63, no. 10, pp. 6499–6509, 2016.

[134] F. Briz, M. W. Degner, J. M. Guerrero, A. Zamarrón, and R. D. Lorenz, "Implementation Issues Affecting the Performance of Carrier Signal Injection

Based Sensorless Controlled AC Drives," *Conf. Rec. 2001 IEEE Ind. Appl. Conf. 36th IAS Annu. Meet. , Chicago, IL, USA*, vol. 4, pp. 2645–2652, 2001.

[135] H. Saavedra, J. R. Riba, and L. Romeral, "Detection of inter-turn faults in five-phase permanent magnet synchronous motors," *Adv. Electr. Comput. Eng.*, vol. 14, no. 4, pp. 49–54, 2014.

[136] P. García, F. Briz, M. W. Degner, and A. B. Diez, "Diagnostics of induction machines using the zero sequence voltage," *Conf. Rec. - IAS Annu. Meet. (IEEE Ind. Appl. Soc.*, vol. 2, no. 2, pp. 735–742, 2004.

[137] B. Vaseghi, N. Takorabet, and F. Meibody-Tabar, "Fault Analysis and Parameter Identification of Permanent-Magnet Motors by the Finite-Element Method," *IEEE Trans. Magn.*, vol. 45, no. 9, pp. 3290–3295, 2009.